

Theory of spatiotemporal control of optical excitations in nanostructures and their application to coherent spectroscopy

Vorgelegt von
Felix Schlosser
aus Lauterbach

von der Fakultät II – Mathematik und Naturwissenschaften
der Technischen Universität Berlin

zur Erlangung des akademischen Grades
Doktor der Naturwissenschaften
– Dr. rer. nat. –

genehmigte Dissertation

Promotionsausschuss

Vorsitzende: Prof. Dr. rer. nat. Ulrike Woggon, TU Berlin

1. Gutachter: Prof. Dr. rer. nat. Andreas Knorr, TU Berlin

2. Gutachter: Prof. Dr.-Ing. Frank Schmidt, Zuse-Institut Berlin

Tag der wissenschaftlichen Aussprache: 12. Dezember 2012

Berlin, 2013

D83

Zusammenfassung

Optische Technologien sind ein sich aktuell schnell entwickelnder Zweig in der Physik. Sie ermöglichen eine Vielzahl von Anwendungen des modernen Lebens. Effiziente Bauelemente bestehen aus optischen Komponenten, deren Abmessungen nur wenige Nanometer betragen. Der Schwerpunkt dieser rein theoretischen Arbeit liegt in der Untersuchung von Metallnanostrukturen hinsichtlich räumlicher und zeitlicher Kontrolle der optischen Anregungen unter Lichteinfall sowie in Anwendungen dieser Lokalisierung. Die Ergebnisse dieser Arbeit unterteilen sich in drei Themen.

Das erste Thema befasst sich mit den Eigenschaften von Metallnanostrukturen. Zuerst wird ein theoretisches Modellsystem für Metalle eingeführt und als Ergebnis werden die Bandstruktur und die Dipolübergangsmatrixelemente von Silber berechnet. Plasmonische Effekte von (Hybrid-)Nanokügelchen werden zur Vorbereitung der Mechanismen für die Lokalisierung von Licht untersucht. Nanoplasmonik beschreibt optische Effekte, die auf Oszillationen des Plasmas der Nanometallsysteme beruhen. Solche Systeme erlauben die Konzentration der optischen Energie in der Größenordnung von Nanometern und Femtosekunden. Ermöglicht wird dies durch Moden, die man Oberflächenplasmonen nennt. Zur raumzeitlichen Lokalisierung von elektromagnetischen Feldern müssen Materialeigenschaften und geometrische Konfigurationen beachtet werden. Beispielsweise werden in dieser Dissertation Resonanzen von unterschiedlichen Metallen für verschiedene Wellenlängen untersucht. Außerdem wird gezeigt, dass nichtresonante Metallschichten für die betrachteten Wellenlängen die Feldverstärkung auf der Oberfläche über eine lange Distanz übertragen und dass durch Abschirmung sinkende Verstärkungen durch die Kopplung von zwei Nanokügelchen kompensiert werden können.

Die zweite Thematik befasst sich mit dem gleichzeitigen Einschränken von optischen Anregungen auf Nanometer-Längenskalen und auf Femtosekunden-Zeitskalen. Die Ortsauflösung von optischen Messungen wird jedoch für konventionelle Lichtquellen durch die Wellenlänge des einfallenden Lichts begrenzt. Dennoch ist eine Lokalisierung unterhalb der Beugungsgrenze wünschenswert, weil sie eine Vielzahl von neuen Methoden zur Untersuchung von Nanosystemen eröffnet. Ermöglicht wird dies durch die Kombination von Nanoplasmonik mit Pulsformungstechniken. Als Lokalisierungsmechanismus dienen Interferenzen von Nah- und Fernfeldern und Polarisierungseffekte. Um die Pulse zu finden, welche die gewünschte Lokalisierung liefern, wird im zentralen Teil dieser Arbeit ein genetischer Algorithmus entworfen, der die Form der eingestrahlten Lichtpulse optimiert. Unterschiedliche Geometrien weisen verschiedene Optimierungsqualitäten auf. Gute Lokalisierungen erhält man durch Metallspitzen oder antennenähnliche Anordnung, welche die Anregung in die Nanostruktur führen.

Das letzte Thema stellt eine Anwendung der erzielten raumzeitlichen Lokalisierung dar. Angewendet wird diese auf komplexen Nanostrukturen wie beispielsweise Halbleiterquantenpunkte oder Farbstoffpigmente, die in Proteinen eingebettet sind, Lichtsammelkomplexe bilden und als optische Emmitter dienen. Wenn diese dicht beieinander angeordnet werden, koppeln sie über Coulombkräfte. Diese Dipol-Dipol-Kopplung zwischen einzelnen Emmitern auf einer Nanometerskala führt zur Bildung neuer kollektiver hybridisierter Quantenzustände, die über die gesamte Nanostruktur delokalisiert sind.

Das wichtigste Ergebnis dieser Arbeit stellt eine neue Art von Quantenzustandtomographie dar. Diese löst die individuellen Beiträge aus der kollektiven optischen Antwort der gekoppelten Emmitter in einer räumlich ausgedehnten Nanostruktur mithilfe lokalisierter Nahfeldspektroskopie auf. Eine kohärente, nichtlineare, mehrdimensionale Spektroskopiemethode (die Methode der doppelten Quantenkohärenz) wird mit Techniken, die das Licht konzentrieren, kombiniert. Vielteilchenwellenfunktionen von gekoppelten Quantenpunkten können durch die Ermittlung der Entwicklungskoeffizienten der Basisdarstellung mithilfe einer Pulssequenz aus drei Lichtpulsen mit kontrollierter Einhüllenden und Phase sowohl für Exzitonen- als auch für Biexzitonenzustände rekonstruiert werden (bis auf eine beliebige Phase). Die Qualität der Rekonstruktion hängt unter anderem von der Qualität der raumzeitlichen Lokalisierung und dem Einfluss von Nachbarresonanzen ab. Filtermethoden können diese Einflüsse reduzieren und verbessern folglich die Rekonstruktion. Insgesamt können mehr Informationen gewonnen werden als nur mithilfe von zweidimensionaler Spektroskopie oder Lokalisation alleine.

Abstract

Recently, optical technologies are a rapidly developing branch of physics with a lot of applications in modern lifestyle. Efficient devices consist of optical components with spatial dimensions of only a few nanometers. The focus of this purely theoretical thesis is to investigate and to control the optical excitations in metal nanostructures simultaneously in space and time under the influence of light and applications of this spatiotemporal control. The results of this thesis are composed of three topics.

The first topic deals with properties of metal nanostructures. A theoretical model system for metals is introduced and as first result, the band structure and dipole transition matrix elements of silver are calculated. Plasmonic effects of metal (hybrid) nanospheres are examined in preparation for the mechanisms of controlling light. Nanoplasmonics describes optical effects based on plasma oscillations of nanostructured metal systems. These systems can keep the optical energy concentrated on nanometer scale and femtosecond scale, enabled by modes called surface plasmons. For spatiotemporally localized enhancement of the electromagnetic field, material properties and geometry settings have to be considered: For example, resonances of different metals at different wavelengths are examined. It is also shown that nonresonant metal layers for the considered wavelengths can transfer field enhancement on the surface over a long distance and that decreasing enhancements due to the screening of thick coatings can be compensated by coupling of two nanospheres.

The second topic deals with confining optical excitations simultaneously on a nanometer length scale and on a femtosecond time scale. For conventional light sources, however, the spatial resolution of optical measurements is limited by the wavelength of the incident light. Still, achieving electronic control below the diffraction limit is desirable because it opens a number of novel methods in investigating nanosystems. It becomes possible by combining nanoplasmonics with pulse shaping techniques. Interferences of near and far fields and polarization effects serve as control mechanism. To find the pulses that supply the desired localization, in the central part of the thesis a genetic algorithm that optimizes the shape of the incoming pulses is generated. Different geometries show varying optimization quality. Good localizations are achieved by using metal tips or antenna-like geometries that guide excitations into the nanostructure.

The last topic is an application of the achieved spatiotemporal control. Control is applied to complex (hybrid) nanostructures (e.g. semiconductor quantum dots or pigments embedded in proteins such as in light harvesting complexes), that serve as optical emitters. If they are placed in vicinity, they couple via Coulomb forces. This dipole-dipole coupling on nanometer scale between individual emitters leads to the formation of new collective hybridized quantum states that are delocalized over the entire nanostructure.

The main result of this work is a new kind of quantum state tomography that disentangles the individual contributions of the coupled emitters in a spatially extended nanostructure from the collective optical response via localized near field spectroscopy. A coherent nonlinear multidimensional spectroscopy method (the double quantum coherence) is combined with light concentrating techniques. Many-particle wave functions of coupled quantum dots for exciton as well as for biexciton states can be reconstructed (up to an arbitrary phase) by finding the expansion coefficients of the basis representation by using a sequence of three polarization shaped light pulses with controlled envelopes and phases. The quality of reconstruction depends among others on the quality of spatiotemporal control and on influences of neighboring resonances. Filtering methods can reduce these influences and thus improve the quality of reconstruction. In all, more information about the system can be revealed than by using two-dimensional spectroscopy or localization alone.

Contents

Zusammenfassung	iii
Abstract	v
Contents	ix
List of Figures	xii
List of Tables	xiii
I Prologue	1
1 Introduction	3
II Localization	7
2 Metals	9
2.1 Electromagnetism of metals	9
2.1.1 Maxwell's equations	9
2.1.2 Linear relationships in materials	10
2.1.3 Wave equations	11
2.1.4 Plane waves	11
2.1.5 Dielectric function	12
2.1.6 Beer-Lambert law	13
2.2 Material model	13
2.2.1 Drude model	13
2.2.2 Equations of motion for the polarization	15
2.2.3 Parameters	16
2.3 Electronic structure	18
2.3.1 Band structure calculations	19
2.3.2 Electron configuration and hydrogen wave functions	20
2.3.3 Dipole transition matrix elements	24
2.3.4 Linear absorption	24
3 Nanoplasmonics	27
3.1 Pure metal nanospheres	28
3.2 Hybrid nanospheres	29
3.3 Coupled nanospheres	31
3.4 Induced surface enhancement	33
4 Numerical Simulations	37
4.1 Finite element method	37
4.1.1 Variational equation	38

Contents

4.1.2	Basic concept	39
4.1.3	Convergence	42
4.1.4	Triangulation	44
4.2	Problem classes	44
4.2.1	Resonance mode problems	45
4.2.2	Propagating mode problems	45
4.2.3	Scattering problems	45
4.3	Transparent boundary conditions	46
4.3.1	Dirichlet-to-Neumann operator	47
4.3.2	Perfectly matched layers	47
5	Spatiotemporal Control	49
5.1	Aim	49
5.2	Control mechanisms	49
5.3	Simulations	51
5.4	Genetic algorithm	52
5.4.1	Principles of the algorithm	52
5.4.2	Cost function	53
5.4.3	Adaptive mutation step size	54
5.4.4	Termination conditions	55
5.4.5	Comparison with gradient bases methods	55
5.5	Geometries	56
5.5.1	Random geometries	56
5.5.2	Antenna-like geometries	57
5.5.3	Waveguide-like geometries	59
III	Spectroscopy	63
6	Theoretical Foundation of Quantum Systems	65
6.1	Density operator	65
6.1.1	Pure state	65
6.1.2	Statistical average	66
6.1.3	Time evolution	66
6.2	Time evolution operator	67
6.3	Quantum mechanical pictures	68
6.4	Perturbation expansion	69
6.5	Coupled quantum systems	71
6.5.1	Quantum dots	71
6.5.2	Single-excitons and two-excitons	71
6.5.3	Coupling	72
6.5.4	Delocalized states in exciton and biexciton basis	72
6.5.5	Full Hamiltonian of our model system	73
7	Multidimensional Coherent Nonlinear Spectroscopy	77
7.1	Nonlinearity	78
7.2	Nonlinear response function	79
7.3	Double-sided Feynman diagrams	81
7.3.1	Rotating wave approximation	83
7.4	Multiwave mixing	85

7.5	Detection	85
7.5.1	Phase matching	86
7.5.2	Phase cycling	86
7.5.3	Homodyne and heterodyne detection	88
7.6	Third-order techniques	89
7.6.1	Two-dimensional spectra	90
7.6.2	Photon echo and inverse photon echo	90
7.6.3	Double quantum coherence	94
IV	Localized Spectroscopy	97
8	Localized Spectroscopy	99
8.1	Localized spectra	99
8.1.1	Localization of pulse 1	100
8.1.2	Localization of pulse 1 and pulse 2	103
8.1.3	Localization of pulse 2	104
8.2	Reconstruction of the wave functions	108
8.2.1	Idea	108
8.2.2	Error analysis	109
8.2.3	Exciton states	110
8.2.4	Biexciton states	115
8.3	Filtering different resonances	118
8.4	Improvement of reconstructing wave functions with filtering method	120
V	Epilogue	125
9	Conclusion and Outlook	127
A	Appendix	131
A.1	Quantum mechanical approach for equations of motion for the polarization	131
A.1.1	Intraband transitions	131
A.1.2	Interband transitions	132
A.2	Atomic wave functions	136
A.2.1	Hydrogenic wave functions	136
A.2.2	Atomic orbitals	137
A.3	Fitting the effective atomic number with overlap calculations	139
A.4	Céa's lemma	140
	Bibliography	xxvii
	Index	xxxi
	Danksagung	xxxi

List of Figures

2.1	Plane wave fronts	12
2.2	Three-level system for the derivation of a material model	15
2.3	The real and imaginary part of the dielectric functions of silver and gold as function of the photon energy	17
2.4	Calculated linear spectrum with the experimentally obtained parameters	18
2.5	First Brillouin zone of a face-centered cubic lattice	20
2.6	Band structure of silver	21
2.7	Band structure of gold	22
2.8	Rotation of the orbitals	23
2.9	Face-centered cubic lattice with the twelve nearest neighbors	23
2.10	Linear absorption of silver	25
3.1	Plasmon oscillation of a metal sphere	28
3.2	Field distribution of a sphere with a dielectric coating and plasmon resonances for different metals	29
3.3	Different components of the field distribution of a silver sphere with a dielectric coating from different illumination directions	30
3.4	Long range plasmon excitation	31
3.5	Two coupled silver spheres with platinum coating of different diameters	32
3.6	Field enhancement spectra for different platinum coating thicknesses	32
3.7	Wavelength shift and two counteracting effects of platinum coating for different thicknesses for the enhancement factor	33
3.8	Silver-silicon-dioxide-platinum electrodes for long range excitation	34
3.9	Field enhancement calculations of silver-silicon-dioxide-platinum geometries	35
4.1	Illustration of the finite element method in two dimensions	40
4.2	Delaunay Triangulation	44
4.3	Scattering Problem	45
5.1	Spatiotemporal control	50
5.2	Shaping pulses via a weighting function	51
5.3	Pulse shaping via superposition of Gaussian shaped pulses in frequency domain	51
5.4	Superposition of two polarization directions of the electric field	52
5.5	Operation of a genetic algorithm	54
5.6	Randomly arranged geometry for spatiotemporal control	56
5.7	Triangle setup to demonstrate polarization effects	57
5.8	Top view of a three dimensional asymmetric ray-like layout	60
5.9	Symmetric geometry with quantum dots between silver triangles	60
5.10	Three-armed waveguide-like model setup for spatiotemporal control of three coupled quantum dots	61
5.11	Dimensions of the three-armed waveguide-like model setup	61
5.12	Optimization results of waveguide-like geometry	62
5.13	Waveguide-like geometry for plasmonic coupling effects	62

List of Figures

6.1	Expansion of delocalized states in localized exciton and biexciton basis of three coupled two-level quantum dots	72
6.2	Single and two-exciton basis elements for a quantum system of three coupled quantum dots	73
7.1	Timeline to illustrate the replacement of the time variables	80
7.2	Simplest double-sided Feynman diagrams	82
7.3	Double-sided Feynman diagrams for third-order experiments	83
7.4	Rotating wave approximation	84
7.5	Sketch of typical optical measurements	85
7.6	Pulse sequence of a third-order coherent nonlinear experiment	86
7.7	Heterodyne detection	88
7.8	Double-sided Feynman diagram for photon echo spectroscopy generated in \mathbf{k}_I direction	91
7.9	Double-sided Feynman diagram for the inverse photon echo spectroscopy generated in \mathbf{k}_{II} direction	92
7.10	Double-sided Feynman diagram for double quantum coherence spectroscopy generated in \mathbf{k}_{III} direction	95
8.1	Full two-dimensional double quantum coherence spectrum of three coupled quantum dots	101
8.2	Localized spectra generated by a localized first pulse	102
8.3	Localized spectra generated by a localized first and second pulse for a perfect localization	105
8.4	Localized spectra generated by a localized first and second pulse for a realistic localization	106
8.5	Localized spectra generated by a localized second pulse	107
8.6	Illustration of adding a global phase to the reconstructed coefficients to fit the original coefficients	110
8.7	Illustration of reconstructed singe-exciton wave function coefficient	114
8.8	Comparison of filtered spectra	119
8.9	Illustration of reconstructed biexciton wave function coefficient	123

List of Tables

2.1	Used parameters for fitting the dielectric function of gold and silver	16
2.2	Effective atomic number for the different orbitals	24
5.1	Optimization results of antenna-like geometries	58
6.1	Hamiltonian in matrix form	74
8.1	Comparison of original with reconstructed coefficients for reconstructing single-exciton wave functions	112
8.2	Comparison of the reconstruction quality of chosen combinations of exciton and biexciton states and comparison of the error calculation values	113
8.3	Comparison of original with reconstructed coefficients for reconstructing two-exciton wave functions	117
8.4	Comparison of original and reconstructed coefficients for a perfect localization with coefficients that are calculated after filtering selected states	121
8.5	Comparison of original and reconstructed coefficients for a realistic localization with coefficients that are calculated after filtering selected states	122

Part I

Prologue

1 Introduction

In today's world, optical technologies are ubiquitous. The prosperity in many areas of life is owed to many high-tech devices that influence our lives significantly. Prominent examples of high-tech optical appliances are lasers, solar cells, optical sensors, waveguides and fibers or semiconductor chips. Such devices are used for modern entertainment systems, processors, solar energy conversion [AP10], medical application, in the transport sector, or meteorology systems, to name but a few examples.

Optical elements for modern devices become always smaller. They reach nanometer length scales. Nanotechnology is one of the fastest growing research fields in the current century. It is not only found in modern information technology (e.g. nanoantennas for light-emitting diodes) or medicine research (e.g. biomedical diagnostics [LCH08, HNES09]) but also in material research like the development of novel hybrid materials. Plasmonic effects are of special interest regarding metal structures on nanometer scales. Plasmons are quanta of plasma oscillation. These quasi particles are collective oscillations of the free electron gas density – being especially important at optical frequencies. In this thesis the wavelength dependencies of different hybrid nanospheres with a silver core and platinum and gold layers are investigated. Also the coupling of two nanospheres is examined.

Nanoplasmonics is a part of optical condensed matter science which corresponds with optical effects of nanostructured metal systems [Sto11a]. It is presently a rather developed science comprising several phenomena and quite a lot applications [Sto11b]. For example, the colors of materials can be controlled: The shape and size of the metal particles determine the types of surface plasmons that can couple to the particles and propagate across it so that the interaction of light with the surface can be controlled [BDE03].

In this work, plasmonic effects are used for controlling and concentrating light simultaneously in space on nanometer length scales and time on femtosecond time scales. Recently, there are many experiments which demonstrate spatiotemporal control of optical excitations. This can be achieved by combining pulse shaping techniques with nanoplasmonics [BASP05, ABB⁺10]. Several other localization methods are known and are already applied to a broad range of nanoemitting structures. For example, near field fiber tips [GLE⁺02, FSW⁺98, BASP05, PRP⁺04, WBSC⁺11, FSW⁺98, GEI⁺99], metal tips [ZWBW⁺09, KYF⁺09, HVT⁺09, MKZ⁺08, NH11, SBC⁺10, PRP⁺04, WBSC⁺11] or nanoantennas [SFB02, ABB⁺07] were used.

An example for complex (hybrid) nanostructures are optical emitters that are coupled via Coulomb forces so that they form collective optical resonances. These include metal nanoparticles, semiconductor quantum dots [GLE⁺02, LRNB03], pigments embedded in proteins such as in light harvesting complexes [ECR⁺07, Wit11, CMN⁺10, SRKR12] or composite systems, such as plasmon lasers [BS03]. In such coupled nanosystems exciton dynamics plays an important role. They are for example essential for natural and artificial photosynthesis processes or in quantum computing and OLEDs. The dipole-dipole coupling on a nanometer scale between the individual emitters leads to the formation of new collective hybridized quantum states that are delocalized over the individual nanostructure.

Far field spectroscopy cannot resolve the internal structure of the delocalized states since the electric field is nearly constant on the spatial dimension of the nanostructure, which is much smaller than the excitation wavelength. Neither absorption, nor pump probe, nor four-

1 Introduction

wave mixing experiments are able to disentangle the individual contributions of the coupled emitters from the collective optical response. Thus, only the collective delocalized exciton states are accessible in optical far field experiments.

For disentangling the individual contributions of the emitters to delocalized states local spectroscopy methods such as near field spectroscopy are needed. While nonlinear one-dimensional spectroscopy methods give the energy and the time evolution of single-exciton and two-exciton states of coupled quantum systems, coherent two-dimensional spectroscopy also investigate the correlations between their states [MTH09, TKS03]. In this thesis, in order to disentangle the delocalized wave functions, spatiotemporal control in near field optics is combined with coherent nonlinear multidimensional spectroscopy methods. A new class of measurement technique is proposed that reveals more information about the system than two-dimensional spectroscopy or localization alone. This technique allow reconstructing the contributions of single emitters to the delocalized wave function in a spatially extended nanostructure – a kind of quantum state tomography. In this work, the method is demonstrated by means of double quantum coherence spectroscopy [APV⁺09, LZBC06]. The method works for exciton [YZAG11] as well as for biexciton states. The feasibility of coherent nonlinear optical measurements on single molecules has been demonstrated recently [BSK⁺10]. Interferometric techniques of soft-x-ray pulses help to image single orbitals [KCCM07, CK07].

The first idea of a quantum state tomography is from FANO [Fan57]. The aim of the method is a direct reconstruction of the time dependent wave function. The importance of the tomography method is based on the fact that a wave function supplies much information about a quantum system but it is seldom directly accessible by experiments [GWH⁺10]. Knowing the wave function opens the possibility of calculating new observables not related to optics at all as transport properties and magnetic moments. There are several applications of such quantum state tomography, especially in quantum information and quantum optics [LKK⁺08]. The method of this thesis uses a sequence of light pulses with controlled envelopes and phases to generate highly localized fields in time and space for reconstructing the wave functions – a technique that was recently applied in coherent spectroscopy for localized detection of photoelectrons [ABF⁺11].

Structure of the thesis

This thesis consists of nine chapters that are divided into five parts. Part I (Ch. 1) serves as introduction and part V (Ch. 9) consists of the conclusion and an outlook, which summarizes and gives suggestions for further research. This leaves part II, part III, and part IV for the remaining seven thematic chapters (Ch. 2 to Ch. 8).

Part IV (Ch. 8) contains the main results – the essence of this work: the localized spectroscopy. This apparently needs two ingredients: “Localization” and “spectroscopy”. Thus, part II and part III provide these prerequisites: Part II (Ch. 2 to Ch. 5) deals with the localization of light simultaneously in space (on nanometer length scale) and time (on femtosecond time scale) and part III (Ch. 6 and 7) contains coherent multidimensional nonlinear spectroscopy methods.

Ch. 2 starts with an introduction to electromagnetism of metals. Subsequently, a simple material model is given. At the end of this chapter, band structure and dipole transition matrix element calculations are presented that lead to a linear absorption spectrum as first result of this work.

The next chapter – *Ch. 3* – describes selected optical properties of metal nanostructures and provides first simulation results. Pure, hybrid and coupled nanospheres are investigated

with focus on field enhancements near the surface. An application of induced surface enhancement is given.

Ch. 4 presents the theoretical background of a method which is used to solve Maxwell's equations: the finite element method. This chapter supplies the theoretical foundation for the simulations that provide field distributions of nanostructures under incident shaped pulses as explained in the next chapter.

In *Ch. 5* control mechanisms are discussed for various geometries and results for different setups are presented. Additionally, a genetic algorithm is conceptualized in detail. All together, this leads to localization that is sufficient for localized spectroscopy, the aim of part II.

Part III starts with *Ch. 6* that gives a theoretical foundation of quantum systems and reminds the reader of the density and the time evolution operator. For perturbation expansion, different quantum mechanical pictures are briefly presented. *Ch. 6* also introduces the theoretical background of coupled quantum systems, including the model system that is used in the next chapters.

Ch. 7 begins with an introduction to nonlinear optics. Subsequently, double-sided Feynman diagrams are explained and different types of signal detection are illustrated. Finally, some third-order techniques are recalled – finishing with a method that is used for demonstrations in the following chapter: the double quantum coherence technique, the aim of part III.

Up to here, both prerequisites for localized spectroscopy have been introduced. The last thematic part, part IV (*Ch. 8*) combines the two previous parts and reveals the main results of this work: the so called localized spectroscopy. This is a way of reconstructing exciton as well as biexciton wave functions using a new kind of quantum state tomography. *Ch. 8* starts with a presentation of localized spectra for different kinds of localization. Adjoining, the reconstruction protocols are given and the quality of reconstruction is extensively discussed. In the end, a filtering method is presented for improving the reconstruction quality.

Part II

Localization

2 Metals

Condensed matter physics deals with the physical properties of solids. The behavior of the material is investigated by using electromagnetism, quantum mechanics, and statistical mechanics. Especially metals are of high interest because of the metallic bond that is characterized by electrostatic attractive forces between positively charged metal ions and the delocalized electrons, that are gathered in an electron cloud.

Metals serve as basis for this work: Through their properties they enable plasmonic effects (Ch. 3) that in turn are used to localize light (Ch. 5) that is needed to reach the goal of localized spectroscopy (Ch. 8).

Thus, the focus in the second chapter of this thesis is on metals. It starts with a short but comprehensive introduction of electromagnetism of metals. Afterwards, a material model is introduced that uses the Drude model to provide equations of motions for intraband and interband transitions. Finally, the electronic band structure is discussed and dipole transition matrix elements are calculated with the help of hydrogen wave functions so that in the end a linear absorption spectrum can be given.

2.1 Electromagnetism of metals

This section presents electromagnetism in a macroscopic view. That means that all occurring quantities such as currents or charges are derived by averaging over the corresponding microscopic quantities [Jac98]. This classical framework is sufficient for understanding interaction of metals with electromagnetic fields, even for metals in the range of a few nanometers since the high number of free electrons form dense energy levels comparable to the continuous bands of a bulk. The strong dependence of the optical properties on frequency is shown in Sec. 2.1.5.

2.1.1 Maxwell's equations

The macroscopic *Maxwell equations* describe the dynamics of electromagnetic fields. They link the electric and the magnetic fields with the charge density ρ_{ext} and the *current density*¹ \mathbf{j}_{ext} as external inhomogeneity: the *dielectric displacement* \mathbf{D} , the *electric field* \mathbf{E} , the *magnetic field* \mathbf{H} and the *magnetic flux density* \mathbf{B} . In differential form they read [Max65, Jac98]²

$$\nabla \cdot \mathbf{D} = \rho_{\text{ext}} \quad (2.1a)$$

$$\nabla \cdot \mathbf{B} = 0 \quad (2.1b)$$

$$\nabla \times \mathbf{E} = -\dot{\mathbf{B}} \quad (2.1c)$$

$$\nabla \times \mathbf{H} = \dot{\mathbf{D}} + \mathbf{j}_{\text{ext}}. \quad (2.1d)$$

Those equations take the properties of matter into account in the form of material parameters. The empty space parameters are the permittivity ϵ_0 and the permeability μ_0 . The pres-

¹Vectorial quantities are shown in bold in this work.

²This work uses the International System of Units.

2 Metals

ence of matter requires that the electric and magnetic field is described respectively by the two additional vector fields \mathbf{D} and \mathbf{H} , that is linked with the other fields via

$$\begin{aligned}\mathbf{D} &= \varepsilon_0 \mathbf{E} + \mathbf{P} \\ \mathbf{H} &= \mathbf{B} / \mu_0 - \mathbf{M}\end{aligned}\quad (2.2)$$

and it is assumed that the bound charge carriers lead to the macroscopic polarization \mathbf{P} and the macroscopic magnetization \mathbf{M} through microscopic processes. The magnetic properties of the media used in the simulations of this work are neglected, so that in the following the description of materials can be limited to electric polarization effects.

The polarization \mathbf{P} represents the material dipole response per volume to optical excitation caused by alignment of microscopic dipoles. The relations to the external quantities [Mai07] are further given by

$$\nabla \cdot \mathbf{P} = -\rho_{\text{int}} \quad (2.3)$$

and (using the *continuity equation* $\nabla \cdot \mathbf{j} = -\dot{\rho}$)

$$\mathbf{j}_{\text{int}} = -\dot{\mathbf{P}}.$$

In this approach the macroscopic electric field includes all polarization effects, both external and internal fields are considered:

$$\varepsilon_0 \nabla \cdot \mathbf{E} \stackrel{(2.2)}{=} -\nabla \cdot \mathbf{P} + \nabla \cdot \mathbf{D} \stackrel{(2.1a)}{=} \rho_{\text{int}} + \nabla \cdot \mathbf{D} \stackrel{(2.3)}{=} \rho_{\text{ext}} + \rho_{\text{int}}$$

with ε_0 as the vacuum permittivity.

2.1.2 Linear relationships in materials

For a complete description of electromagnetic fields in matter, the *material equations* are needed. They describe a material's ability to be polarized by the electric or magnetic field. Under the simplified assumptions of linear, isotropic and nonmagnetic media, Eq. (2.2) can be written as³

$$\mathbf{D} \stackrel{(2.2)}{=} \varepsilon_0 \mathbf{E} + \mathbf{P} \stackrel{(2.5)}{=} \varepsilon_0 \mathbf{E} + \varepsilon_0 \chi \mathbf{E} = \varepsilon_0 (1 + \chi) \mathbf{E} = \varepsilon_0 \varepsilon \mathbf{E} \quad (2.4a)$$

$$\mathbf{B} = \mu_0 \mu \mathbf{H} \quad (2.4b)$$

where the *dielectric susceptibility* tensor $\chi = \varepsilon - 1$ is introduced to describe the linear relationship between \mathbf{P} and \mathbf{E} :

$$\mathbf{P} = \varepsilon_0 \chi \mathbf{E} \quad (2.5)$$

and ε is the dielectric constant, that becomes a frequency dependent function for metals (cf. Sec. 2.1.5). Analogously, the vacuum permeability μ_0 and the relative permeability μ are introduced. In an isotropic material, the susceptibility tensor reduces to a scalar function and in a homogeneous environment, χ does not depend on spatial coordinates. In a nonlinear optical regime, the susceptibility depends on the electric field strength. Then, the response is not any longer proportional to the electric field. Nonlinear effects are discussed in detail in Ch. 7.

³The dielectric function is described by ε in this work. Some textbooks describes it by ε_r and introduce $\varepsilon = \varepsilon_0 \varepsilon_r$. This notation is omitted here.

2.1.3 Wave equations

Combining Maxwell's Equations (2.1) in different ways and using vectorial calculation rules, there exist a number of derived differential equations. Without external current ($\mathbf{j}_{\text{ext}} = 0$) the curl equations (2.1c) and (2.1d) simplifies after a Fourier transform ($\frac{\partial}{\partial t} \rightarrow -i\omega$) and using Eq. (2.4) to

$$\begin{aligned}\nabla \times \mathbf{E}(\mathbf{x}, \omega) &= i\omega\mu_0\mu\mathbf{H}(\mathbf{x}, \omega) \\ \nabla \times \mathbf{H}(\mathbf{x}, \omega) &= -i\omega\varepsilon_0\varepsilon\mathbf{E}(\mathbf{x}, \omega)\end{aligned}\quad (2.6)$$

with $\mathbf{x} \in \mathbb{R}^3$ and ω as the *angular frequency*. Eq. (2.6) can be written in matrix notation

$$\begin{pmatrix} 0 & \frac{1}{i\varepsilon_0\varepsilon}\nabla \times \\ -\frac{1}{i\mu_0\mu}\nabla \times & 0 \end{pmatrix} \cdot \begin{pmatrix} \mathbf{E} \\ \mathbf{H} \end{pmatrix} = \omega \begin{pmatrix} \mathbf{E} \\ \mathbf{H} \end{pmatrix}$$

so that reapplying the matrix gives

$$\begin{pmatrix} \frac{1}{\varepsilon_0\varepsilon}\nabla \times \frac{1}{\mu_0\mu}\nabla \times & 0 \\ 0 & \frac{1}{\varepsilon_0\varepsilon}\nabla \times \frac{1}{\mu_0\mu}\nabla \times \end{pmatrix} \cdot \begin{pmatrix} \mathbf{E} \\ \mathbf{H} \end{pmatrix} = \omega^2 \begin{pmatrix} \mathbf{E} \\ \mathbf{H} \end{pmatrix}$$

and a wave equation for the electric field is obtained:

$$\frac{1}{\varepsilon_0\varepsilon}\nabla \times \frac{1}{\mu_0\mu}\nabla \times \mathbf{E} = \omega^2 \mathbf{E}. \quad (2.7)$$

With some assumptions, Eq. (2.7) can be written just for two dimensions. Using⁴ $\partial_z \mathbf{E} = 0$ for example, vector calculation rules, and $\nabla_{xy} \cdot E_z = 0$, one finds [Sch91]

$$\nabla_{xy} \cdot \nabla_{xy} E_z + \omega^2 \varepsilon_0 \varepsilon \mu_0 \mu E_x = 0$$

and for one dimension

$$\partial_x^2 E + k^2 E = 0 \quad (2.8)$$

with the *angular wavenumber* $k = \frac{\omega}{c}$ and the velocity of light $c = \frac{1}{\sqrt{\varepsilon_0\mu_0}}$ and the assumption of vacuum with $\varepsilon\mu = 1$. Eq. (2.8) is called *Helmholtz equation* [NV73] that becomes important in Sec. 4.1. In the following, μ is neglected since for the materials used in this work no magnetizability is assumed⁵.

2.1.4 Plane waves

A plane wave is a constant-frequency wave with infinite parallel planes as wavefronts. The amplitude normal to the phase velocity vector is constant. The dot product of the wave vector \mathbf{k} and the position vector \mathbf{x} is constant as seen in Fig. 7.2.

A mathematical versatile formulation for waves is a representation as a complex function, using the ansatz

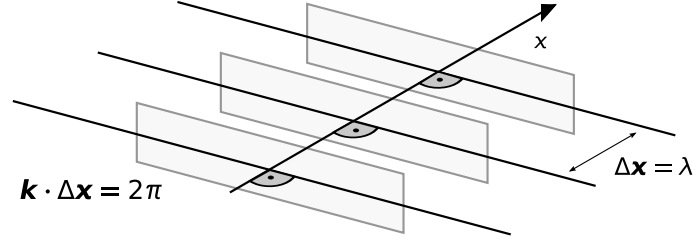
$$\mathbf{E}(\mathbf{x}, t) = \mathbf{E}_0 e^{i(\mathbf{k} \cdot \mathbf{x} - \omega t + \phi)} \quad (2.9)$$

with e as the natural exponent, i as the imaginary number, $\mathbf{k} \in \mathbb{R}^3$ as the wave's wave number vector, t as time and \mathbf{x} as the vector that gives the position in the three-dimensional space. For plane wave, the vector can be reduced to one dimension since the other dimensions lead

⁴The expression ∂_x is a short form for the derivative operator $\frac{\partial}{\partial x}$ with respect to the variable x .

⁵That additionally avoids confusions with the dipole matrix μ .

Figure 2.1:
Plane wave fronts: A constant distance separates same amplitudes of planar waves radiating in x direction with the wave vector \mathbf{k} .



to be the same at every point on any given y - z plane. The phase shift ϕ of the wave has the units of radians. The constant vector $\mathbf{E}_0 \in \mathbb{C}^3$ represents the amplitude of the wave.

The real part of Eq. (2.9) provides a physically description of a plane wave:

$$\text{Re}(\mathbf{E}) = A \cos(\mathbf{k} \cdot \mathbf{x} - \omega t + \phi)$$

with $A = \text{Re}(\mathbf{E}_0) \in \mathbb{R}^3$.

Assuming a constant relative permeability $\mu = 1$, applying Eq. (2.7) for the ansatz (2.9) yields

$$\begin{aligned} \frac{1}{\varepsilon_0 \varepsilon \mu_0} \mathbf{i} \mathbf{k} \times \mathbf{i} \mathbf{k} \times \mathbf{E}_0 e^{i(\mathbf{k} \cdot \mathbf{x} - \omega t + \phi)} &= \omega^2 e^{i(\mathbf{k} \cdot \mathbf{x} - \omega t + \phi)} \mathbf{E}_0 \\ \Leftrightarrow \mathbf{k} \times \mathbf{k} \times \mathbf{E}_0 &= -\varepsilon_0 \varepsilon \mu_0 \omega^2 \mathbf{E}_0. \end{aligned}$$

Using vectorial calculation rules for the double cross product and the fact that for plane waves the vector of the amplitude of the electric field \mathbf{E}_0 is perpendicular to the vector in propagation direction \mathbf{k} , that means that $\mathbf{k} \cdot \mathbf{E}_0 = 0$, provide

$$|\mathbf{k}|^2 = \varepsilon_0 \varepsilon \mu_0 \omega^2 \stackrel{\varepsilon = n^2}{=} \varepsilon_0 \mu_0 \omega^2 n^2 = k_0^2 n^2$$

with k_0 the vacuum value of k .

2.1.5 Dielectric function

The behavior of the metal interacting with light varies with the type of metal and with the frequency of the light. For instance, alkali metals show other properties than noble metals. Each metal has its own complex *dielectric function* $\varepsilon(\omega)$ that describes the dispersive properties.

Through generalizing the linear relationship (2.4a) to

$$\mathbf{D}(\mathbf{r}, t) = \varepsilon_0 \iint dt' d\mathbf{r}' \varepsilon(\mathbf{r} - \mathbf{r}', t - t') \mathbf{E}(\mathbf{r}', t') \quad (2.10)$$

the non-locality in time and space are taken into account. Fourier transform of Eq. (2.10) and simplifying to a spatially local response (motivated by longer wavelengths than the mean free path of the electrons) provide

$$\mathbf{D}(\omega) = \varepsilon_0 \varepsilon(\omega) \mathbf{E}(\omega).$$

In general, the dielectric function is a complex function of the angular frequency ω and the square of the complex *refractive index* $n^{\text{C}}(\omega) = \sqrt{\varepsilon(\omega)}$ with the relations

$$\begin{aligned} n^{\text{C}} &= n_1 + i n_2 = n + i \kappa, \\ \varepsilon &= \varepsilon_1 + i \varepsilon_2, \\ \varepsilon_1 &= n^2 - \kappa^2, \text{ and} \\ \varepsilon_2 &= 2n\kappa \end{aligned}$$

where κ is the *extinction coefficient* that is proportional to the absorption coefficient (cf. Sec. 2.1.6).

2.1.6 Beer-Lambert law

The decreasing of the intensity I due to absorption can be described with the *Beer-Lambert law*. It relates the absorption of light that travels through a material in z direction to the properties of this material. It reads

$$I(z) = |E(z, t)|^2 = I_0 e^{-\alpha(\omega)z}$$

with the *absorption coefficient* α . It is determined by [HK04]

$$\alpha(\omega) = 2\frac{\omega}{c}\kappa(\omega) = 2\frac{\omega}{c}\frac{1}{2n(\omega)}\text{Im}(\chi(\omega)) = \frac{\omega}{n(\omega)c}\text{Im}\left(\frac{P(\omega)}{E(\omega)}\right) \quad (2.11)$$

where κ is the extinction coefficient of Sec. 2.1.5 and c the velocity of light.

2.2 Material model

A simple approach of providing an estimation of all material parameters needed for the solution of Maxwell's equations is given. This is done by derivating a description for the intraband and interband transitions in a metal to provide space-time dynamics for the dipole density \mathbf{P} .

After presenting equations of motion for the polarization, the occurring parameters and a linear spectra for the absorption are supplied. For this, the section starts by introducing the Drude model to describe the dielectric function of the free electron gas [ZC09]. The quantum mechanical derivation of the equations can be found in the appendix.

2.2.1 Drude model

The dielectric function of the free electron gas can be described by a *Drude model*. This classical model permits an estimate of phenomena especially in metals whose detailed understanding requires a much more complex treatment.

The model is described by an electric conductor in which electrons can move freely and form an electron gas. An external electric field \mathbf{E} accelerates the electrons via the force $F_{\text{el}} = qE$. Instead of a continuous acceleration, the electrons bounce with the lattice ions and slow down. This ensures Ohm's law: after a short time, the mean velocity of the electron is proportional to the electric field strength. The collision process is described phenomenological by a relaxation time τ – the mean collision time between two collisions. An increasing temperature decreases the mean collision time. That explains the decreasing conductivity of the metals.

The equation of motion for the electrons reads

$$m\dot{\mathbf{v}} + \frac{m}{\tau}\mathbf{v}_D = -e\mathbf{E}, \quad (2.12)$$

with the electron mass m and elementary charge e , the electron velocity v , the drift velocity v_D (drift velocity minus the thermal velocity), and the collision time τ . The latter is often also given by the characteristic collision frequency $\gamma = 1/\tau$. At room temperature, a typical value is $\gamma = 100\text{THz}$ [Mai07].

2 Metals

For the stationary state is $\dot{v} = 0$ and consequently $\mathbf{v}_D = -\frac{e\tau}{m}\mathbf{E}$. With this, the current density \mathbf{j} is given by

$$\mathbf{j} = -en\mathbf{v}_D = \frac{e^2\tau n}{m}\mathbf{E}$$

with the charge carrier density n .

As a further result, the *Drude conductivity* σ is

$$\sigma = \frac{\mathbf{j}}{\mathbf{E}} = \frac{e^2\tau n}{m}.$$

In this plasma model, the details of the electron-electron interactions or lattice potential are not taken into account.

For an harmonic time dependence of the driving electric field $\mathbf{E}(t) = \mathbf{E}_0 e^{-i\omega t}$ a particular solution of Eq. (2.12) is $\mathbf{v}(t) = \mathbf{v}_0 e^{-i\omega t}$ with \mathbf{v}_0 given so that [Mai07]

$$\mathbf{v}(t) = \frac{e}{m(\omega^2 + i\gamma\omega)}\mathbf{E}(t)$$

and thus for the macroscopic polarization $\mathbf{P} = -ne\mathbf{v}$ is

$$\mathbf{P} = -\frac{ne^2}{m(\omega^2 + i\gamma\omega)}\mathbf{E}.$$

Inserting this result in Eq. (2.4a) leads to

$$\mathbf{D} = \varepsilon_0 \left(1 - \frac{\omega_{\text{pl}}^2}{\omega^2 + i\gamma\omega} \right) \mathbf{E}$$

with the *plasma frequency*

$$\omega_{\text{pl}}^2 = \frac{n(\mathbf{r})e^2}{\varepsilon_0 m_{\text{eff}}}. \quad (2.13)$$

Here, m_{eff} is the effective electron mass and $n(\mathbf{r})$ the electron density in the considered band.

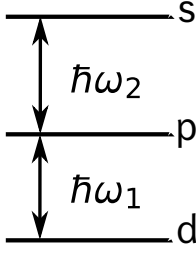
With this, the dielectric function of the free electron gas is given by

$$\varepsilon(\omega) = 1 - \frac{\omega_{\text{pl}}^2}{\omega^2 + i\gamma\omega} \quad (2.14)$$

with the real part $\varepsilon_1(\omega) = 1 - \frac{\omega_{\text{pl}}^2\tau^2}{1+\omega^2\tau^2}$ and the imaginary part $\varepsilon_2(\omega) = \frac{\omega_{\text{pl}}^2\tau}{\omega(1+\omega^2\tau^2)}$.

While in a free electron model $\varepsilon \rightarrow 1$ at $\omega \gg \omega_{\text{pl}}$, for noble metals, the model has to be extended for the region $\omega > \omega_{\text{pl}}$. In this region, the response is dominated by free s electrons and the filled d band causes a highly polarized environment close to the Fermi surface [Mai07]. This positive background of the ion cores is described by the high frequency limit ε_∞ of the dielectric function (that is one in a pure Drude model) so that

$$\varepsilon(\omega) = \varepsilon_\infty - \frac{\omega_{\text{pl}}^2}{\omega^2 + i\gamma\omega}. \quad (2.15)$$

**Figure 2.2:**

Three-level system for the derivation of a material model: The three levels d , p , and s involves two interband transitions (cf. Fig. 2.7).

2.2.2 Equations of motion for the polarization

It can be assumed that the total polarization \mathbf{P} of a metal, depending on space and time, consists of an intraband and an interband part [ERM07]:

$$\mathbf{P}(\mathbf{r}, t) = M(\mathbf{r}) [\mathbf{P}_{\text{intra}}(\mathbf{r}, t) + \mathbf{P}_{\text{inter}}(\mathbf{r}, t)] \quad \text{where} \quad M(\mathbf{r}) = \begin{cases} 1 & \text{for } \mathbf{r} \in V_{\text{metal}} \\ 0 & \text{else} \end{cases}$$

defines the spatial extension of the nanoparticle. While interband transitions stand for electron transitions between two different energy bands, intraband transitions describe electron transitions within the same energy band. Band theory and calculation possibilities are introduced in Sec. 2.3.1.

In a simple approach a Drude model for the intraband component (p band) is used and for the interband transitions a ground state d and two excited quantum states p and s (see figure 2.2) is taken into account. The two parts can be calculated by solving the equations of motion for the intraband part

$$\left[\frac{\partial^2}{\partial t^2} - \gamma_{\text{pl}} \frac{\partial}{\partial t} \right] \mathbf{P}_{\text{intra}}(\mathbf{r}, t) = \varepsilon_0 \omega_{\text{pl}}^2 \mathbf{E}(\mathbf{r}, t), \quad (2.16)$$

and the interband part

$$\left[i\hbar \frac{\partial}{\partial t} - (\hbar\omega_1 + i\gamma_1) \right] \mathbf{P}_{\text{inter}}^{(1)}(\mathbf{r}, t) = -\varepsilon_0 A_1 \varepsilon_1 \mathbf{E}(\mathbf{r}, t) \quad \text{and} \quad (2.17a)$$

$$\left[i\hbar \frac{\partial}{\partial t} - (\hbar\omega_2 + i\gamma_2) \right] \mathbf{P}_{\text{inter}}^{(2)}(\mathbf{r}, t) = -\varepsilon_0 A_2 \varepsilon_2 \mathbf{E}(\mathbf{r}, t) \quad (2.17b)$$

where γ_{pl} is the plasmonic dephasing, ω_{pl} the plasma frequency and ε_0 the vacuum permittivity. The equations contains also the transition energies ε_1 and ε_2 , dimensionless amplitudes A_1 and A_2 , damping parameters for the transition peaks γ_1 and γ_2 and the electric field \mathbf{E} . Index 1 represents the d-p transition, index 2 the p-s transition.

In App. A.1, a derivation for the corresponding equations using quantum theory can be found. This quantum mechanical approach serves as a well controlled model system. There, the creation operator $a_{\lambda\mathbf{k}}^\dagger$ and the annihilation operator $a_{\lambda\mathbf{k}}$ are used. They create or annihilate an electron with the momentum vector \mathbf{k} in the band λ , respectively (more about energy bands can be found in Sec. 2.3.1). These operators fulfill the Fermi commutation relation for electrons:

$$[a_{\mathbf{k}_\alpha}, a_{\mathbf{k}_\beta}]_+ = 0 = [a_{\mathbf{k}_\alpha}^\dagger, a_{\mathbf{k}_\beta}^\dagger]_+ \quad \text{and} \quad [a_{\mathbf{k}_\alpha}, a_{\mathbf{k}_\beta}^\dagger]_+ = \delta_{\alpha\beta}.$$

These anticommutator relations automatically obey the Pauli principle.

Table 2.1:

Used parameters for fitting the dielectric function (2.18) of gold and silver: Gold parameters are taken from [ERM07] and silver is fitted with initial values taken from [Kaw01, MJ77] to the dielectric function measured by [JC72].

	Silver		Gold	
ε_∞	0.825		1.54	
$\hbar\omega_{\text{pl}}/\text{eV}$	9.143		8.23	
$\gamma_{\text{pl}}/\text{eV}$	0.021		0.08	
A_1, A_2	0.313,	1.329	1.27,	1.1
$\hbar\omega_1/\text{eV}, \hbar\omega_2/\text{eV}$	4.080,	5.227	2.5,	3.62
Φ_1, Φ_2	-1.372,	-0.456	$-\pi/4,$	$-\pi/4$
$\gamma_1/\text{eV}, \gamma_2/\text{eV}$	0.446,	2.812	0.62,	1.11

2.2.3 Parameters

The dielectric function of the Drude model (Eq. (2.14)) describes the optical response of metals for photon energies below the threshold of interband transitions. For transitions between electronic bands (they occur for some noble metals for energies of one electron volt), the material model has to be extended [HFH⁺93].

An analytic description of the dielectric function of metals is given in [ERM07] and reads in frequency space

$$\varepsilon_{\text{total}}(\mathbf{r}, \omega) = \underbrace{\varepsilon_\infty - \frac{\omega_{\text{pl}}^2}{\omega(\omega + i\frac{\gamma_{\text{pl}}}{\hbar})}}_{\text{Drude part (see Eq. (2.15))}} + \underbrace{\sum_i A_i \omega_i \left(\frac{e^{i\Phi_i}}{\omega_i - \omega - i\frac{\gamma_i}{\hbar}} + \frac{e^{-i\Phi_i}}{\omega_i + \omega + i\frac{\gamma_i}{\hbar}} \right)}_{\text{Interband transition part}} \quad (2.18)$$

where $i \in \{1, 2\}$ denotes the two interband transitions, $-\frac{\omega_{\text{pl}}^2}{\omega(\omega + i\gamma_{\text{pl}})} = \hat{\chi}$ and γ_{pl} is the damping rate. The sum, typically ranging from one to two for metals, describes the interband transitions [ERM06].

This model enables finding all parameters needed in the equations of motion for the polarization of Sec. 2.2.2 (equations (2.16) and (2.17)). It includes dimensionless amplitudes A_i , interband transition frequencies ω_i , phases Φ_i and damping parameters γ_i for the transitions peaks. The values for the material dependent parameters ε_∞ , ω_{pl} and γ_{pl} can be found in table 2.1.

This table provides the fitting values for the dielectric function of silver as well as for gold. While gold parameters are taken from [ERM07], the parameters for silver are fitted with initial values taken from [Kaw01, MJ77] in order to achieve a large resemblance to the dielectric function measured by [JC72] (shown in figure 2.3)⁶. All these parameters will be mapped to constant values in equations (2.16) and (2.17).

A linear spectrum, represented by the linear susceptibility $\chi(\omega) = \varepsilon(\omega) - 1$ can be extracted from experimental data [JC72]. Fig. 2.3 shows the real (ε_1) and imaginary (ε_2) part of the dielectric functions of silver and gold. These two noble metals are the most important metals for plasmonic studies in the visible and near-infrared. Johnson and Christy [JC72] determined the data experimentally. The two parts contribute to the complex refractive index $n^C = n + ik$ with $\varepsilon_1 = n^2 - k^2$ and $\varepsilon_2 = 2nk$.

In the experimental data is visible that interband transitions influence the dielectric function beginning at four electron volts for silver and two electron volts for gold. For lower fre-

⁶Reprinted figure with permission from P. B. Johnson and R. W. Christy, Physical Review B, 6, 4370-4379 (1972). Copyright (2013) by the American Physical Society. Readers may view, browse, and/or download material for temporary copying purposes only, provided these uses are for noncommercial personal purposes. Except as provided by law, this material may not be further reproduced, distributed, transmitted, modified, adapted, performed, displayed, published, or sold in whole or part, without prior written permission from the American Physical Society.

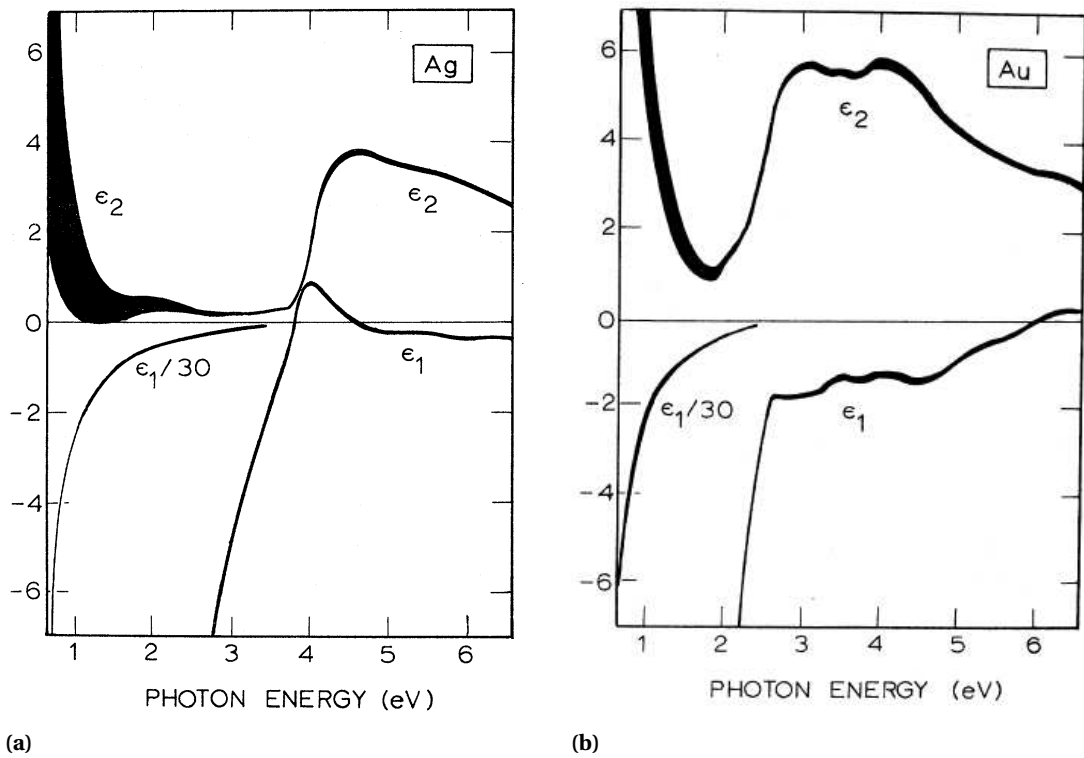
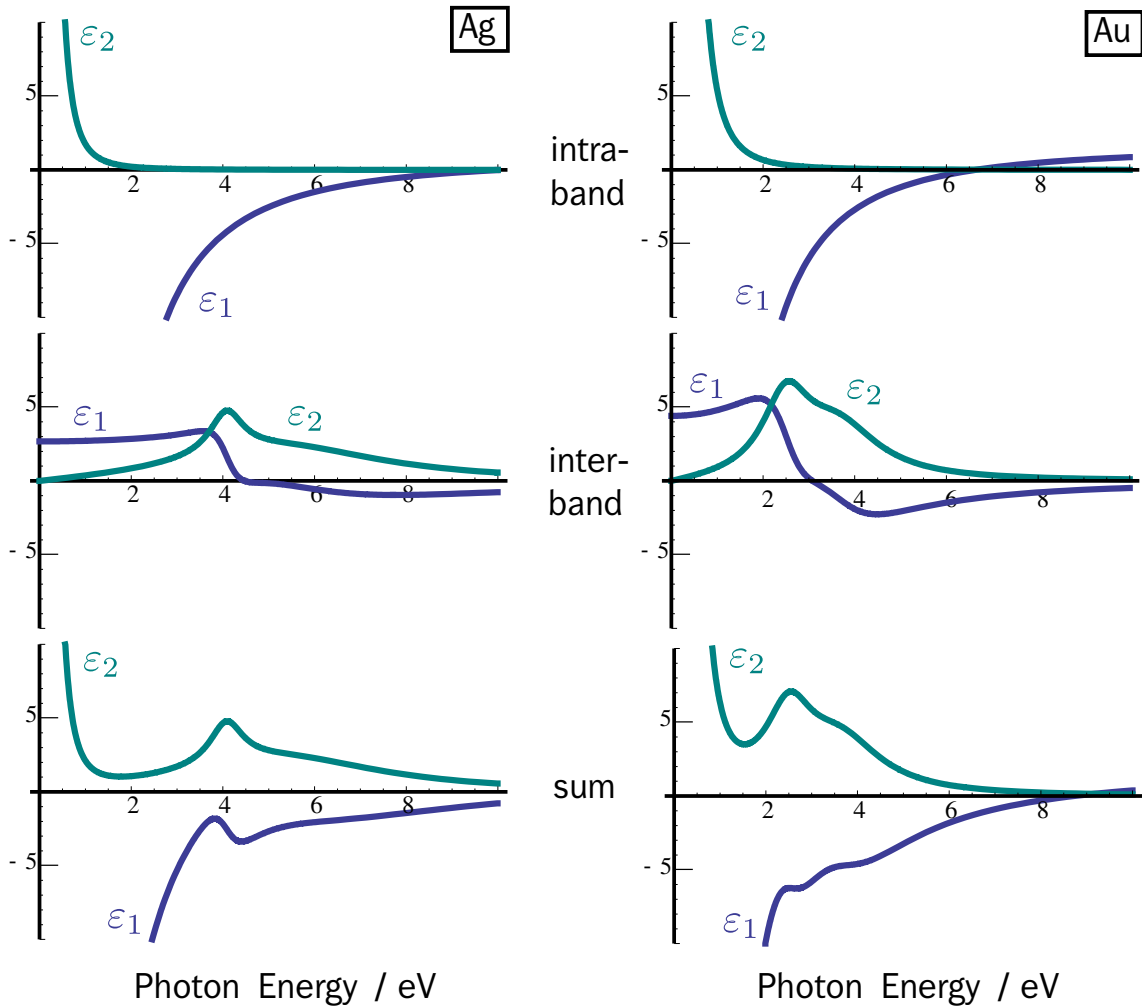


Figure 2.3:

The real (ϵ_1) and imaginary (ϵ_2) part of the dielectric functions of silver (a) and gold (b) as functions of the photon energy extracted from experimental data by [JC72]: Interband transitions influence the dielectric function beginning at 4 eV for silver and 2 eV for gold. For lower frequencies ϵ behaves Drude-like. The figures are taken from [JC72].

**Figure 2.4:**

Calculated linear spectrum with the experimentally obtained parameters: The real (ϵ_1) and imaginary (ϵ_2) part of the dielectric functions of silver (on the left) and gold (on the right) are shown as functions of the photon energy calculated by Eq. (2.18) with the parameters given in Tab. 2.1. The total spectrum is the sum of the intraband and the interband transition part which is in a good resemblance to the experimental data (see Fig. 2.3).

quencies ϵ behaves Drude-like. These results can be reproduced via Eq. (2.18) with the parameters given in table 2.1. The curves are plotted in Fig. 2.4. This results in a reasonable resemblance to the experimental data using equations (2.16) and (2.17).

2.3 Electronic structure

The electron configuration as used mainly in atomic physics and quantum chemistry describes the distribution of electrons of a physical structure (mostly an atom or a molecule) in atomic or molecular orbitals.

This section introduces band structure theory and atomic orbital theory using the example of silver [FTB⁺90]. After discussing the band structure, the electronic wave function is expanded in terms of hydrogen wave functions to calculate the dipole transition matrix el-

ements for interband transitions in silver. With these results in the end a linear absorption spectrum of silver is obtained.

2.3.1 Band structure calculations

Band theory in solid-state physics describes the behavior of electrons in solids, especially the connection between energy and momentum (dispersion). Allowed energy ranges for electrons are given in momentum space by energy bands. The energy ranges that are covered by the function that gives the energy in dependence of the momentum vector $E(\mathbf{k})$ is determined by the molecular orbitals that are generated by splitting of the single atomic orbitals of each atom caused by the coupling of the high number of atoms in bulk material (cf. Sec 6.5). Discrete energy levels become continuous bands.

Band theory helps describing many physical properties of solids. In this work it is used, among other things, to find the linear optical absorption for silver.

There exist several approaches to find the band structure of an bulk solid-state material. They can be derived from the dynamical theory of diffraction of the quantum mechanical electron waves by using that the waves live in a periodic crystal lattice structured by a *Bravais lattice*⁷. Additionally, often symmetries are exploited.

One method for band structure calculations is the tight binding technique. As an opposite to a nearly free electron approximation, the tight binding model holds on the atomic description of the energy level while assuming that the overlap of the atomic wave function is strong enough to demand corrections of the picture of an arrangement of isolated atoms [AM07]. Since the tight binding method uses an approximate set of wave functions based upon superposition of wave functions for isolated atoms located at each atomic site, it is closely related to the *LCAO* method. The abbreviation stands for *linear combination of atomic orbitals*.

In the LCAO method the one-electron wave function is represented by linear combination of Bloch sums (see Sec. 2.3.2). Inserting such an expansion of the wave function into the Schrödinger equation (see Eq. (6.5)) with the Hamiltonian \bar{H} gives a set of simultaneous linear equations with a nonzero solution if the determinant of the coefficients vanishes [Pap86]: $H - ES = 0$ with the matrix elements

$$H_{nm} = \sum_{\mathbf{R}_j} e^{i\mathbf{k}\cdot(\mathbf{R}_j-\mathbf{R}_i)} \int \varphi_n^*(\mathbf{r}-\mathbf{R}_i) \bar{H} \varphi_m(\mathbf{r}-\mathbf{R}_j) dV \quad (2.19a)$$

$$S_{nm} = \sum_{\mathbf{R}_j} e^{i\mathbf{k}\cdot(\mathbf{R}_j-\mathbf{R}_i)} \int \varphi_n^*(\mathbf{r}-\mathbf{R}_i) \varphi_m(\mathbf{r}-\mathbf{R}_j) dV \quad (2.19b)$$

with \mathbf{R}_i and \mathbf{R}_j as the positions of the atoms located on orbitals φ_n and φ_m , respectively.

The number of atoms per unit cell and the number of atomic orbitals determine the size of the matrices H and S . Since silver has a *face-centered cubic* (fcc) structure with one atom per unit cell in the ground state, H and S are 9×9 matrices (five d orbitals, three p orbitals and one s orbital).

Using the Slater-Koster parameters an easy diagonalization of the matrix is possible to obtain the energy bands and densities of states for a given material. The Slater-Koster method serves as an interpolation scheme [SK54, PM03]. The integrals from Eq. (2.19), that are commonly calculated by first principles, are replaced by the Slater-Koster parameters taken from [Pap86].

Fig. 2.5 shows the first Brillouin zone of a face-centered cubic lattice with its symmetry labels. Along these lines, the band structure is plotted. The L point is in the center of the

⁷The Bravais lattices represent the set of all possible unit cells in a crystal.

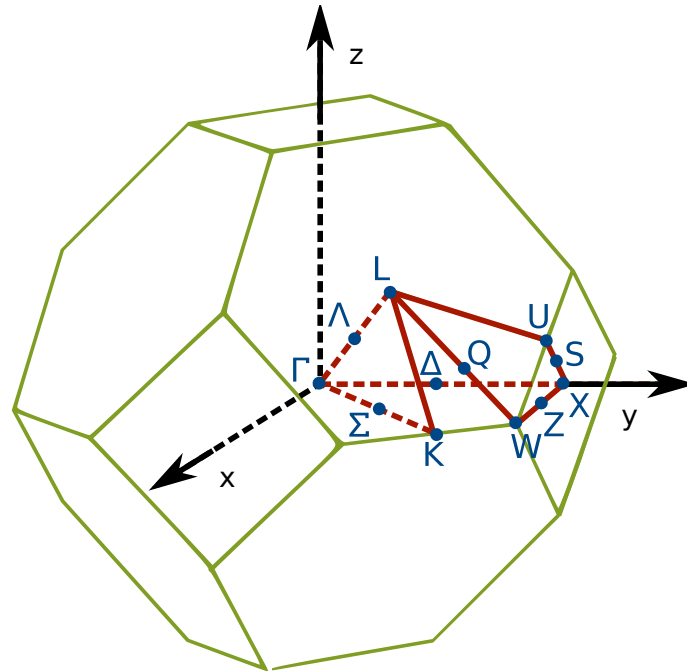


Figure 2.5:

First Brillouin zone of a face-centered cubic lattice: The red path along the symmetry labels corresponds to the x axis of the band structure plot.

hexagonal surface. The band structure of silver as given in Fig. 2.6 is determined with the Slater-Koster parameters [PM03, MP96].

The band structure shows five bands that are completely filled since they are below the *Fermi level*⁸. They are called d bands because they represent the d orbitals (see Sec. 2.3.2). Three s bands are unfilled since their energy lie above the Fermi energy. Only one band – the p band – is half filled and can consequently gain or lose electrons. The d bands are only able to donate electrons while the s bands are electron absorbers. This reduces the possibilities of electron transitions between two bands, the interband transitions.

Optical transitions are direct. That means that electrons are emitted at the same \mathbf{k} value as the electrons are absorbed. Thus, the \mathbf{k} ranges for possible transitions are restricted. The lowest energy gap for possible transitions – assuming no further \mathbf{k} positions that are disregarded because of the two-dimensional nature of the band structure plot – is found near the X and the L symmetry point (this is for example confirmed by [SHW⁺01, ACRS74, FS75, EP62, BS64]). This is the reason why the focus for reconstructing the dipole moments of Sec. 2.3.3 is around that symmetry points.

The band structure of gold resembles the structure of silver [Chr76, Chr72, Ram70, PS69]. The most important transitions are at the same wave vector positions (see Fig. 2.7): At the X symmetry point there is also a transition between the fifth and the sixth band and for the L point, the transition is between band six and seven.

2.3.2 Electron configuration and hydrogen wave functions

The *electron configuration* gives the distribution of a physical structure in atomic or molecular orbitals.

The electron configuration for silver is $1s^2 2s^2 2p^6 3s^2 3p^6 3d^{10} 4s^2 4p^6 4d^{10} 5s$ where the number gives the shell, the letters the orbital and the exponent gives the number of electrons assigned to each orbital in the ground state. An electron shell contains electrons which share

⁸The Fermi level gives the highest energy of a particle in a many-particle system in the ground state at zero Kelvin.

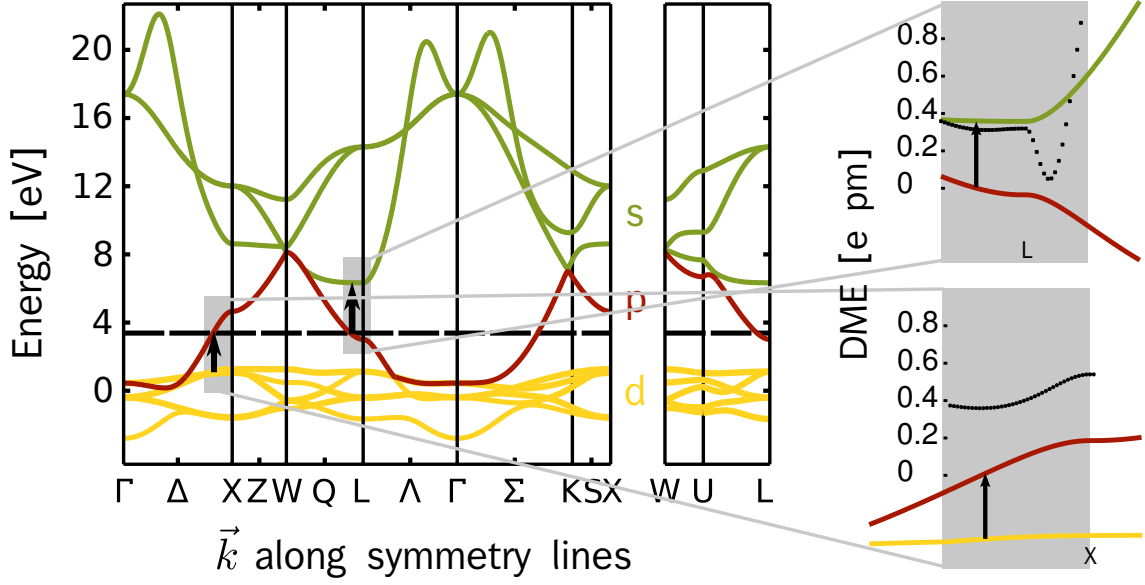


Figure 2.6:

Band structure of silver: On the left, the band structure of silver is plotted along the symmetry lines of a face-centered cubic lattice (see Fig. 2.5). On the right, a zoom into two important interband transitions of silver with the calculated dipole transitions elements (DME) is illustrated [PM03, MP96] (cf. Sec. 2.3.3).

the same principal quantum number n while a subshell is the set of states defined by an azimuthal quantum number l where $l = 1, 2, 3, 4$ is labeled by s, p, d and f, respectively.

In the linear combination of atomic orbitals theory, the space depending wave functions $\Psi_{\mathbf{k}n}$ for band n with the wave vector \mathbf{k} are a linear combination of the Bloch functions $b_{\mathbf{k}m}$ with coefficients v_{nm} , that are eigenvectors for band n of the Slater-Koster Hamiltonian [Pap86, JS83]:

$$\Psi_{\mathbf{k}n}(\mathbf{r}) = \sum_m v_{nm}(\mathbf{k}) b_{\mathbf{k}m}(\mathbf{r}). \quad (2.20a)$$

The linear combination of atomic orbitals area

$$b_{\mathbf{k}m}(\mathbf{r}) = N^{-1/2} \sum_j e^{i\mathbf{k}\mathbf{R}_j} \varphi_m(\mathbf{r} - \mathbf{R}_j). \quad (2.20b)$$

This Bloch wave functions result of the nine atomic basis wave functions φ_m for $m = 1, \dots, 9$. The sum is over all N atoms at position \mathbf{R}_j .

In general, the hydrogen wave function can be split in the hydrogen radial part R and in spherical harmonics Y via $\Psi_{nlm} = R_{nl}(r) Y_{lm}(\theta, \phi)$ [Jen06]. The hydrogen wave functions that are relevant for the calculation of the silver dipole transition elements are given in App. A.2.1.

Atomic orbitals are one-electron wave functions in atoms. The value of the angular momentum quantum number gives the name of the orbital: There are one s orbital ($l = 0$), three p orbitals ($l = 1$) and five d orbitals ($l = 2$). The orbitals φ_m corresponds to the hydrogen wave functions as given in App. A.2.2.

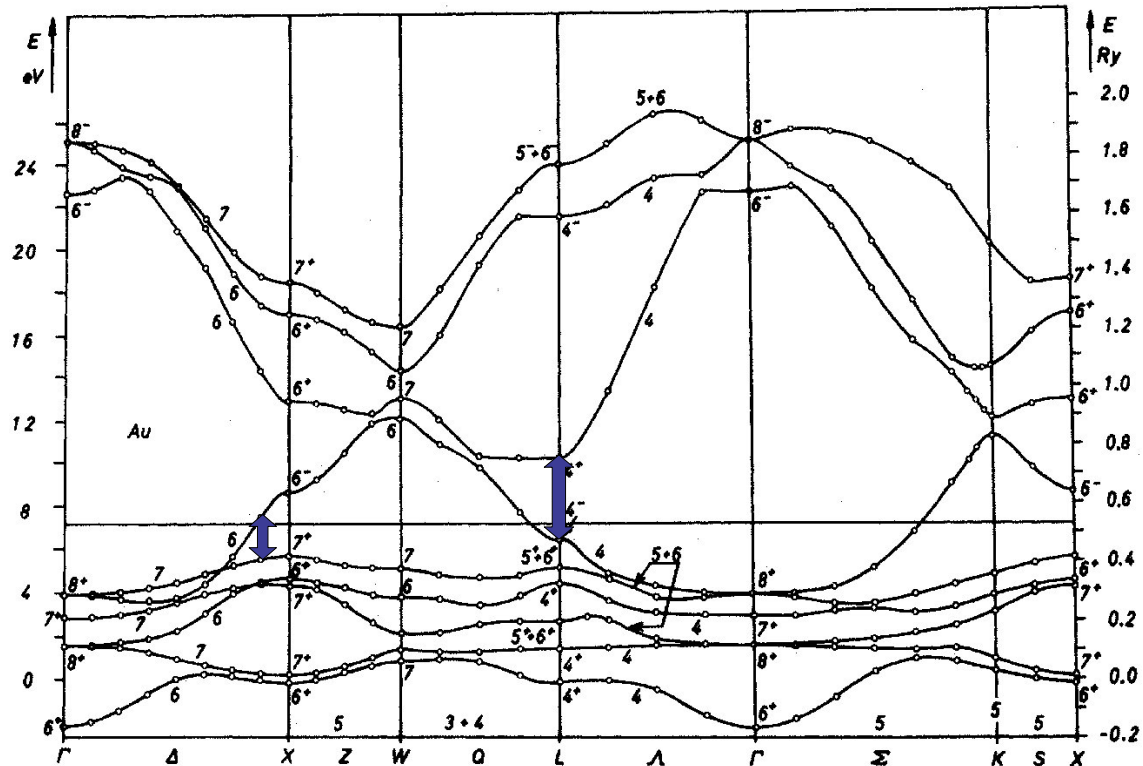


Figure 2.7:

Band structure of gold: The blue arrows show two possible interband transitions (from d to p and from p to the s band). The bands below the Fermi level are the d bands, the bands above are the s bands. The sixth band is half filled (p band). The figure is taken from [CS71]⁹.

To maximize the overlap the p orbitals are rotated by $\pi/4$ around the 010-direction (see Fig. 2.8) via the transformation:

$$\begin{pmatrix} x' \\ y' \\ z' \end{pmatrix} \rightarrow \begin{pmatrix} x \cos \omega - z \sin \omega \\ y \\ x \sin \omega + z \cos \omega \end{pmatrix} = \begin{pmatrix} \frac{x}{\sqrt{2}} - \frac{z}{\sqrt{2}} \\ y \\ \frac{x}{\sqrt{2}} + \frac{z}{\sqrt{2}} \end{pmatrix}.$$

But this rotation can only optimize the overlap of two of the three p orbitals (here p_z and p_x). Also for d orbitals there is no plain orientation.

Effective atomic number

The atomic number of hydrogen is $Z = 1$. In order to use hydrogen wave functions for silver or gold calculations, the atomic number of these materials ($Z_{\text{silver}} = 47$) has to be replaced by an *effective atomic number*. Because of the screening of the inner electrons, the outer electrons only interact with a core that is screened by the electrons between the electron of interest and

⁹Reprinted figure with permission from N. Egede Christensen and B. O. Seraphin, Physical Review B, 4,3321-3344 (1971). Copyright (2013) by the American Physical Society. Readers may view, browse, and/or download material for temporary copying purposes only, provided these uses are for noncommercial personal purposes. Except as provided by law, this material may not be further reproduced, distributed, transmitted, modified, adapted, performed, displayed, published, or sold in whole or part, without prior written permission from the American Physical Society.

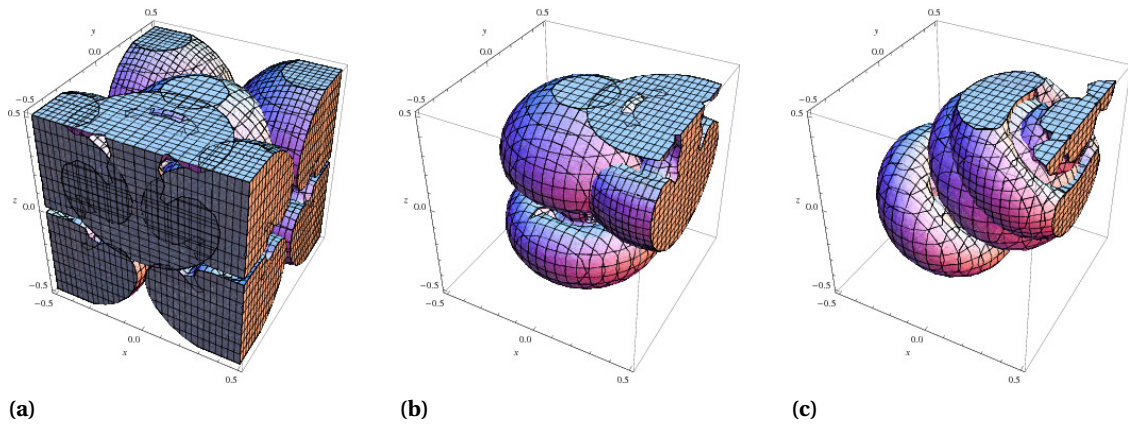


Figure 2.8:

Rotation of the orbitals: Part (a) shows a p orbital of the center atom and five of its twelve next neighbors (for a clear representation). In part (b) and (c) origin and rotated alignment of the center orbital and one of its next neighbor are plotted, respectively.

nucleus [Sla30, CRR67]. It cancels some of the positive nuclear charge given by the constant S via

$$Z_{\text{eff}} = Z - S.$$

In literature, there are different values for the effective atomic numbers – depending on the way of calculation. For example, the value for Z_{eff} for silver varies according to [Ems89] from 4.20 (SLATER) over 8.03 (CLEMENTI) up to 11.35 (FROESE-FISCHER).

With the help of the given Slater-Koster parameters for the overlap matrix elements in [Pap86], it is approximately possible to reconstruct the effective atomic numbers that are used for calculating the band structure via Eq. (2.19b) that gives the overlap matrix elements S for two orbitals φ_n and φ_m :

$$S_{nm} = \sum_{\mathbf{R}_j} e^{i\mathbf{k} \cdot (\mathbf{R}_j - \mathbf{R}_i)} \int \varphi_n^*(\mathbf{r} - \mathbf{R}_i) \varphi_m(\mathbf{r} - \mathbf{R}_j) dV.$$

The overlap is calculated between the twelve nearest neighbors of an atom in a face-centered cubic structure (see Fig. 2.9). In App. A.3 a more detailed explanation of these calculations is given. The results are shown in Tab. 2.2.

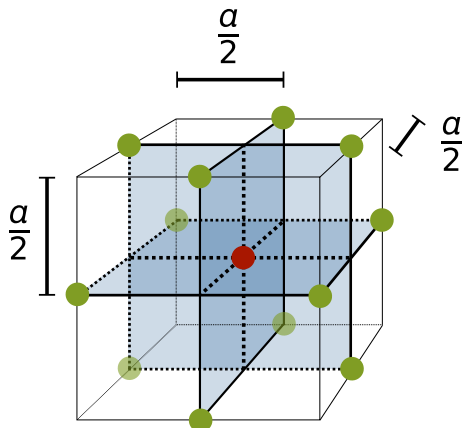


Figure 2.9:

Face-centered cubic lattice with the twelve nearest neighbors: The orbital of the centered atom (red) interacts with the orbitals of the twelve nearest neighbor atoms (green). The side length is of cubic cell is a .

2 Metals

Orbital	Orbital function	Character of angular momentum	Overlap matrix element S	Z_{eff}
5s	$\varphi_1 = \Psi_{5s}$	s	1.52560	1.63 or 9.07
4p _z	$\varphi_2 = \Psi_{4p_z}$	p	1.05290	≈ 3.75
4p _x	$\varphi_3 = \Psi_{4p_x}$	p	1.05290	≈ 3.75
4p _y	$\varphi_4 = \Psi_{4p_y}$	p	1.05290	≈ 3.75
$x^2 - y^2$	$\varphi_5 = \Psi_{4d_{x^2-y^2}}$	e_g	0.93772	≈ 4.75
$3z^2 - r^2$	$\varphi_6 = \Psi_{4d_{3z^2-r^2}}$	e_g	0.93772	≈ 5.75
xy	$\varphi_7 = \Psi_{4d_{xy}}$	t_{2g}	1.02074	≈ 2.3 or ≈ 5.5
zx	$\varphi_8 = \Psi_{4d_{zx}}$	t_{2g}	1.02074	≈ 2.25 or ≈ 4.25
yz	$\varphi_9 = \Psi_{4d_{yz}}$	t_{2g}	1.02074	≈ 2.3 or ≈ 4.25

Table 2.2:

Effective atomic number for the different orbitals: Overlap calculations supply Slater-Koster parameters. The effective atomic number Z_{eff} is then determined in a way that the overlap matrix elements S fits the given parameters [Pap86]. The notation e_g and t_{2g} describes representations of d orbitals. The g in the subscript denotes inversion symmetry.

2.3.3 Dipole transition matrix elements

The *dipole transition matrix elements* give information about the probability of a transition between two bands. With the reconstructed basis wave functions of Sec. 2.3.2 it is now possible to calculate these matrix elements. They are determined by

$$d_{ij}^{\mathbf{k}} = e \int_{-\infty}^{\infty} d^3r \Psi_{i\mathbf{k}}^*(\mathbf{r}) \mathbf{r} \Psi_{j\mathbf{k}}(\mathbf{r})$$

for each wave vector \mathbf{k} in a face-centered structure and for every transition from band i to band j where e is the elementary charge. The wave functions $\Psi_{i\mathbf{k}}$ are given by Eq. (2.20):

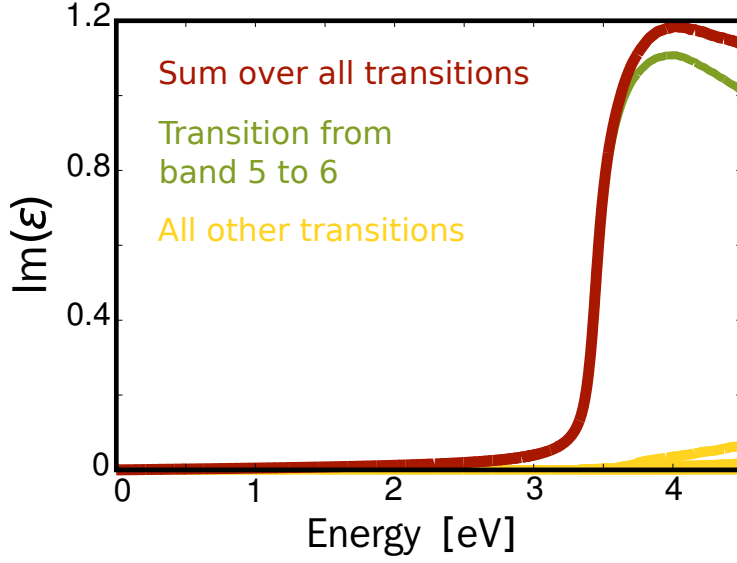
$$\Psi_{i\mathbf{k}} = \sum_{m=1}^9 v_{im} \frac{1}{\sqrt{N}} \underbrace{\sum_p e^{i\mathbf{k}\mathbf{R}_p} \varphi_m(\mathbf{r} - \mathbf{R}_p)}_{b_{\mathbf{k}m}}.$$

Since the reconstructed hydrogen wave functions are only an approximation, also the results of the dipole matrix moment are not exact. Not for every region and every transition good results are obtained. In Fig. 2.6 for small \mathbf{k} ranges around the most important symmetry points for interband transitions X and L, dipole moments are plotted in the band structure environment.

2.3.4 Linear absorption

The absorption spectrum of silver can be determined by calculating the temporal dynamics of the microscopic response of the material $\mathbf{p}_{\mathbf{k}}(t) = \langle a_{i\mathbf{k}}^\dagger a_{j\mathbf{k}} \rangle$ for two considered bands i and j . It is connected to the macroscopic polarization via

$$\mathbf{P}(t) = \frac{1}{V} \sum_{\mathbf{k}, i, j > i} \left(\mathbf{p}_{\mathbf{k}}(t) d^{ij} + \mathbf{p}_{\mathbf{k}}(t) d^{ij*} \right) \quad (2.21)$$

**Figure 2.10:**

Linear absorption of silver: The red curve shows the complete absorption of all interband transitions in silver. The green curve, that gives only the spectrum of transitions from the fifth to the sixth band, contributes the most of the complete absorption. All other transitions do not contribute notable for the plotted energy range. The slope at about 3.5 nm is in a good agreement with the band structure (cf. 2.6).

with the volume V of the silver bulk [HK04] for all transitions between the bands i and j .

The interband transition spectrum then is calculated by the absorption that is given in Sec. 2.1.6 by Eq. (2.11) and that says that

$$\alpha(\omega) \propto \omega \operatorname{Im} \left(\frac{P(\omega)}{E(\omega)} \right) = \omega \operatorname{Im}(\chi(\omega)).$$

The susceptibility χ can be calculated analogously to Eq. (A.10) and is then

$$\chi(\omega) = \sum_{\mathbf{k}, i, j > i} \frac{(N_{\mathbf{k}}^j - N_{\mathbf{k}}^i) d_{\mathbf{k}}^{ij*}}{\epsilon_0 (\hbar\omega_{\mathbf{k}}^{ij} - \hbar\omega - i\gamma_{ij})} + \frac{(N_{\mathbf{k}}^j - N_{\mathbf{k}}^i) d_{\mathbf{k}}^{ij*}}{\epsilon_0 (\hbar\omega_{\mathbf{k}}^{ij} + \hbar\omega + i\gamma_{ij})}$$

with the particle density $N_{\mathbf{k}}^i = \frac{1}{V} \sum_{\mathbf{k}} n_{\mathbf{k}}^i$ and $n_{\mathbf{k}}^i = \langle a_{i,\mathbf{k}}^\dagger a_{i,\mathbf{k}} \rangle$, $\hbar\omega_{\mathbf{k}}^{ij} = \epsilon^i - \epsilon^j$ and a phenomenological damping constant γ_{ij} .

As discussed in Sec. 2.3.1, the most important transition in silver is between the fifth and the sixth band. This is verified by the linear absorption spectrum plotted in Fig. 2.10. Since the calculated dipole transition elements (see Sec. 2.3.3) use reconstructed hydrogen wave function and are consequently not reliable, the linear absorption gives only a rough course of the graph. For example, the transition from the sixth to the seventh band should appear for smaller energies than it does in this spectrum.

3 Nanoplasmonics

Optical properties of an increasing variety of metallic nanostructures are investigated – mostly with the aim of concentrating light into nanoscale volumes. Nanoplasmonics is a recently developed science with numerous effects and rich applications [Sto11b]. The characteristic that makes nanoplasmonics so important for this work is the ability of such systems to keep the optical energy concentrated on the nanoscale. This effect is enabled on modes called surface plasmons [Sto11a].

The existence of surface plasmons is based on the fact that the dielectric function ϵ (see Sec. 2.1.5) has a negative real part [Sto11a]. For small losses, that means for example $\text{Im}(\epsilon) \ll -\text{Re}(\epsilon)$, the surface plasmons are well pronounced as resonances. A metal that satisfies these two properties is a good plasmonic metal. In silver most of the visible region fulfills this properties.

For a more detailed understanding of specific enhancement effects this section is focused on two causes of plasmonic effects: material properties and geometry settings. In this section, nanospheres serve as an already good investigated model system.

At specific optical frequencies, the resonantly driven oscillation produces a strong charge displacement and leads to a field concentration. This is due time-varying electric light fields that force the gas of negatively charged electrons inside a metal to a collective oscillation [SBC⁺10].

For nanostructures sized much smaller than the free-space wavelength of the incident light, the structure experiences a constant electric field over its entire size. This explains the field distribution within such a nanoparticle: Solving the electrostatic potential for a structure of given dielectric constant and geometry determines resonance effects. Hereby, the particle is embedded within an uniform electric field. This assumption is called *quasistatic approximation*.

In this chapter, some plasmonic properties are presented and investigated and some results of this work are given. The focus is on metal nanospheres. More examples of plasmonic effects are given in Ch. 5. In the first section, the behavior of pure metal nanospheres without another metallic coating (but with a dielectric layer) in a linear polarized electric field is examined, especially the plasmonic enhancement on the surface of the sphere. After that, the effects of additional layers are investigated and then the plasmonic effects for coupled nanospheres are considered. All these effects are chosen to end the chapter by presenting an application that is based on these effects: long range transfer for plasmon excitations. For this, nanostructured metal-insulator surfaces combined with immobilized biological molecules are investigated. They are of interest for improving processes in bioelectronic catalysis. Due to localized surface plasmonic effects, these devices are suitable for electron transfer effects and for the design of surface enhanced Raman spectroscopy phenomena. Field distributions of some selected geometries are simulated with a Maxwell solver to support the experimental findings.

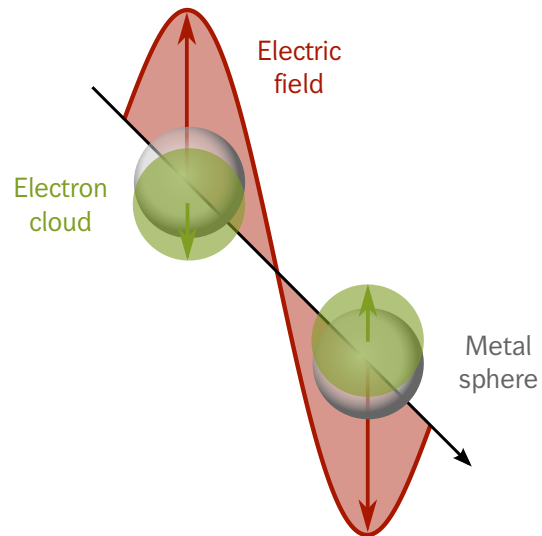


Figure 3.1: Plasmon oscillation of a metal sphere: The sketch shows the displacement of the conduction electron charge cloud in relation to the nuclei [KCZS03].

3.1 Pure metal nanospheres

In the following, the focus is exemplarily chosen on metal nanospheres. The behavior of a sphere in an electric field is well studied [SBC⁺10, DRK⁺10, GMK75].

Fig. 3.1 illustrates the coherent oscillation of conduction electrons caused by the electric field in small spherical nanoparticles. The electronic cloud is displaced relatively to the nuclei, so that a restoring force caused by Coulomb attraction between electrons and nuclei results in that oscillation. Beside shape and size of the particle, material properties like the density of electrons and the effective electron mass influences the oscillation frequency, the *dipole plasmon resonance* of the particle. Also higher modes of plasmon excitation can occur. For quadrupole mode, for example, the half of the electrons move parallel to the applied electric field and the other half moves antiparallel. A theoretical description for dipole and quadrupole modes can be found in [KCZS03].

Spherical nanoparticles exhibit a dipolar plasmonic resonance at wavelengths for which the ratio of the permittivities of the metal ϵ_m and the dielectric ϵ_d is given by $\epsilon_m/\epsilon_d = -2$. As a consequence, the resonance frequency shifts red for surroundings with increasing dielectric permittivities. The resonant condition ϵ_m/ϵ_d is given in [SBC⁺10] as a function of aspect-ratio parameter for quasistatic spheroidal particles.

Electric field distributions of pure metallic nanoparticles can be found in [Dav09], for example. For applications in surface enhanced Raman spectroscopy (cf. Sec. 3.4), often various nanostructured multilayer devices are of interest. Thus, the simulated setup in this work consists of silicon dioxide (SiO_2) coated metal spheres.

Fig. 3.2a shows a field distribution for a metal sphere with a radius of 20 nanometer, coated with a two nanometer dielectric layer for three different materials: silver (Ag), gold (Au), and platinum (Pt). The silver sphere is surrounded by water and the values for the dielectric functions are taken from [Pal85]. The field distribution is generated via “JCMsuite” [PBZS07]. This Maxwell solver is used for the calculation of field distributions throughout this work. It uses the finite element method that is introduced in detail in Ch. 4.

The plasmonic field enhancement is visible on the top and the bottom of the sphere for incident light that is polarized in vertical direction (see Fig. 3.2a). That is in accordance to the plasmon oscillations of Fig. 3.1.

Fig. 3.3 shows further field distributions for different incident directions and polarization directions. The same silver sphere as in Fig. 3.2 is illuminated from the right with different

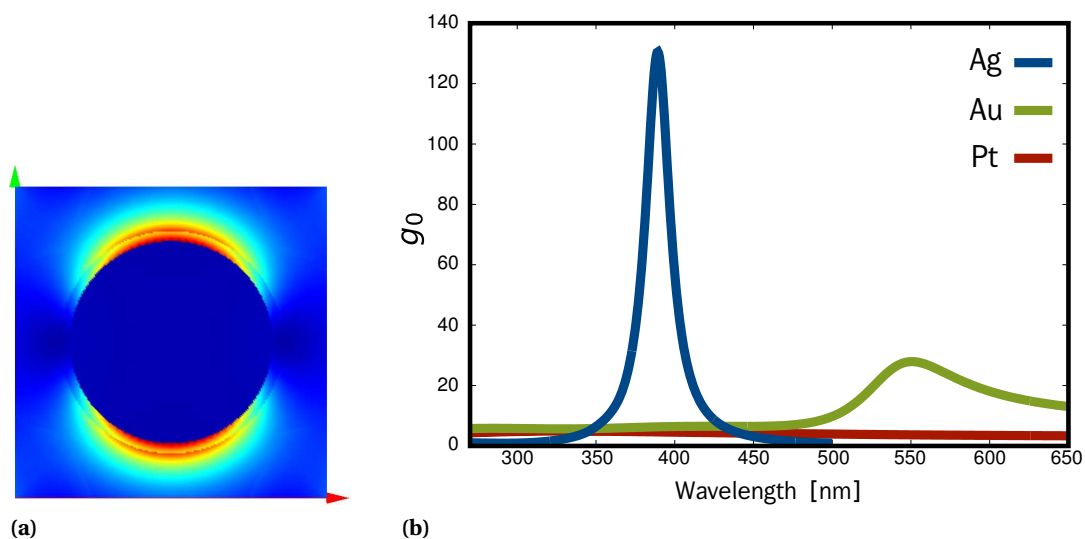


Figure 3.2:

Field distribution of a sphere with a dielectric coating and plasmon resonances for different metals: Part (a) shows the absolute value of the electric field of a resonant silver sphere with a radius of 20 nm that is radiated with a wavelength of 415 nm from the front in a vertical polarization direction. The sphere is coated with a 2 nm dielectric. Part (b) shows a wavelength scan for three different metal spheres. The measurement point is directly on top of the coating centered horizontally. The function g_0 describes the local field enhancement, see Eq. (3.1). The silver sphere is again surrounded by water and the values for the dielectric functions are taken from [Pal85].

polarization directions. The light has again a wavelength of 415 nanometers. In contrast to Fig. 3.2a, here, only some components of the electric fields are plotted. Fig. 3.3a shows the x component of the electric field, Fig. 3.3b the y component. For both figures the light incides from the right side with a polarization in y direction. The x contributions are caused by reflections of the incoming light. Since the slice is regarded in the center of the sphere, the z component is zero. Together, they result in Fig. 3.2a. Hence, a sphere irradiated with z polarized light only reveals contributions in z direction (Fig. 3.3c). Reflections of the incoming light become visible: the field enhancements are more prominent on the right side – the direction of the incoming light.

The plot in Fig. 3.2b shows the plasma resonance for three different metals. Here, the function g_0 describes the local field enhancement, that is given by

$$g_0 = \left| \frac{\mathbf{E}(\mathbf{r}, \omega)}{\mathbf{E}_0} \right|^2. \quad (3.1)$$

More studies for metal spheres and especially nanoparticles with arbitrary shapes and the dielectric environment are exemplarily found in [KCZS03, SNB03].

3.2 Hybrid nanospheres

To describe the transport and the optical scattering mechanisms within particular bioelectronic devices, often dielectric nanolayers-layers are used [DRK⁺10]. Such devices can be optimized with respect to their distance controlled electron transfer between the molecule and the electrode (cf. Sec. 3.4).

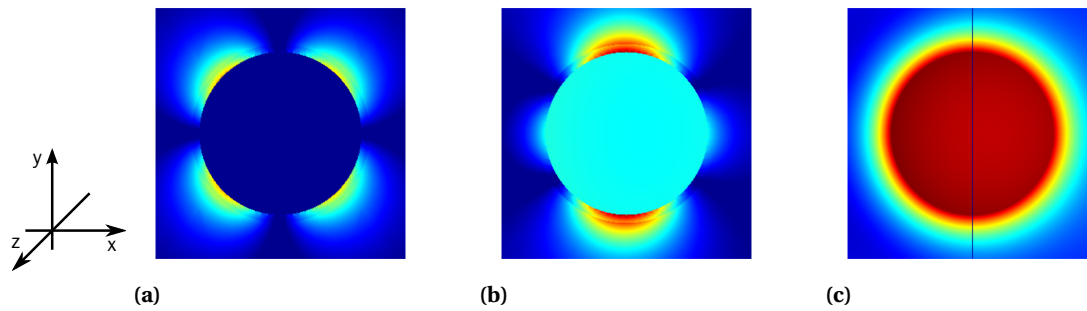


Figure 3.3:

Different components of the field distribution of a silver sphere with a dielectric coating from different illumination directions: The silver sphere with a radius of 20 nm and a dielectric layer with a thickness of 2 nm is illuminated from the right with a vertical polarization in y direction (a, b) and a polarization direction perpendicular to the illustration plane (z direction) (c). The light has a wavelength of 415 nm. Part (a) shows the x component of the electric field, part (b) shows the y value of the electric field. The z component equals zero. Part (c) shows the z component for a z polarization. Here, all other components vanishes within the center slice. The silver sphere is again surrounded by water and the values for the dielectric functions are taken from [Pal85].

To investigate Raman scattering cross sections, two effects are important: On the one hand, the protein can be described as an injector for charges, which are transported through the complex hybrid device [GKW⁺10, LCF07]. The second important effect is the long range transfer of plasmon excitation from the electrode to the respective molecule that is investigated also with the help of a self-consistent solution of Maxwell's equations and material equations for metals.

The comparison of the materials in Fig. 3.2b shows, that they have different responses to certain wavelengths. To demonstrate *long range plasmon excitation* in a theoretical way, the metal sphere with the dielectric layer is coated with an additional layer: gold or platinum. These metals do not have any plasmon resonance for the relevant wavelength in surface enhanced Raman experiments of Sec. 3.4 as can be seen in Fig. 3.2b.

The effects of the long range plasmon excitation are investigated in Fig. 3.4 [FGHW10, LKF⁺12]. Exemplarily, a platinum coating is chosen. Also gold would be an alternative since both, gold and platinum, do not have a plasma resonance in the range of 415 nanometers. In Fig. 3.4a a silver sphere with a radius of 20 nanometers and a silicon dioxide spacer of two nanometers is coated by a ten nanometers platinum layer and a dielectric border of two nanometer and the plasmonic effects are made visible. Fig. 3.4b shows the field enhancement g_0 for a centered vertical section through the sphere for different coating diameters. As a benchmark, the red curve gives the field enhancement for a silver core without coating.

It can be clearly seen, that the field enhancement decreases through the coating and that the reduction depends on the thickness of the platinum layer. The larger the diameter of the coating, the smaller the enhancement, that means platinum has a screening effect. The advantage of the coating is now, that although the platinum layer is screening the plasmonic effects, the enhancement of the electric field strength can be transferred to higher radii. If the coating's diameter is high enough, the maximum field enhancement will decrease on the one hand but on the other, it leads to comparably high fields in a great distance from the center of the sphere, compared to the case without the coating, as can be seen in Fig. 3.4b. So it is possible to transfer the plasmon excitation over a long distance.

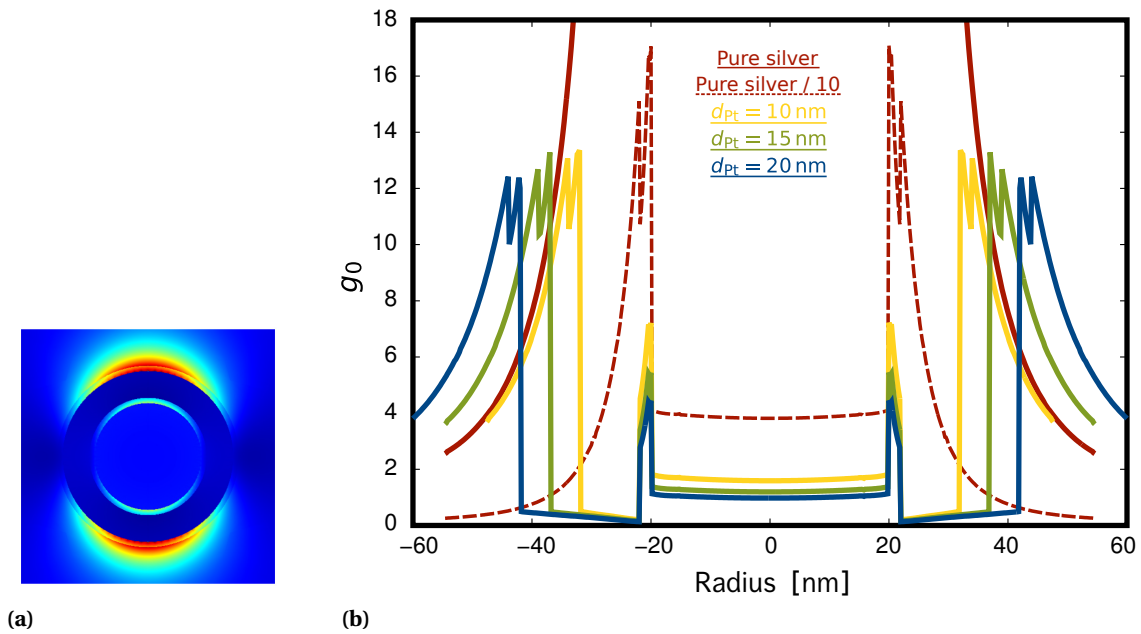


Figure 3.4:

Long range plasmon excitation: Part (a) shows the absolute value of the electric field of a multilayer sphere: a 20 nm Ag core, a 2 nm SiO₂ spacer, 10 nm Pt coating and finally a 2 nm dielectric. The sphere is radiated with a wavelength of 415 nm from the front in a vertical polarization direction. Part (b) shows the field distribution along the centered vertical line through the sphere for different platinum thicknesses. The field enhancement g_0 is calculated via Eq. (3.1). The silver sphere is again surrounded by water and the values for the dielectric functions are taken from [Pal85].

3.3 Coupled nanospheres

A further possibility to achieve strong field enhancements is bringing the sphere in close vicinity to another metal sphere. Fig. 3.5 illustrates the coupling of two coated metal nanospheres. The multilayer sphere consists of a silver core with a 30 nanometers radius, followed by a two nanometers thick silicon dioxide spacer. Then, a platinum coating with variable thickness (from one to eight nanometers) is laid on. The outer layer is a four nanometers thick dielectric.

As a result, it can be seen that the closer the borders of the spheres, the higher is the resulting coupling of them. It has to be noted that the centers of the spheres are at a fixed position. That means, that in this example, the spheres move closer together only due to the increasing coating. Changing the proximity of the spheres like that reveals an additional effect: The thicker the platinum coating, the smaller is the field enhancement at the surface of the sphere. This has been the a result from Sec. 3.2. In Fig 3.5 it can also be seen that the silver core of the spheres is darker for a higher platinum coating. All three subfigures are scaled identically.

The wavelength scan of Fig. 3.6 confirms these two effects. Increasing platinum coating shifts the maximum to higher wavelengths. Additionally, the peak first decreases – for more than four nanometer coating, the maximum is increasing. The shift to higher wavelengths is plotted in Fig. 3.7 (red curve) as well as the illustration of the two counteracting effects of screening and coupling (blue curve).

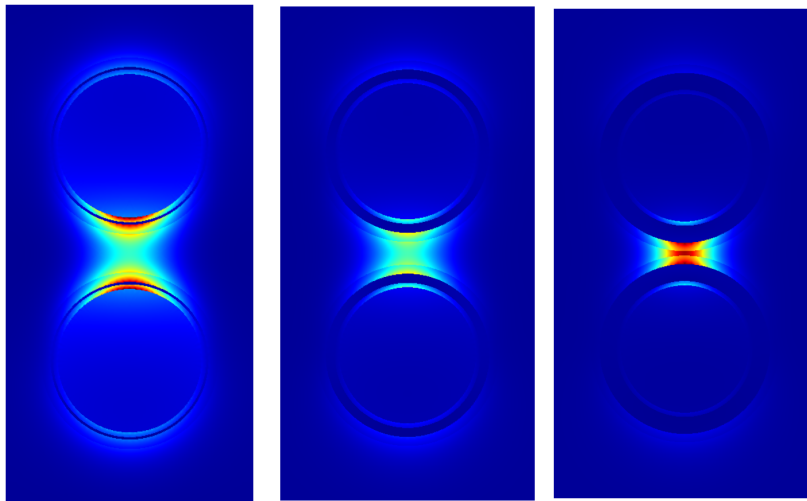
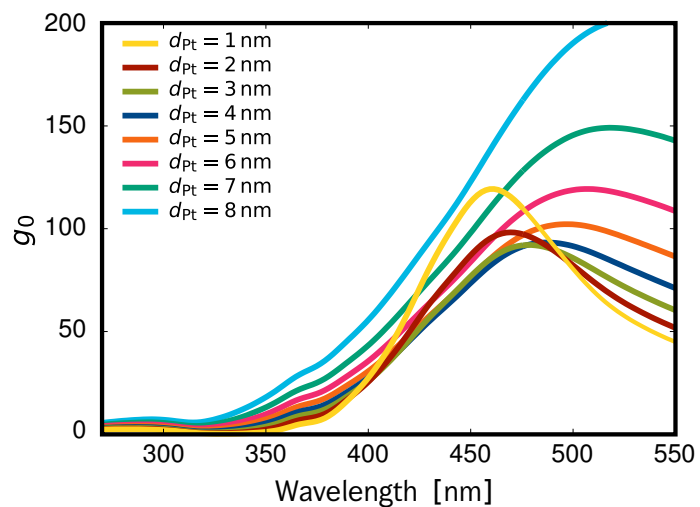


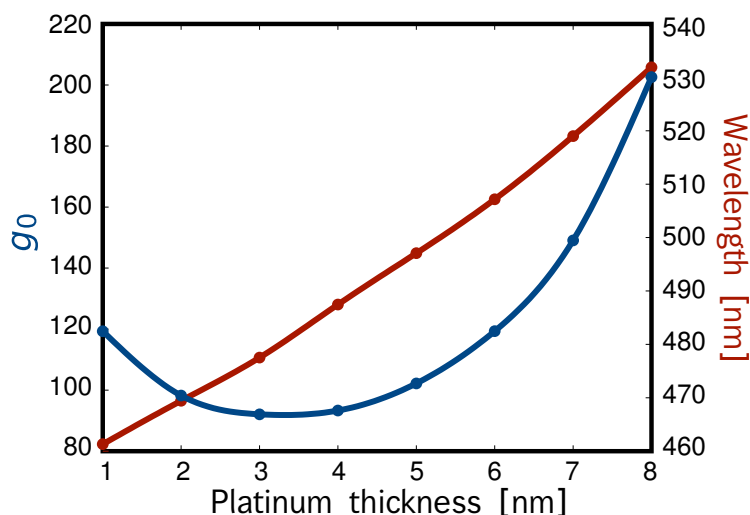
Figure 3.5:

Two coupled silver spheres with platinum coating of different diameters: The center of the Ag spheres with a radius of 30 nm stay at fixed positions. The thicker the Pt coating (1, 4, and 8 nm) the lower is the electric field inside the sphere (the three figures are scaled identically). That applies to the outside of the sphere but here the coupling due to the low distance between the borders of the spheres, enhances the electric field between the spheres.

Figure 3.6:

Field enhancement spectra for different platinum coating thicknesses: For the setup of Fig. 3.5, the field enhancement is measured for different wavelength in the center of the gap between the two Ag spheres with Pt coating. The wavelength scan is shown for different coating thicknesses of the Pt coating. Regarding the maximum of each curve, two counteracting effects can be seen: the screening of the Pt layer versus the field enhancement due to the plasmonic coupling of the spheres. A further result is the increasing wavelength for the maximum resonance for thicker Pt coatings.



**Figure 3.7:**

Wavelength shift and two counteracting effects of platinum coating for different thicknesses for the enhancement factor: The blue curve demonstrates the two counteracting effects. Lower Pt thickness decreases the screening of the layer, higher thickness leads to more coupling of the spheres. The red curve shows the wavelength shift. Both curves are extracted from values of Fig. 3.6.

3.4 Induced surface enhancement

Nobel metals play an important role in heterogeneous catalysis in several surface reactions with catalytic efficiency that sensitively depends on the support material as well as on the surface morphology and temperature. A profound understanding of the underlying reaction mechanism at the surface is required for a rational design of catalytic supports [FGS⁺09, FGHW10].

For this purpose, a highly sensitive in-situ technique that is able to monitor the interfacial processes on a molecular level under ambient conditions is needed. Established techniques in this field require ultrahigh vacuum or at least low pressure conditions as the methods rely on ions and electrons as probes. An alternative is the vibrational spectroscopy, especially the surface enhanced Raman spectroscopy (also known under the abbreviation SER). It provides structural information under in-situ conditions.

Since the surface enhanced Raman spectroscopy is limited to metallic supports with strong surface plasmon resonances upon light excitation, the models of the plasmonic investigations of the previous sections can be used: Silver and gold provide sufficient intrinsic plasmonic activity for surface enhanced Raman spectroscopy applications while other metals relevant in catalysis like platinum show only very weak plasmon induced surface enhancement and are consequently not suitable.

To overcome this restriction, novel Pt-Ag hybrid supports are examined [LKF⁺12]. They combine the optical properties of silver with the surface properties of platinum. For fabricating a rough silver support is surrounded by a dielectric spacer. Then, the device is covered with a thin electro-deposited platinum film. As a result, a quasi-closed platinum layer with a continuous thin platinum coverage over the coral structure of the silver support decorated with small platinum islands is obtained (see Fig. 3.8a) [LKF⁺12]. This setup corresponds with the real structure of Ag-SiO₂-Pt electrodes as shown in Fig. 3.8b.

To test the performance of the Pt-Ag devices, surface enhanced Raman spectra of different Raman probes can be collected as a function of spacer material, spacer length and laser excitation (see [LKF⁺12]). It is possible to record high quality Raman spectra of only slightly lower intensities compared to the ones obtained on pure rough silver structures. The findings of [LKF⁺12] imply that surface enhanced Raman activity is induced on the platinum surface by a long range plasmon coupling between the outer metal and the silver support [FGHW10, DRK⁺10].

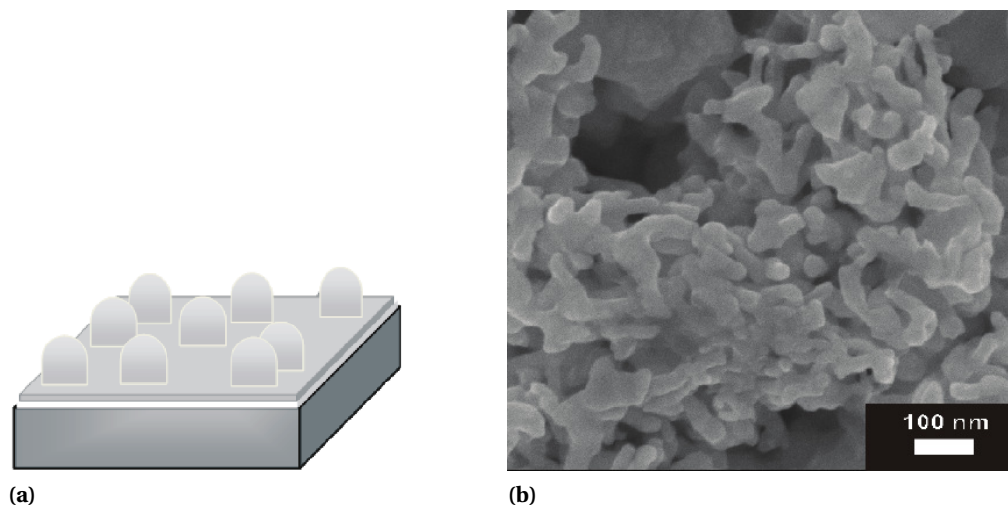


Figure 3.8:

Electrodes of Ag-SiO₂-Au for long range excitation: Part (a) gives a schematic presentation of the Ag-SiO₂-Pt electrode preparation. In comparison, part (b) shows a surfaced enhanced Raman picture of such electrodes. Both pictures are taken from [LKF⁺ 12] (Copyright (2012) by the American Chemical Society).

On the left in Fig. 3.9 a simplified model of Fig. 3.8a is simulated via the Maxwell solver “JCMsuite”. The cross section is similar to the platinum island but the profile has a cylindrical continuation with the y axis as rotation axis. This setup is sufficient to show the enhancement effects due to plasmonic effects: Sharp edges increases the field enhancements. So it is concluded that a nonperfect coating of the platinum island film promotes the efficiency of the induced platinum surface enhanced Raman activity.

In the simulations (see Fig. 3.9, right side) it is carried out that an incomplete platinum covering film by introducing hole-like defects (that gives a closer resemblance to the true experimental situation) results in strong fields which raises the average surface enhanced spectroscopy enhancement by about 80 percent. Furthermore, a comparison with similar measurements on Ag-SiO₂-Au electrodes suggests that the chemical nature of the metal island films plays only a minor role for the surface enhanced Raman intensity.

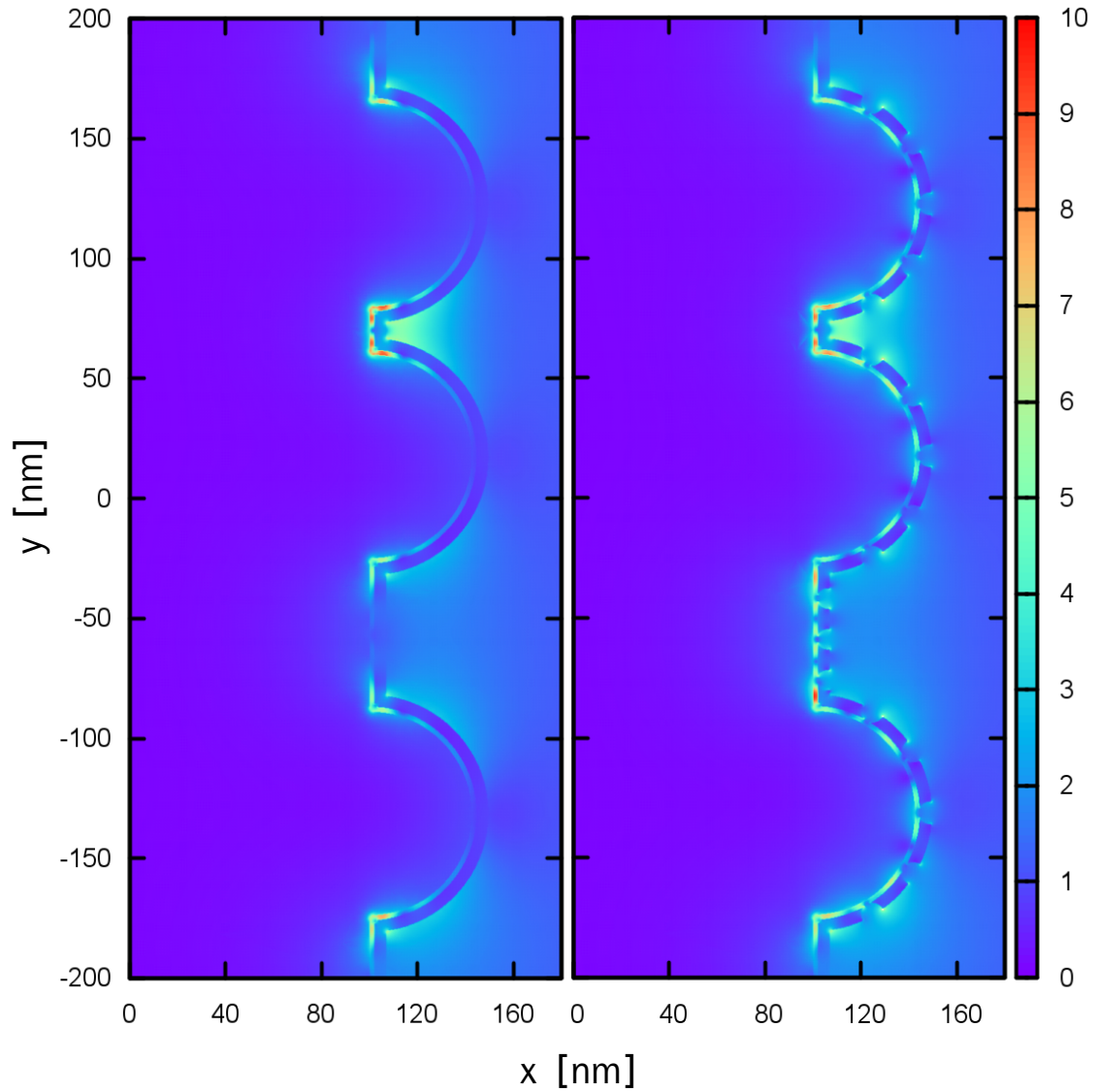


Figure 3.9:

Field enhancement calculations of Ag-SiO₂-Pt geometries: On the left side, a defect-free Pt film is simulated while on the right side the Pt film contains defects. Strong field enhancement effects are visible especially on sharp edges. This figure is taken from [LKF⁺12].

4 Numerical Simulations

The interaction between metals and other nanostructures with light is determined by Maxwell's equations. For calculating field distributions, partial differential equations have to be solved. Since the analytical solution is hard to find, numerical solutions have to be chosen. As explained in Sec. 5.3, for the intentions of this work, a Maxwell solver in frequency domain is the most recommended.

In this work, the solver "JCMsuite" is used [PBZS07]. It is based on the finite element method. This method differs from other numerical solving methods in time domain like the finite-difference time-domain method and the Discontinuous Galerkin method.

The electric field is complex with vectorial character. In the following, only certain components – absolute values or phases of the electric field vectors – may be regarded. Such field distributions are needed to investigate spatiotemporal control that is done in Ch. 5.

The chapter starts with presenting the finite element method including an example, a convergence discussion and a section that is focused on the triangulation. After that, three problem classes that occurs while working with light propagations are presented. Finally, two possibilities for transparent boundary conditions are introduced.

4.1 Finite element method

The finite element method is a numerical procedure for solving variational problems, differential and variational equations. The modern method of calculation is often used in engineering applications. Furthermore, it is a standard tool for the simulation of solids.

The method decomposes the underlying domain into simple sub-regions. Then, it generates an equation system for approximated values of the unknown function in distinguished points of the domain.

The method provides an approximation for the exact solution of the differential equation, whose accuracy can be improved by increasing of the degrees of freedom and hence the computational effort. After solving the system of equations, the values of the unknowns of the distinguished points are approximately known.

An advantage of the finite element method is providing systematic control for the generation of stable numerical schemes. Furthermore, it is relatively easy to consider complicated two- or three-dimensional geometries.

The basic idea of the finite element method (presented in detail in Sec. 4.1.2) is dividing the computational domain in an arbitrarily large number of elements. The name of the method derives from the fact that these elements are finite and not infinitely small. Within these elements, ansatz functions are defined. These functions are inserted into the differential equations that describes the problem that has to be solved. Combining them with start or boundary conditions yields a system of equations, that is usually solved numerically and gives the numerical solution of the differential equation. Its size depends significantly of the number of finite elements.

In the first subsection, a possibility of generating a system of equations is presented via a variational equation. Afterwards, the basis idea of finite elements is explained in more detail

with an extensive example. In the end, some theoretical reflections about the convergence behavior are given.

4.1.1 Variational equation

There are two access points to obtain a discrete problem: the variational principle and a boundary value problem. On the one hand, there exist direct accesses: For the variational principle the Ritz method [NV73] and for a boundary value problem the method of weighted residuals lead to the discrete problem. The Ritz method in general is easier to apply but usually there is no variational principle available [GRT93].

On the other hand it is possible to use a *variational equation* in order to find the discrete problem. Such an equation reads

$$\text{Find } u \in V : \quad a(u, v) = b(v) \quad \forall v \in V, \quad (4.1)$$

with V as a set of all continuously differentiable functions in a domain Ω that vanish at the boundaries, a as a bilinear form on $V \times V$, and b as a linear form on V .

To obtain a variational equation from a boundary value problem, usually integral theorems (especially the Gaussian integral theorem) are used. Here, the example applies a partial integration. Starting point is the one-dimensional Helmholtz equation (2.8) as presented in Sec. 2.1.3

$$\partial_x^2 u(x) + k^2(x)u(x) = 0$$

with the boundary condition $u(x) = u_0$ for $x \in \partial\Omega$ at the boundaries of the computational domain Ω . If the function u satisfies only a general *Dirichlet boundary condition* $u(x) = u_0$ for¹⁰ $x \in \partial\Omega$, a conversion into a 0-Dirichlet boundary condition $u(x) = 0$ for $x \in \partial\Omega$ is possible by introducing a function g that is twice differentiable and satisfies the Dirichlet boundary condition $g(\partial\Omega) = u_0$:

$$\begin{aligned} \partial_x^2(u - g + g) + k^2(u - g + g) &= 0 \\ \Leftrightarrow \quad \partial_x^2(u - g) + k^2(u - g) &= \underbrace{-\partial_x^2 g - k^2 g}_{=: f}. \end{aligned}$$

Then $(u - g)(\partial\Omega) = 0$ and $u - g$ satisfies the 0-Dirichlet boundary condition and is only called u in the following so that

$$\partial_x^2 u(x) + k^2 u(x) = f(x) \quad \text{and} \quad u(\partial\Omega) = 0.$$

As domain the interval $\Omega = (0, 1)$ is assumed. A main trick of the finite element method is multiplying the equation with the test function $v \in V$, that is once differentiable and satisfied the 0-Dirichlet condition $v(0) = v(1) = 0$. Integration over the whole computational domain yields

$$\int_0^1 v(\partial_x^2 u + k^2 u) = \int_0^1 v f \, d\Omega.$$

Integration by parts and using the boundary conditions for the first summand on the left hand side of this equation provides the variational equation:

$$\text{Find } u \in V : \quad \int_0^1 \partial_x v \partial_x u \, d\Omega - \int_0^1 k^2 v u \, d\Omega = - \int_0^1 v f \, d\Omega \quad \forall v \in V, \quad (4.2)$$

¹⁰ $\partial\Omega$ stands for the boundaries of the domain Ω

with the bilinear form $a(u, v) = \int_{\Omega} (\partial_x v \partial_x u d\Omega - k^2 v u) d\Omega$ and the linear form $b(v) = - \int_{\Omega} v f d\Omega$ with the continuous function $f = -\partial_x^2 g - k^2 g$.

Obtaining a variational equation is also possible via a variational calculation. The minimization of the functional

$$J(u) := \frac{1}{2} \int_0^1 \partial_x u \partial_x u - \frac{1}{2} \int k^2 u u + \int_0^1 u f \quad (4.3)$$

via the demand $\frac{\partial J(u+tv)}{\partial t} \stackrel{!}{=} 0$ is another way to obtain the variational equation (see [Bra07]).

The variational equation is used for setting up the system of equations of the discrete problem, which is solved by the finite element method.

4.1.2 Basic concept

The essence of the finite element method is presented in this section. After outlining the general concept, an example follows.

General concept of the finite element method

For obtaining the solution of the given problem, a function u of a given set of functions V has to be found that satisfies the variational equation (4.1): $a(u, v) = b(v)$ for all $v \in V$.

The central idea of the finite element method is now to get the *discrete problem*

$$\text{Find } u_h \in V_h: a(u_h, v_h) = b(v_h) \quad \forall v_h \in V_h \quad (4.4)$$

by projecting Eq. (4.1) from V to V_h .

For this purpose a subspace $V_h \subset V$ is introduced that is the set of all linear combinations

$$\sum_{i=1}^N u_i v_i$$

where u_i are constants and v_i are N linearly independent basis functions.

Instead of searching for an exact solution function u , the finite element methods helps finding an *approximate solution* $u_h \in V_h$ with the ansatz

$$u_h = \sum_{i=1}^N u_i v_i \quad (4.5)$$

with the N unknown constants u_i .

It is sufficient to claim that

$$a(u_h, v_j) = b(v_j) \quad (4.6)$$

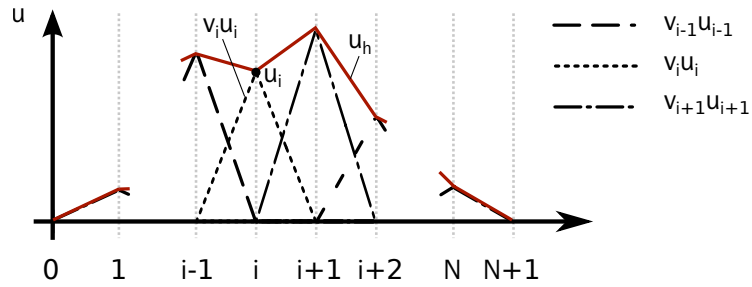
for just one certain $v_j \in V_h \setminus \{0\}$ because multiplication by the constants c_j and summation over j gives

$$\sum_{j=1}^N c_j a(u_h, v_j) = \sum_{j=1}^N c_j b(v_j)$$

and with using the properties of bilinear and linear forms it is equivalent to Eq. (4.4).

Figure 4.1:

Illustration of the finite element method in two dimensions: The dashed lines represents the N basis functions. In red, the approximation solution u_h is illustrated.



Inserting the ansatz (4.5) of u_h into Eq. (4.6) and use again the properties of bilinear forms a system of equations with N equations for N unknowns u_i is obtained:

$$\sum_{i=1}^N \underbrace{a(v_i, v_j)}_{a_{i,j}} u_i = \underbrace{b(v_j)}_{b_j}, \quad j = 1, \dots, N, \quad (4.7)$$

with the coefficient matrix A , that consists of the elements $a_{i,j}$.

Solving the discrete problem means solving the system of equations $Au = b$. The matrix elements $a_{i,j} = a(v_i, v_j)$ and the values $b_i = b(v_i)$ can be found by the basis functions v_i . Finally, the approximate solution function is given by Eq. (4.5).

In classical Ritz and Galerkin methods, the trial function is formulated as a combination out of a set of basis functions that are defined over the entire domain, so that the combination must have the ability to represent the true solution at least approximately. Additionally, it has to satisfy proper boundary conditions. Those methods differs from the finite element method since in this case, the trial function is a combination out of a set of basis functions that are defined only over subdomains. These subdomains cover the entire domain. Thus, the subdomains are small and the basis functions that are defined over such a subdomain can be quite simple [Jin02]. Especially for two- or three dimensional geometries small functions defined on subdomains are more advantageous since it is often impossible to find the required entire-domain trial functions.

Example

For illustrating the general concept a simple example is given. The one-dimensional computational domain Ω is defined on the interval $[0, N + 1]$. The N ansatz functions serve as a set of linear independent basis elements $w_i \in V_h$ [BWS10]

$$w_i(x) = \begin{cases} \frac{x-x_{i-1}}{x_i-x_{i-1}}, & \text{if } x \in [x_{i-1}, x_i], \\ -\frac{x-x_{i+1}}{x_{i+1}-x_i}, & \text{if } x \in [x_i, x_{i+1}], \\ 0, & \text{otherwise,} \end{cases} \quad i = 1, \dots, N,$$

that cover the computational domain (cf. Fig. 4.1).

The i th row of Eq. (4.7) yields

$$\begin{aligned} & a(w_{i-1}u_{i-1} + w_i u_i + w_{i+1}u_{i+1}, w_i) \\ & = a(w_{i-1}, w_i)u_{i-1} + a(w_i, w_i)u_i + a(w_{i+1}, w_i)u_{i+1} = b(w_i) \end{aligned}$$

since just the neighbor functions are unequal zero.

4 Numerical Simulations

ber of subdomains in which the function is represented by simple interpolation functions with unknown coefficients. The following basic steps describe a finite element analysis of a boundary-value problem [Jin02]:

1. Discretization or subdivision of the domain
2. Selection of the interpolation functions
3. Formulation of the system of equations
4. Solution of the system of equations

4.1.3 Convergence

Instead of the exact solution $u \in V$ of the variational equation, the finite element method only supplies the solution $u_h \in V_h$ of the discrete problem. There are different factors that influence the quality of the approximate solution, for example the way of partitioning the computational domain or the choice of basis functions w_i [KFR90]. The latter is crucial for the feasibility of the method. There are certain requirements on the basis functions. They must satisfy both continuity conditions and the required boundary conditions. Within this latitude the basis functions are chosen so that the discrete problem is as simple as possible. For a good approximate solution a large number of basis functions is recommended but this also means a large matrix. This is why there are often basis functions chosen that are nonzero only on small subdomains $\Omega_i \subset \Omega$, so that many matrix elements equal zero, as seen in the example of Sec. 4.1.2.

Convergence of order p occurs, if for the maximum diameter h of the used elements for the partition of Ω exists a constant C that is independent of h with

$$\|u - u_h\| \leq Ch^p.$$

Typically, the H^0 or L^2 norm $\|u\|_0^2 = \int_{\Omega} \bar{u}u \, dx$ with \bar{u} as the complex conjugate of u is used. To consider the amount of the derivatives, in some cases the H^1 norm with $\|u\|_1^2 = \int_{\Omega} \bar{u}u \, dx + \int_{\Omega} \partial_x \bar{u} \partial_x u \, dx$ is applied.

In the following the idea of an error estimate for *Poisson's equation* [CS80]

$$\partial_x^2 u = -\frac{\rho}{\epsilon}$$

with $\int_{\Omega} \partial_x u \partial_x v \, dx =: a(u, v)$ and $\int_{\Omega} \frac{\rho}{\epsilon} v \, dx =: f(v)$ is given. For this purpose the convergence problem is transferred to an approximation problem (*Céa's lemma*) that says that it exists a constant C independent of V_h with

$$\|u - u_h\| \leq C \inf_{v_h \in V_h} \|u - v_h\|. \quad (4.8)$$

The proof of this lemma is given in App. A.4, using the Galerkin orthogonality condition and the Lax-Milgram theorem. For the Helmholtz equation the proof is more complicated since for example condition (2) is not fulfilled. Up to here, one can say, that the method of finite elements finds that function from the space spanned of basis functions for which the error in the requested norm is minimal.

Finally, an equation is derived that provides a proposition about the order. Since in generally it is difficult to find the approximation error of Céa's lemma (4.8), the approximation

error is replaced by an interpolation error. The solution u_i that is found by an approximation holds

$$\inf_{v_h \in V_h} \|u - v_h\| \leq \|u - u_i\|.$$

One simple possibility to approximate a function is a Taylor expansion. The common remainder term is given in the integral form and reads for order n

$$R_n(x) = \int_a^x \frac{(x-t)^n}{n!} u^{(n+1)}(t) dt$$

for the approximation at point a for the function u . With this term following estimations can be found:

$$|R_{n+1}| \leq c h^{n+1} \max_{x_i \leq \xi \leq x_{i+1}} |u^{(n+1)}(\xi)| \quad (4.9a)$$

$$|R'_{n+1}| \leq \tilde{c} h^n \max_{x_i \leq \xi \leq x_{i+1}} |u^{(n+1)}(\xi)| \quad (4.9b)$$

with $h = x_{i+1} - x_i$.

Let $h = x_{i+1} - x_i$ be the length of the interval for an approximation of a piecewise linear function u_i . Then

$$\begin{aligned} \|u - u_i\|_1^2|_{x_i, x_{i+1}} &= \underbrace{\int_{x_i}^{x_{i+1}} |u - u_i|^2 dx}_{\text{use (4.9a)}} + \underbrace{\int_{x_i}^{x_{i+1}} |\partial_x(u - u_i)|^2 dx}_{\text{use (4.9b)}} \\ &\leq \left(\int_{x_i}^{x_{i+1}} c h^2 h^2 dx + \int_{x_i}^{x_{i+1}} \tilde{c} h h dx \right) \left(\max_{x_i \leq \xi \leq x_{i+1}} |u^{(2)}(\xi)| \right)^2 \\ &= c h^5 + \tilde{c} h^3 \left(\max_{x_i \leq \xi \leq x_{i+1}} |u^{(2)}(\xi)| \right)^2. \end{aligned} \quad (4.10)$$

Through addition of all $N = \frac{1}{h}$ parts of the interval and neglecting the h^5 term

$$\|u - u_h\|_1 \stackrel{(4.8)}{\leq} \tilde{C} \inf_{v_h \in V_h} \|u - v_h\|_1 \leq \tilde{C} \|u - u_i\|_1 \stackrel{(4.10)}{\leq} C h \max_{0 \leq \xi \leq L} u^{(2)}(\xi) = C h \|u\|_2 \quad (4.11)$$

with L as the boundary of the one-dimensional computational domain, is obtained. If u is sufficiently differentiable, the generalized form of (4.11) reads

$$\|u - u_h\|_1 \leq C h^p \|u\|_{1+p} \quad (4.12)$$

with p as the polynomial degree. Using *Nitsche's trick* [Bra07], a rewriting of (4.12) for the L^2 norm is possible:

$$\|u - u_h\|_0 \leq C h^{p+1} \|u\|_{1+p}. \quad (4.13)$$

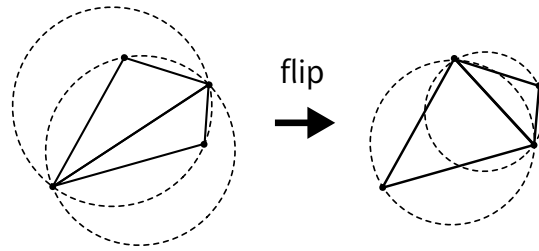
That serves as final error estimation for the finite element method.

In the example of Sec. 4.1.2 piecewise linear basis functions are used. As presented here, the solution of the differential equation becomes better by using piecewise polynomial basis functions instead. Eq. (4.13) shows: The higher the polynomial degree p , the lower the error, with a constant discretization width h .

For all simulations described in Sec. 5.5, a convergence analysis is done to find reliable results with acceptable computation time.

Figure 4.2:

Delaunay Triangulation: The both triangles on the left hand side do not meet the Delaunay condition since the circumcircles contain more than three points. After flipping the common edge, on the right hand side a Delaunay triangulation for the four points is produced.



4.1.4 Triangulation

The presented numerical method of this chapter uses an underlying grid. As described in Sec. 4.1.2, the finite element method uses, as the name implies, finite elements. Latter are generated by partition of the computational domain in triangles (2d) or tetrahedron (3d). For an optimal calculation process this *triangulation* has to satisfy some requirements. Thus, mesh generators form often a separate part of a finite element program. One exemplary requirement for optimized calculations is avoiding too sharp or at least too blunt triangles [GRT93].

A common technique to create a triangle mesh of a set of points is the *Delaunay triangulation*. With that method, points in \mathbb{R}^2 are connected to triangles in a way that no mesh point is inside the circumcircle of any triangle. It is possible to show that this method maximizes the minimum angle of all angles of the triangles [PS85, Wat81]. Thus, the triangles exhibit large internal angles that optimize the calculations. The Delaunay triangulation is not unique. It can be generalized for more dimensions. In a three dimensional space, the condition says that no mesh point is inside the circum-hypersphere of any polygon.

There exist a few algorithms to achieve a Delaunay triangulation. For two dimensions, the *flip algorithm* enables producing a Delaunay triangulation of an arbitrarily created mesh based on an evaluation of the local circumcircle condition. Each triangle that does not satisfy this condition flips the common edge of both triangles, so that the two points that were not previously connected form a new edge. An example is shown in Fig. 4.1.4. Thus, the neighboring triangles have to be checked again if they are Delaunay, that makes the computational effort of the order of n^2 for n triangles. An advantage of the algorithm is its convergence.

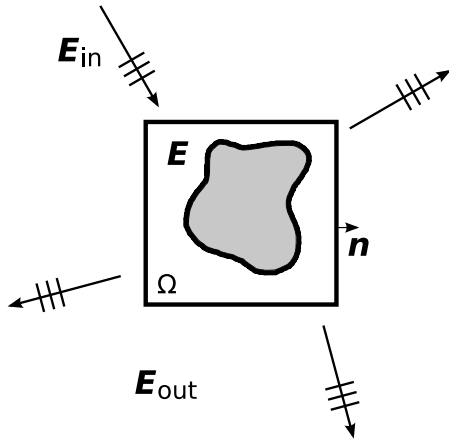
After generating [FG00] and optimization of a mesh, it can be changed with the help of the information provided by the assessment of quality as a last step. If these three steps are automatized, the finite element method and its implementation is called *adaptive*. There exist different procedures for an adaptive mesh refinement [ZBK⁺05, BZPS08, ZBPS07]. Common refinements are the decomposition of a triangle by halving all the sides into four congruent triangles or the decomposition of a triangle in two triangles by bisecting one side. Other procedures are presented in [Bän91, SS05].

4.2 Problem classes

Problems occurring while working with light propagations described by the wave equation (2.7)

$$\frac{1}{\varepsilon_0} \nabla \times \frac{1}{\mu_0} \nabla \times \mathbf{E} = \omega^2 \mathbf{E} \quad (4.14a)$$

$$\nabla \cdot \varepsilon_0 \mathbf{E} = 0 \quad (4.14b)$$

**Figure 4.3:**

Scattering problem: The incident light field E_{in} interacts with the scatterer within the computational domain Ω (with normal vector \mathbf{n} and excites an outgoing field E_{out}). In case of three dimensions, the computational domain is often a layer of glass or gallium arsenide with mounted with metal nanostructures.

can be divided into two types of problems [Zsc09]: Eigenvalue problems and boundary value problems. While the latter usually means scattering problems, the former can be divided into two subproblems: Waveguide eigenvalue (propagating mode) problems and resonance (resonance mode) problems. Here, a short introduction is presented using the example of the Helmholtz equation.

4.2.1 Resonance mode problems

Resonance problems describe finding eigenmodes in resonators, as modes of laser cavities or band structures of photonic crystals. They correspond to the mathematical problem: Find a tuple (E, ω^2) , so that the Eq. (4.14) is satisfied.

4.2.2 Propagating mode problems

Propagating mode problems deal with guided light fields in wave guide structures. Typical fibers are photonic crystals.

Since all these structures are characterized by the invariance in one spatial direction but with arbitrarily structured cross section of the waveguide, the electric field is harmonic in the waveguide direction z :

$$\mathbf{E} = \mathbf{E}_{\perp}(x, y) e^{ik_z z} \quad (4.15)$$

with k_z as the propagation constant.

A propagating mode solves the time harmonic Maxwell equation. In contrast to Sec. 4.2.1, here, the mathematical problem is: Find a tuple $(\mathbf{E}_{\perp}(x, y), k_z)$, so that Eq. (4.14) is satisfied.

4.2.3 Scattering problems

The problem class all simulations of this work are dealing with are scattering problems. In Fig. 4.3 a scheme of a scattering problem is presented in two dimensions. An incoming light field E_{in} enters the computational domain Ω with outward pointing normal vector \mathbf{n} and interacts with a scatterer (in this work nanoparticles). The scattered light field E_{out} leaves the computational domain in different directions.

Three components characterize a scattering problem: an illumination problem, a scatterer object and a detector [Zsc09]. In experiments, often complex arrangements are needed. For numerical interests, there exist a number of idealizations [ZKSS06]. Here, only the electric field distribution of the near field of nanostructures is of interest (see Ch. 5).

4 Numerical Simulations

For theoretical considerations, the following conditions have to be satisfied for a *scattering problem* (cf. Eq. (2.7)) [Pom09]:

1. The electric fields in the exterior of the computational domain must fulfill

$$\frac{1}{\varepsilon_0 \varepsilon} \nabla \times \frac{1}{\mu_0 \mu} \nabla \times \mathbf{E}_{\text{in}} = \omega^2 \mathbf{E}_{\text{in}} \quad \text{and} \quad (4.16a)$$

$$\frac{1}{\varepsilon_0 \varepsilon} \nabla \times \frac{1}{\mu_0 \mu} \nabla \times \mathbf{E}_{\text{out}} = \omega^2 \mathbf{E}_{\text{out}}, \quad (4.16b)$$

2. the field \mathbf{E} in the interior domain must fulfill

$$\frac{1}{\varepsilon_0 \varepsilon} \nabla \times \frac{1}{\mu_0 \mu} \nabla \times \mathbf{E} = \omega^2 \mathbf{E},$$

3. inner and outer domain has to be continuous, that means that on the boundary of the computational domain is

$$\begin{aligned} \mathbf{n} \times \mathbf{E} &= \mathbf{n} \times (\mathbf{E}_{\text{in}} + \mathbf{E}_{\text{out}}) \quad \text{and} \\ \mathbf{n} \times (\nabla \times \mathbf{E}) &= \mathbf{n} \times (\nabla \times (\mathbf{E}_{\text{in}} + \mathbf{E}_{\text{out}})), \end{aligned}$$

4. and the radiating boundary condition must be fulfilled, that means that \mathbf{E}_{out} is strictly outward retarding:

$$\lim_{|x| \rightarrow \infty} |x| ((\nabla \times \mathbf{E}_{\text{out}}) \times \mathbf{n} - i|\mathbf{k}| \mathbf{E}_{\text{out}}) = 0, \quad \text{uniformly continuous.}$$

It is possible to subdivide scattering problems according to their symmetry. Cylindrical problems are calculated in a different way than planar problems or a three dimensional stack of structured layers. The symmetries can be exploited to minimize computational time and memory consumption. The discussed setups of Ch. 5 can be divided in such problem groups.

Since in this work plane waves serve as incoming light of scattered problems (see Sec. 2.1.4), light scattering off the structures in the exterior domain has to be considered. Sec. 4.3 will explain how to evaluate the outgoing wave outside the computational domain.

4.3 Transparent boundary conditions

Scattering problems as described in Sec. 4.2.3 require a special treatment regarding outgoing waves outside the computational domain. *Transparent boundary conditions* are introduced for the interface between the computational domain and its surroundings [Zsc09]. The transparent boundary conditions have to guarantee that the calculated light field within the computational domain is identical to the original solution of the scattering problem for the entire space. They must guarantee that the radiation condition holds and the scattered field is strictly outward radiating.

There exist different concepts for the numerical realization of transparent boundaries. Two of them will be presented in the following.

4.3.1 Dirichlet-to-Neumann operator

The *Dirichlet-to-Neumann operator* maps the values of the solution u on the boundary of Ω to the normal derivative on the boundary of Ω . To calculate this, the Helmholtz equation (Eq. (2.8)) for the scattered field has to be solved:

$$\partial_x^2 u_{\text{sc}} + k^2 u_{\text{sc}} = 0.$$

The time dependent possible solution of this equation is

$$u_{\text{sc}}(x, t) = \text{Re} \left(c_+ e^{i(kx - \omega t)} + c_- e^{i(kx + \omega t)} \right) \quad (4.17)$$

with constants c_+ and c_- . The interest is only on the part of the equation that results from the scattering and is moving in direction of the exterior domain. That is valid for the first term since for a fixed phase and a continuous time k has to increase. So, an additional condition is formulated that lets the second term be zero. Constitute the normal derivative of this condition is $\partial_x u_{\text{sc}}(x, t) = c_+ i k e^{i(kx - \omega t)} = i k u_{\text{sc}}(x, t)$ that gives the Dirichlet-to-Neumann operator

$$\partial_x u_{\text{sc}} = i k u_{\text{sc}}.$$

To calculate the derivative on the boundary of Ω , the total solution is splitted in the unknown scattering solution and the known input field:

$$\begin{aligned} \partial_x u &= \partial_x (u_{\text{sc}} + u_{\text{in}}) = \partial_x u_{\text{sc}} + i k u_{\text{sc}} = \partial_x u_{\text{in}} + i k (u - u_{\text{in}}) \\ \Leftrightarrow \partial_x u &= i k u + \partial_x u_{\text{in}} - i k u_{\text{in}}. \end{aligned}$$

Therefore, the unknown Neumann equation is calculated for the boundary, that is needed for the variational formulation.

The operator brings the boundary condition from infinity to the boundary of the computational domain. The Dirichlet-to-Neumann operator can be defined on the boundary of a domain for the solution for the Helmholtz equation in the exterior of the domain [Pom09].

4.3.2 Perfectly matched layers

The concept that is used in the Maxwell solver of this work for transparent boundary conditions is the *perfectly matched layers* method, also known by the abbreviation PML [Ber94, Zsc09].

The idea of the PML method is damping the outgoing wave within a buffer zone so that there are no reflections at the boundary of the computational domain, independent of the incident angle.

For this purpose, a special coordinate system is introduced for the exterior domain $\mathbb{R}^3 \setminus \Omega$. The basic idea of the PML method is a complexification of the generalized distance variable ξ to do a complex coordinate stretching in radial direction [Pom09]:

$$\xi \mapsto (1 + i\sigma)\xi$$

with a positive constant σ .

Considering again the scattering solution u_{sc} as in Eq. (4.17), a complex expansion yield

$$e^{i k \xi} \mapsto e^{i k \xi (1 + i\sigma)} \quad (4.18a)$$

$$e^{-i k \xi} \mapsto e^{-i k \xi (1 + i\sigma)}. \quad (4.18b)$$

4 Numerical Simulations

Reaching the exterior domain, ξ is increasing and since σ is positive, Eq. (4.18a) is converting to zero while the second term of Eq. (4.17), Eq. (4.18b), is divergent.

5 Spatiotemporal Control

Spatial resolution of optical measurements with conventional light sources is limited by the wavelength of the incident light. Achieving electronic control below the diffraction limit opens a number of novel methods in investigating nanosystems. One of them, the “localized spectroscopy“, is presented in Ch. 8. In this chapter, it is shown how confining optical excitations simultaneously on a nanometer length scale and on a femtosecond time scale becomes possible by combining nanoplasmonics with pulse shaping techniques [BG01].

Before presenting some underlying mechanisms of controlling optical excitations on length scales smaller than the wavelength of light, the purpose of the procedure should be emphasized. Metal nanostructures are illuminated by short polarization-shaped optical pulses that are formed with the help of a genetic algorithm. A theoretical description of the computational simulation methods and a presentation of the genetic algorithm in detail is given. This chapter ends with discussing the advantages and disadvantages of several tested geometries for confining fields.

The techniques and results described in this chapter are published in [SSH⁺12, SSB⁺11, SSB⁺12].

5.1 Aim

The aim of this chapter is finding an arbitrarily setup that allows control simultaneously in time and in space. More precisely, it should be possible to excite a region in a nanostructure, that firstly is very confined (only a few nanometers) and secondly the excitation time is only a few femtoseconds. A third aim is that the position for this localization spot is not arbitrary but should be controllable. For this it is sufficient to be able to control at least three selected points. These points have to be in close vicinity. Fig. 5.1 illustrates one possibility of a desired result.

The application of this spatiotemporal control is “localized spectroscopy“ that is shown in Ch. 8. The results of the current chapter allow exciting only one of three coupled quantum dots: For this purpose, the requirement of at least three controllable locations in close vicinity is needed. And it becomes clear why the position of localization must be confined: Only one of the three quantum dots should be excited. Such a coupled quantum dot system is introduced in Sec. 6.5.

There exist a lot of publications that demonstrate the experimental possibility of spatiotemporal control [ABB⁺07, BAS⁺06, BASP05, BASP06, ABP07, RM09, ABB⁺10, MBS⁺11]. All these works show a control in time and space but do not meet the requirements mentioned in the last paragraphs: The hotspots have to be in close vicinity and it should be more than two. Additionally, for localized spectroscopy, a quantum dot should be excited about more than a factor 10 higher in terms of the electric field than the non-excited ones.

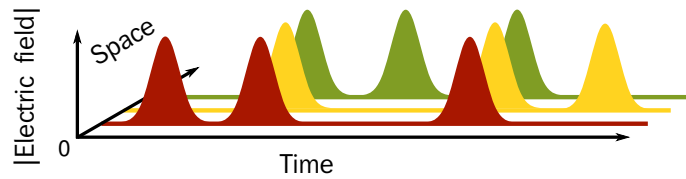
5.2 Control mechanisms

A confinement of optical excitations in a subwavelength precision is possible by combining nanoplasmonics with pulse shaping techniques [ABB⁺07, BASP05, ABB⁺10]. As seen in

5 Spatiotemporal Control

Figure 5.1:

Spatiotemporal control: This figure illustrates the aim of control excitations within a nanostructure simultaneously in time and space.



Ch. 3, nanoplasmonics exploit their frequency dependent properties and use different arrangements of metals or hybrids like nanoantennas [HVT⁺09, MKZ⁺08, NH11] and sharp triangles or metal tips [BASP05].

To achieve field confinements, in the following setups combinations of different plasmonic materials with dielectrics are used. Ref. [Pal85] provides dielectric functions for resonant materials like silver, gallium arsenide or indium arsenide (cf. Sec. 2.1.5). With these data the presented arrangements are simulated. They produce an enhanced electric field dependence on the frequency of the incoming light.

Not only the optical material resonances but also the size, the form and the orientation of the nanostructures influences the spatial field distribution. All these effects interplay in the geometries described in Sec. 5.5.2.

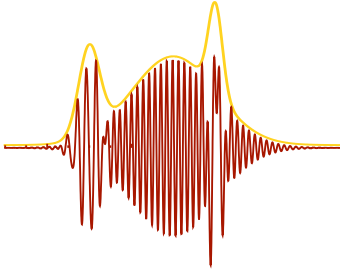
The setups used there are dominated by triangles with different sizes and different orientations. The sharp vertices of the tips are able to concentrate the field. With different sizes it is possible to address different optical frequencies. Finally, the position of the triangles and their alignment with each other play an important role for polarization effects because of the use of polarization shaped pulses. Further discussions of such polarization effects can be found in Sec. 5.5.2.

A principle effect of locating light works via constructive or destructive interference. A superposition of many light sources can generate a high number of light patterns but no arbitrary pattern within lengthscales much smaller than the wavelength of light! This changes if there are interferences between near and far fields, for example through enhancement of electromagnetic fields via local reflections and plasmon effects. The plasmonic effects that occur are exemplarily discussed for a metal sphere in Ch. 3.

In the geometries presented in this work nanostructures generate near field effects: Since the local fields are generated by the external polarization components of the incoming light, they are not all perpendicular to each other. Thus, they can interfere dependent on the polarization of the incoming field. Constructive and destructive interferences are used to optimize the field distribution.

Although all the hinted effects contribute to control of excitations within subwavelength precision, one incoming pulse is often not enough to achieve sufficient control. In some setups, more than one light sources are used to combine the interference effects of the sources and the near field enhancements. Just one incoming pulse does not supply enough degrees of freedom: If the electric field in the center of three coupled quantum dots should be determined, nine electric field components have to be controlled (three for every spatial direction) for a fixed frequency. Every incoming pulse allows the determination of two electric field components, one for each polarization direction. Consequently, more incoming pulses raise the possibility that a desired field distribution can be reached.

To achieve sufficient control of three coupled quantum dots, in the important setup of Sec. 5.5.3, three incoming pulses with individual shapes from different directions are used. Thus, the fields of the incoming pulses can additionally interfere constructively or destructively at the sample.

**Figure 5.2:**

Shaping pulses via a weighting function: The field distribution is simulated with an incoming pulse with a field amplitude of 1. the function g (illustrated in yellow) weights the electric field of each frequency in time domain.

5.3 Simulations

For a theoretical simulation of the field localization the time harmonic results from the Maxwell solver of "JCMsuite" [PBZS07, BZPS08] are used. Maxwell's equations are solved in frequency domain using the finite element method. A detailed introduction to this method is given in Ch. 4.

The resulting electric fields $E_v^\gamma(\omega, \mathbf{r})$ are evaluated at the center of the quantum dots for all incoming directions γ and the polarization directions $v = p, s$. For controlling the field distributions in time domain, a Fourier transform is applied (cf. Fig. 5.3):

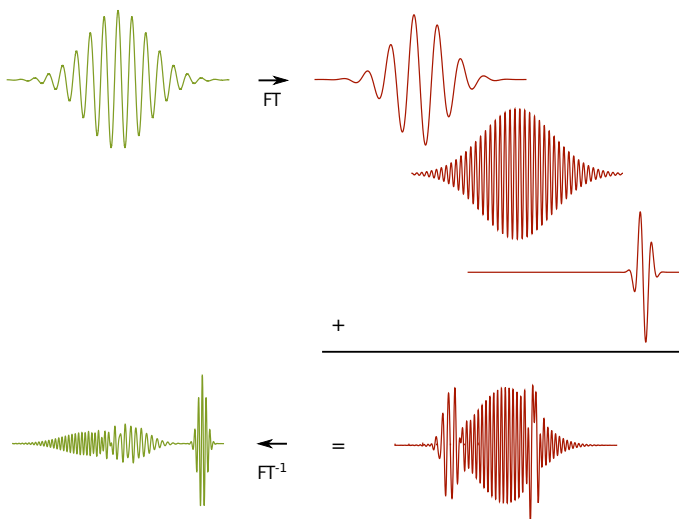
$$E(t, \mathbf{r}) = \frac{1}{\sqrt{2\pi}} \int_{-\infty}^{\infty} d\omega e^{i\omega t} \sum_{\gamma, v} g_v^\gamma(\omega) E_v^\gamma(\omega, \mathbf{r})$$

where g is a weighting function, that enables us to shape the incoming pulses. In Fig. 5.2 the effect of the weighting function is illustrated: The field distributions for all frequencies are simulated with incoming pulses with a field strength amplitude of 1. With the help of the weighting function, the electric field of each frequency can be weighted stronger or weaker in time domain. Mind, that all field simulations are linear.

The function g represents a Fourier transformed composition of n Gaussian shaped pulses (similar to [RM09]):

$$g_v^\gamma(\omega) = \sum_n f_v(\vartheta_n^\gamma) \frac{A_n^\gamma}{\sqrt{2\pi}} e^{-\frac{(\eta_n^\gamma - \omega)^2 \sigma_n^{\gamma 2}}{2}} e^{i\omega \tau_n^\gamma} e^{i\varphi_n^\gamma},$$

with $f_p = \cos$ and $f_s = \sin$. Thus, it is possible to simulate the incoming electric field with a fixed amplitude and to weight each frequency individually only by changing the parameters of g : the polarization angle ϑ_n^γ , the amplitudes A_n^γ , the center times τ_n^γ , inner frequencies

**Figure 5.3:**

Pulse shaping via superposition of Gaussian shaped pulses in frequency domain: The Gaussian shaped pulses are superposed in frequency domain (red). Afterwards, the resulting shaped function $g_v^\gamma(\omega)$ is transformed back into time domain.

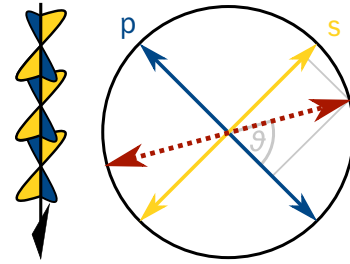


Figure 5.4:

Superposition of two polarization directions of the electric field: The two solutions $E_p^\gamma(\omega, \mathbf{r})$ and $E_s^\gamma(\omega, \mathbf{r})$ are superposed. Trigonometric functions ensure that the pulse envelope still keeps normalized.

η_n^γ , widths σ_n^γ , and the phases φ_n^γ . For gaining a polarization shaped pulse, the two solutions $E_p^\gamma(\omega, \mathbf{r})$ and $E_s^\gamma(\omega, \mathbf{r})$ are superposed in a ratio so that the pulse envelope still keeps normalized (see Fig. 5.4).

The higher the number of pulses the complexer the pulse can be shaped. In the simulations in this work it turned out that $n = 20$ pulses can form the pulses sufficiently for the desired optimizations.

Composing the electric fields in this way reduces considerably the computational costs since all fields have to be simulated only once (for each frequency). In contrast to a time domain solver, in frequency domain there is no new simulation needed for altered incoming pulses.

Three incoming directions and twenty composed Gaussian pulses results in $6 \cdot 3 \cdot 20 = 360$ parameters to be optimized simultaneously. This task is performed by a genetic algorithm that is introduced in the next section.

5.4 Genetic algorithm

For localized spectroscopy (see Ch. 8), the field distribution of the electric field has to satisfy the requirements mentioned in Sec. 5.1. Shaped pulses can generate complex field distributions caused by effects introduced in Sec. 5.2. But there exists no analytic way to predict the form of the shaped pulses to obtain the desired field distribution.

In order to obtain the shaped pulses that satisfy our requested field distribution, a *genetic algorithm* [RM09, Rec73, ABB⁺07] is helpful. There are several other methods, for example a gradient descent. Some advantages and disadvantages are discussed in Sec. 5.4.5.

In this work, an algorithm has been implemented for the intentions of localized spectroscopy. Its task is optimizing the six parameters of the weighting function g for every pulse from which g is composed: ϑ , A , τ , η , σ , and φ .

The results of optimization are shown in the subsections of the corresponding setup, scheduled in Sec. 5.5. The optimization results of geometry described in Sec. 5.5.3, the achieved localization of the optical excitation is presented in two versions in Fig. 5.12.

5.4.1 Principles of the algorithm

The basic principle of the genetic algorithm used in this work consists of three steps for every generation: Mutation, evaluation, and selection.

Mutation: A set of n optimization parameters can be expressed as a n -dimensional vector a . In every generation 300 mutated copies a_{child} of the parent pulse a_{parent} are created by adding the parameter dependent mutation step size Δa multiplied with a Gaussian distributed random number χ_i for every of the 360 (see Sec. 5.3) variation parameters a :

$$a_{\text{child},i} = a_{\text{parent},i} + \chi_i \cdot \Delta a_i$$

Evaluation: Next, each child is assigned a quality. This is done by evaluating a scalar cost function for every child and selecting the one with the smallest cost value. The chosen cost function compares the electric field distribution in the center of the excited quantum dot caused by the pulse with a target distribution. Different kinds of cost or fitness functions are presented in Sec. 5.4.2.

There is one condition for each quantum dot. While the electric field distribution at position r_1 should match with a Gaussian shaped excitation, the field distribution at positions r_2 and r_3 should be minimal.

The requested time dependence of the absolute value of this electric field distribution at the excited dot at r_1 is given by a target function

$$\text{tar}(t) = B e^{-(t-T)^2/\epsilon^2} \quad (5.1)$$

that exhibits a Gaussian shaped excitation with an amplitude B that depends on the chosen geometry, a time T at which the excitation is centered, and an excitation width ϵ . In our simulations, $T = 0$ fs and $\epsilon = 8$ fs is chosen. Since the other quantum dots should not be excited the target function for positions r_2 and r_3 is identically zero.

Selection: Now, the best child is selected. The child with the lowest value of the cost function (that are presented in Sec. 5.4.2) acts as parent pulse for the next generation. In dependence of the step size Δa , a new generation is created. Sec. 5.4.3 explains how this step size is calculated.

There exist many different ways to implement a genetic algorithm. For example, different kind of general parameters have to be chosen, such as children per generation or the start values for the optimization parameters. Since for the genetic algorithm no clear convergence can be seen (cf. Sec.5.4.4), and because the success depends on chance, it is not easy to find the best parameters. For the results presented here, 300 children per generation are generated. Depending on the geometry, some simulations use the same incoming pulses for all directions, some others use different start values for each directions. Another possibility for altering the algorithm is to consider the former parent as a valid choice in the selection process or to select two or more children and combine their properties – for example by mixing parameters or taking the average. Such a process forms the forth step: *Recombination*.

A illustration of the principle operation of a genetic algorithm is given in Fig. 5.5.

5.4.2 Cost function

The *fitness* or the *cost function* assigns a value to each child. The higher the fitness value or the lower the cost value the higher the quality of child, that means the better the agreement of the target function with the real behavior of the electric field. In the following, only cost functions are used.

There exist many possibilities for a mapping of the "cost". Here, only the first of three pulses should be Gaussian distributed, the both other excitation curves in time domain should be zero. These three conditions can be combined by fitting to one target function

$$\text{cost}(\text{child}) = \int_{-\infty}^{\infty} |E_{\text{child}}(t, r_1) - \text{tar}(t)|^2 + |E_{\text{child}}(t, r_2)|^2 + |E_{\text{child}}(t, r_3)|^2 dt$$

where $E_{\text{child}}(t, r_i)$ is the electric field in the center of quantum dot i and $\text{tar}(t)$ the target function (5.1). To weight larger deviations stronger than smaller ones the square of the absolute value of the difference between the target and the actual distribution is calculated. Then, an integration over all times is done. Consequently, a higher integration result represents a bad matching. It is important to scale the target function (5.1) with the factor B , which is in the

5 Spatiotemporal Control

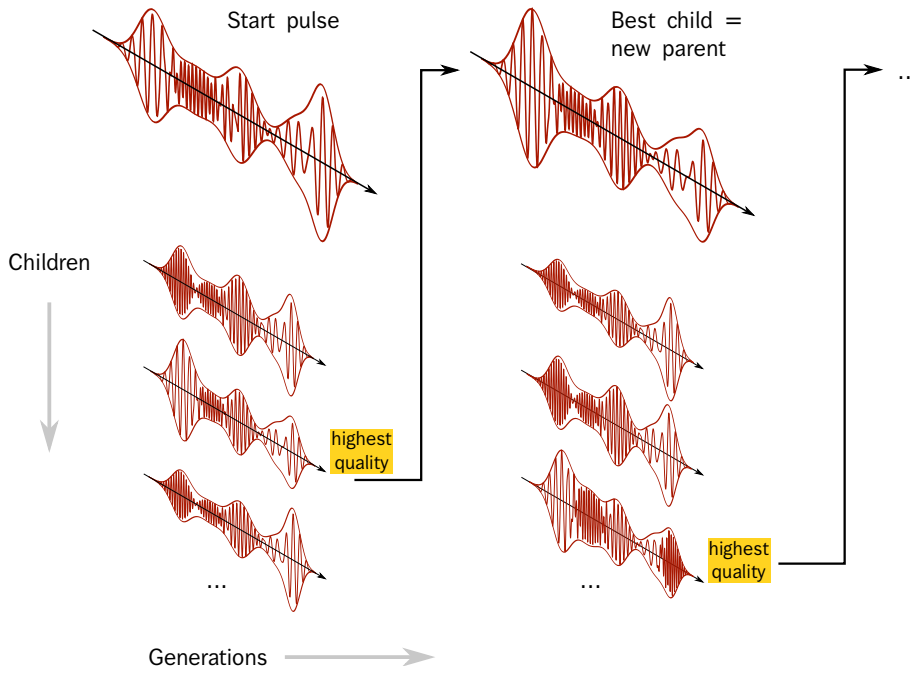


Figure 5.5: Operation of a genetic algorithm: A parent gets children (*Mutation*), the best child is found (*Evaluation*) and finally the best child becomes new parent (*Selection*).

range of the expected maximum field strength within the quantum dot, to weight deviations from the target function as well as deviations of the other two quantum dots from the zero function. The factor is constant in time and generation.

Some other cost functions have been tested, such as a cost function that is aimed on getting a high difference between $E_{\text{child}}(t, r_1)$ and the other two electric fields of the children instead of fitting $E_{\text{child}}(t, r_2)$ and $E_{\text{child}}(t, r_3)$ to zero. Also different weightings for the three conditions are tried. It turned out that all conditions are fulfilled most uniform if a cost function is minimized given by:

$$\text{cost}(\text{child}) = \max \left(\int_{-\infty}^{\infty} |E_{\text{child}}(t, r_1) - E_{\text{target}}(t)|^2 dt, \int_{-\infty}^{\infty} |E_{\text{child}}(t, r_2)|^2 dt, \int_{-\infty}^{\infty} |E_{\text{child}}(t, r_3)|^2 dt \right)$$

This cost function is used for the results of that work.

5.4.3 Adaptive mutation step size

A genetic algorithm can be improved by introducing an adaptive *mutation step size*. Instead of a constant step size for each mutation Δa_i (multiplied with a random number), an adaptive mutation step size Δa is used. It varies depending on the average of the step sizes of the previous parents [Rec73].

The influence of the chance plays an important role for the mutation. The Gaussian random numbers allow that also another minimum can be found (by rare big step sizes). But they also allow to find the lowest point (by frequent small step sizes).

Big step sizes make no sense if no improvement is achieved. Otherwise, small steps are not useful for parameters that improves the fitness significantly. For this, the last best children are saved. For each parameter, the variance of these last parents are calculated. Let b_i the

parameter of the last parents ($i = 1, \dots, 100$) and \bar{b} the average over all b_i . Then, the new mutation step size reads:

$$\Delta a_i = \sqrt{\frac{\sum_{j=1}^n (b_i^j - \bar{b}^j)^2}{n-1}}.$$

Mind, that the randomness is not restricted but only the strength of the mutation.

In this work, the last $n = 100$ parents are saved in memory. Thus a quick approach to the minimum of the cost function is possible. The lowest values are reached with finer steps.

5.4.4 Termination conditions

The algorithm used in this work resembles an evolutionary algorithm of the nature. But in nature there is no end of evolution and no unambiguous maximum of quality, so here a termination condition has to be found and several local maxima are expected.

Four different termination conditions are used: Since the optimal pulse is not known and needed, the algorithm can be terminated successfully if the quality of the parent has sufficient quality. If there have been more than 60000 generations without a sufficient result or (only in some simulations) 1000 generation without a new parent, the algorithm is terminated unsuccessfully. If the mutation step size is very small, the algorithm also finishes since then it can be assumed that a local maximum is found.

Repeating the experiment with other random numbers χ or with other start mutation step sizes can influence the result but this does not happen very often. In most cases it has been clear within 10000 generations if the algorithm will terminate successfully or without any success.

5.4.5 Comparison with gradient bases methods

In general, a genetic algorithm is used for problems that behave like a black box with little insight on the inner structure. The strong point of this kind of algorithm is that it can be used for a number of problems, especially problems without gradient information such as discontinuous ones. The influence of chance allows finding maxima that could not be found with gradient methods. The advantage of gradient methods is that it often leads more directly to the goal because for each generation the parameters that supply the strongest improvement are changed. As a trade-off, there are two disadvantages: The most important one is, that for each parameter a change in quality has to be calculated to find the gradient while for a genetic algorithm only the number of children decide the number of time-consuming calculations. That means that the velocity of the gradient method decreases drastically for a huge number of parameters to be optimized. The second disadvantage is that the probability of finding the global maximum depends strongly on the start value. The algorithm often finds the nearest local maximum in cases where the genetic algorithm perhaps finds an higher local or even the global maximum with the help of the Gaussian distributed random numbers that allow (a few) high step sizes. For a simulation that works successfully in less than 10000 generations it is possible to see if the chosen geometry provides a highly localized excitation.

There exist also algorithms that mix the genetic and the gradient method. For example, the gradient method can be improved by adding a random choice. This could be choosing only a part of parameters for finding the gradient on a hyperplane, Also the genetic algorithm can become more gradient-like, by considering the recombination step of the algorithm, for example by averaging the parameters of the best children.

Generally one can say that there exists no perfect algorithm. Every method has advantages and disadvantages and their suitability depend on the knowledge of the present problem.

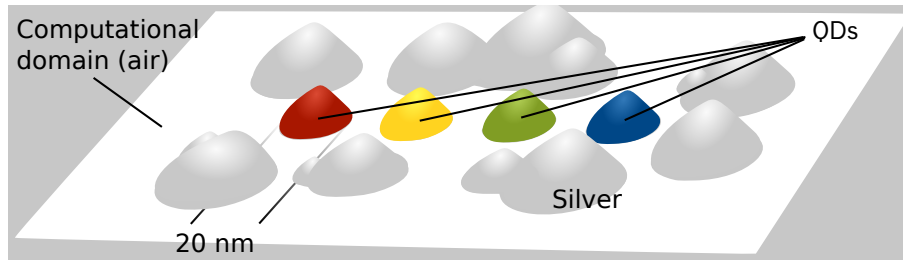


Figure 5.6:

Randomly arranged geometry: In this illustration of plasmonic structure for spatiotemporal control studies four InAs quantum dots are surrounded by randomly distributed silver particles on a GaAs layer. The arrangement is situated in air. As described in Sec. 5.5.1, that setup turns out to be inefficient.

The genetic method mostly provides the desired results. Unfortunately, this means that in many setups it is not clear if the geometry does not allow a good optimization or whether just the genetic algorithm does not find it. Through repetitions with other random numbers and variation of the start values of the parameters and the mutation step sizes, it becomes possible to evaluate the quality of the current setup. In Tab. 5.1, the number of needed generations for an optimization is given exemplarily.

5.5 Geometries

As stressed in Sec. 5.2, the geometrical form of a setup strongly influences the field distribution. Thus, not all geometries are well-suited for an optimization process. So in the following subsections is discussed how to find the optimized geometry.

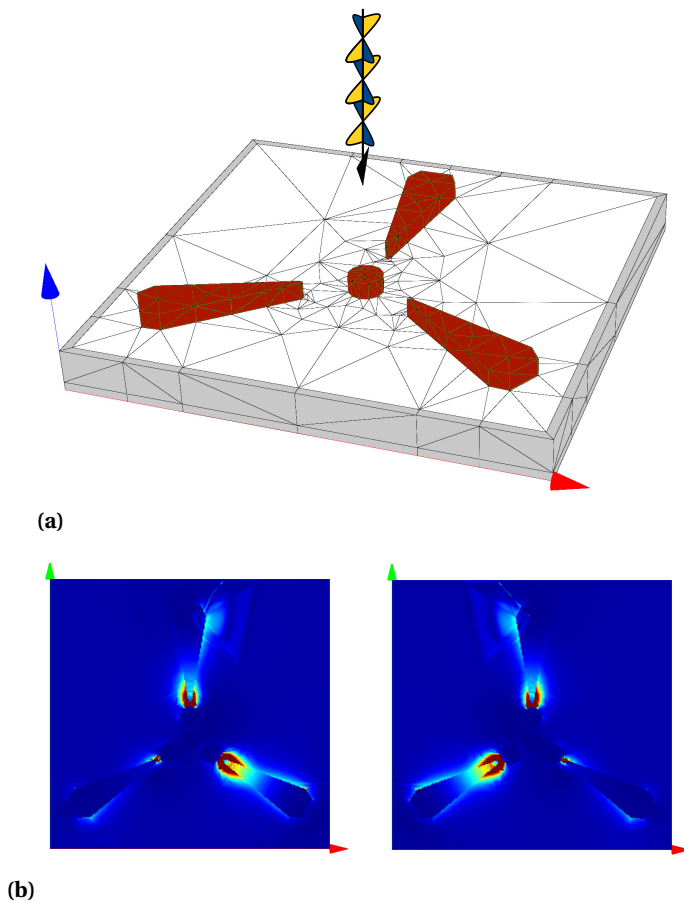
There already exists a number of well-known setups, for example in [ABB⁺07, BASP05, ABB⁺10]. All setups used there provide spatiotemporal control. As mentioned in Sec. 5.1, the works of the other authors does not fulfill the requirements needed here. Their setups have to be adapted within the context of changing controlling properties in such a way that localized spectroscopy (see Ch. 8) becomes possible.

To investigate a quantum system of three or more coupled quantum dots, a control of the excitations at more than two spatial positions is needed. The examined spatial points also have to be in close vicinity. In particular, the focus is on spatial points no farther than 50 nanometers. Within that range, also time control is required and the electric field of the excited quantum dot should at least be larger by a factor of 10, that means a factor of 100 for the intensity.

5.5.1 Random geometries

In a naive approach a randomly arranged setup would be a reasonable starting point. In that case, the intention of using as many of the discussed effects as possible is pursued. But this idea overestimates the possibilities of field control by shaping pulses via the genetic algorithm used in this work.

In Fig. 5.6 a tested randomly arranged geometry is presented. The indium arsenide quantum dots have a diameter of 20 nanometer and are placed on a gallium arsenide layer, surrounded by randomly distributed silver particles. That arrangement is situated in air. Note, that in Ch. 3 the geometry is surrounded by water.

**Figure 5.7:**

Triangle setup to demonstrate polarization effects: In part (a) the setup consists of three silver triangles and a silver cylinder on a glass substrate. There are no quantum dots in the simulation. Just the electric field within the region allocated for the quantum dots is focused. The polarization direction of the incoming plane wave can be regulated (cf. Sec. 5.3). In part (b) it can be seen that the field distribution of the layout depends on the incoming polarization direction. On the left s-polarized, on the right p-polarized light is used.

Fig. 5.6 shows that in randomly arranged setups always some quantum dots are placed in a more preferential position than other dots. This advantageous position is caused, for example, because the quantum dots are closer at metal structures than other quantum dots. The metals have the possibility of high field amplifications that the quantum dot can absorb. In that case, the electric excitation can be confined easily in such a dot. But if another dot that is not close to a field amplifier should be the excited one, it is hard to bring the excitation into the dot without inadvertently exciting the metal near another dot that is undesired to be excited.

In other words, it turns out that localization of the electric field has a bad quality for quantum dots at disadvantaged positions such as those not close enough to a metal structure.

To illustrate the principle of localized spectroscopy, in the rest of the current chapter the focus is on symmetric arrangements.

5.5.2 Antenna-like geometries

This kind of geometry affords a good study of polarization shaping effects because of the different orientations of the nanostructures, that serve as nanoantennas [NH11, MKZ⁺08].

The first simple setup is shown in Fig. 5.7a. Three silver triangles are on a glass layer with a silver disk in the center. To demonstrate polarization effects, just one polarization shaped incoming pulse incidents perpendicular from above. In general, the largest field enhancements occur always on those boundaries of metal structures, which lie in the direction of the polarization vector. The effect that is seen for a sphere in Ch. 3, can be transferred to the triangles given in Fig. 5.7b. The picture shows field distributions for two perpendicular polarization

5 Spatiotemporal Control

Table 5.1:

Optimization results of antenna-like geometries: For different scaling factors of the metallic surrounding, the localization factor is given. It gives the electric field of the not excited quantum dot divided by the electric field of the one that is excited. Additionally, the number of generations that are needed to achieve the localization are given.

Geometry	Fig. 5.9a		Fig. 5.9b		Fig. 5.13		
	Scale	Loc.	Gen.	Loc.	Gen.	Loc.	Gen.
	0.5	5.6	11000	13.5	8000	22.5	11000
	0.6	17.6	13000	13.7	11000	35.5	7000
	0.7	33.3	4000	13.1	11000	3.3	12000
	0.8	17.1	10000	16.5	6000	11.3	9000
	0.9	13.9	5000	> 50	11000	5.0	8000
	1.0	20.5	9000	25.8	21000	13.7	10000
	1.1	17.1	8000	≈ 30	10000	12.5	110000
	1.2	14.3	7000	14.32	10000	5.0	2000
	1.3	14.3	14000	15.9	17000	12.6	12000
	1.4	15.2	12000	13.4	11000	3.4	13000
	1.5	12.1	19000	13.2	13000	3.3	12000

directions: On the left hand the s- and on the right hand the p-polarization effects are visible in Fig. 5.7b.

The idea of this geometry is placing the quantum dots between the silver tips and the center circle. It is assumed that the field strength is taking over into the dots and does not distort the field distribution. Optimization with the genetic algorithm shows, that this geometry allows an excitation of two of the three quantum dots simultaneously. But that is not the aim. So the desired geometry has to look different. The calculations show, that the ratio between the excitation strength of the two quantum dots and the excitation of the weak excited quantum dot is not high enough for the purpose of this work.

A better localization ratio can be reached by implementing each triangle with a different size to have different resonance frequencies. Deforming the triangles or replacing them by rods to change the optical properties of nanoparticles [MKZ⁺08, KCZS03] helps achieving a better ratio of localization.

Most ideas of antenna-like geometries provide some enhancements but ultimately, up to now no structure achieves sufficient localization. Displacing them to an antisymmetric setup like in Fig. 5.8 leads to the same problems as discussed in Sec. 5.5.1: only for spatially advantageously positioned dots a localization is possible.

The fact that the layout of Fig. 5.7 only can optimize two quantum dots simultaneously leads to the idea of bringing the dots between two triangles as shown in Fig. 5.9. These setups supply sufficient localization. In Tab. 5.1 for both geometries the inverse amplification ratio (field strength of the quantum dot that should not be excited divided by the field strength of the excited quantum dot) are given. Additionally, the results are presented for different sizes of triangles. Scale 1 corresponds to the triangle sizes as seen in Fig. 5.9. This size is scaled by the given factors. One can see that the results depend on size but this does not necessarily follow from the underlying physics! Mind, that the genetic algorithm uses random numbers and each simulation can differ from another one. Local maxima could be found or inappropriate initial parameters do not lead to convergence. Additionally, the table shows the number of generations that has been needed to achieve the localization factor.

While Fig. 5.9a leads to better localization results, Fig. 5.9b is the preferred geometry since the distance between the quantum dots and the metals is higher, so that influences of the metals to the properties of the quantum dots can be neglected [VVKH12].

5.5.3 Waveguide-like geometries

The first found layout that satisfied the desired requirements is shown in Fig. 5.10. This setup serves as an example in the next sections. It shows a three-armed metal nanostructure, similar to a waveguide, inspired by nanoantennas, that can guide electric field strength into the nanostructures. The large metal area exists of silver and is applied on a gallium arsenide bulk layer. The structure keeps a full 120° symmetry where each of the three paths is illuminated by one independent shaped pulse. The indium arsenide quantum dots in the center have a radius of ten nanometers and have a height of four nanometers (while silver has a height of 16 nanometers), so that the main part of the incoming pulses, that have wave vectors almost parallel to the layer plane, can only reach the quantum dots through the wave guides.

The geometry is surrounded by air and the dimensions of the structure can be found in Fig. 5.11. Parameters like dot distance and size, coupling constants and energy shifts are known from experiment [UML⁺05] and theory [RAK⁺06]. The energies of the self organized GaAs/InAs quantum dots are given in Sec. 6.5. The setup is particularly suitable since there are no sharp vertices and the 120° symmetry helps to save computational time and avoids a position dependent chirp of the phase.

The shape of the excitation in time domain for the absolute value of the electric field in the center of the silver disks is given in Fig. 5.12a. It can be clearly seen that quantum dot 1 is much higher excited than the other ones. Since in Ch. 8 the electric field is considered in frequency domain, the factor of field distribution is determined after a Fourier transform of the values of Fig. 5.12a. As a result, in frequency domain, this setup yields a localized amplification ratio of $1 : 0.1205 : 0.0761$. That means, that for a frequency which is typical for the chosen quantum dots (about 1.1 eV) the electric field in the center of the second quantum dot is only 12.05 percent of the field within the first quantum dot and the third one only 7.61 percent. Fig. 5.12b shows the field distribution at $t = 0$ fs where the field amplification has a maximum. The figure shows a section at the half of the quantum dot height.

A last geometry that is presented in this work is a further waveguide-like setup in Fig. 5.13. Its layout achieves a very high field localization, due to the proximity of the metals. Plasmonic coupling effects (cf. Sec. 3.3) can be selected by polarization shaped fields particularly well. But in the following the first presented waveguide-like structure serves for demonstrations since the near contact of the metals could influence the properties of the quantum dots (see Sec. 5.5.2). The results of the optimization process is also given in Tab. 5.1.

Figure 5.8:
 Top view of a three dimensional asymmetric ray-like layout: The geometry with three InAs quantum dots (green) and silver rods and disks (red) shows different optimization qualities depending on which quantum dot is excited. The rounded corners cause softer field gradients and consequently save computational costs and corresponds more a realistic structure.

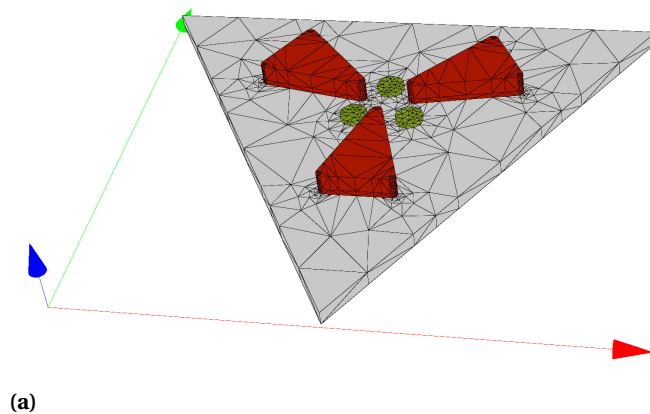
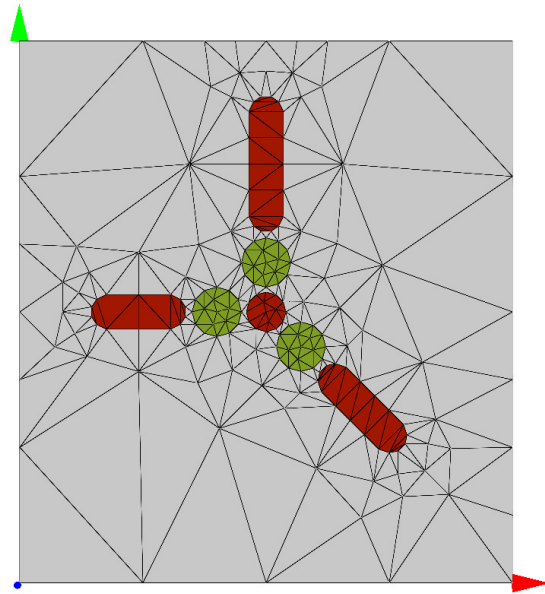
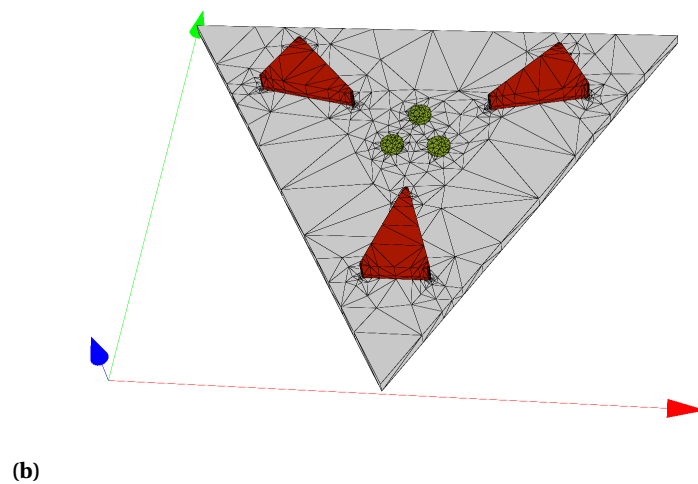


Figure 5.9:
 Symmetric geometry with quantum dots between silver triangles: These setups lead to good optimization results (given in Tab. 5.1). In part (a) the triangles are closer to the dots than in part (b) – the sizes of the triangles and the InAs disks are the same.



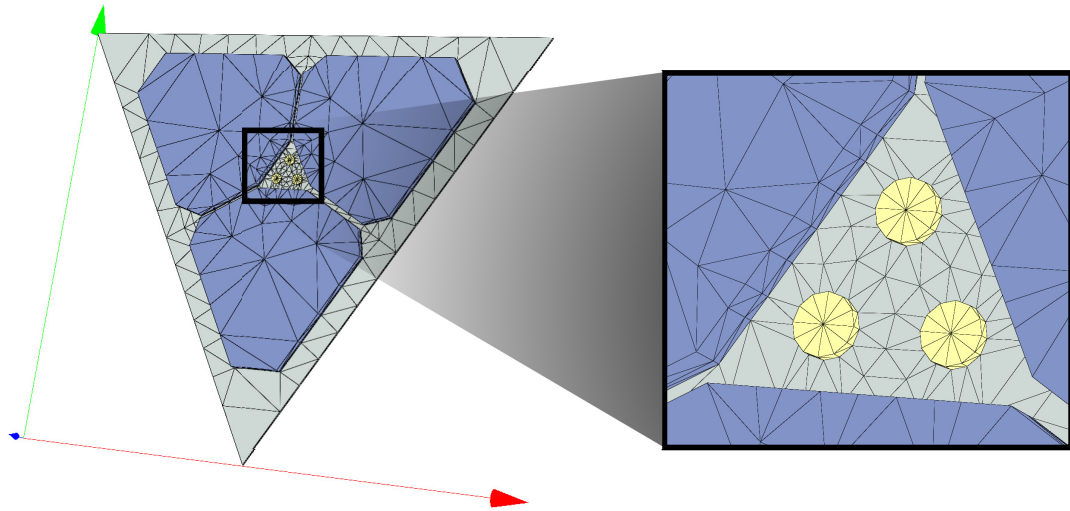


Figure 5.10:

Three-armed waveguide-like model setup for spatiotemporal control of three coupled quantum dots: The three InAs quantum dots on a GaAs layer have a radius of 10nm and a distance of about 40nm and they are surrounded by three silver polygons with 250nm for the longest edge (see Fig. 5.11). They were illuminated by three individual polarization shaped pulses with incoming directions parallel to the waveguide arms. The field strength is measured in the center of the quantum dots. This setup satisfies the desired requirements.

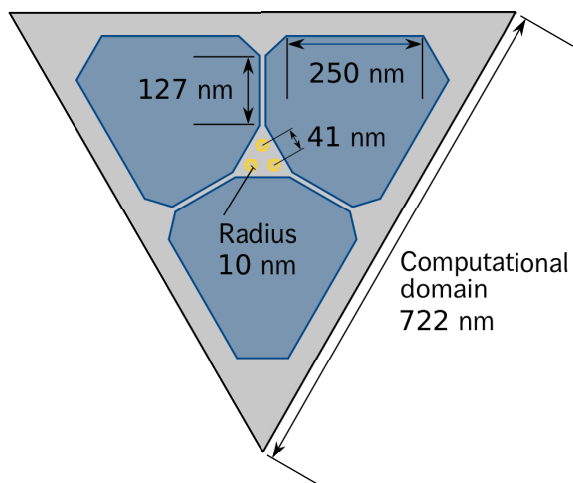


Figure 5.11:

Dimensions of the three-armed waveguide-like model setup: This figures shows the dimensions of Fig. 5.10.

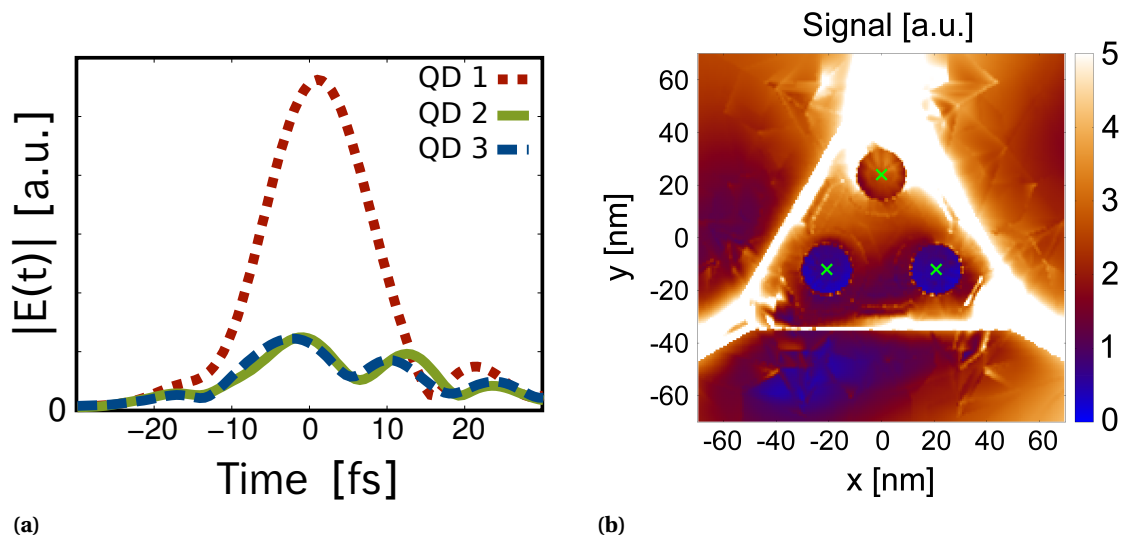
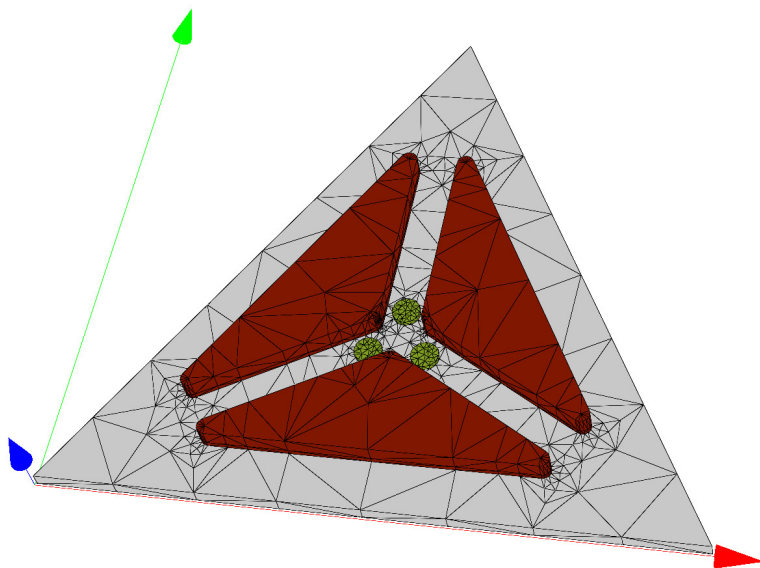


Figure 5.12:

Optimization results of waveguide-like geometry: In part (a) the excitation is given in time domain. Quantum dot 1 is much higher excited than the other ones. A Fourier transform gives a localized amplification ratio of $1 : 0.1205 : 0.0761$ in frequency domain (see Sec. 5.5.3). Part (b) is a slice through the geometry at the half of the quantum dot height. The upper quantum dot is significantly brighter than the lower two. This figure is published in [RSS⁺12] (Copyright (2012) by the American Physical Society).

Figure 5.13:

Waveguide-like geometry for plasmonic coupling effects: This layout allows a good localization due to the plasmonic effects that are generated by the polarization shaped pulses.



Part III

Spectroscopy

6 Theoretical Foundation of Quantum Systems

The structures of the last chapters are chosen based on a possible application in the field of coupled quantum dots. This and the next chapter serve as preparation for Ch. 8, which supplies the main results of the work.

For this, the recent chapter starts with theoretical essentials for working with nanostructures in density matrix theory. After introducing the density and the time evolution operator, the perturbation expansion is given in the interaction picture. Finally, the chapter ends by presenting coupled quantum systems – especially three coupled quantum dots that serves as model system for Ch. 8.

6.1 Density operator

The state of a treated system is often determined only incompletely because of its mesoscopic size. To yield nevertheless comprehensive predictions, it is necessary to find a formalism for the quantum mechanical description that can handle the incomplete information. The *density operator* allows a simple and elegant description of a statistical average.

First, it will be introduced for pure states, then for a statistical average and afterwards, its time evolution is presented.

6.1.1 Pure state

The density operator of a pure quantum state $|\varphi\rangle$ is given by¹¹

$$\rho = |\varphi\rangle\langle\varphi| \quad (6.1)$$

with the (many-particle) wave function $|\varphi\rangle$ that describes the state of the system. Its expansion for the time t is [CTDL07]

$$|\varphi(t)\rangle = \sum_n c_n(t)|u_n\rangle$$

in the set of $\{|u_n\rangle\}$ that forms an orthonormal basis and the expansion coefficients $c_n(t)$. The normalization condition is $\sum_n |c_n(t)|^2 = 1$. By implication, the expectation value for an observable O is given by

$$\langle O \rangle(t) = \langle \varphi(t) | O | \varphi(t) \rangle = \sum_{n,m} c_n^*(t) c_m(t) O_{nm} \quad (6.2)$$

with the matrix elements $O_{nm} = \langle u_n | O | u_m \rangle$.

With the definition of the density operator (6.1) one obtains

$$\rho(t) = \sum_{n,m} c_n c_m^* |u_n\rangle\langle u_m|$$

¹¹The Dirac notation describes a wave function φ with help of the ket vector $|\varphi\rangle$. Each ket $|\varphi\rangle$ corresponds to a bra vector $\langle\varphi|$ that belongs to the corresponding dual space (see e.g. [CTDL07]).

6 Theoretical Foundation of Quantum Systems

and thus for the matrix elements of the density operator, there is

$$\rho_{nm}(t) = \langle u_n | \rho(t) | u_m \rangle = c_n(t) c_m^*(t). \quad (6.3)$$

Finally, with (6.2) and (6.3) for the expectation value of the observable O

$$\langle O \rangle(t) = \sum_{n,m} \langle u_m | \rho(t) | u_n \rangle \langle u_n | O | u_m \rangle = \sum_m \langle u_m | \rho(t) O | u_m \rangle = \text{tr}(\rho(t) O) \quad (6.4)$$

is obtained [CTDL07]. Here, $\text{tr}(M)$ means the trace of matrix M defined by

$$\text{tr}(M) = \sum_n M_{nn}.$$

The vectors $|\varphi(t)\rangle$ and $e^{i\theta}|\varphi(t)\rangle$ (for an arbitrary real number θ) characterize the same physical state. This becomes important in Sec. 8.2.2. The definition of the density operator (6.1) shows that the two vectors consequently belong to the same density operator.

6.1.2 Statistical average

While for a pure state the system can be described by a state vector as well as by the density operator (see also the time evolution in Sec. 6.1.3), for a statistical average there is no way to write a wave function.

The density operator for a statistical average is defined as

$$\rho = \sum_k p_k \rho_k = \sum_k p_k \cdot |\varphi_k\rangle \langle \varphi_k|$$

with p_k as the probability for the system to be in state $|\varphi_k\rangle$. For the probabilities is $0 \leq p_k \leq 1$ and $\sum_k p_k = 1$.

As can be seen in more detail in [CTDL07], all physical statements can be described with the help of ρ , the average of the density operators ρ_k , because of the linearity of the relations that uses the density operator.

While introducing the density matrix allows the implementation of environmental influences or an easy treatment of open systems such as electrons coupled to vibrations, a problem is that calculations become complexer since the N -dimensional *Hilbert space*¹² of the wave functions become N^2 -dimensional. This can be seen in the representation of basis elements:

$$\begin{aligned} |\varphi\rangle &= \sum_n \langle n | \varphi \rangle | n \rangle = \sum_n c_n \underbrace{| n \rangle}_{\text{basis}} \\ \rho &= \sum_{nm} | n \rangle \langle n | \rho | m \rangle \langle m | = \sum_{nm} \langle n | \rho | m \rangle | n \rangle \langle m | = \sum_{nm} \rho_{nm} \underbrace{| n \rangle \langle m |}_{\text{basis}}. \end{aligned}$$

6.1.3 Time evolution

In the Schrödinger picture (cf. 6.3), the time evolution of the wave function $|\varphi\rangle$ is described by the *Schrödinger equation*

$$\frac{d}{dt} |\varphi(t)\rangle = -\frac{i}{\hbar} H(t) |\varphi(t)\rangle. \quad (6.5)$$

¹²A Hilbert space is an abstract vector space possessing the structure of an inner product.

The time variation for the density operator is given by the differential equation [CTDL07]

$$\frac{d}{dt}\rho(t) = -\frac{i}{\hbar}[H, \rho(t)]. \quad (6.6)$$

This equation is called the *Liouville-Von Neumann equation*. For pure states, it is identical to the the Schrödinger equation (6.5) as shown here:

$$\begin{aligned} \frac{d}{dt}\rho(t) &= \left(\frac{d}{dt}|\varphi(t)\rangle\right)\langle\varphi(t)| + |\varphi(t)\rangle\left(\frac{d}{dt}\langle\varphi(t)|\right) \\ &= -\frac{i}{\hbar}H(t)|\varphi(t)\rangle\langle\varphi(t)| + \frac{i}{\hbar}|\varphi(t)\rangle\langle\varphi(t)|H(t) \\ &= -\frac{i}{\hbar}H(t)\rho(t) + \frac{i}{\hbar}\rho(t)H(t) = -\frac{i}{\hbar}[H, \rho(t)]. \end{aligned}$$

In *Liouville space*, the density matrix ρ is an operator in the Hilbert space. The operation $[H, \dots]$ is written as a superoperator \mathcal{L} , that acts on operators in Hilbert space [Muk03]. The Liouville-Von Neumann equation (6.6) becomes

$$\frac{d}{dt}\rho(t) = -\frac{i}{\hbar}\mathcal{L}\rho(t).$$

Mathematically, the Liouville space is a Hilbert space, These spaces, however, are distinguished for improving physical intuition.

6.2 Time evolution operator

With the help of the linear *time evolution operator* $U(t, t_0)$, a time evolution of a system can be calculated. It is defined as

$$|\varphi(t)\rangle = U(t, t_0)|\varphi(t_0)\rangle. \quad (6.7)$$

Inserting this equation into the Schrödinger Equation (6.5) yields to a differential equation in first order

$$i\hbar\frac{\partial}{\partial t}U(t, t_0) = H(t)U(t, t_0). \quad (6.8)$$

With the initial conditions $U(t_0, t_0) = 1$ (that follows directly from the definition of the time evolution operator (6.7)) one obtains [CTDL07]

$$U(t, t_0) = 1 - \frac{i}{\hbar} \int_{t_0}^t H(t')U(t', t_0) dt'. \quad (6.9)$$

Fundamental transformations [CTDL07] show that

$$U(t_2, t_0) = U(t_2, t_1)U(t_1, t_0). \quad (6.10)$$

Since $H(t)$ is Hermitian, $U(t, t_0)$ is unitary with

$$U^\dagger(t, t_0) = U^{-1}(t, t_0) = U(t_0, t) \quad (6.11)$$

where U^\dagger symbolizes the Hermitian adjoint of the operator U .

For a time-independent Hamiltonian, Eq. (6.8) is simple to integrate and it follows an explicit form of the time evolution operator

$$U(t, t_0) = e^{-iH(t-t_0)/\hbar}. \quad (6.12)$$

6 Theoretical Foundation of Quantum Systems

For a time-dependent Hamiltonian the time evolution operator can be iteratively expressed through the *Dyson series*

$$U(t, t_0) = 1 + \sum_{n=1}^{\infty} \left(-\frac{i}{\hbar}\right)^n \int_{t_0}^t d\tau_n \int_{t_0}^{\tau_n} d\tau_{n-1} \dots \int_{t_0}^{\tau_2} d\tau_1 H(\tau_n) H(\tau_{n-1}) \dots H(\tau_1)$$

with $t_0 < \tau_1 < \tau_2 < \dots < \tau_{n-1} < \tau_n < t$ by inserting Eq. (6.9) into itself [Ham05].

It is possible to replace the time ordered expression by an ordinary one. This is done by introducing a time-ordering operator \mathcal{T} . For a time-dependent operator $H(t)$ its definition is

$$\mathcal{T}[H(t_1)H(t_2)] = \Theta(t_1 - t_2)H(t_1)H(t_2) + \Theta(t_2 - t_1)H(t_2)H(t_1)$$

with Θ as the Heaviside step function¹³. For n operators, the time-ordering is also maintained. That allows interchanging the Operators H . Applying the operator enables integrating to t for each integration. But this has to be compensated by the factor $n!$. Thus arises

$$\begin{aligned} U(t, t_0) &= 1 + \sum_{n=1}^{\infty} \left(-\frac{i}{\hbar}\right)^n \int_{t_0}^t d\tau_n \int_{t_0}^{\tau_n} d\tau_{n-1} \dots \int_{t_0}^{\tau_2} d\tau_1 H(\tau_n) H(\tau_{n-1}) \dots H(\tau_1) \\ &= 1 + \sum_{n=1}^{\infty} \frac{1}{n!} \left(-\frac{i}{\hbar}\right)^n \mathcal{T} \left(\int_{t_0}^t d\tau H(\tau) \right)^n = \mathcal{T} e^{-\frac{i}{\hbar} \int_{t_0}^t d\tau H(\tau)}. \end{aligned}$$

These steps can also be carried out for the time evolution operator in Liouville space. That results in (cf. [Muk95])

$$\mathcal{U}(t, t_0) = \mathcal{T} e^{-\frac{i}{\hbar} \int_{t_0}^t d\tau \mathcal{L}(\tau)}.$$

6.3 Quantum mechanical pictures

If the operators of the assigned observable are time independent and all evolution of time is contained in the state vector $|\varphi(t)\rangle$ (described by the Schrödinger equation (6.5)), then the formalism is called *Schrödinger picture*. The state vector for any time t is given by the initial state via¹⁴

$$|\varphi_S(t)\rangle = U(t, t_0)|\varphi_S(t_0)\rangle$$

with $U(t, t_0)$ as the time evolution operator of Sec. 6.2.

In contrast, in the *Heisenberg picture* the operators are time-dependent, the wave functions are not. To change into the Heisenberg picture, an unitary transformation is executed [CTDL07]:

$$|\varphi_H\rangle = U^\dagger(t, t_0)|\varphi_S(t)\rangle = U^\dagger(t, t_0)U(t, t_0)|\varphi_S(t_0)\rangle = |\varphi_S(t_0)\rangle$$

For an operator in the Heisenberg picture

$$A_H(t) = U^\dagger(t, t_0)A_S U(t, t_0)$$

is valid. For the time evolution of an operator in the Heisenberg picture, the Liouville-Von Neumann equation

$$\frac{d}{dt} A_H(t) = -\frac{i}{\hbar} [H, A_H(t)]$$

¹³The Heaviside step function is defined as the integral of the Dirac delta function: $\Theta(x) = \int_{-\infty}^x \delta(t) dt$. It is 0, if $x < 0$ and 1 for $x \geq 0$.

¹⁴The index S shows a quantity in Schrödinger picture, the letter H will represent the Heisenberg picture and D the Interaction or also called Dirac picture.

can be derived (see Eq. (6.1.3) in Sec. 6.1.3). Both pictures describe the same physics, they are just different kinds of representation. This fact is illustrated by the equation $\langle \varphi_S(t) | A_S | \varphi_S(t) \rangle = \langle \varphi_H | A_H(t) | \varphi_H \rangle$.

A third representation is the *interaction picture*, that is a combination of the Schrödinger and the Heisenberg picture. For the perturbation theory the interaction picture, that is also called *Dirac picture*, is the most suitable. As explained in the following section, the Hamiltonian is split in two parts, an undisturbed system H_0 , that is time-independent and treated in the Heisenberg picture, and the small time-dependent perturbation $H'(t)$, which is considered in the Schrödinger picture.

The time evolution operator with respect to the undisturbed Hamiltonian of the system H_0 is

$$U_0(t, t_0) = e^{-\frac{i}{\hbar} H_0(t-t_0)}$$

and the wave function in the interaction picture is defined as

$$|\varphi(t)\rangle = U_0(t, t_0) |\varphi_D(t)\rangle \quad (6.13)$$

where $|\varphi(t)\rangle$ represents the wave function with respect to the full Hamiltonian $H(t)$ while $|\varphi_D(t)\rangle$ is the wave function caused by the perturbation H' . By plugging Eq. (6.13) into the Schrödinger equation,

$$\frac{d}{dt} |\varphi_D(t)\rangle = -\frac{i}{\hbar} H'_D(t) |\varphi_D(t)\rangle \quad (6.14)$$

with $H'_D(t) = U_0^\dagger(t, t_0) H'(t) U_0(t, t_0)$ is obtained [Muk95].

The density operator in Interaction picture reads

$$\underbrace{|\varphi(t)\rangle \langle \varphi(t)|}_{\rho(t)} = U_0(t, t_0) \cdot \underbrace{|\varphi_D(t)\rangle \langle \varphi_D(t)|}_{\rho_D(t)} \cdot U_0^\dagger(t, t_0).$$

Its time evolution is given again through the Liouville-Von Neumann equation

$$\frac{d}{dt} \rho_D(t) = -\frac{i}{\hbar} [H'_D(t), \rho_D(t)].$$

6.4 Perturbation expansion

In a naive approach, solving the Schrödinger equation (6.5) can be done by integrating and plugging the result

$$|\varphi(t)\rangle = |\varphi(t_0)\rangle - \frac{i}{\hbar} \int_{t_0}^t H(\tau) |\varphi(\tau)\rangle d\tau$$

into itself to obtain [Ham05]

$$|\varphi(t)\rangle = |\varphi(t_0)\rangle + \sum_{n=1}^{\infty} \left(-\frac{i}{\hbar}\right)^n \int_{t_0}^t d\tau_n \int_{t_0}^{\tau_n} d\tau_{n-1} \dots \int_{t_0}^{\tau_2} d\tau_1 \cdot H(\tau_n) H(\tau_{n-1}) \dots H(\tau_1) |\varphi(t_0)\rangle. \quad (6.15)$$

Expansion for the density matrix introduced in Sec. 6.1 yields analogous to Eq. (6.15) for the Liouville-Von Neumann equation (6.6)

$$\begin{aligned}\rho(t) &= \rho(t_0) + \sum_{n=1}^{\infty} \left(-\frac{i}{\hbar}\right)^n \int_{t_0}^t d\tau_n \int_{t_0}^{\tau_n} d\tau_{n-1} \dots \int_{t_0}^{\tau_2} d\tau_1 \\ &\quad \cdot [H(\tau_n), [H(\tau_{n-1}), \dots [H(\tau_1), \rho(t_0)] \dots]]. \\ &= \rho(t_0) + \sum_{n=1}^{\infty} \left(-\frac{i}{\hbar}\right)^n \int_{t_0}^t d\tau_n \int_{t_0}^{\tau_n} d\tau_{n-1} \dots \int_{t_0}^{\tau_2} d\tau_1 \\ &\quad \cdot \mathcal{L}(\tau_n) \mathcal{L}(\tau_{n-1}) \mathcal{L}(\tau_1) \rho(t_0).\end{aligned}\tag{6.16}$$

But Eqs. (6.15) and (6.16) do not converge sufficiently. Using perturbation theory can improve the results. The non-perturbatively approach can be lead into a perturbative one by using that the interaction with the electric field H' is much weaker than internal fields of the molecule with

$$H = H_0 + H'(t) = H_0 + \boldsymbol{\mu} \cdot \mathbf{E}(t).\tag{6.17}$$

For this purpose, it must be assumed that the stationary states of the molecule itself are known [Muk95]. The operator H_0 is the unperturbed Hamiltonian that is typically already solved, the time dependent electric field is given by $\mathbf{E}(t)$, and $\boldsymbol{\mu}$ describes the dipole matrix element via

$$\boldsymbol{\mu} = \sum_{ab} \boldsymbol{\mu}_{ab} |a\rangle \langle b|$$

with $\boldsymbol{\mu}_{ab}$ as the transition dipole between states a and b [KAK02, APV⁺09].

In Liouville space, similar to Eq. (6.17) the perturbation can be described via

$$\mathcal{L} = \mathcal{L}_0 + \mathcal{L}'(t)$$

with $\mathcal{L}_0(t)O = [H_0(t), O]$, and $\mathcal{L}'(t)O = [H'(t), O]$.

For a time-dependent perturbation, it is suitable to consider the interaction picture as introduced in Sec. 6.3. There, also Eq. (6.14) is given, that can be transformed analogously to Eq. (6.15) to obtain

$$\begin{aligned}|\varphi_D(t)\rangle &= |\varphi_D(t_0)\rangle + \sum_{n=1}^{\infty} \left(-\frac{i}{\hbar}\right)^n \int_{t_0}^t d\tau_n \int_{t_0}^{\tau_n} d\tau_{n-1} \dots \int_{t_0}^{\tau_2} d\tau_1 \\ &\quad \cdot H'_D(\tau_n) H'_D(\tau_{n-1}) \dots H'_D(\tau_1) |\varphi_D(t_0)\rangle.\end{aligned}\tag{6.18}$$

or for the density matrix analogously to Eq. (6.16)

$$\begin{aligned}\rho_D(t) &= \rho_D(t_0) + \sum_{n=1}^{\infty} \left(-\frac{i}{\hbar}\right)^n \int_{t_0}^t d\tau_n \int_{t_0}^{\tau_n} d\tau_{n-1} \dots \int_{t_0}^{\tau_2} d\tau_1 \\ &\quad \cdot \mathcal{L}'_D(\tau_n) \mathcal{L}'_D(\tau_{n-1}) \mathcal{L}'_D(\tau_1) \rho_D(t_0).\end{aligned}\tag{6.19}$$

The index D still symbolizes the interaction picture.

As a last step to become prepared for nonlinear spectroscopy of Ch. 7, the quantum mechanical picture is changed by inserting Eq. (6.13). With $|\varphi^{(0)}(t)\rangle = U_0(t, t_0)|t_0\rangle$ as the zero-order wave function, Eq. (6.18) becomes to

$$\begin{aligned}|\varphi(t)\rangle &= |\varphi^{(0)}(t)\rangle + \sum_{n=1}^{\infty} \left(-\frac{i}{\hbar}\right)^n \int_{t_0}^t d\tau_n \int_{t_0}^{\tau_n} d\tau_{n-1} \dots \int_{t_0}^{\tau_2} d\tau_1 \\ &\quad \cdot U_0(t, t_0) H'_D(\tau_n) H'_D(\tau_{n-1}) \dots H'_D(\tau_1) |\varphi(t_0)\rangle.\end{aligned}$$

With $H'_D(t) = U_0^\dagger(t, t_0)H'(t)U_0(t, t_0)$ and Eqs. (6.10) and (6.11) it is

$$|\varphi(t)\rangle = |\varphi^{(0)}(t)\rangle + \sum_{n=1}^{\infty} \left(-\frac{i}{\hbar}\right)^n \int_{t_0}^t d\tau_n \int_{t_0}^{\tau_n} d\tau_{n-1} \dots \int_{t_0}^{\tau_2} d\tau_1 \cdot U_0(t, \tau_n)H'(\tau_n)U_0(\tau_n, \tau_{n-1})H'(\tau_{n-1}) \dots U_0(\tau_2, \tau_1)H'(\tau_1)U_0(\tau_1, t_0)|\varphi(t_0)\rangle. \quad (6.20)$$

The interpretation of this equation is discussed in Sec. 7.3.

For the density matrix, Eq. (6.19) becomes analogously to

$$\rho(t) = \rho^{(0)}(t) + \sum_{n=1}^{\infty} \left(-\frac{i}{\hbar}\right)^n \int_{t_0}^t d\tau_n \int_{t_0}^{\tau_n} d\tau_{n-1} \dots \int_{t_0}^{\tau_2} d\tau_1 \cdot \mathcal{U}_0(t, t_0)\mathcal{L}'_D(\tau_n)\mathcal{L}'_D(\tau_{n-1})\mathcal{L}'_D(\tau_1)\rho(t_0)\mathcal{U}_0^\dagger(t, t_0) \quad (6.21)$$

where \mathcal{U} describes the time evolution operator in Liouville space with $\mathcal{U}(t, t_0) = \mathcal{U}_I(t, t_0)\mathcal{U}_D(t, t_0)$ [Ham05].

Perturbation theory higher than the first order is typically very complex: Often, graphical illustrations help setting formulas and finding solutions. For this reason, Sec. 7.3 introduces a possibility to visualize equations.

6.5 Coupled quantum systems

Low-dimensional systems have received much attention for a long time. They are well understood both experimentally and theoretically [LRNB03, DAFK06, DMR⁺10]. Coupled quantum systems occur in different areas. Not only in electric devices but also in nature, many systems as molecular aggregates (that are clusters of small molecules) can be seen due their dimensions as quantum systems [GCF09, BSV⁺05, SCIF11].

6.5.1 Quantum dots

The simplest model for such systems are coupled quantum dots as they appear in semiconductor physics [RAK⁺06, GLE⁺02, Bor02]. Quantum dots consist of a nanoscopic material structure that confines the mobility of their carrier (electrons or holes) simultaneously in all three spatial dimensions. Commonly, they are produced artificially with semiconductor structures using techniques such as etching or grid metal gates [Ali96, LKR⁺93]. Often they are formed like disks or small pyramids with a diameter of ten to a few hundred nanometers and only a few nanometers thick. Consequently, their energy is no longer continuous, it is quantized in discrete energy levels with energy spacings of a few micro or millielectron volt.

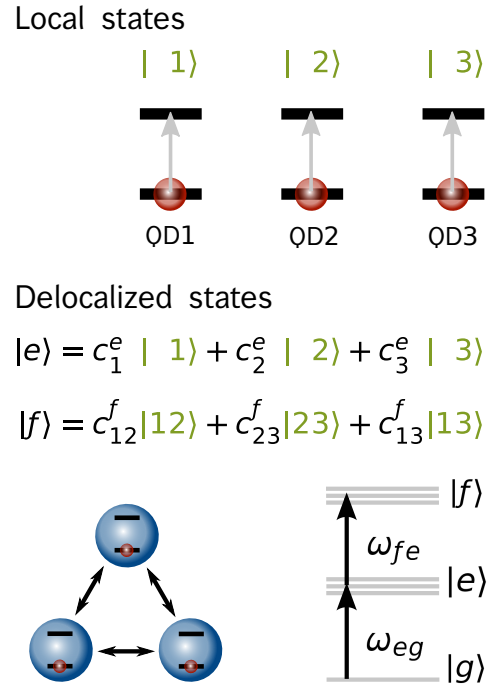
6.5.2 Single-excitons and two-excitons

One type of elementary excitations in quantum dots are excitons [Que92]. These electrically neutral quasiparticles can be created by photons near an absorption edge and they exist in insulators, semiconductors and in some liquids. They describe a bound state of an electron and hole which are attracted to each other by the electrostatic Coulomb force. They can transport energy without transporting electric charge [Lia70]. Excitons in quantum dots are investigated in experiments [BHLK88] and in theory [HLK90] very intensively.

For non-linear response, also the biexcitonic contributions have to be considered. Biexcitons are created by two free single-excitons [LWS⁺03, CSB⁺02]. That can be done for example by pump-probe experiments, two-photon absorption of light from the ground state to the

Figure 6.1:

Expansion of delocalized states in localized exciton and biexciton basis of three coupled two-level quantum dots: Three uncoupled quantum dots are shown in their local basis. Bringing the dots closer together, they can couple due to Coulomb effects (Förster interaction). Thus, they form new delocalized states: For the excitation energies in this work, one ground state $|g\rangle$, three single-exciton states $|e\rangle$ and three biexcitonic states $|f\rangle$ with a transition energy ω_{eg} and ω_{fe} , respectively, are obtained. The many-particle exciton state can be written as a superposition of single particle states weighted with factors c_i^e that gives information about the probability of presence of the electrons within the coupled quantum dot system. Also the biexcitonic states can be written as an expansion of a biexcitonic basis with expansion coefficients c_{ij}^f .



biexciton state or by luminescence experiments from a biexciton state made up from two free excitons in a dense exciton system [Vek94].

6.5.3 Coupling

Bringing the dots to close vicinity, they are still spatially localized but they can couple electromagnetically. The resonant energy transfer between excitons of neighboring quantum dots is described by *Förster coupling* [För65, NLB⁺05]. Such an exciton transfer can be treated similar for coupled quantum dots as well as between molecular systems and biosystems – especially for photosynthesis. Note, that coupled excitations are possible even if no wave function overlap is assumed.

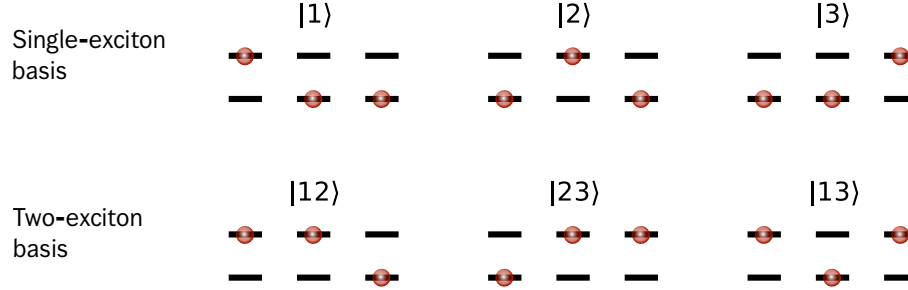
6.5.4 Delocalized states in exciton and biexciton basis

Excitations of one state results in a perturbation of another state by reason of intra- or intermolecular interactions between the states. The coupling of the quantum dots leads to generating new states. These new states cannot be connected to a certain quantum dot, they are delocalized [IF10]. That means that the probability of presence is spread over the whole quantum system. Fig. 6.1 illustrates the delocalization of the states for three coupled quantum dots.

If the distance between the N quantum dots is small enough, they couple due to Coulomb effects (Förster interaction) and build new delocalized states: a ground state $|g\rangle$, N single-exciton states $|e\rangle$ and $N(N-1)/2$ two-exciton states $|f\rangle$. The new states can be expressed as an expansion in exciton or biexciton basis, respectively, as displayed in Fig. 6.1 for $N=3$:

$$|e\rangle = \sum_i c_i^e |i\rangle \quad (6.22a)$$

$$|f\rangle = \sum_{i,j \neq i} c_{ij}^f |ij\rangle. \quad (6.22b)$$

**Figure 6.2:**

Single and two-exciton basis elements for a quantum system of three coupled quantum dots: Two excitons creates a biexcitonic state.

The exciton basis elements are described by the state $|i\rangle$ which stands for a local, uncoupled quantum dot system where only quantum dot i is excited.

On the top of Fig. 6.1, the level scheme of three coupled two-level quantum dots is depicted. The basis elements for a system of three quantum dots are shown in Fig. 6.2 and consist of the vectors $|1\rangle$, $|2\rangle$, and $|3\rangle$. The biexcitonic basis is denoted by $|ij\rangle$. Here, the basis elements describe a system of two excited quantum dots i and j . These elements are also depicted in Fig. 6.2 for three quantum dots. The basis elements in this case are $|12\rangle$, $|23\rangle$, and $|13\rangle$. For excitation energies chosen in this work, one ground state g , three single-exciton states e_1 , e_2 , and e_3 and three two-exciton states f_1 , f_2 , and f_3 are obtained. This system of three quantum dots serve as model to explain and demonstrate the ideas of localized spectroscopy in Ch. 8.

6.5.5 Full Hamiltonian of our model system

Three coupled self-organized semiconductor quantum dots serve as a model system for the rest of this work. In Ch. 5 already typical dot sizes and distances are used. Further, it is assumed that the distances are sufficiently large to have no electronic wave function overlap. Further assumptions are that the dots have no spin-orbit splitting, they have big enough biexcitonic shifts, they are negatively charged or they have spin-orbit coupling bigger than the inter quantum dot couplings [JHW98, BLS⁺01].

The dipole coupling is assumed as about several microelectron volts with a Lorentzian zero phonon line width of $\gamma = 1 \mu\text{eV}$ for low temperatures (e.g. $T = 4\text{K}$) [SDW⁺11, BLS⁺01]. It is possible to neglect the influence of the phonon side bands because their amplitude in the spectra is one to two orders smaller than the amplitude of the zero phonon line resonance at low temperatures [SDW⁺11, BLS⁺01].

This section begins with introducing the full Hamiltonian of the model system of this work in a local basis. In the second part of this section, the Hamiltonian is transformed into the delocalized basis.

Local basis

The full Hamiltonian $H = H_0 + H_{e-1} + H_C$ of the system treated in this work consists of three parts: The free part, that corresponds to the energy of a freely moved electron, the field-matter part, that describes the coupling to a classical electric field via a dipole operator, and the

6 Theoretical Foundation of Quantum Systems

$\langle i H_0 j\rangle$	1	2	3
1	-2.2	-0.4	-0.6
2	-0.4	0.2	-0.3
3	-0.6	-0.3	2.5
$\langle ij H_0 kl\rangle$	1,2	1,3	2,3
1,2	$\langle 1 H_0 1\rangle + \langle 2 H_0 2\rangle - 0.4$	$\langle 3 H_0 2\rangle$	$\langle 3 H_0 1\rangle$
1,3	$\langle 2 H_0 3\rangle$	$\langle 1 H_0 1\rangle + \langle 3 H_0 3\rangle + 0.2$	$\langle 2 H_0 1\rangle$
2,3	$\langle 1 H_0 3\rangle$	$\langle 1 H_0 2\rangle$	$\langle 2 H_0 2\rangle + \langle 3 H_0 3\rangle + 0.8$

Table 6.1:

Hamiltonian in matrix form: The upper table gives energies in microelectron volts for the exciton block, the lower table for biexciton states.

Coulomb part, that represents the Coulomb interaction. It contains the Förster interaction, the ground state, monoexcitonic and biexcitonic shift. The free part reads

$$H_0 = \sum_i \epsilon_i |i\rangle\langle i| + \epsilon_0 |g\rangle\langle g| + \sum_{i,j \neq i} (\epsilon_i + \epsilon_j) |ij\rangle\langle ij|. \quad (6.23a)$$

For the energies ϵ are chosen: $\epsilon_0 = 0$, $\epsilon_1 = -2.2$, $\epsilon_2 = 0.2$, and $\epsilon_3 = 2.5$ (cf. Tab. 6.1).

The electron-light part is:

$$\begin{aligned} H_{e-1} = & \sum_i^n \boldsymbol{\mu}_{gi} \cdot \mathbf{E}(t) |g\rangle\langle i| + \sum_{i,j \neq i}^n \boldsymbol{\mu}_{ij} \cdot \mathbf{E}(t) |i\rangle\langle ij| \\ & + \sum_i^n \boldsymbol{\mu}_{gi}^* \cdot \mathbf{E}^*(t) |i\rangle\langle g| + \sum_{i,j \neq i}^n \boldsymbol{\mu}_{ij}^* \cdot \mathbf{E}^*(t) |ij\rangle\langle i| \end{aligned} \quad (6.23b)$$

with $\mathbf{E}(t)$ as the electric field, that is given for example in Eq. (7.11).

Finally, the Coulomb interaction is given by

$$H_C = \sum_{i>j} V_{ij} |ij\rangle\langle ji| + \sum_{i,j \neq i} V_{ij}^F |i\rangle\langle j| + \sum_{k,i \neq k, j \neq k} V_{ij}^F |ki\rangle\langle kj| \quad (6.23c)$$

with the coupling parameters $V_{12}^F = -0.4$, $V_{13}^F = -0.6$, $V_{23}^F = -0.3$, $V_{12} = -0.4$, $V_{13} = 0.2$, and $V_{23} = 0.8$. These parameters and the energies are given additionally in matrix form in Tab. 6.1.

Delocalization basis

Coulomb coupling between the quantum dots leads to the formation of delocalized states given in Eq. (6.22):

$$|e\rangle = \sum_i c_i^e |i\rangle \quad \text{and} \quad |f\rangle = \sum_{i,j \neq i} c_{ij}^f |ij\rangle.$$

The full delocalized wave function is normalized:

$$\sum_i |c_i^e|^2 = 1. \quad (6.24)$$

The Hamiltonian of Eq. (6.23) can be written in the new delocalized basis. The matrix entries of the pure electronic part ($H_0 + H_C$) including the coupling between the nanostructure can be calculated by diagonalizing [CKR09]. As a result one obtains in delocalized basis

$$H_0 + H_C = \epsilon_g |g\rangle\langle g| + \sum_e \epsilon_e |e\rangle\langle e| + \sum_f \epsilon_f |f\rangle\langle f|$$

with ϵ_g , ϵ_e , and ϵ_f as the eigenenergy for the ground state, the single-exciton state and the double-exciton state, respectively.

Here, the rewriting of H_{e-1} is exemplarily shown. As starting point the light-matter part of the Hamiltonian, Eq. (6.23b), reads

$$H_{e-1} = \sum_i \boldsymbol{\mu}_{gi} \cdot \mathbf{E}(t) |g\rangle\langle i| + \sum_{i,j \neq i} \boldsymbol{\mu}_{ij} \cdot \mathbf{E}(t) |i\rangle\langle ij| + \text{h.c.}$$

From Eq. (6.22a) follows by multiplying with c_k^{e*} , summing up over e , using¹⁵

$$\sum_i \sum_e c_k^{e*} c_i^e = \sum_i \delta_{ik} = 1 \quad (6.25)$$

and finally rename k by i the equality

$$\sum_e c_i^{e*} |e\rangle = |i\rangle \Leftrightarrow \sum_e c_i^e \langle e| = \langle i|. \quad (6.26a)$$

Analogous, Eq. (6.22b) provides

$$\sum_f c_{ij}^{f*} |f\rangle = |ij\rangle \Leftrightarrow \sum_f c_{ij}^f \langle f| = \langle ij|. \quad (6.26b)$$

With these two Eqs. (6.26a) and (6.26b) for the field-matter Hamiltonian of Eq. (6.23b) a new expression is obtained:

$$H_{e-1} = \sum_{ie} c_i^e \boldsymbol{\mu}_{gi} \cdot \mathbf{E}(t) |g\rangle\langle e| + \sum_{i,j \neq i,e,f} c_i^{e*} c_{ij}^f \boldsymbol{\mu}_{gj} \cdot \mathbf{E}(t) |e\rangle\langle f| + \text{h.c.}$$

With the expansion of the dipole moments

$$\boldsymbol{\mu}_{ge} = \sum_i c_i^e \boldsymbol{\mu}_{gi} \quad (6.27a)$$

$$\boldsymbol{\mu}_{ef} = \sum_{i,j \neq i} c_i^{e*} \boldsymbol{\mu}_{gj} c_{ij}^f \quad (6.27b)$$

one obtains a reformulated version of Eq. (6.23b) in delocalized basis

$$H_{e-1} = \sum_e \boldsymbol{\mu}_{ge} \cdot \mathbf{E}(t) |g\rangle\langle e| + \sum_{ef} \boldsymbol{\mu}_{ef} \cdot \mathbf{E}(t) |e\rangle\langle f| + \text{h.c.}$$

¹⁵The symbol δ_{ik} means the Kronecker delta, that equals 1 if $i = k$ and 0 if $i \neq k$

7 Multidimensional Coherent Nonlinear Spectroscopy

Spectroscopy as an optical technique is an invaluable tool to provide a microscopic understanding of nature. If incoming light perturbs the optical properties of a medium in a way such that the subsequent light fields can see changes in the molecular structure of the sample, the processes are nonlinear [Wri11]. That this can happen, the light fields have to interact with the molecular states over time periods that are shorter than dephasing or relaxation periods of the population, so that the effects of the first interaction still persist [BLW⁺05].

The most common and simplest approach is *pump-probe spectroscopy*. In this technique, two optical pulses with variable time delay between them are used to investigate the microscopic processes that happen during the light interaction. In optics, typically the first pulse pumps a system in an excited state and the second pulse probes the progress of the interaction a certain period of time after initiation. The probe pulse changes its response according to the reaction of the system. Varying the time delay between pump and probe pulses and observing the response gives new insights into the microscopic processes within the system. Such one-dimensional nonlinear experiments gives information about how quantum states evolve in time and supplies understanding of the evolution of coherences¹⁶ and populations of the investigated systems.

For the model system treated in this work (see Sec. 6.5), coherent spectroscopy is used to find new information about single and two-exciton states [LW08]. But since not only the energies of these states but also the couplings between them are of interest, a further dimension comes into consideration: two-dimensional spectroscopy.

Multidimensional spectroscopy is a new field [BZ83, HAFJ98, Muk00]. It uses multiple excitation pulses to excite multiple vibrational or electronic quantum states [Cho08, Jon03b, MTH09, Cho09]. Recent advances in practice and theory of multidimensional coherent spectroscopy enable researchers to gain deeper insights into the mechanism of excited state processes and dynamics [KMS09, YF99a]. Measuring the frequency dependent electric field output as a function of the input laser frequencies, a multidimensional spectrum is obtained. While the diagonal peaks are the frequencies of individual states, the off-diagonal cross-peaks define which states are coupled [Wri11].

Multidimensional spectroscopy have been developed extensively by *nuclear magnetic resonance* experiments (often abbreviated with NMR) [EBW87]. Such methods are commonly used for structure determination in complex molecules [GCF09]. It can resolve their structure with atomic resolution but its millisecond time scale is not fast enough to follow ultrafast dynamics, that works on time-scales in a range of ten femtoseconds to picoseconds. Femtosecond optical two-dimensional spectroscopy can be seen as the direct optical analog of two-dimensional nuclear magnetic resonance [SM02, Jon03a, TKS03, KTW99]. Feynman et al. have shown that the transitions between two quantum states are equivalent to the spin excitations in nuclear magnetic resonance experiments. The interest in developing the optical analogous of nuclear magnetic resonance origins from the power of this technique to probe

¹⁶Coherences are quantum mechanical superposition states between two quantum states. They are time dependent and oscillate at their difference frequency.

complex systems with great selectivity. So it can provide advantages over existing techniques for extracting spectral information.

While the nuclear magnetic resonance is based on the interaction of the magnetic field component with the magnetic dipole moment of nuclear spins, molecular spectroscopy of electronic states is based on the interaction of molecules with the electric field component of electromagnetic radiation fields by the induced molecular electric dipole moments. Despite some similarities, the molecular spectroscopies differs significantly from the nuclear magnetic resonance method because the nuclei in this technique are well protected by the thermal environment while in molecular spectroscopy, the electrical quantum states strongly interact with the environment leading to much broader transitions between the states.

Coherent multidimensional optical spectroscopy has great potential for revealing molecular structural details and dynamics in complex systems – such as multichromophore or other complex aggregates or nanostructures like semiconductors [KMS09, AK04, IF12, SCDF12].

This chapter starts with an introduction to nonlinearity and its formal treatment. Afterwards, the perturbation expansion of Ch. 6 is continued by presenting the nonlinear response function that describes the response of the system to the interaction with the incoming light, connected with the observable in optics: the polarization. A further important section of this chapter is the introduction of the double-sided Feynman diagrams that illustrate the processes that happen in coherent multidimensional optical spectroscopies. The rotating wave approximation applied for this system is also introduced.

Optical spectroscopy can be classified by a variety of criteria. Sec. 7.4 presents an overview of a few nonlinear spectroscopy methods that can be grouped by the order of the response with respect to the applied fields. Afterwards, this chapter shows some experimental details and explains on which way the response of the system can be detected, including two methods: the phase matching and the phase cycling technique. Differences between homodyne and heterodyne detection are also discussed.

Furthermore, a classification for third-order techniques is introduced. Finally, after discussing two-dimensional spectra, two important third-order coherent nonlinear optical spectroscopy methods are presented: the photon echo and the double quantum coherence spectroscopy.

7.1 Nonlinearity

A possibility for classification of optical measurements is the power-law dependence on their external electrical radiation field. The relevant material quantity that couples with this field is the polarization P that can be approximately written by a Taylor series (cf. Eq. (2.4a) of Sec. 2.1.2)

$$\mathbf{P} = \mathbf{P}^{(1)} + \underbrace{\mathbf{P}^{(2)} + \mathbf{P}^{(3)} + \dots}_{\mathbf{P}_{\text{NL}}} = \epsilon_0 \chi^{(1)} \cdot \mathbf{E}^{(1)} + \epsilon_0 \chi^{(2)} \cdot \mathbf{E}^{(2)} + \epsilon_0 \chi^{(3)} \cdot \mathbf{E}^{(3)} + \dots \quad (7.1)$$

where $\mathbf{P}^{(n)}$ is the component of the polarization to the n th order in the field, $\mathbf{E}^{(n)}$ the electric field and χ the optical susceptibility¹⁷ of order n (cf. Sec. 2.1). Just $\mathbf{P}^{(1)}$ as the *linear polarization* controls the *linear optical response*. Neglecting higher orders than the linear term is sufficient for optical processes such as absorption or propagation for weak incoming fields only. Mind, that Eq. (7.1) is just an approximation for the frequency domain: In time domain, the polarization is a convolution of the susceptibility and the electric field as can be seen in Eq. (7.3).

¹⁷Mind, that in fact the electric field is a vector and the nonlinear susceptibilities are tensors.

For incoming fields with stronger intensities, the higher orders cannot be neglected. Non-linearity occurs if the effects of a perturbation are large and thus, the response to the perturbation does not follow the perturbation's magnitude any longer. Then, the electric field strength of light is greater or equal than the electric fields in the sample, so that the polarization induced in matter by the light is distorted. That acquires new frequencies which correspond to combinations of the sum and differences of frequencies of the exciting light and modifies the amplitudes of the previous frequencies.

Expanding Eq.(7.1) for higher orders, the occurring terms are responsible for different nonlinear processes. Each term can be associated with different processes, such as frequency doubling, photon echo, the optical Kerr effect or degenerate four-wave mixing, depending on the experimental conditions.

Higher orders of the polarization successively carry more information about the microscopic system. Only the nonlinear terms allow to reveal relaxation times or to eliminate some broadening mechanisms. Some of the nonlinear spectroscopy techniques are presented in the remainder of this chapter.

7.2 Nonlinear response function

The perturbation expansion of the density operator is given in Eq. (6.21):

$$\rho(t) = \rho^{(0)}(t) + \sum_{n=1}^{\infty} \left(-\frac{i}{\hbar}\right)^n \int_{t_0}^t d\tau_n \int_{t_0}^{\tau_n} d\tau_{n-1} \dots \int_{t_0}^{\tau_2} d\tau_1 \\ \cdot \mathcal{U}_0(t, t_0) \mathcal{L}'_D(\tau_n) \mathcal{L}'_D(\tau_{n-1}) \mathcal{L}'_D(\tau_1) \rho(t_0) \mathcal{U}_0^\dagger(t, t_0).$$

It provides an order-by-order expansion in the field. So it is possible to rewrite it in

$$\rho(t) = \rho^{(0)}(t) + \sum_{n=1}^{\infty} \rho^{(n)}(t)$$

with

$$\rho^{(n)}(t) = \left(-\frac{i}{\hbar}\right)^n \int_{t_0}^t d\tau_n \int_{t_0}^{\tau_n} d\tau_{n-1} \dots \int_{t_0}^{\tau_2} d\tau_1 \mathbf{E}(\tau_n) \mathbf{E}(\tau_{n-1}) \dots \mathbf{E}(\tau_1) \\ \cdot \mathcal{U}_0(t, t_0) [\boldsymbol{\mu}_D(\tau_n), [\boldsymbol{\mu}_D(\tau_{n-1}), \dots [\boldsymbol{\mu}_D(\tau_1), \rho(t_0)] \dots]] \mathcal{U}_0^\dagger(t, t_0). \quad (7.2)$$

Here, Eq. (6.17) is used for $H'(t) = \boldsymbol{\mu} \cdot \mathbf{E}(t)$ and the dipole operator in the Dirac picture is $\boldsymbol{\mu}_D(t) = \mathcal{U}_0^\dagger(t, t_0) \boldsymbol{\mu} \mathcal{U}_0(t, t_0)$.

In optical experiments, where the system is driven optical via $H'(t) = \boldsymbol{\mu} \cdot \mathbf{E}(t)$, the observable that is influenced by the light enters into the polarization. The induced polarization of order n is given by the expectation value of the dipole operator that can be calculated via the trace (see Eq. (6.4)) of its product with the density operator

$$\mathbf{P}^{(n)} = \langle \boldsymbol{\mu} \rangle = \text{tr}(\boldsymbol{\mu} \rho^{(n)}(t)) \quad (7.3)$$

with a time-independent $\boldsymbol{\mu}_S = \boldsymbol{\mu}$ in the Schrödinger picture.

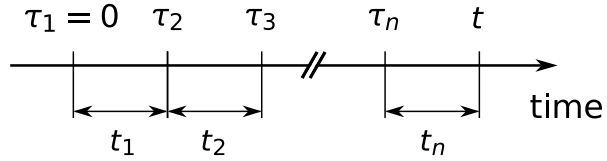
Inserting Eq. (7.2) in Eq. (7.3), a cyclic permutation within the trace and discarding the subscript D so that $\boldsymbol{\mu}_D(t) = \boldsymbol{\mu}(t) = \mathcal{U}_0^\dagger(t, t_0) \boldsymbol{\mu} \mathcal{U}_0(t, t_0)$ gives

$$\mathbf{P}^{(n)}(t) = \left(-\frac{i}{\hbar}\right)^n \int_{t_0}^t d\tau_n \int_{t_0}^{\tau_n} d\tau_{n-1} \dots \int_{t_0}^{\tau_2} d\tau_1 \mathbf{E}(\tau_n) \mathbf{E}(\tau_{n-1}) \dots \mathbf{E}(\tau_1) \\ \cdot \text{tr}(\boldsymbol{\mu}(t) [\boldsymbol{\mu}(\tau_n), [\boldsymbol{\mu}(\tau_{n-1}), \dots [\boldsymbol{\mu}(\tau_1), \rho(t_0)] \dots]]).$$

7 Multidimensional Coherent Nonlinear Spectroscopy

Figure 7.1:

Timeline to illustrate the replacement of the time variables: The interaction between matter and the radiation field takes place at time-ordered points $\tau_1 \leq \tau_2 \dots \tau_n$. The time intervals between these interactions are given by t_1 to t_n [Muk95].



This polarization – the source of a new optical field – can be rewritten by replacing the times τ_1 to τ_n by time intervals t_1 to t_n via

$$\begin{aligned} 0 &= \tau_1 \\ t_1 &= \tau_2 - \tau_1 \\ t_2 &= \tau_3 - \tau_2 \\ &\vdots \\ t_n &= t - \tau_n \end{aligned}$$

and is therefore

$$\begin{aligned} \mathbf{P}^n(t) &= \left(-\frac{i}{\hbar}\right)^n \int_0^\infty dt_n \int_0^\infty dt_{n-1} \dots \int_0^\infty dt_1 \mathbf{E}(t - t_n) \mathbf{E}(t - \tau_n - t_{n-1}) \dots \mathbf{E}(t - t_n - t_{n-1} - \dots - t_1) \\ &\quad \cdot \text{tr}(\boldsymbol{\mu}(t_n + t_{n-1} + \dots + t_1) [\boldsymbol{\mu}(t_{n-1} + \dots + t_1), \dots [\boldsymbol{\mu}(0), \rho(t_0)] \dots]). \end{aligned}$$

Fig. 7.1 illustrates the replacement of the time variables.

Each order in this expansion represents a different class of optical measurement techniques (cf. Sec. 7.4). While $\mathbf{P}^{(1)}$ represents linear optics, the second-order polarization terms are responsible for nonlinear processes like frequency sum generation. The third-order polarization terms $\mathbf{P}^{(3)}$ is correlated with several techniques as four-wave mixing or pump-probe spectroscopy [MHM⁺06, MM96].

As seen in Sec. 2.1.2 and 7.1, the polarization is linked with the electric field by the susceptibility as a response function of the material (cf. Eqs. (2.4) and (7.1)). For this nonlinear excitation, the polarization can be written as [SM08]

$$\begin{aligned} \mathbf{P}^{(n)}(t) &= \int_0^\infty dt_n \int_0^\infty dt_{n-1} \dots \int_0^\infty dt_1 \\ &\quad \cdot \mathbf{E}(t - t_n) \mathbf{E}(t - t_n - t_{n-1}) \dots \mathbf{E}(t - t_n - t_{n-1} - \dots - t_1) R^{(n)}(t_n, t_{n-1}, \dots, t_1). \end{aligned} \quad (7.4)$$

with the *nonlinear response function* $R^{(n)}$ of order n :

$$\begin{aligned} R^{(n)}(t_n, t_{n-1}, \dots, t_1) &= \\ &\quad \left(-\frac{i}{\hbar}\right)^n \text{tr}(\boldsymbol{\mu}(t_n + t_{n-1} + \dots + t_1) [\boldsymbol{\mu}(t_{n-1} + \dots + t_1), \dots [\boldsymbol{\mu}(0), \rho(t_0)] \dots]). \end{aligned} \quad (7.5)$$

The response function contains the complete microscopic information that is necessary for the calculation of optical measurements.

7.3 Double-sided Feynman diagrams

The perturbation theoretical expression of Eqs. (6.20) and (6.21) of Sec. 6.4 for the quantum mechanical wave function

$$|\varphi(t)\rangle = |\varphi^{(0)}(t)\rangle + \sum_{n=1}^{\infty} \left(-\frac{i}{\hbar}\right)^n \int_{t_0}^t d\tau_n \int_{t_0}^{\tau_n} d\tau_{n-1} \dots \int_{t_0}^{\tau_2} d\tau_1 \\ \cdot U_0(t, \tau_n) H'(\tau_n) U_0(\tau_n, \tau_{n-1}) H'(\tau_{n-1}) \dots U_0(\tau_2, \tau_1) H'(\tau_1) U_0(\tau_1, t_0) |\varphi(t_0)\rangle.$$

or the density operator

$$\rho(t) = \rho^{(0)}(t) + \sum_{n=1}^{\infty} \left(-\frac{i}{\hbar}\right)^n \int_{t_0}^t d\tau_n \int_{t_0}^{\tau_n} d\tau_{n-1} \dots \int_{t_0}^{\tau_2} d\tau_1 \\ \cdot \mathcal{U}_0(t, t_0) \mathcal{L}'_D(\tau_n) \mathcal{L}'_D(\tau_{n-1}) \mathcal{L}'_D(\tau_1) \rho(t_0) \mathcal{U}_0^\dagger(t, t_0)$$

describe the time evolution under a perturbation: The factor $U(\tau_1, t_0)$ of Eq. (6.20) represents a system that propagates as given by the Hamiltonian H_0 until time τ_1 (represented by $U_0(\tau_1, t_0)$), then, the perturbation $H'(\tau_1)$ is interacting with it. Then, the system again propagates until time τ_2 . There, it again interacts with the perturbation Hamiltonian for time τ_2 . This physical interpretation of the time evolution can be described in this way until time t . It can be illustrated by *doubled-sided Feynman diagrams* [HZ11] as shown in this section.

Calculating the nonlinear polarization (Eq. (7.4)), especially the response function (Eq. (7.5)) with its commutator

$$[\boldsymbol{\mu}(t_{n-1} + \dots + t_1), \dots [\boldsymbol{\mu}(0), \rho(t_0)] \dots]$$

has to be evaluated. It has 2^n terms. For the most important spectroscopic methods presented in this chapter, the two terms of the linear and the eight terms of the third-order response will be shown here explicitly. Using the invariance of the trace on cyclic permutation and that all operators are hermitian since they are operators of observables, one obtains:

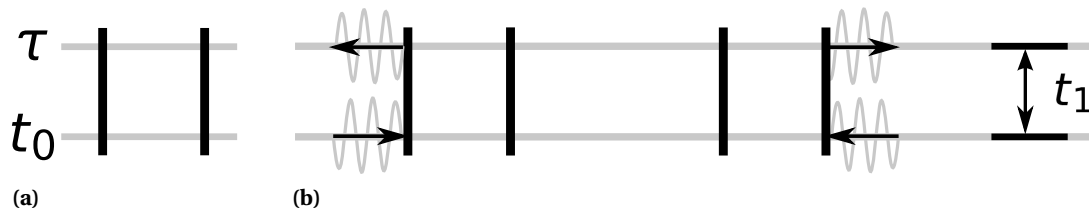
$$\begin{aligned} \text{tr}(\boldsymbol{\mu}(t_1) \rho(t_0) \boldsymbol{\mu}(0)) &= \text{tr}(\rho(t_0) \boldsymbol{\mu}(0) \boldsymbol{\mu}(t_1)) = \text{tr}(\rho^\dagger(t_0) \boldsymbol{\mu}^\dagger(0) \boldsymbol{\mu}^\dagger(t_1)) \\ &= \text{tr}((\rho(t_0) \boldsymbol{\mu}(0) \boldsymbol{\mu}(t_1))^\dagger)^\dagger) = \text{tr}(\rho(t_0) \boldsymbol{\mu}(0) \boldsymbol{\mu}(t_1))^* . \end{aligned} \quad (7.6)$$

With this, the linear response function reads

$$\begin{aligned} R^{(1)}(t_1) &= -\frac{i}{\hbar} \text{tr}(\boldsymbol{\mu}(t_1) [\boldsymbol{\mu}(0), \rho(t_0)]) = -\frac{i}{\hbar} (\text{tr}(\boldsymbol{\mu}(t_1) \boldsymbol{\mu}(0) \rho(t_0)) - \text{tr}(\boldsymbol{\mu}(t_1) \rho(t_0) \boldsymbol{\mu}(0))) \\ &\stackrel{(7.6)}{=} -\frac{i}{\hbar} (\text{tr}(\boldsymbol{\mu}(t_1) \boldsymbol{\mu}(0) \rho(t_0)) - \text{tr}(\rho(t_0) \boldsymbol{\mu}(0) \boldsymbol{\mu}(t_1))^*) \end{aligned}$$

and the third-order response is [Ham05]

$$\begin{aligned} R^{(3)}(t_1, t_2, t_3) &= \left(-\frac{i}{\hbar}\right)^n \text{tr}(\boldsymbol{\mu}(t_3 + t_2 + t_1) [\boldsymbol{\mu}(t_2 + t_1), [\boldsymbol{\mu}(t_1), [\boldsymbol{\mu}(0), \rho(t_0)]]]) = \left(-\frac{i}{\hbar}\right)^n \\ &\cdot \left(\text{tr}(\boldsymbol{\mu}(t_3 + t_2 + t_1) \boldsymbol{\mu}(t_2 + t_1) \boldsymbol{\mu}(t_1) \boldsymbol{\mu}(0) \rho(t_0)) - \text{tr}(\boldsymbol{\mu}(t_3 + t_2 + t_1) \boldsymbol{\mu}(t_2 + t_1) \boldsymbol{\mu}(t_1) \rho(t_0) \boldsymbol{\mu}(0)) \right. \\ &\quad - \text{tr}(\boldsymbol{\mu}(t_3 + t_2 + t_1) \boldsymbol{\mu}(t_2 + t_1) \boldsymbol{\mu}(0) \rho(t_0) \boldsymbol{\mu}(t_1)) + \text{tr}(\boldsymbol{\mu}(t_3 + t_2 + t_1) \boldsymbol{\mu}(t_2 + t_1) \rho(t_0) \boldsymbol{\mu}(0) \boldsymbol{\mu}(t_1)) \\ &\quad - \text{tr}(\boldsymbol{\mu}(t_3 + t_2 + t_1) \boldsymbol{\mu}(t_1) \boldsymbol{\mu}(0) \rho(t_0) \boldsymbol{\mu}(t_2 + t_1)) + \text{tr}(\boldsymbol{\mu}(t_3 + t_2 + t_1) \boldsymbol{\mu}(t_1) \rho(t_0) \boldsymbol{\mu}(0) \boldsymbol{\mu}(t_2 + t_1)) \\ &\quad \left. + \text{tr}(\boldsymbol{\mu}(t_3 + t_2 + t_1) \boldsymbol{\mu}(0) \rho(t_0) \boldsymbol{\mu}(t_1) \boldsymbol{\mu}(t_2 + t_1)) - \text{tr}(\boldsymbol{\mu}(t_3 + t_2 + t_1) \rho(t_0) \boldsymbol{\mu}(0) \boldsymbol{\mu}(t_1) \boldsymbol{\mu}(t_2 + t_1)) \right) \end{aligned}$$


Figure 7.2:

Simplest double-sided Feynman diagrams: In part (a) only a pathway for $U(t_1, t_2)$ is shown – without any interaction. Part (b) shows the Feynman diagrams belonging to the linear response function. The right diagram, that corresponds to the trace of $\boldsymbol{\mu}(t_1)\boldsymbol{\mu}(0)\rho_{t_0}$, is the conjugate complex of the left ($-\text{tr}(\rho_{t_0}\boldsymbol{\mu}(0)\boldsymbol{\mu}(t_1))$). This is why it is not shown explicitly in general.

$$\stackrel{(7.6)}{=} \left(-\frac{i}{\hbar}\right)^n \left(\text{tr}(\boldsymbol{\mu}(t_3 + t_2 + t_1)\boldsymbol{\mu}(0)\rho(t_0)\boldsymbol{\mu}(t_1)\boldsymbol{\mu}(t_2 + t_1)) + \text{c.c.} \right) \quad (7.7a)$$

$$+ \text{tr}(\boldsymbol{\mu}(t_3 + t_2 + t_1)\boldsymbol{\mu}(t_1)\rho(t_0)\boldsymbol{\mu}(0)\boldsymbol{\mu}(t_2 + t_1)) + \text{c.c.} \quad (7.7b)$$

$$+ \text{tr}(\boldsymbol{\mu}(t_3 + t_2 + t_1)\boldsymbol{\mu}(t_2 + t_1)\rho(t_0)\boldsymbol{\mu}(0)\boldsymbol{\mu}(t_1)) + \text{c.c.} \quad (7.7c)$$

$$+ \text{tr}(\boldsymbol{\mu}(t_3 + t_2 + t_1)\boldsymbol{\mu}(t_2 + t_1)\boldsymbol{\mu}(t_1)\boldsymbol{\mu}(0)\rho(t_0)) + \text{c.c.} \Big). \quad (7.7d)$$

Four of the eight terms are the complex conjugate of the other four.

Depending on the kind of spectroscopic method, only a selection of these terms of the commutators contribute to the signal. This section will show how to select these *Liouville pathways*¹⁸. It is possible to translate a double-sided Feynman diagram into an equation that describes the effect of a disturbance and vice versa. The translation is given in a short way also in this section.

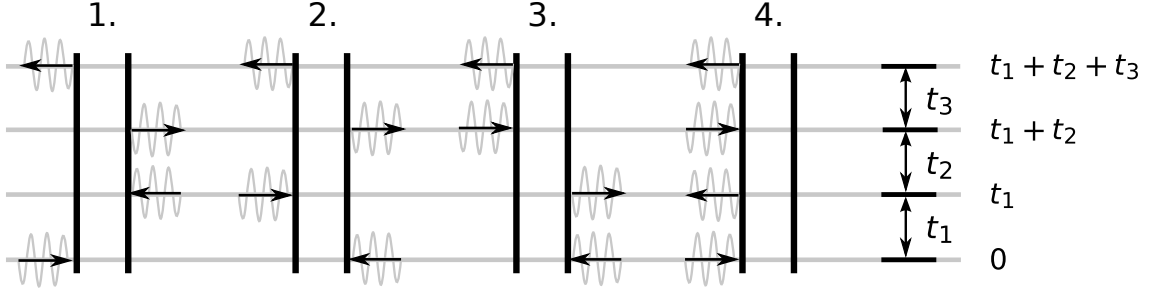
The double-sided Liouville diagrams facilitate the handling of the polarization of Eq. (7.4). The interactions of the terms from the commutator acts on different sides of the density matrix. For this purpose, each Feynman diagram consists of two vertical lines that represent the time evolution (bottom-up): the left one for the ket and the right one for the bra of the density matrix. In Fig. 7.2a a simple pathway for $U(t_1, t_2)$ is given. In all other diagrams shown in this work additional interactions are depicted.

The interactions with the light field are indicated by arrows on the ket or the bra of the density matrix. While the interactions at times that are evaluated inside the commutator generate a non-equilibrium density matrix $\rho^{(n)}$ and represent the perturbation of the density matrix, the last interaction at time $t_n + t_{n-1} + \dots + t_1$ emits a light field (it originates from Eq. (7.3): $\mathbf{P}^{(n)} = \text{tr}(\boldsymbol{\mu}\rho^{(n)}(t))$).

From Eq. (7.6) follows that the complex conjugate of one diagram is just the vertically mirrored one. Fig. 7.2b shows the two Feynman diagrams for the linear response function. For each interaction one arrow is depicted. There exist as much interactions as the order of the polarization in one diagram. One additional arrow (the last one) represents emission of light from the non-equilibrium density matrix by the dipole operator outside of the commutator. It is a convention that this last arrow for the observable on the top of the diagram is on the left side.

The negative term of each commutation describes an interaction from the right. This is the reason why the overall sign of a diagram can be determined by the number of interactions from the right to the density matrix. For n interactions, the sign is given by $(-1)^n$.

¹⁸The name "pathways" is because they represent a path integral in Liouville space.

**Figure 7.3:**

Double-sided Feynman diagrams for third-order experiments: The diagrams illustrate the time evolution of the interaction for different pathways of Eq. (7.7) according to rules that are described in Sec. 7.3. Each term can be connected to a certain diagram. The first pathway corresponds with part (7.7a), the second with part (7.7b), pathway 3 with (7.7c), and the last term ((7.7d)) can be illustrated with pathway four. The conjugate complex of each term is presented by a Feynman diagram that is mirrored at the vertical without the top arrow.

The four corresponding double-sided Feynman diagrams of to Eq. (7.7) are illustrated in Fig. 7.3. It can be seen that all factors on the left of Eq. (7.7) interact on the left vertical line while all factors on the right interact on the right time line. The direction of the arrows in this example necessarily results from the fact that arrows pointing to the time lines mean absorption, arrows pointing away from the time lines mean emission of light (as a consequence of the rotating wave approximation, see Sec. 7.3.1) [Ham05]. Since the electric field can be separated into positive and negative frequencies $\mathbf{E}(t) = \mathbf{E}_0(t) (e^{-i(\omega t - \mathbf{k} \cdot \mathbf{r})} + e^{i(\omega t - \mathbf{k} \cdot \mathbf{r})})$, this is also illustrated in the diagrams by the rule that arrows to the right represents an electric field with the factor $e^{-i(\omega t - \mathbf{k} \cdot \mathbf{r})}$ and arrows to the left contains the factor $e^{i(\omega t - \mathbf{k} \cdot \mathbf{r})}$. The last interaction has always to end in a population state [Muk95] (cf. Figs. 7.8, 7.9, and 7.10).

Besides the double-sided Feynman diagram, there exist also other diagrams for illustrating optical transitions in multi-level systems. The wave mixing energy level, that is also abbreviated WMEL, serves as an example [Lee85].

7.3.1 Rotating wave approximation

Calculating the third-order polarization, the four final pathways for a response function of Eq. (7.7) have to be multiplied with six terms of the electric field:

$$\mathbf{P}^{(3)}(t) = \int_0^\infty dt_3 \int_0^\infty dt_2 \int_0^\infty dt_1 \mathbf{E}(t - t_3) \mathbf{E}(t - t_3 - t_2) \mathbf{E}(t - t_3 - t_2 - t_1) R^{(n)}(t_3, t_2, t_1) \quad (7.8)$$

with

$$\mathbf{E}(t) = \mathbf{E}_1(t) e^{i\omega t} + \mathbf{E}_1^*(t) e^{-i\omega t} + \mathbf{E}_2(t) e^{i\omega t} + \mathbf{E}_2^*(t) e^{-i\omega t} + \mathbf{E}_3(t) e^{i\omega t} + \mathbf{E}_3^*(t) e^{-i\omega t}$$

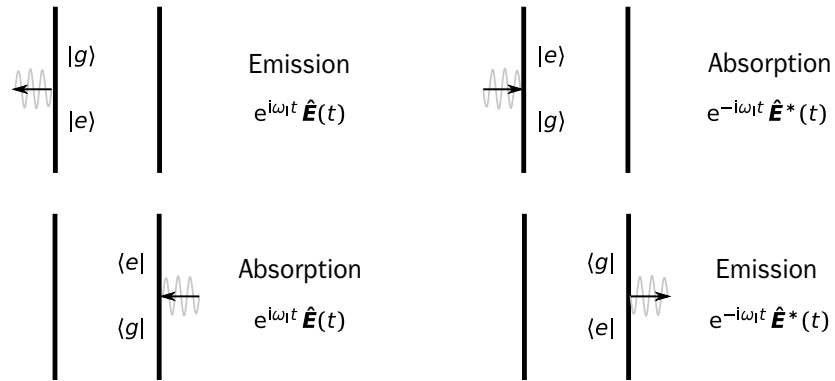
or for real amplitudes in the simpler form

$$\mathbf{E}(t) = \mathbf{E}_1(t) (e^{i\omega t} + e^{-i\omega t}) + \mathbf{E}_2(t) (e^{i\omega t} + e^{-i\omega t}) + \mathbf{E}_3(t) (e^{i\omega t} + e^{-i\omega t}).$$

Since the three electric fields $\mathbf{E}_1(t)$, $\mathbf{E}_2(t)$, and $\mathbf{E}_3(t)$ of the three time ordered pulses are shorter than the time separation between them, it is possible to connect each pulse with just one interaction $\boldsymbol{\mu}$. Thus, each $\mathbf{E}(t)$ in Eq. (7.8) has only two terms instead of six: $e^{-i\omega t}$ and $e^{i\omega t}$.

Figure 7.4:

Rotating wave approximation: Due to the neglect of fast rotations the number of diagrams are reduced (energy conservation). The interaction becomes directional and – depending on the side – represents an absorption or an emission.



For resonant excitations, often the *rotating wave approximation* (also known by the acronym RWA) is applied. This approximation reduces the number of term from two to one – only $e^{-i\omega t}$ or $e^{i\omega t}$ contributes to the electric field.

In a first step, the field is separated in the slowly varying envelope \hat{E} or \hat{E}^* and a fast oscillating factor $e^{\pm i\omega_L t}$ with the laser frequency ω_L :

$$\mathbf{E}(t) = \hat{\mathbf{E}}(t) e^{i\omega_L t} + \hat{\mathbf{E}}^*(t) e^{-i\omega_L t}. \quad (7.9)$$

With this, for example the exciton part of the field-matter Hamiltonian of Sec. 6.5.5, that describes the interaction, consists of four terms:

$$\begin{aligned} H_{e-1}(t) = & \sum_e \mu_{ge} \cdot \hat{\mathbf{E}}(t) e^{(i\omega_L - i\omega_{ge})t} |g\rangle \langle e| + \sum_e \mu_{ge} \cdot \hat{\mathbf{E}}^*(t) e^{(-i\omega_L - i\omega_{ge})t} |g\rangle \langle e| \\ & + \sum_e \mu_{eg} \cdot \hat{\mathbf{E}}^*(t) e^{(-i\omega_L + i\omega_{ge})t} |e\rangle \langle g| + \sum_e \mu_{eg} \cdot \hat{\mathbf{E}}(t) e^{(i\omega_L + i\omega_{ge})t} |e\rangle \langle g| \end{aligned}$$

with $\omega_{ij} = \omega_i - \omega_j$. The last row is the complex conjugate of the first row. The variables g , e , and f still represent the ground state, the excitons and the two-exciton states, respectively, of a three-model system introduced in Sec. 6.5. In each term, the first exponential function comes from the rotating part of the electric field and the last one from the rotating part of the states.

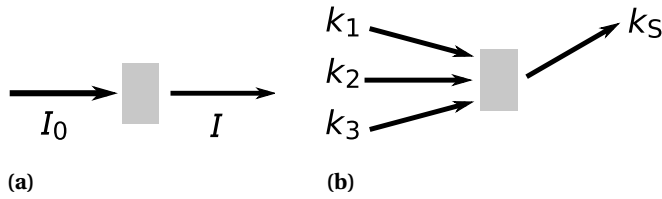
Since the excitation is resonant, it is $\omega_L \approx \omega_{ge}$. Applying the approximation means omitting the terms where both frequencies have the same sign since these terms have an exponential function that is fast oscillating because of the high value of the imaginary exponent while terms with opposite signs have exponential functions that vary slowly in time. When integrating these terms, the terms with a high oscillation can be neglected:

$$H_{e-1}(t) \xrightarrow{\text{RWA}} \sum_e \mu_{ge} \cdot \hat{\mathbf{E}}(t) e^{(i\omega_L - i\omega_{ge})t} |g\rangle \langle e| + \sum_e \mu_{eg} \cdot \hat{\mathbf{E}}^*(t) e^{(-i\omega_L + i\omega_{ge})t} |e\rangle \langle g|.$$

Consequently, each interaction between the system and the electric field happens with $e^{i\omega_L t}$ or with $e^{-i\omega_L t}$. Thus it is possible to give the interactions a direction.

With the rotating wave approximation, the conservation of energy is ensured. One can connect each interaction to an absorption or an emission. Fig. 7.3.1 shows all possibilities for a two-level system.

Mind, that this approximation disregard strong off-resonant processes such as second-harmonic generation or Raman spectroscopy or two photon absorption.

**Figure 7.5:**

Sketch of typical optical measurements [Muk95]: In part (a) is shown that in absorption spectroscopy an incident light beam is damped by the medium. Part (b) illustrates that in a four-wave mixing experiment three incident beams generate a coherent signal in a fourth direction.

7.4 Multiwave mixing

There exist several different spectroscopy experiments. In Fig. 7.5 a schematic representation of some typical optical measurements is given. While absorption spectroscopy is a typical and simple optical measurement method (Fig. 7.5a), the methods treated in this work are related to *multiwave mixing* experiments (e.g. four-wave mixing in Fig. 7.5b) [SM08]. That means that the interactions of n laser fields are involved with the material system.

Three wave mixing processes occur for $n = 2$. They are related to $\mathbf{P}^{(2)}$, like second-harmonic generation or sum/difference frequency generation. In media with inversion symmetry, such as isotropic samples, only terms of odd order contribute to the polarization in Eq. (7.1) since the polarization does not reverse for terms of even order [Wri11].

Thus, the third-order processes are the most interesting low order nonlinearities and play an important role for nonlinear phenomena studies in materials with inversion symmetry (isotropic material like gallium arsenide). The nonlinear processes that result from the $\chi^{(3)}E^{(3)}$ term (that means $n = 3$) involves three exciting fields and one output field. They are called *four-wave mixing* because three waves mix to create a fourth wave [BL07]. There are many spectroscopic methods related to $\mathbf{P}^{(3)}$, such as third-harmonic generation, pump-probe spectroscopy, photon echo or the double quantum coherence spectroscopy.

A typical current third-order nonlinear optical experiment uses a pulse sequence to excite optical excitations in a well-controlled way [SM01, CSFM92, MPP06]: A sequence of three time-ordered pulses created by pulse shaper travels along different directions with wave vectors \mathbf{k}_1 , \mathbf{k}_2 and \mathbf{k}_3 , that have variable time delays t_1 , t_2 , and t_3 . A sketch of a setup is shown in Fig. 7.5b and the pulse sequence is illustrated in Fig. 7.6 [KMS09].

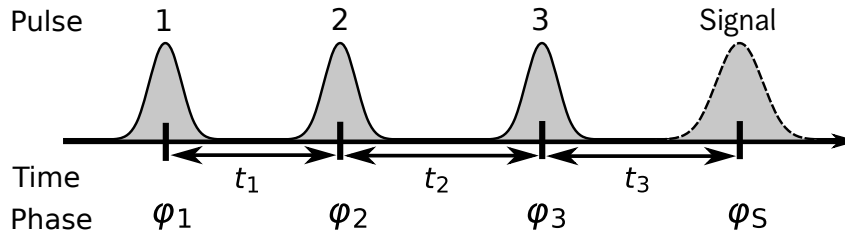
The first pulse takes the system in a particular coherence, that oscillates during the period t_1 until the oscillation is interrupted by the second and the third pulse. A new coherence is created [TKSW03]. After a delay of t_3 , the complete polarization \mathbf{P} is detected, that can be plotted after a Fourier transform with respect to two time delays as a two-dimensional spectrum (see Sec. 7.6.1).

There exist also higher order terms and higher wave mixing techniques, that are more important the higher the light intensity is.

7.5 Detection

Quantum pathways allow a detailed analysis of quantum dynamics in the material. In experiments, the pathways superpose and interfere with each other, so not many information can be gained. But there exist some techniques to separate contributions of the signal that belongs just to a few paths.

Directional selectivity and phase selectivity will be presented in this section. Spatial selectivity uses detectors in different directions of the experimental setup [ZCM99, TKS03, ML86]. In contrast, the phase cycling technique [ME00, KTW99, KT01] selects the polariza-


Figure 7.6:

Pulse sequence of a third-order coherent nonlinear experiment: The pulse direction is collinear and all pulses have well-defined phases.

tion signal by its phase dependence coadding experimental results that are obtained with different interpulse phases. Afterwards, the desired nonlinear polarization is selected.

Finally, it will be discussed why the heterodyne detection is chosen for our intention.

7.5.1 Phase matching

Adding wave vectors \mathbf{k}_i ($i = 1, \dots, n$) to the exponential function of the electric field, so that the field is

$$\mathbf{E}(t) = \sum_i^n \mathbf{E}_i(t) e^{i(\omega_i t - \mathbf{k}_i \cdot \mathbf{r})} + \sum_i^n \mathbf{E}_i^*(t) e^{-i(\omega_i t - \mathbf{k}_i \cdot \mathbf{r})}$$

the product $\mathbf{E}(t - t_n)\mathbf{E}(t - t_n - t_{n-1}) \cdots \mathbf{E}(t - t_n - t_{n-1} - \cdots - t_1)$ generates a signal S with the wave vector [Muk95, ZCM99]

$$\mathbf{k}_S = \pm \mathbf{k}_1 \pm \mathbf{k}_2 \pm \mathbf{k}_3 \dots \pm \mathbf{k}_n. \quad (7.10)$$

This signal is, for example, the emitted light that is illustrated by the last interaction in the double-sided Feynman diagrams. It has a wave vector and a frequency which is the sum of the input wave vectors and frequencies, respectively – considering the appropriate signs (cf. Fig. 7.5b).

At each position \mathbf{r} within the nonlinear medium, the oscillating n -th-order polarization radiates with angular frequency ω_n and has the corresponding wave vector \mathbf{k}_S . Due to the fact, that constructive interference will occur only if Eq. (7.10) is fulfilled, only at these positions \mathbf{r} there is a high intensity in the ω_n field. Eq. (7.10) is the *phase matching* condition. Since the signal is proportional to the exponential function, its argument – the phase – is connected to the contributions of the corresponding pathways. The simultaneous run in an experiment with different phases leads to the emission of the signal in different directions depending on the contributing quantum paths.

Which linear combination of \mathbf{k}_i is chosen, depends on the certain experiment: Examples for second-order processes are the second-harmonic generation with $\mathbf{k}_S = 2\mathbf{k}_1$ or the sum/difference frequency generation with $\mathbf{k}_d = \mathbf{k}_1 \pm \mathbf{k}_2$. The phase matching conditions for three-order processes will be discussed in the next sections. The signal of the photon echo, as an example, is found by measuring just one unique direction: $\mathbf{k}_S = -\mathbf{k}_1 + \mathbf{k}_2 + \mathbf{k}_3$.

7.5.2 Phase cycling

Phase matching offers the possibility of spatial separation of the desired signal from the undesired one. But this advantage must be paid with a complex experimental setup since many absorbers with a spatial distribution much higher than $1/\Delta k$ are needed, with Δk as the dif-

ference between the wave vectors of the electric field and the corresponding polarization [TKSW03].

This is why for the most of the presented simulations in this work, the signal cannot be measured in one specific direction \mathbf{k}_s since only one single nanostructure and not an ensemble of the same nanostructure is regarded. Here, a pulse shaper creates also a sequence of three time-ordered pulses that have also variable time delays t_1 , t_2 , and t_3 but they are collinear. In Fig. 7.6 the sequence is illustrated.

In contrast to phase matching techniques, the *phase cycling* method measures different phases to select pathways instead of detecting at different directions. This leads to the separation of Liouville pathways.

The electric field envelopes are composed of the field envelopes \mathbf{E}_1 , \mathbf{E}_2 , \mathbf{E}_3 of the three incoming pulses (with assumption of no overlap in time, see Sec. 7.3.1):

$$\begin{aligned} \mathbf{E}(\mathbf{r}, t) = & \mathbf{E}_1(\mathbf{r}, t - t_3 - t_2 - t_1) e^{i\omega_1(t-t_3-t_2-t_1)+i\varphi_1} + \text{c.c.} \\ & + \mathbf{E}_2(\mathbf{r}, t - t_3 - t_2) e^{i\omega_2(t-t_3-t_2)+i\varphi_2} + \text{c.c.} \\ & + \mathbf{E}_3(\mathbf{r}, t - t_3) e^{i\omega_3(t-t_3)+i\varphi_3} + \text{c.c.} \end{aligned} \quad (7.11)$$

with $\omega_1 = \omega_2 = \omega_3 = \omega_L$ the laser frequency.

A general adaption of Eq. (7.10) for a four-wave mixing experiment is written as

$$\varphi_S = l\varphi_1 + m\varphi_2 + n\varphi_3$$

with integers l , n , and m that are chosen according to the coherent third-order experiment.

The detected total polarization can be written as [ME00, KTW99]

$$\mathbf{P}(t, \varphi_1, \varphi_2, \varphi_3) = \mathcal{P}(t, \varphi_1, \varphi_2, \varphi_3) + \mathcal{P}^*(t, \varphi_1, \varphi_2, \varphi_3) = 2 \operatorname{Re}(\mathcal{P}(t, \varphi_1, \varphi_2, \varphi_3))$$

with

$$\mathcal{P}(t, \varphi_1, \varphi_2, \varphi_3) = \sum_{l,m,n} \mathbf{P}_{l,m,n}(t) e^{i(l\varphi_1 + m\varphi_2 + n\varphi_3)}.$$

The sum over the integers l , m , and n gives all possible phase combinations. For the double quantum coherence, for example, the only relevant combination is $l = 1$, $m = 1$, $n = -1$.

In general, the sum is restricted to a finite number of terms. Ref. [ME00] gives an example for reducing the terms within three steps. First, the symmetry properties of the given system can reduce the number of possible combinations of l , m , and n . Second, when using weak field strengths, only a small sum of the absolute values of the coefficients $|l| + |m| + |n|$ are sufficient. And third, since only resonant transitions between the electric states play a role, the result of $l + m + n$ can be restricted. Let q be the number of all relevant combinations in the following.

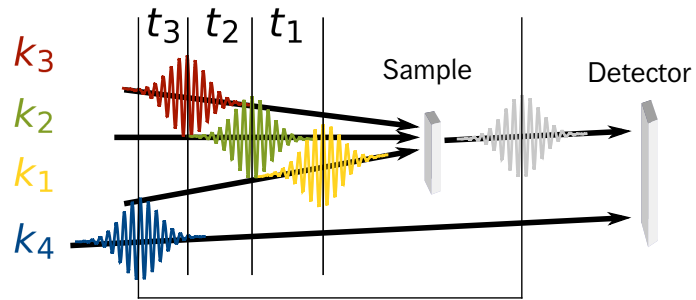
For extracting just one certain polarization $\mathbf{P}_{l,m,n}(t)$ from the total polarization, the experiment is repeated sufficiently often (q times [KT01, KTW99]) with varying phase combinations. The equations for each phase combination $\boldsymbol{\phi}_i = (\varphi_1, \varphi_2, \varphi_3)$ and each combination of phase prefactors $\mathbf{r}_i = (l, m, n)$ for $i = 1, \dots, q$ can be arranged in matrix form [KT01, ME00]:

$$\begin{pmatrix} e^{i\boldsymbol{\phi}_1 \cdot \mathbf{r}_1} & e^{i\boldsymbol{\phi}_1 \cdot \mathbf{r}_2} & \dots & e^{i\boldsymbol{\phi}_1 \cdot \mathbf{r}_q} \\ e^{i\boldsymbol{\phi}_2 \cdot \mathbf{r}_1} & e^{i\boldsymbol{\phi}_2 \cdot \mathbf{r}_2} & \dots & e^{i\boldsymbol{\phi}_2 \cdot \mathbf{r}_q} \\ \vdots & \vdots & \ddots & \vdots \\ e^{i\boldsymbol{\phi}_q \cdot \mathbf{r}_1} & e^{i\boldsymbol{\phi}_q \cdot \mathbf{r}_2} & \dots & e^{i\boldsymbol{\phi}_q \cdot \mathbf{r}_q} \end{pmatrix} \begin{pmatrix} \mathbf{P}_{\mathbf{r}_1}(t) \\ \mathbf{P}_{\mathbf{r}_2}(t) \\ \vdots \\ \mathbf{P}_{\mathbf{r}_q}(t) \end{pmatrix} = \begin{pmatrix} \mathcal{P}(t, \boldsymbol{\phi}_1) \\ \mathcal{P}(t, \boldsymbol{\phi}_2) \\ \vdots \\ \mathcal{P}(t, \boldsymbol{\phi}_q) \end{pmatrix}$$

The exponent carries the scalar product $\boldsymbol{\phi}_i \cdot \mathbf{r}_i = l\varphi_1 + m\varphi_2 + n\varphi_3$.

Figure 7.7:

Heterodyne detection: This figure illustrates a typical coherent third-order nonlinear experiment. Three incoming pulses in three different directions – separated by variable time delays – hit a sample and create a signal that is measured at the same time and in the same direction as a fourth signal, the local oscillator. With its help a phase sensitive detection becomes possible (see Sec. 7.5.3).



For the q unknown terms $\mathbf{P}_{r_i}(t) = \mathbf{P}_{l,m,n}(t)$ at least q different combinations of phases r_i are needed to make the matrix of the exponential functions invertible – that means that the determinant is non-zero. Consequently, it is possible by inverting the matrix to extract a specific polarization $\mathbf{P}_{l,m,n}(t)$ that belongs to the corresponding phase combination that describes the selected pathways of the nonlinear response function.

Typical examples for experiments using the phase cycling technique are the photon-echo ($\varphi_s = -\varphi_1 + \varphi_2 + \varphi_3$), the anti-photon-echo ($\varphi_s = \varphi_1 - \varphi_2 + \varphi_3$), or the double quantum coherence spectroscopy ($\varphi_s = \varphi_1 + \varphi_2 - \varphi_3$) [APV⁺09].

7.5.3 Homodyne and heterodyne detection

There exist different detection schemes for the signal. Most commonly, *homodyne* and *heterodyne detection* are used.

The former measures the signal by placing the detector in phase matching direction. The measured field intensity $I(t)$ is for homodyne detection

$$I_{\text{hom}}(t) \propto |\mathbf{E}_S(t)|^2. \quad (7.12)$$

For analyzing the measured signals in this work, the interest lies not only in the intensity but also in the real and the imaginary part of the signal field. For detecting also the phase of the signal field, the three incoming pulses are mixed with a fourth one, the *local oscillator* with a strong field \mathbf{E}_{LO} [Eic86]. In Fig. 7.7 the experimental setup is illustrated.

In contrast to Eq. (7.12), the measured intensity for the heterodyne detection is then [Muk95, BLMH99]

$$I_{\text{het}}(t) \propto |\mathbf{E}_S(t) + \mathbf{E}_{\text{LO}}(t)|^2 = |\mathbf{E}_S(t)|^2 + 2\text{Re}(\mathbf{E}_S(t)\mathbf{E}_{\text{LO}}^*(t)) + |\mathbf{E}_{\text{LO}}(t)|^2.$$

The first term is equivalent to the intensity of the signal that is very small compared to the oscillator amplitude ($E_S \ll E_{\text{LO}}$) and can consequently be neglected. The second term can be measured because its order is linear and not quadratic. Since the last term is equivalent to the known intensity of the local oscillator, it can be subtracted. Thus, the measurable intensity is just proportional to the term $2\text{Re}(\mathbf{E}_S(t)\mathbf{E}_{\text{LO}}^*(t))$. Repeating the measurement with varying phase of the local oscillator field reveals the electric field of the signal \mathbf{E}_S inclusive the phase [APV⁺09]. Thus, this technique is called a phase-sensitive detection. The spectral resolution depends on the precision of the control of the time delays and on the phase stability.

7.6 Third-order techniques

Ideal time-domain resonant four-wave mixing methods allow a classification by the wave vector of the signal [CSFM92]. "Ideal" means that all three pulses are well-separated.

As seen in Sec. 7.5.1, the possible four-wave mixing signals of the electric field given in Eq. (7.11) show up in all of the eight directions $\mathbf{k}_S = \pm \mathbf{k}_1 \pm \mathbf{k}_2 \pm \mathbf{k}_3$ of Eq. (7.10) where just some of them are dominant [Muk95]:

$$\begin{aligned}\mathbf{k}_I &= -\mathbf{k}_1 + \mathbf{k}_2 + \mathbf{k}_3, \\ \mathbf{k}_{II} &= +\mathbf{k}_1 - \mathbf{k}_2 + \mathbf{k}_3, \text{ and} \\ \mathbf{k}_{III} &= +\mathbf{k}_1 + \mathbf{k}_2 - \mathbf{k}_3.\end{aligned}$$

A negative \mathbf{k} direction is obtained by a complex conjugation ($\mathbf{P}^{(3)}(-\mathbf{k}, t) = (\mathbf{P}^{(3)}(\mathbf{k}, t))^*$) [Muk95]. In all following chapters, the underlying structure is a three-band system as introduced in Sec. 6.5.

The complete polarization for all directions of \mathbf{k}_S is given by [APV⁺09]

$$\mathbf{P}^{(3)}(t, \mathbf{r}) = \sum_{\mathbf{k}_S} \mathbf{P}_{\mathbf{k}_S}(t) e^{i\mathbf{k}_S \cdot \mathbf{r}}$$

Combining the third-order polarization of Eq. (7.8) with the electric field of Eq. (7.11) yield for $\mathbf{k}_S = \mathbf{k}_I, \mathbf{k}_{II},$ and \mathbf{k}_{III}

$$\begin{aligned}\mathbf{P}_{\mathbf{k}_I}(t) &= \left(\frac{i}{\hbar}\right)^3 e^{-i(-\omega_1 + \omega_2 + \omega_3)(t - \tau_3)} e^{-i(\omega_2 - \omega_1)(\tau_3 - \tau_2)} e^{i\omega_1(\tau_2 - \tau_1)} \\ &\cdot \int_0^\infty dt_3 \int_0^\infty dt_2 \int_0^\infty dt_1 R_{\mathbf{k}_I}^{(3)} e^{i(-\omega_1 + \omega_2 + \omega_3)t_3} e^{i(\omega_2 - \omega_1)t_2} e^{-i\omega_1 t_1} \\ &\cdot \mathbf{E}_3(t - t_3 - \tau_3) \mathbf{E}_2(t - t_3 - t_2 - \tau_2) \mathbf{E}_1^*(t - t_3 - t_2 - t_1 - \tau_1),\end{aligned}\quad (7.13a)$$

$$\begin{aligned}\mathbf{P}_{\mathbf{k}_{II}}(t) &= \left(\frac{i}{\hbar}\right)^3 e^{-i(\omega_1 - \omega_2 + \omega_3)(t - \tau_3)} e^{i(\omega_2 - \omega_1)(\tau_3 - \tau_2)} e^{-i\omega_1(\tau_2 - \tau_1)} \\ &\cdot \int_0^\infty dt_3 \int_0^\infty dt_2 \int_0^\infty dt_1 R_{\mathbf{k}_{II}}^{(3)} e^{i(\omega_1 - \omega_2 + \omega_3)t_3} e^{-i(\omega_2 - \omega_1)t_2} e^{i\omega_1 t_1} \\ &\cdot \mathbf{E}_3(t - t_3 - \tau_3) \mathbf{E}_2^*(t - t_3 - t_2 - \tau_2) \mathbf{E}_1(t - t_3 - t_2 - t_1 - \tau_1),\end{aligned}\quad (7.13b)$$

and

$$\begin{aligned}\mathbf{P}_{\mathbf{k}_{III}}(t) &= \left(\frac{i}{\hbar}\right)^3 e^{-i(\omega_1 + \omega_2 - \omega_3)(t - \tau_3)} e^{-i(\omega_2 + \omega_1)(\tau_3 - \tau_2)} e^{-i\omega_1(\tau_2 - \tau_1)} \\ &\cdot \int_0^\infty dt_3 \int_0^\infty dt_2 \int_0^\infty dt_1 R_{\mathbf{k}_{III}}^{(3)} e^{i(\omega_1 + \omega_2 - \omega_3)t_3} e^{i(\omega_2 + \omega_1)t_2} e^{i\omega_1 t_1} \\ &\cdot \mathbf{E}_3^*(t - t_3 - \tau_3) \mathbf{E}_2(t - t_3 - t_2 - \tau_2) \mathbf{E}_1(t - t_3 - t_2 - t_1 - \tau_1).\end{aligned}\quad (7.13c)$$

In Fig. 7.3 the corresponding double-sided Feynman diagrams to \mathbf{k}_I (1.), $-\mathbf{k}_I$ (2.), \mathbf{k}_{II} (3.), and $-\mathbf{k}_{II}$ (4.) are illustrated. Additionally, in Figs. 7.8, 7.9, and 7.10 the double-sided Feynman diagrams for the $\mathbf{k}_I, \mathbf{k}_{II},$ and \mathbf{k}_{III} signal are given, respectively.

In echo experiments, signals with a wave vector \mathbf{k}_I and \mathbf{k}_{II} are considered. This is discussed in more detail in Sec. 7.6.2. The double quantum coherence technique, which is connected to wave vectors in \mathbf{k}_{III} direction is shown in Sec. 7.6.3. The \mathbf{k}_{VI} signal, which is responsible for third-harmonic generation, is not considered in this work.

7.6.1 Two-dimensional spectra

The way of calculating a two-dimensional signal for coherent optical spectroscopy method depends on the detection mode. In Sec. 7.5 two detection modes are presented. As explained in that section, here, the heterodyne detected signal is calculated.

The heterodyne third-order signal is calculated via

$$S_{\mathbf{k}_s}^{(3)}(t_3, t_2, t_1) = \int_{-\infty}^{\infty} dt \mathbf{P}_{\mathbf{k}_s}(t) \mathbf{E}_{\text{LO}}^*(t - \tau_s) e^{i\omega_s(t - \tau_s)} \quad (7.14)$$

where $\mathbf{E}_{\text{LO}}^*(t - \tau_s)$ is the fourth field, the local oscillator, that is centered at time τ_s and that is detected at the same time and in the same direction as the polarization $\mathbf{P}_{\mathbf{k}_s}$.

For calculating the polarization induced by a resonant excitation, the response functions introduced in Sec. 7.2 is used. For this purpose, the response functions of the corresponding process (Eqs. (7.17), (7.18), or (7.6.3)) have to be inserted into Eq. (7.13). Mind, that temporally well-separated pulses are assumed [MOY07].

The signal $S^{(3)}(t_1, t_2, t_3)$ is a three-dimensional oscillating function. Due to its complexity, it is not easy to visualize. This is why multidimensional signals are commonly displayed in the frequency domain. Therefore, three Fourier transforms can be executed [SM08]:

$$S_{\mathbf{k}_s}^{(3)}(\Omega_1, \Omega_2, \Omega_3) = \int_0^{\infty} dt_1 \int_0^{\infty} dt_2 \int_0^{\infty} dt_3 e^{i\Omega_1 t_1 + i\Omega_2 t_2 + i\Omega_3 t_3} S_{\mathbf{k}_s}^{(3)}(t_1, t_2, t_3). \quad (7.15)$$

Commonly, just two of the three arguments of the signal are transformed. For the two-dimensional plots in the following, the Fourier transform is with respect to time interval t_1 and time interval t_2 at a fixed time T_3 to obtain a signal $S_{\mathbf{k}_s}^{(3)}(\Omega_1, \Omega_2, T_3)$ that can be plotted in two dimensions: The first axis shows the frequency Ω_1 and the other axis represents the frequency Ω_2 . In Fig. 8.1 a typical 2d spectrum is shown.

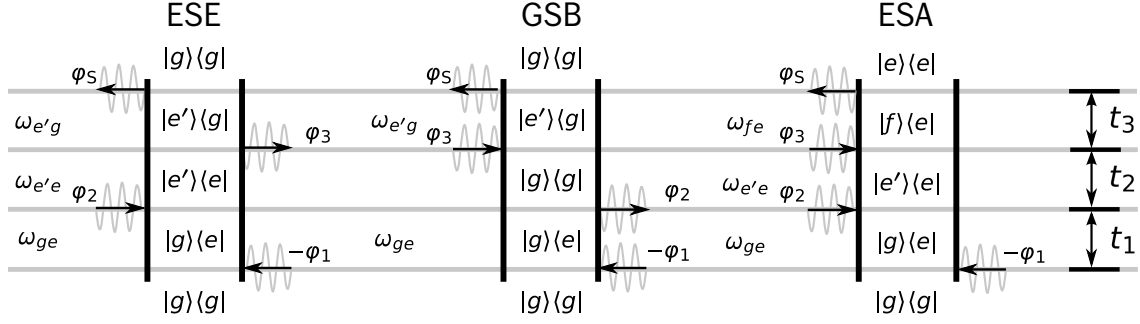
Two-dimensional spectra provide significant insights into the dynamics and interactions of complex molecular systems or semiconductors [LZBC06, GLE⁺02]. The spectra can reveal the homogeneous linewidth of a signal and its different dynamic contributions [GCF09, SCCG⁺09]. Another example is that it is possible to characterize and identify coherent excitation energy transfer dynamics in molecular aggregates such as photosynthetic systems and conjugated polymers [ZMCM97].

Cross-peaks support different kinds of information. They illustrate – for example in pump-probe experiments – that a system has a response at other frequencies than it is excited and they reveal correlations of states and sometimes they help to identify states in congested spectra. It is even possible to track excitation energy flow [GCF09]. Often, the sign and the amplitude of the cross-peaks can give information about intermolecular electronic coupling.

In the next subsections, the spectra of different two-dimensional coherent experiments are explained. The spectra for the double quantum coherence technique are discussed in detail in the following chapter.

7.6.2 Photon echo and inverse photon echo

The first class of third-order experiments consists of photon echo techniques [ELG09, YF99b]. Photon echo was one of the first examples of an optical analogue of the nuclear magnetic resonance. Experiments that consider wave vectors in $\mathbf{k}_I = -\mathbf{k}_1 + \mathbf{k}_2 + \mathbf{k}_3$ direction [TKSW03] are called two-dimensional *photon echo spectroscopy* [MCM97]. The contributing terms are (7.7b) and (7.7c). The experiments which consider wave vectors in $\mathbf{k}_{II} = \mathbf{k}_1 - \mathbf{k}_2 + \mathbf{k}_3$ direction are *inverse photon echo spectroscopy* [YM08a]. Here, the other two terms, (7.7a) and (7.7d) are contributing.

**Figure 7.8:**

Double-sided Feynman diagrams for photon echo spectroscopy generated in \mathbf{k}_1 direction in the coherent limit: The three possible pathways are named ESE (excited state emission), GSB (ground state bleaching), and ESA (excited state absorption). The pulses are denoted with phases φ instead of directions \mathbf{k} since the phase cycling technique is used to extract selected pathways (see Sec. 7.5.2).

Fig. 7.8 shows the double-sided Feynman diagrams for the \mathbf{k}_1 signal. Between the first interactions at time interval t_1 , the aggregate density matrix is in an optical coherence with a characteristic frequency ω_{ge} . This frequency is given by the energy difference between states e and g . Afterwards, the density matrix is in the ground state or in the single excited state manifold with the frequency $\omega_{e'e}$ [APV⁺09]. Finally, at t_3 , it oscillates with $\omega_{e'g}$ or ω_{fe} .

The various contributions to the signal are denoted by ESE, GSB, and ESA. The nomenclature is chosen according to the physical processes during the interactions. The left diagram in Fig. 7.8 shows that the system is excited by the first and second pulse – the pump pulses – and stimulated back by the third pulse (light emission) – the probe pulse. It represents stimulated emission and is thus called *excited-state stimulated emission* (ESE). The pathway called GSB describes a *ground state bleaching*: the density matrix returns to the ground-state at t_2 so that the following interaction reduces the population of this state. Instead of an emission, the second interaction in the last diagram is followed from an absorption of the next interaction. The process is called *excited state absorption* (ESA).

Often, $\mathbf{k}_2 = \mathbf{k}_3$ is chosen, so that $\mathbf{k}_1 = -\mathbf{k}_1 + 2\mathbf{k}_2$. This two-pulse photon echo spectroscopy is a special case of the stimulated three-pulse version.

The name of this experiment – photon echo – is given because of the analogy to the spin echo that appears in magnetic resonance. There, the spin vector flips by the first pulse. Each individual spin oscillates with a slightly different frequency. Thus, the signal is inhomogeneously broadened in the frequency domain. All spin vectors will spread out after some time and consequently, the macroscopic polarization disappears. The second pulse then flips all vectors to the other side of the Bloch sphere. Therefore, all spin vectors recombine – they rephase. So, after the same time as separation between both pulses, the vectors are perfectly recombined and send an echo signal. In the photon echo process, the first pulse excites the system in a coherence that is oscillating in $e^{i\omega t}$ direction. The third pulse flips this direction into a rotation in $e^{-i\omega t}$ direction. Hence, analogously to the spin vectors, a photon echo signal will occur.

Signal

For calculating the response function $R_{\mathbf{k}_1}^{(3)}$, the time evolution operator $U(t, t_0)$ of Ch. 6 has to be considered. The operator of Eq. (6.12) $U(t, t_0) = e^{-iH(t-t_0)/\hbar}$ is replaced by a Green's function that depends only on the time interval t and uses the Heaviside step function to

7 Multidimensional Coherent Nonlinear Spectroscopy

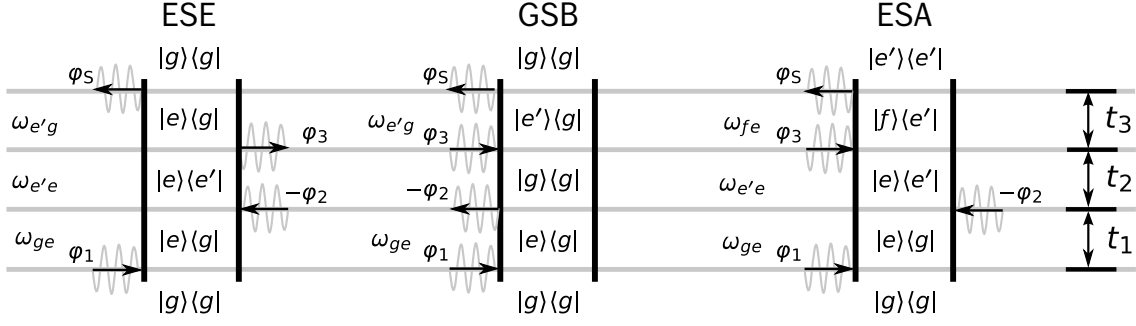


Figure 7.9:

Double-sided Feynman diagrams for the inverse photon echo spectroscopy generated in k_{\parallel} direction in the coherent limit: The three possible pathways are named in the same way as Fig. 7.8. Also here, the pulses are denoted with phases φ instead of directions k since the phase cycling technique is used to extract selected pathways (see Sec. 7.5.2).

ensure causality – what means that the response can only depend on the fields at earlier times [HM08, MHM08]:

$$G_{ij}(t) = e^{-i\omega_{ij}t - \gamma_{ij}t} \Theta(t)$$

where ω_{ij} describes the interband frequency $(\epsilon_i - \epsilon_j) / \hbar$ and γ_{ij} is a phenomenological dephasing rate for the ij coherence without relaxation. The Fourier transform of the Green's function reads

$$G_{ij}(\Omega) = \int_0^{\infty} dt e^{i\Omega t} e^{-i\omega_{ij}t - \gamma_{ij}t}. \quad (7.16)$$

After the first interaction, the left diagram of Fig. 7.8 describes a density matrix in the state ρ_{ge} so that its evolution gives the factor $e^{-i\omega_{ge}t_1}$ while the second interaction gives an $e^{-i\omega_{e'e}t_2}$ and the last one a factor $e^{-i\omega_{e'g}t_3}$. With the short form $\xi_{ij} = \omega_{ij} - i\gamma_{ij}$ the three response functions of Fig. 7.10 read

$$\begin{aligned} R_{k_{\parallel}}^{\text{ESE}}(t_3, t_2, t_1) &= \left(\frac{i}{\hbar}\right)^3 \Theta(t_1)\Theta(t_2)\Theta(t_3) \sum_{e,e'} \mu_{ge'} \mu_{eg} \mu_{e'g} \mu_{ge} e^{-i\xi_{ge}t_1 - i\xi_{e'e}t_2 - i\xi_{e'g}t_3} \\ R_{k_{\parallel}}^{\text{GSB}}(t_3, t_2, t_1) &= \left(\frac{i}{\hbar}\right)^3 \Theta(t_1)\Theta(t_2)\Theta(t_3) \sum_{e,e'} \mu_{ge'} \mu_{e'g} \mu_{eg} \mu_{ge} e^{-i\xi_{ge}t_1 - \eta t_2 - i\xi_{e'g}t_3} \\ R_{k_{\parallel}}^{\text{ESA}}(t_3, t_2, t_1) &= \left(\frac{i}{\hbar}\right)^3 \Theta(t_1)\Theta(t_2)\Theta(t_3) \sum_{e,e'} \mu_{ef} \mu_{fe} \mu_{ge'} \mu_{ge} e^{-i\xi_{ge}t_1 - i\xi_{e'e}t_2 - i\xi_{fe}t_3}. \end{aligned} \quad (7.17)$$

The corresponding response functions to Fig. 7.9 read

$$\begin{aligned} R_{k_{\parallel}}^{\text{ESE}}(t_3, t_2, t_1) &= \left(\frac{i}{\hbar}\right)^3 \Theta(t_1)\Theta(t_2)\Theta(t_3) \sum_{e,e'} \mu_{ge} \mu_{e'g} \mu_{ge'} \mu_{eg} e^{-i\xi_{eg}t_1 - i\xi_{ee'}t_2 - i\xi_{eg}t_3} \\ R_{k_{\parallel}}^{\text{GSB}}(t_3, t_2, t_1) &= \left(\frac{i}{\hbar}\right)^3 \Theta(t_1)\Theta(t_2)\Theta(t_3) \sum_{e,e'} \mu_{ge'} \mu_{e'g} \mu_{ge} \mu_{eg} e^{-i\xi_{eg}t_1 - \eta t_2 - i\xi_{e'g}t_3} \\ R_{k_{\parallel}}^{\text{ESA}}(t_3, t_2, t_1) &= \left(\frac{i}{\hbar}\right)^3 \Theta(t_1)\Theta(t_2)\Theta(t_3) \sum_{e,e'} \mu_{e'f} \mu_{fe} \mu_{ge'} \mu_{eg} e^{-i\xi_{eg}t_1 - i\xi_{ee'}t_2 - i\xi_{fe}t_3}. \end{aligned} \quad (7.18)$$

For the ground state energy the variable η is introduced that converges to zero from positive direction.

For heterodyne detection the signal can be calculated via Eq. (7.14). It uses the response functions from Eqs. (7.17) and (7.18) and their Fourier transform via Eq. (7.15) where also Eq. (7.16) for the Green function is used. After integrating and considering that the pulses are all temporally well-separated, the resulting signal for \mathbf{k}_I is [APV⁺09, YM08b]

$$S_{\mathbf{k}_I}^{(3)}(\Omega_1, \Omega_2, \Omega_3) = S_{\mathbf{k}_I}^{\text{ESE}}(\Omega_1, \Omega_2, \Omega_3) + S_{\mathbf{k}_I}^{\text{GSB}}(\Omega_1, \Omega_2, \Omega_3) + S_{\mathbf{k}_I}^{\text{ESA}}(\Omega_1, \Omega_2, \Omega_3)$$

with

$$\begin{aligned} S_{\mathbf{k}_I}^{\text{ESE}}(\Omega_1, \Omega_2, \Omega_3) &= -\frac{1}{\hbar^3} \sum_{e e'} \frac{1}{(\Omega_3 - \xi_{e'g})(\Omega_2 - \xi_{e'e})(\Omega_1 - \xi_{ge})} \\ &\quad \cdot \boldsymbol{\mu}_{e'g}^* \cdot \mathbf{E}_4^*(\omega_{e'g}) \boldsymbol{\mu}_{eg} \cdot \mathbf{E}_3(\omega_{eg}) \boldsymbol{\mu}_{e'g} \cdot \mathbf{E}_2(\omega_{e'g}) \boldsymbol{\mu}_{eg}^* \cdot \mathbf{E}_1^*(\omega_{eg}) \\ S_{\mathbf{k}_I}^{\text{GSB}}(\Omega_1, \Omega_2, \Omega_3) &= -\frac{1}{\hbar^3} \sum_{e e'} \frac{1}{(\Omega_3 - \xi_{e'g})(\Omega_2 - i\eta)(\Omega_1 - \xi_{ge})} \\ &\quad \cdot \boldsymbol{\mu}_{e'g}^* \cdot \mathbf{E}_4^*(\omega_{e'g}) \boldsymbol{\mu}_{e'g} \cdot \mathbf{E}_3(\omega_{e'g}) \boldsymbol{\mu}_{eg} \cdot \mathbf{E}_2(\omega_{eg}) \boldsymbol{\mu}_{eg}^* \cdot \mathbf{E}_1^*(\omega_{eg}) \\ S_{\mathbf{k}_I}^{\text{ESA}}(\Omega_1, \Omega_2, \Omega_3) &= \frac{1}{\hbar^3} \sum_{e e' f} \frac{1}{(\Omega_3 - \xi_{fe})(\Omega_2 - \xi_{e'e})(\Omega_1 - \xi_{ge})} \\ &\quad \cdot \boldsymbol{\mu}_{fe}^* \cdot \mathbf{E}_4^*(\omega_{fe}) \boldsymbol{\mu}_{fe} \cdot \mathbf{E}_3(\omega_{fe}) \boldsymbol{\mu}_{e'g} \cdot \mathbf{E}_2(\omega_{e'g}) \boldsymbol{\mu}_{eg}^* \cdot \mathbf{E}_1^*(\omega_{eg}) \end{aligned}$$

and for \mathbf{k}_{II}

$$S_{\mathbf{k}_{II}}^{(3)}(\Omega_1, \Omega_2, \Omega_3) = S_{\mathbf{k}_{II}}^{\text{ESE}}(\Omega_1, \Omega_2, \Omega_3) + S_{\mathbf{k}_{II}}^{\text{GSB}}(\Omega_1, \Omega_2, \Omega_3) + S_{\mathbf{k}_{II}}^{\text{ESA}}(\Omega_1, \Omega_2, \Omega_3)$$

with

$$\begin{aligned} S_{\mathbf{k}_{II}}^{\text{ESE}}(\Omega_1, \Omega_2, \Omega_3) &= -\frac{1}{\hbar^3} \sum_{e e'} \frac{1}{(\Omega_3 - \xi_{eg})(\Omega_2 - \xi_{ee'})(\Omega_1 - \xi_{eg})} \\ &\quad \cdot \boldsymbol{\mu}_{eg}^* \cdot \mathbf{E}_4^*(\omega_{eg}) \boldsymbol{\mu}_{e'g} \cdot \mathbf{E}_3(\omega_{e'g}) \boldsymbol{\mu}_{e'g}^* \cdot \mathbf{E}_2^*(\omega_{e'g}) \boldsymbol{\mu}_{eg} \cdot \mathbf{E}_1(\omega_{eg}) \\ S_{\mathbf{k}_{II}}^{\text{GSB}}(\Omega_1, \Omega_2, \Omega_3) &= -\frac{1}{\hbar^3} \sum_{e e'} \frac{1}{(\Omega_3 - \xi_{e'g})(\Omega_2 - i\eta)(\Omega_1 - \xi_{eg})} \\ &\quad \cdot \boldsymbol{\mu}_{e'g}^* \cdot \mathbf{E}_4^*(\omega_{e'g}) \boldsymbol{\mu}_{e'g} \cdot \mathbf{E}_3(\omega_{e'g}) \boldsymbol{\mu}_{eg}^* \cdot \mathbf{E}_2^*(\omega_{eg}) \boldsymbol{\mu}_{eg} \cdot \mathbf{E}_1(\omega_{eg}) \\ S_{\mathbf{k}_{II}}^{\text{ESA}}(\Omega_1, \Omega_2, \Omega_3) &= \frac{1}{\hbar^3} \sum_{e e' f} \frac{1}{(\Omega_3 - \xi_{fe})(\Omega_2 - \xi_{ee'})(\Omega_1 - \xi_{eg})} \\ &\quad \cdot \boldsymbol{\mu}_{fe}^* \cdot \mathbf{E}_4^*(\omega_{fe}) \boldsymbol{\mu}_{fe} \cdot \mathbf{E}_3(\omega_{fe}) \boldsymbol{\mu}_{e'g} \cdot \mathbf{E}_2^*(\omega_{e'g}) \boldsymbol{\mu}_{eg} \cdot \mathbf{E}_1(\omega_{eg}) \end{aligned}$$

where e and e' describe the single-exciton states and f the two-exciton states. The frequencies are detuned around the single and double gap frequency, respectively. The resonances will occur at both positive and negative frequency Ω . The field \mathbf{E}_4 is the electric field of the local oscillator due to heterodyne detection. The fraction with the frequency differences in the denominator comes from the Fourier transform and corresponds to the argument of the exponential function.

Spectra

In 2d spectra assuming a Lorentzian dephasing model, the resonances appear as Lorentzians with a homogeneous linewidth. The dephasing rate γ_{ij} for the coherences between the states i and j determine the width of the Lorentzian [BLS⁺02, BLMZ06]. In experiments, several processes reshape this theoretical form of a perfect Lorentzian.

7 Multidimensional Coherent Nonlinear Spectroscopy

For a Fourier transform with respect to t_1 and t_3 , there is just one peak at $-\Omega_1 = \Omega_3 = \omega_{eg}$ in a two-level system for the excited state emission pathway. For a number of two-level systems with the same states (but fluctuating transition energies), an inhomogeneous broadening along the diagonal ($-\Omega_1 = \Omega_3$) is found due to the slightly different transition frequencies of each system. This oval peak can be seen as the superposition of the contributions of each two-level system.

For systems with several states, the resonance peaks are found on the diagonal for $-\Omega_1 = \Omega_3$. Only in case of relaxation or coupling, there are additional peaks in the off-diagonal part of the spectrum. This shows that the states are not completely independent, for example, they have the same ground state (as can be seen in the Feynman diagrams). The form of the off-diagonal peaks – more precisely the direction of inhomogeneous broadening – depends on the statistical properties of the distribution.

Up to now, just one pathway is discussed. Consequently, no interference effects can appear so far. For the ground state bleaching part of the signal, an analogous discussion is possible.

For the excited state absorption, the peaks are not found on the diagonal $-\Omega_1 = \Omega_3$, they are displaced along the vertical for a distance that corresponds to the biexcitonic shift. Without that shift, the spectrum could be interpreted analogous to the excited state emission spectrum. In that case, this path would extinguish one of the other pathway contributions. Two-dimensional photon echo spectroscopy allows not only to read the ground to the single-exciton transition energy but also the single to two-exciton transition energy.

In every case, all three pathways are interfering constructively and destructively and the resulting spectrum is seen in two-dimensional photon echo spectroscopy experiments.

The spectrum for the inverse photon echo spectroscopy can be discussed in the same way as for the photon echo. The only difference is, that the first coherence and the last coherence are no longer the opposite since the first coherence is now ω_{eg} instead of ω_{ge} . Therefore, some inhomogeneous broadening processes cannot be canceled out here.

By measuring the echo intensity as a function of delay time, it is possible to obtain the population changes of the ground and excited state population and thus the dephasing rate γ_{ji} of the ij coherence.

7.6.3 Double quantum coherence

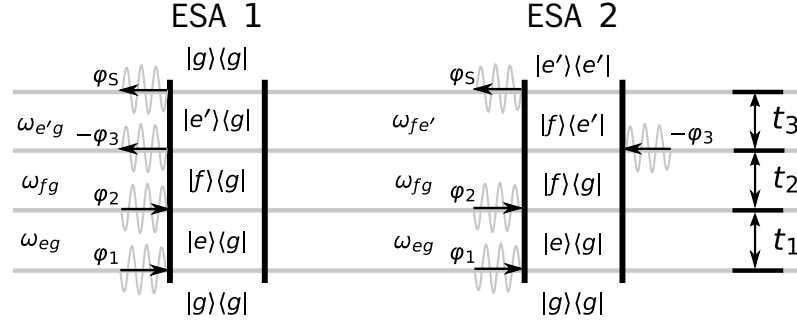
The *double quantum coherence spectroscopy* is a two-dimensional coherent measuring technique that maps electronic states and enables thus insights into the electronic structure of excited states [KMS09]. Deeper knowledge about how electron correlations change upon photoexcitation can be gained.

The double quantum coherence spectroscopy [RM10b] considers the wave vectors in the direction of $\mathbf{k}_{\text{III}} = \mathbf{k}_1 + \mathbf{k}_2 - \mathbf{k}_3$. The response function is derived in the same way as Eqs. (7.17) and (7.18) and reads

$$R_{\mathbf{k}_{\text{III}}}^{\text{ESA } 1}(t_3, t_2, t_1) = \left(\frac{i}{\hbar}\right)^3 \Theta(t_1)\Theta(t_2)\Theta(t_3) \sum_{e,e'} \boldsymbol{\mu}_{e'f} \boldsymbol{\mu}_{ge'} \boldsymbol{\mu}_{fe} \boldsymbol{\mu}_{eg} e^{-i\xi_{eg} t_1 - i\xi_{fg} t_2 - i\xi_{f'e'} t_3}$$

$$R_{\mathbf{k}_{\text{III}}}^{\text{ESA } 2}(t_3, t_2, t_1) = \left(\frac{i}{\hbar}\right)^3 \Theta(t_1)\Theta(t_2)\Theta(t_3) \sum_{e,e'} \boldsymbol{\mu}_{ge'} \boldsymbol{\mu}_{e'f} \boldsymbol{\mu}_{fe} \boldsymbol{\mu}_{eg} e^{-i\xi_{eg} t_1 - i\xi_{fg} t_2 - i\xi_{e'g} t_3}.$$

The double-sided Feynman diagrams [TKSW03, YM08c] in Fig. 7.10 shows the two possible pathways of excitation. The first pulse of the sequence creates a single-exciton (single quantum coherence), the second creates a double exciton state (double quantum coherence) and the third one again a single-exciton state.

**Figure 7.10:**

Double-sided Feynman diagrams for double quantum coherence spectroscopy generated in \mathbf{k}_{III} direction in the coherent limit: In contrast to photon echo experiments, here two possible excited state absorption (ESA) pathways exist. Again, the pulses are denoted with phases φ instead of directions \mathbf{k} since the phase cycling technique is used to extract selected pathways (see Sec. 7.5.2).

The standard double quantum coherence spectroscopy signal then yields [APV⁺09]

$$S_{\mathbf{k}_{\text{III}}}^{(3)}(\Omega_1, \Omega_2, \Omega_3) = S_{\mathbf{k}_{\text{III}}}^{\text{ESA } 1}(\Omega_1, \Omega_2, \Omega_3) + S_{\mathbf{k}_{\text{III}}}^{\text{ESA } 2}(\Omega_1, \Omega_2, \Omega_3) \quad (7.19)$$

with

$$S_{\mathbf{k}_{\text{III}}}^{\text{ESA } 1}(\Omega_1, \Omega_2, \Omega_3) = \frac{1}{\hbar^3} \sum_{ee'f} \frac{1}{(\Omega_3 - \xi_{fe'}) (\Omega_2 - \xi_{fg}) (\Omega_1 - \xi_{eg})} \\ \cdot \boldsymbol{\mu}_{fe'}^* \cdot \mathbf{E}_4^*(\omega_{fe'}) \boldsymbol{\mu}_{e'g}^* \cdot \mathbf{E}_3^*(\omega_{e'g}) \boldsymbol{\mu}_{fe} \cdot \mathbf{E}_2(\omega_{fe}) \boldsymbol{\mu}_{eg} \cdot \mathbf{E}_1(\omega_{eg}) \\ S_{\mathbf{k}_{\text{III}}}^{\text{ESA } 2}(\Omega_1, \Omega_2, \Omega_3) = -\frac{1}{\hbar^3} \sum_{ee'f} \frac{1}{(\Omega_3 - \xi_{e'g}) (\Omega_2 - \xi_{fg}) (\Omega_1 - \xi_{eg})} \\ \cdot \boldsymbol{\mu}_{e'g}^* \cdot \mathbf{E}_4^*(\omega_{e'g}) \boldsymbol{\mu}_{fe'}^* \cdot \mathbf{E}_3^*(\omega_{fe'}) \boldsymbol{\mu}_{fe} \cdot \mathbf{E}_2(\omega_{fe}) \boldsymbol{\mu}_{eg} \cdot \mathbf{E}_1(\omega_{eg})$$

with the Fourier transform of the electric field envelopes $\mathbf{E}_i(\omega)$ for the pulses $i = 1, 2, 3, 4$ (the fourth pulse comes from the heterodyne detection), the dipole matrix element $\boldsymbol{\mu}_{ij}$ for the transitions from exciton state j to i , the frequencies $\omega_{ij} = \omega_i - \omega_j$, the exciton frequency ω_i , and $\xi_{ij} = \omega_{ij} + i\gamma_{ij}$ with the dephasing γ_{ij} . Again, the frequencies are detuned around the single and double gap frequency, respectively.

The double quantum coherence signal does not exist for two-level systems. The reason is, that the second pulse in positive direction can only interact on the left since due to the RWA on the right side there cannot be an emission. The third pulse is the first of the pulses that is able to interact as emission (ESA 2) or as absorption on the right (ESA 1).

The pathways of the double quantum coherence spectroscopy are characterized by the fact that there are no density states but only coherences. A further interesting point is, that for uncoupled two-level systems, both pathways will interfere destructively because of the reverse sign of the signal that comes from the different numbers of intersection on the right side of a Feynman diagram.

A further special feature of the double quantum coherence is, that it is possible to create a coherence $|f\rangle\langle g|$, although there exists no dipole moment! Two-dimensional spectroscopy allows only create new coherences by controlling through suitable selection of pathways. It is even possible to measure energies of dark states if it is possible to select the certain integrals.

The double quantum coherence spectra are interpreted and discussed in detail in the next chapter.

Part IV

Localized Spectroscopy

8 Localized Spectroscopy

Many different kinds of nanostructures are not completely understood. Especially coupled clusters of small molecules like molecular aggregates are often very complex so that decoding their structure is a challenge [GCF09, AVM08]. The complex molecular systems have interesting properties. For example, they can channel excitation energy over remarkable distances, that is the case in photosynthetic light harvesting processes.

As shown in the last chapter, coherent two-dimensional optical spectroscopy methods are a nonlinear technique that provide significant insight into the dynamics and interactions of such coupled systems like photosynthetic light-harvesting complexes and other aggregates. A special attribute of these techniques is resolving excitation and emission energies over significant bandwidths spectrally, within a femtosecond resolution.

One of the main results of this work is presented in this chapter. Three key topics will be combined to reveal new information of couplings of electronic states and their wave functions: After introducing how optical excitations can be confined within a nanometer length scale in Ch. 5 and presenting the double quantum coherence as a multidimensional coherent spectroscopy in Ch. 7, these two different topics will be combined to do a recent kind of spectroscopy, the *localized spectroscopy*. Three coupled two-level quantum dots that form delocalized states serve as a sample for the double quantum coherence spectroscopy. Such a coupling is presented in Ch. 6.

In the first section generating two-dimensional spectra with localized pulses is shown and the newly gained insights are pointed out. Afterwards, applications of these methods are exhibited, such as reconstruction of the wave function or filtering different resonances.

All presented formulas for localized spectra or for the derivation of a reconstructing protocol assume a perfect localization. The signals can be calculated for both, a perfect localization and for a more realistic one that is found using the genetic algorithm in Ch. 5. In the end, the gained protocol is also used for reconstructing wave functions with spectra that correspond to a theoretical possible degree of localization.

The presented protocols for reconstructing many-particle wave functions will be applicable for exciton states and biexciton states of coupled nanostructures. The protocols and the results of this chapter are published in [RSS⁺12]¹⁹ and [SKMR12]²⁰.

8.1 Localized spectra

In Ch. 7 two-dimensional spectroscopy is introduced. It is explained how a two-dimensional spectrum is generated and interpreted. Here, the generation of those spectra will be modified to reveal more information than is possible in common two-dimensional spectroscopy.

In this chapter, the double quantum coherence spectroscopy, that is presented in Sec. 7.6.3, is chosen for demonstrating the localized spectroscopy. It is called "localized spectroscopy" since pulses that can localize optical excitations within one quantum dot are the key difference to the common techniques. So the possibilities of controlling light in subwavelength precision described in Ch. 5 serves as an ingredient for localized spectroscopy.

¹⁹Copyright (2012) by the American Physical Society.

²⁰Copyright (2012) by the Institute of Physics.

8 Localized Spectroscopy

Three coupled two-level quantum dots serve as a sample for presenting the method. The Hamiltonian that describes their electronic states and their couplings is given in Sec. 6.5.5. The parts of the full Hamiltonian $H = H_0 + H_C + H_{e-1}$ reads in local basis

$$\begin{aligned} H_0 &= \epsilon_0 |g\rangle\langle g| + \sum_i \epsilon_i |i\rangle\langle i| + \sum_{i,j \neq i} (\epsilon_i + \epsilon_j) |ij\rangle\langle ij| \\ H_C &= \sum_{i>j} V_{ij} |ij\rangle\langle j| + \sum_{i,j \neq i} V_{ij}^F |i\rangle\langle j| + \sum_{k,i \neq k, j \neq k} V_{ij}^F |ki\rangle\langle kj| \\ H_{e-1} &= \sum_i^n \boldsymbol{\mu}_{gi} \cdot \mathbf{E}(t) |g\rangle\langle i| + \sum_{i,j \neq i}^n \boldsymbol{\mu}_{ij} \cdot \mathbf{E}(t) |i\rangle\langle ij| + \text{h.c.} \end{aligned}$$

and becomes in delocalized basis to

$$\begin{aligned} H_0 + H_C &= \epsilon_g |g\rangle\langle g| + \sum_e \epsilon_e |e\rangle\langle e| + \sum_f \epsilon_f |f\rangle\langle f| \\ H_{e-1} &= \sum_e \boldsymbol{\mu}_{ge} \cdot \mathbf{E}(t) |g\rangle\langle e| + \sum_{ef} \boldsymbol{\mu}_{ef} \cdot \mathbf{E}(t) |e\rangle\langle f| + \text{h.c.} \end{aligned}$$

A detailed derivation is given in Sec. 6.5.

The basic idea is modifying the pulse sequence of the double quantum coherence spectroscopy by replacing one or two pulses of the sequence with polarization shaped pulses that excite just one single quantum dot [RM10a]. All other pulses still excite all dots equally. The pulse sequence is illustrated in Fig. 7.6 and the Liouville pathways to show the kind of excitation are presented in Fig. 7.10. The next sections differ in which pulses of the sequence are localized.

8.1.1 Localization of pulse 1

Before presenting the calculated spectra, in each case a description of the signal in a theoretical way is given.

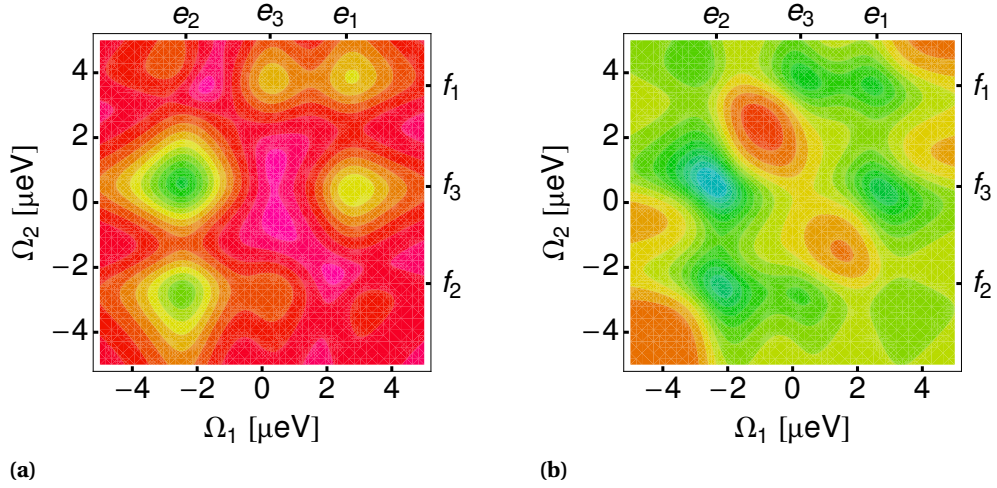
Signal

The double quantum coherence spectroscopy signal (Eq. (7.19)), that can be interpreted as the sum over the Liouville pathways, is deduced in Sec. 7.6.3. A Fourier transform only with respect to time intervals t_1 and t_2 yields²¹

$$\begin{aligned} S_{k_{\text{III}}}(\Omega_1, \Omega_2, t_3) &= \frac{1}{\hbar^3} \sum_{e,e',f} \frac{1}{(\Omega_2 - \xi_{fg})(\Omega_1 - \xi_{eg})} \\ &\cdot \left(\boldsymbol{\mu}_{ef} \cdot \mathbf{E}_4^*(\omega_{f'e'}) \boldsymbol{\mu}_{ge'} \cdot \mathbf{E}_3^*(\omega_{e'g}) \boldsymbol{\mu}_{ef}^* \cdot \mathbf{E}_2(\omega_{fe}) \boldsymbol{\mu}_{ge}^* \cdot \mathbf{E}_1(\omega_{eg}) e^{-i\xi_{f'e'} t_3} \right. \\ &\quad \left. - \boldsymbol{\mu}_{ge'} \cdot \mathbf{E}_4^*(\omega_{e'g}) \boldsymbol{\mu}_{e'f} \cdot \mathbf{E}_3^*(\omega_{f'e'}) \boldsymbol{\mu}_{ef}^* \cdot \mathbf{E}_2(\omega_{fe}) \boldsymbol{\mu}_{ge}^* \cdot \mathbf{E}_1(\omega_{eg}) e^{-i\xi_{e'g} t_3} \right), \end{aligned} \quad (8.1)$$

with the same notations explained in Sec. 7.6.3: \mathbf{E}_1 to \mathbf{E}_3 are the Fourier transform of the electric field envelopes of the pulse sequence, \mathbf{E}_4 is the local oscillator, the dipole matrix elements are $\boldsymbol{\mu}_{ij}$, the frequencies $\omega_{ij} = \omega_i - \omega_j$, ω_i describe the exciton energy, and ξ_{ij} equals $\omega_{ij} + i\gamma_{ij}$ with the dephasing γ_{ij} . Mind that the frequencies are detuned around the single and double gap frequency, respectively. In the following the dipole moments are replaced via $\boldsymbol{\mu}_{ab} = \boldsymbol{\mu}_{ba}^*$.

²¹The layout of writing the signals in this chapter is a compromise of saving space and preserving clarity: the fractions that come from the Fourier transform are factorized from both pathways but the sequence of interactions remains in separate terms.

**Figure 8.1:**

Full two-dimensional double quantum coherence spectrum of three coupled quantum dots: Part (a) shows the absolute value, part (b) the imaginary one. The corresponding Hamiltonians are shown in Sec. 6.5.5.

The first presented modification of the double quantum coherence spectroscopy signal assumes a localization of the first incoming pulse of the sequence. For this purpose, Eq. (8.1) is rewritten within two steps for a localized excitation. The term that represents the first pulse is

$$\boldsymbol{\mu}_{ge}^* \cdot \mathbf{E}_1(\omega_{eg})$$

for both pathways. This term becomes

$$\sum_k c_k^{e*} \boldsymbol{\mu}_{gk}^* \cdot \mathbf{E}_{1,i}^{\text{loc}}(r_k, \omega_{eg})$$

through inserting the delocalized dipole moment of the single-exciton $\boldsymbol{\mu}_{ge}^* = \sum_k c_k^{e*} \boldsymbol{\mu}_{gk}^*$ (Eq. (6.27a)) into Eq. (8.1) for the first pulse. The electric field $\mathbf{E}_1(\omega_{eg})$ is now written as $\mathbf{E}_{1,i}^{\text{loc}}(r_k, \omega_{eg})$. The electric field is no longer constant over the entire nanostructure, it depends on the position r . The index i gives the excited quantum dot. Here, r_k marks the position of one of the three quantum dots k , c_k^e is the exciton wave function for quantum state e . The signal now reads

$$\begin{aligned} S_{k_{\text{III}}, E_1}^{\text{loc}}(\Omega_1, \Omega_2, t_3) = & \frac{1}{\hbar^3} \sum_{e, e', f} \sum_k \frac{1}{(\Omega_2 - \xi_{fg})(\Omega_1 - \xi_{eg})} \\ & \cdot \left(\boldsymbol{\mu}_{e'f} \cdot \mathbf{E}_4^*(\omega_{f'e'}) \boldsymbol{\mu}_{ge'} \cdot \mathbf{E}_3^*(\omega_{e'g}) \boldsymbol{\mu}_{ef}^* \cdot \mathbf{E}_2(\omega_{fe}) c_k^{e*} \boldsymbol{\mu}_{gk}^* \cdot \mathbf{E}_{1,i}^{\text{loc}}(r_k, \omega_{eg}) e^{-i\xi_{f'e'} t_3} \right. \\ & \left. - \boldsymbol{\mu}_{ge'} \cdot \mathbf{E}_4^*(\omega_{e'g}) \boldsymbol{\mu}_{e'f} \cdot \mathbf{E}_3^*(\omega_{f'e'}) \boldsymbol{\mu}_{ef}^* \cdot \mathbf{E}_2(\omega_{fe}) c_k^{e*} \boldsymbol{\mu}_{gk}^* \cdot \mathbf{E}_{1,i}^{\text{loc}}(r_k, \omega_{eg}) e^{-i\xi_{e'g} t_3} \right). \end{aligned}$$

Now, a perfect localized excitation is assumed. That means that just one quantum dot is excited and the electric field in the other quantum dots equals zero. In this case of a localization ratio of 1 : 0 : 0, a further step is possible. Then, the localized electric field of the first pulse can be written as

$$\mathbf{E}_{1,i}^{\text{loc}}(r_k) = \mathbf{E}_{1,i}^{\text{loc}} \delta_{ik} \quad (8.2)$$

8 Localized Spectroscopy

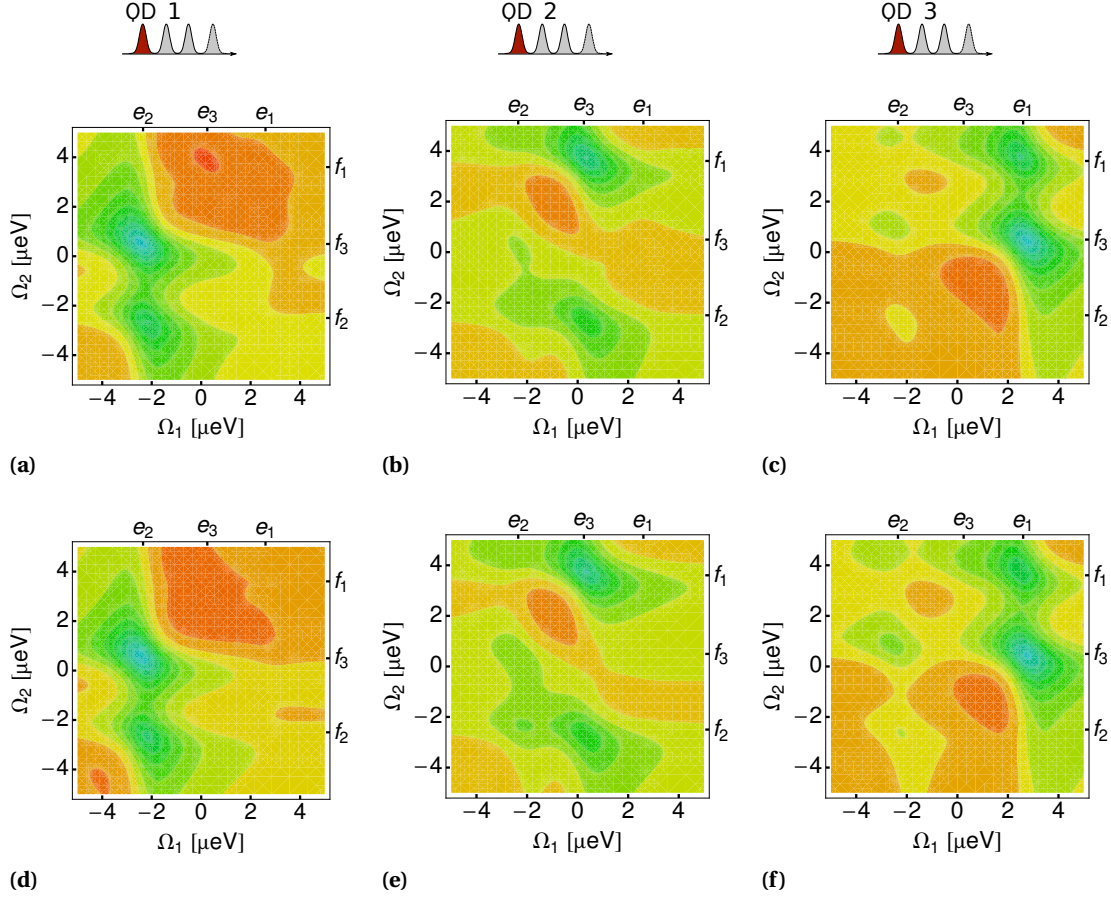


Figure 8.2:

Localized spectra generated by a localized first pulse: The imaginary part of the signal is plotted for a double quantum coherence signal with a localized first pulse of the sequence. The first pulse only excites (a) quantum dot (QD) 1, (b) quantum dot 2 and (c) the third quantum dot. The three spectra can be seen as a decomposition of the full imaginary spectrum of Fig. 8.1b. In part (a-c) a perfect localization is assumed (cf. Eq. (8.3)), (excitation ratio 1 : 0 : 0) while part (d-f) a localization that may be reached in real is plotted (excitation ratio 1 : 0.1205 : 0.0761).

if quantum dot i is the excited one. Thus, the sum over k vanishes and the signal simplifies to

$$S_{k_{\text{III}}, E_1}^{\text{loc}}(i, \Omega_1, \Omega_2, t_3) = \frac{1}{\hbar^3} \sum_{e, e', f} \frac{1}{(\Omega_2 - \xi_{fg})(\Omega_1 - \xi_{eg})} \cdot \left(\begin{aligned} & \left(\boldsymbol{\mu}_{e'f} \cdot \mathbf{E}_4^*(\omega_{f'e'}) \quad \boldsymbol{\mu}_{ge'} \cdot \mathbf{E}_3^*(\omega_{e'g}) \quad \boldsymbol{\mu}_{ef}^* \cdot \mathbf{E}_2(\omega_{fe}) \quad c_i^{e*} \boldsymbol{\mu}_{gi}^* \cdot \mathbf{E}_{1,i}^{\text{loc}}(\omega_{eg}) \quad e^{-i\xi_{f'e'}t_3} \right. \\ & \left. - \boldsymbol{\mu}_{ge'} \cdot \mathbf{E}_4^*(\omega_{e'g}) \quad \boldsymbol{\mu}_{e'f} \cdot \mathbf{E}_3^*(\omega_{f'e'}) \quad \boldsymbol{\mu}_{ef}^* \cdot \mathbf{E}_2(\omega_{fe}) \quad c_i^{e*} \boldsymbol{\mu}_{gi}^* \cdot \mathbf{E}_{1,i}^{\text{loc}}(\omega_{eg}) \quad e^{-i\xi_{e'g}t_3} \right). \end{aligned} \right. \quad (8.3)$$

If it is additionally assumed that for all isolated excited quantum dots the same electric field strength is reached, the index i for the localized electric field of pulse 1 is not necessary any longer.

Spectra

In Fig. 8.1 the absolute value and the imaginary part of the spectrum generated by a quantum system with the Hamiltonian shown in Sec. 6.5.5 are plotted. Calculating the localized

spectrum with help of the newfound equations provides new information: It is possible now to connect the certain quantum dots to the resonances that occur in the spectrum.

The decomposition of the imaginary part of the signal is presented in Fig. 8.2. On the first look, one can connect each single-exciton state with exact one quantum dot: While the peaks at single exciton state e_2 arises from a transition of quantum dot 1, almost all peaks at e_3 are connected to quantum dot 2 and all resonances for that the third quantum dot is responsible are for e_1 . For a more detailed look, there exist also small correlations. For the first quantum dot there are just correlations from e_2 to the transitions f_3 and f_2 . Similarly, the most resonances for quantum dot 2 are at e_3 – a strong one to transition f_1 and the smaller one to f_2 . But here, one can find also connections with the second exciton state: a small contribution for the strong resonance at e_2 with f_3 and a shoulder in direction of e_2 with f_2 . The third quantum dot contributes mainly to the peaks of e_1 at f_1 and f_3 and it also has a small contribution at e_2 with f_3 .

Fig. 8.2 furthermore compares two cases. The spectra of Fig. 8.2a-c are described by Eq. (8.3). Assumption (8.2) is applied, that means one quantum dot is the only excited one, the excitations of all others equals zero. Additionally, in Fig. 8.2, the spectra in case of a non-perfect localization is illustrated. That means, that the localization has a quality that may be reached in reality. Here, the signal can be calculated with Eq. (8.1.1).

As a result, it is found that the differences of Fig. 8.2a-c and 8.2d-f are small. It seems that the reached localization of Sec. 5.5.3 is of a quality that is high enough for statements regarding the connection of resonances to quantum dots. The consequences of the difference becomes more visible in reconstructing the wave function coefficients in Sec. 8.2.

For each set of assumed parameters of the Hamiltonian localized spectroscopy enables a decomposition of the corresponding spectrum. These gained localized spectra would not be possible without spatiotemporal control.

For better comparability, all spectra in this chapter that shows the imaginary part are scaled identically.

8.1.2 Localization of pulse 1 and pulse 2

Modifying the pulse sequence by an additional localization of the second pulse opens further insights into the correlation between quantum states.

Signal

Analogously to Sec. 8.1.1, the two steps to derive a formula for the localized signal for a perfect localization can be repeated. The expansion of the biexciton dipole moment (Eq. (6.27b)) is inserted in additionally into the localized signal (Eq. (8.1.1)) so that the terms belonging to the second pulse $\boldsymbol{\mu}_{e'f}^* \cdot \mathbf{E}_2(\omega_{fe})$ become $\sum_{k,l \neq k} c_k^e c_{kl}^{f*} \boldsymbol{\mu}_{gl}^* \cdot \mathbf{E}_{2,j}^{\text{loc}}(r_l, \omega_{fe})$ and the full signal reads

$$S_{k_{\text{III}}, E_1, E_2}^{\text{loc}}(\Omega_1, \Omega_2, t_3) = \frac{1}{\hbar^3} \sum_{e, e', f} \sum_{k, l \neq k} \frac{1}{(\Omega_2 - \xi_{fg})(\Omega_1 - \xi_{eg})} \cdot \left(\boldsymbol{\mu}_{e'f} \cdot \mathbf{E}_4^*(\omega_{fe}) \boldsymbol{\mu}_{ge'} \cdot \mathbf{E}_3^*(\omega_{e'g}) c_k^e c_{kl}^{f*} \boldsymbol{\mu}_{gl}^* \cdot \mathbf{E}_{2,j}^{\text{loc}}(r_l, \omega_{fe}) c_k^{e*} \boldsymbol{\mu}_{gk}^* \cdot \mathbf{E}_1^{\text{loc}}(\omega_{eg}) e^{-i\xi_{fe'} t_3} - \boldsymbol{\mu}_{ge'} \cdot \mathbf{E}_4^*(\omega_{e'g}) \boldsymbol{\mu}_{e'f} \cdot \mathbf{E}_3^*(\omega_{fe}) c_k^e c_{kl}^{f*} \boldsymbol{\mu}_{gl}^* \cdot \mathbf{E}_{2,j}^{\text{loc}}(r_l, \omega_{fe}) c_k^{e*} \boldsymbol{\mu}_{gk}^* \cdot \mathbf{E}_1^{\text{loc}}(\omega_{eg}) e^{-i\xi_{e'g} t_3} \right).$$

8 Localized Spectroscopy

For an additional second localized field at quantum dot j , a derivation analogous to Eq. (8.3) with $\mathbf{E}_{2,j}^{\text{loc}}(r_l) = E_2^{\text{loc}} \delta_{j,l}$ is used. In case of a perfect localization

$$S_{k_{\text{III}}, E_1, E_2}^{\text{loc}}(i, j, \Omega_1, \Omega_2, t_3) = \frac{1}{\hbar^3} \sum_{e, e', f} \sum_{k \neq j} \frac{1}{(\Omega_2 - \xi_{fg})(\Omega_1 - \xi_{eg})} \cdot \left(\boldsymbol{\mu}_{e'f} \cdot \mathbf{E}_4^*(\omega_{fe'}) \quad \boldsymbol{\mu}_{ge'} \cdot \mathbf{E}_3^*(\omega_{e'g}) \quad c_k^e c_{kj}^{f*} \boldsymbol{\mu}_{gj}^* \cdot \mathbf{E}_{2,j}^{\text{loc}}(\omega_{fe}) \quad c_k^{e*} \boldsymbol{\mu}_{gk}^* \cdot \mathbf{E}_{1,i}^{\text{loc}}(\omega_{eg}) \quad e^{-i\xi_{fe'} t_3} \right. \\ \left. - \boldsymbol{\mu}_{ge'} \cdot \mathbf{E}_4^*(\omega_{e'g}) \quad \boldsymbol{\mu}_{e'f} \cdot \mathbf{E}_3^*(\omega_{fe'}) \quad c_k^e c_{kj}^{f*} \boldsymbol{\mu}_{gj}^* \cdot \mathbf{E}_{2,j}^{\text{loc}}(\omega_{fe}) \quad c_k^{e*} \boldsymbol{\mu}_{gk}^* \cdot \mathbf{E}_{1,i}^{\text{loc}}(\omega_{eg}) \quad e^{-i\xi_{e'g} t_3} \right). \quad (8.4)$$

is obtained, still under the assumption of a localization of the first pulse at quantum dot i . The index j for the electric field of the second pulse makes only sense in the case of a non-symmetric geometry so that different field strengths are needed for exciting different quantum dots.

Spectra

Measuring with such a localization, an additional decomposition for each of the three plots of Fig. 8.2 becomes possible. The nine new subplots of Fig. 8.3 provide a more detailed look: The influences of the quantum dots to the biexciton states become visible. While in Fig. 8.2 the quantum dots can be connected to the exciton states, now every peak of the exciton state can be connected to a biexciton state.

Localization of the first pulse at quantum dot 1 shows two peaks at exciton state e_2 . Resolving in localizations of the second pulse gives connections between the biexciton states and the quantum dots: The upper of the strong peaks at e_2 with f_2 originates from quantum dot 2 while the lower resonance of e_2 with f_2 arises from the third dot.

Similarly, the biexciton states of the two strongest peaks of Fig. 8.2b and 8.2c can be associated with certain quantum dots: The peak at e_3 and f_2 arises from quantum dot 1, with f_1 quantum dot 3 is responsible. For e_1 with f_3 quantum dot 1, for e_1 with the biexciton state f_1 quantum dot 2 contributes most.

The diagonal plots of Fig. 8.3 shows almost no resonances. That is explainable by the biexciton basis (cf. Sec. 6.5.4). For a biexciton state, two different quantum dots have to be excited. The biexciton basis consists of the basis elements $|12\rangle$, $|13\rangle$ and $|23\rangle$. So if now the first quantum dot is excited, the biexciton states dominate if the second pulse excites one of the other two quantum dots. In each of the three decompositions this is the case. Since the biexcitonic basis elements are $|ij\rangle$ for $i \neq j$, the states $|11\rangle$, $|22\rangle$, or $|33\rangle$ are not allowed. So the spectra of the diagonals of Figs. 8.3 and 8.4 should show no resonances. That there is still a small resonance demonstrates the overlapping of the peaks for other quantum states due to the delocalized states. Ignoring the dipole moments, the signal is proportional to the product $c_i^e c_j^f$, so even interferences of positive and negative values of the spectra are conceivable. For the perfect localization in Fig. 8.3, there are less resonances seen than in the non-perfect localization of Fig. 8.4.

8.1.3 Localization of pulse 2

For reconstructing the biexciton wave function (see Sec. 8.2.4) it is sufficient to localize the second pulse only.

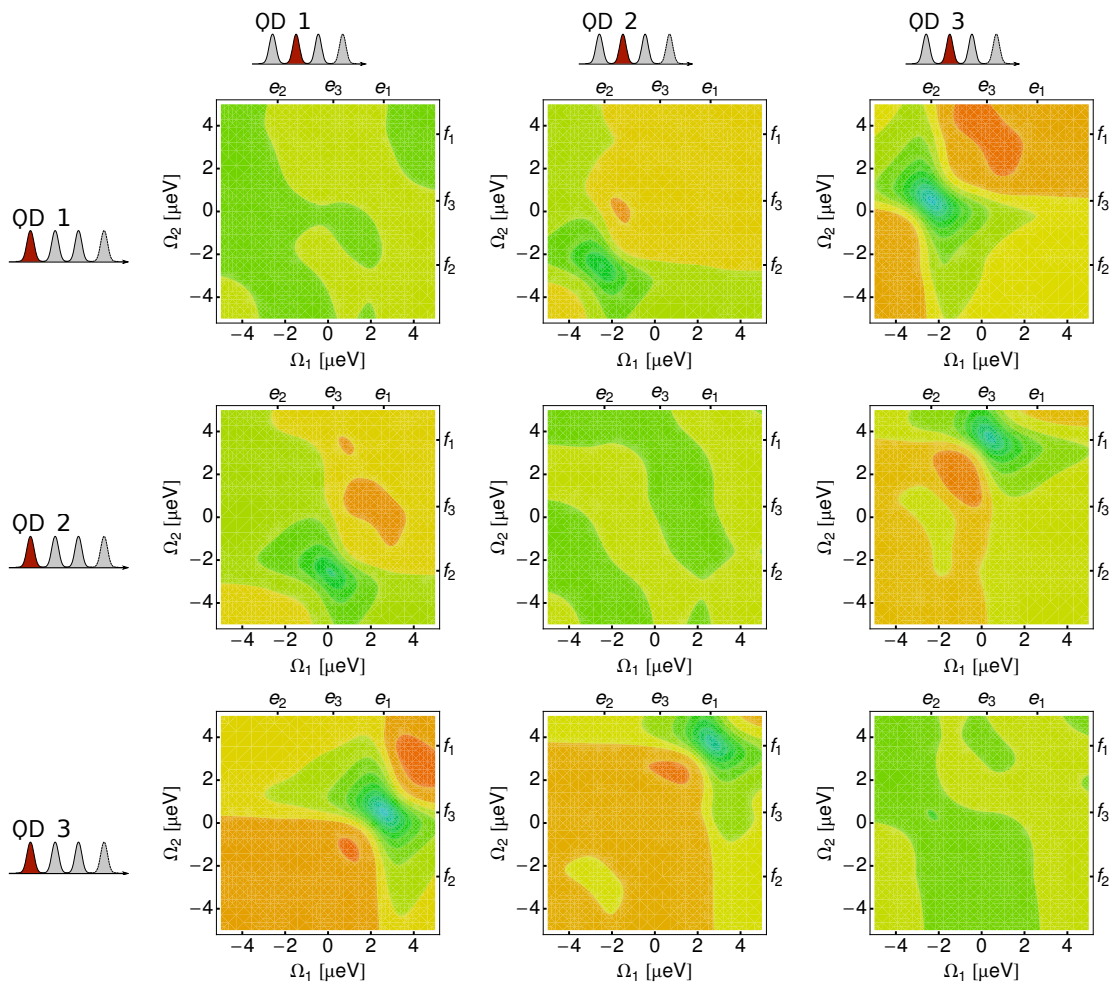


Figure 8.3:

Localized spectra generated by a localized first and second pulse for a perfect localization: The imaginary part of the signal is plotted for a double quantum coherence signal generated by a localized first pulse for each quantum dot (columns) and a localized second pulse for each quantum dot (lines) of the sequence. On the diagonal, no significant signal can be seen. The nine spectra are an additional of Fig. 8.2. A perfect localization is assumed.

8 Localized Spectroscopy

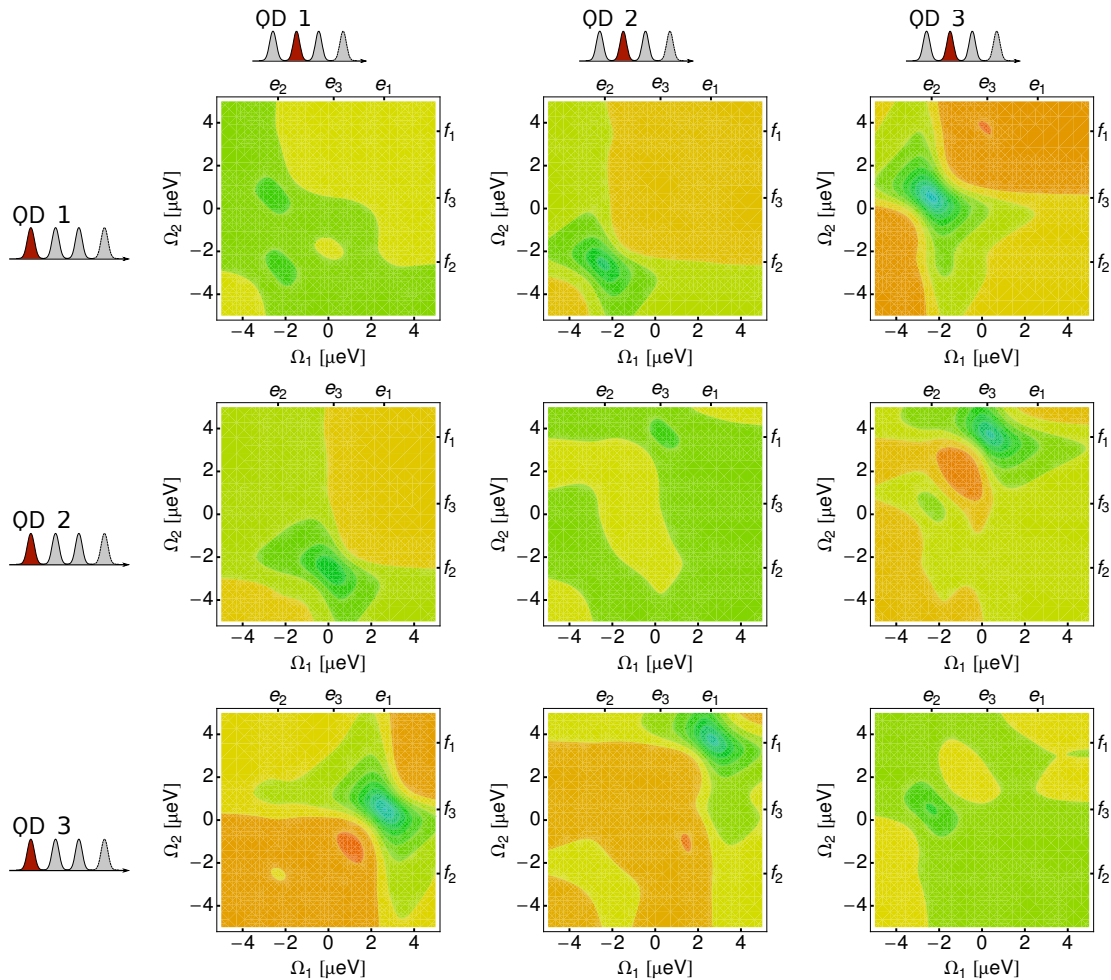
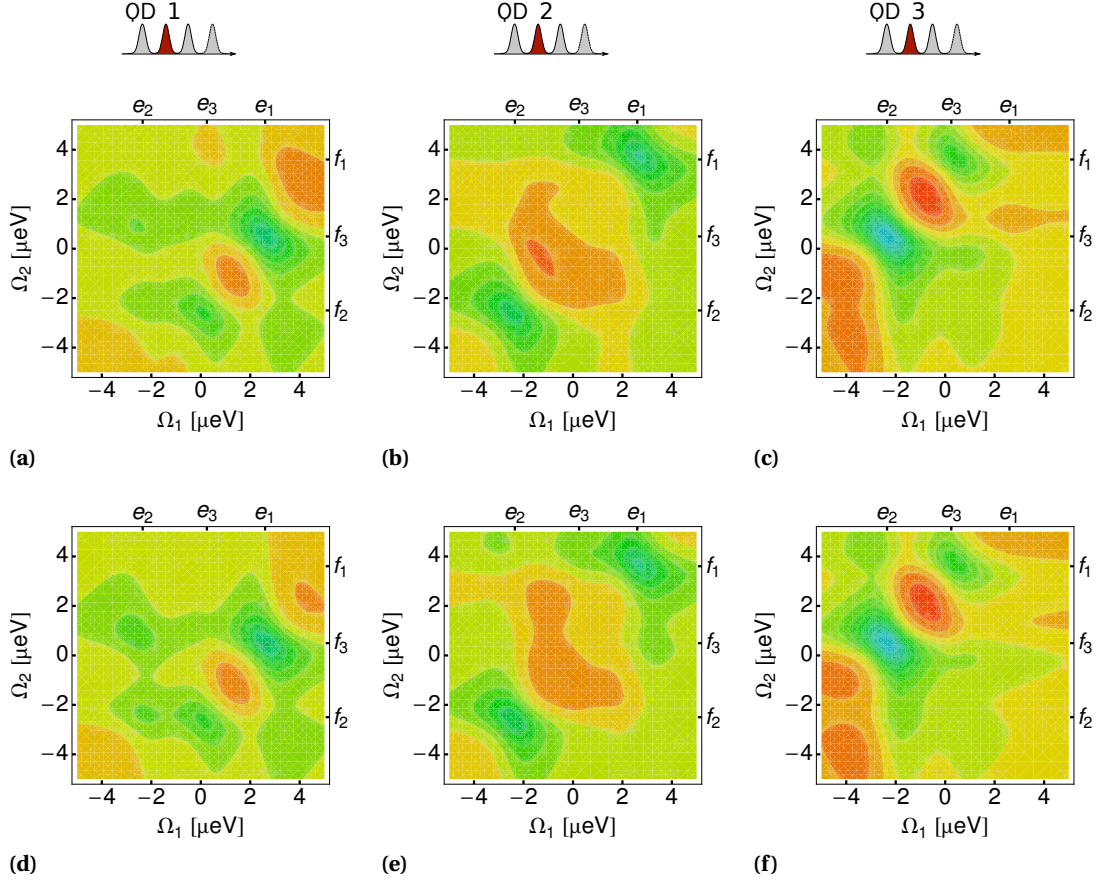


Figure 8.4:

Localized spectra generated by a localized first and second pulse for a realistic localization: Again, the imaginary part of the signal is plotted for a double quantum coherence signal generated by a localized first pulse for each quantum dot (columns) and a localized second pulse for each quantum dot (lines) of the sequence. On the diagonal, no significant signal can be seen. The nine spectra are an additional of Fig. 8.2. A realistic localization is assumed. In comparison to Fig. 8.3, a bit stronger signals can be seen as an error due to the non-perfect localization.

**Figure 8.5:**

Localized spectra generated by a localized second pulse: The imaginary part of the signal is plotted for a double quantum coherence signal with a localized second pulse of the sequence. The second pulse only excites (a) quantum dot (QD) 1, (b) quantum dot 2 and (c) the third quantum dot. The three spectra can be seen, analogous to Fig. 8.2, as a decomposition of the full imaginary spectrum of Fig. 8.1b. In part (a-c) a perfect localization is assumed (excitation ratio 1 : 0 : 0) while part (d-f) a localization that may be reached in real is plotted (excitation ratio 1 : 0.1205 : 0.0761).

Signal

The signal for an idealized localization and for just localizing pulse 2 reads

$$\begin{aligned}
 S_{k_{\text{III}}, E_2}^{\text{loc}}(j, \Omega_1, \Omega_2, t_3) = & \frac{1}{\hbar^3} \sum_{e, e', f} \sum_{k \neq j} \frac{1}{(\Omega_2 - \xi_{fg})(\Omega_1 - \xi_{eg})} \\
 & \cdot \left(\boldsymbol{\mu}_{e'f} \cdot \mathbf{E}_4^*(\omega_{f'e'}) \boldsymbol{\mu}_{ge'} \cdot \mathbf{E}_3^*(\omega_{e'g}) c_k^e c_{kj}^{f*} \boldsymbol{\mu}_{gj}^* \cdot \mathbf{E}_{2,j}^{\text{loc}}(\omega_{fe}) \boldsymbol{\mu}_{ge}^* \cdot \mathbf{E}_1(\omega_{eg}) e^{-i\xi_{f'e'} t_3} \right. \\
 & \left. - \boldsymbol{\mu}_{ge'} \cdot \mathbf{E}_4^*(\omega_{e'g}) \boldsymbol{\mu}_{e'f} \cdot \mathbf{E}_3^*(\omega_{f'e'}) c_k^e c_{kj}^{f*} \boldsymbol{\mu}_{gj}^* \cdot \mathbf{E}_{2,j}^{\text{loc}}(\omega_{fe}) \boldsymbol{\mu}_{ge}^* \cdot \mathbf{E}_1(\omega_{eg}) e^{-i\xi_{e'g} t_3} \right). \quad (8.5)
 \end{aligned}$$

The first pulse excites all quantum dots equally like the third and fourth pulse.

Spectra

In Fig. 8.5 spectra found by Eq. (8.5) with perfect localization are shown. They represent – in contrast to Fig. 8.2 – another decomposition of the imaginary part of the full spectrum.

The biexciton states cannot be connected to a certain quantum dot in such a simple way as in the exciton case of Sec. 8.1.1. Here, more correlations are found. The results are consistent

with the split spectra of the localization for both pulses in Fig. 8.3: The strongest peak in the localization of quantum dot 1 is e_1 with f_3 . By splitting the spectrum seen in Fig. 8.2c, f_3 shows also the biggest resonance for quantum dot 1. The same is valid for the strongest peak of Fig. 8.5: It is found for the third quantum dot at state e_2 combined with f_3 . That could be expected because of the results for two localizations. There, the main part of the resonance at e_2 with f_3 comes from quantum dot 3.

8.2 Reconstruction of the wave functions

The presented techniques of localizing the double quantum coherence spectrum allows not only connecting resonances to certain quantum dots. Localized spectroscopy enables several new applications. The most important application presented in this work is found in this section. Another application – filtering different resonances – is shown in Sec. 8.3. Afterwards, the filtering technique is applied to improve the results of the current part in Sec. 8.4.

The newfound data of localized spectra can be used to obtain more information about coupled quantum dots. In this section, a protocol is presented to reconstruct the wave functions of single-exciton states as well as for biexciton states.

As presented in Sec. 6.5, the one and two-exciton state functions can be written as a superposition of the single or double-exciton basis (Eq. (6.22)):

$$|e\rangle = \sum_i c_i^e |i\rangle$$

$$|f\rangle = \sum_{i,j \neq i} c_{ij}^f |ij\rangle.$$

Consequently, only the expansion coefficients c_i^e and c_{ij}^f of Eqs. (6.22) and (6.27) have to be found to reconstruct the exciton and biexciton wave functions $|e\rangle$ and $|f\rangle$, respectively, if known single particle wave functions are assumed. The square of the absolute value of the prefactors gives information about how the delocalized wave function is spread over the different quantum dots.

Before the protocol is explained in detail, a short sketch is given to anticipate the main idea of reconstruction wave functions.

8.2.1 Idea

The main idea that enables reconstructing wave functions is that the measured signal is proportional to the dipole moment for a transition between delocalized states. The dipole moment can be written as an expansion of the dipole moments for the local transitions according to Eq. (6.27):

$$S(\Omega_1, \Omega_2, T_3) \propto \sum_e \boldsymbol{\mu}_{ge} \cdot \mathbf{E}_1 = \sum_e \sum_i c_i^e \boldsymbol{\mu}_{gi} \cdot \mathbf{E}_1.$$

The signal S can be measured – thus, for extracting the coefficients c_i^e only the sum must be eliminated. Choosing one resonance that dominates, for example $\Omega_1 = e_\alpha$ and $\Omega_2 = f_\beta$, helps eliminating the sum over e :

$$S(e_\alpha, f_\beta, T_3) \propto \sum_i c_i^{e_\alpha} \boldsymbol{\mu}_{gi} \cdot \mathbf{E}_1.$$

The possibility of measuring localized spectra enables eliminating additionally the sum over i :

$$S_{E_1}^{\text{loc}}(i, e_\alpha, f_\beta, T_3) \propto c_i^{e_\alpha} \boldsymbol{\mu}_{gi} \cdot \mathbf{E}_1.$$

Assuming that all dipole moments are known or are at least identical, the coefficient $c_i^{e_\alpha}$, that are needed for finding the exciton wave function, can be extracted. This is possible only without an arbitrarily global phase.

The protocol of extracting the coefficients can be applied in a similar way for the biexciton states but with more complicated calculations.

In the following, a calculation and measurement instruction for reconstructing the wave functions for a certain single-exciton state e_α and a certain biexciton state f_β is presented in more detail.

8.2.2 Error analysis

To evaluate the quality of the reconstructed single- and two-exciton wave function coefficients of the two following subsections, a method for calculating the error with a meaningful output is needed. This is necessary since those results enable an extensive discussion about the quality of the reconstruction script.

The error function has to compare the values of the complex coefficients c_i^{org} for the original wave function coefficient and c_i^{rec} for the reconstructed one.

It is useful to measure the quality via the Euclidean norm, that means in terms of the squared error of the difference of the original wave function coefficient and the reconstructed one. But there exist two fundamental different methods: Calculating the difference of the complex coefficients directly or calculating the difference after determining the square of the absolute value. For both possibilities their difference and the advantages and disadvantages are presented in the following.

Error 1

The error that gives the reconstruction quality of the coefficient c_i^{rec} can be determined via

$$\text{Error1}(c_i^{\text{rec}}, c_i^{\text{org}}) = \sqrt{\sum_{i=1}^n |c_i^{\text{rec}} - c_i^{\text{org}}|^2}. \quad (8.6)$$

Since for forming the difference, the phase of the complex coefficients is considered, the result of $\text{Error1}(c_i^{\text{rec}}, c_i^{\text{org}})$ depends also on the phase of c_i^{rec} . But as can be seen in the following sections, this coefficient can be reconstructed only without an arbitrarily global phase. Thus, for determining a meaningful error estimation, the smallest error for one certain global phase has to be found. For this purpose, the derivative of Eq. (8.6) is set to zero to find the coefficient $c_i^{\text{rec}} \cdot e^{i\phi_{\min}}$ that supplies the smallest error value:

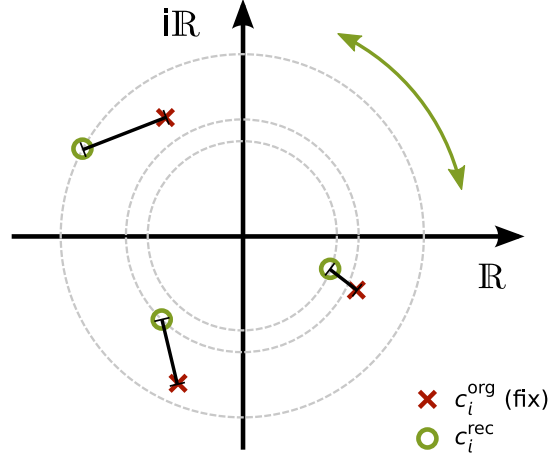
$$\frac{d}{d\phi_{\min}} \text{Error1}(c_i^{\text{rec}} \cdot e^{i\phi_{\min}}, c_i^{\text{org}}) \stackrel{!}{=} 0.$$

Multiplying the reconstructed wave function coefficient with the factor $e^{i\phi_{\min}}$ can be seen as a rotation in the complex plain around the origin. The three vector components are rotated simultaneously until the norm of the differences between each component of the reconstructed coefficient and its corresponding origin is the shortest one. This illustration is sketched in Fig. 8.6.

The multiplication with $e^{i\phi_{\min}}$ is reasonable for obtaining a meaningful error estimation. But keep in mind, that for an experimentalist it is not possible to achieve this multiplication because the origin wave function coefficients are unknown. This is why in Tabs. 8.1, 8.3, 8.4, and 8.5 the results of $\arg(c_i^{\text{rec}})$ are given without the factor $e^{i\phi_{\min}}$ for $i = 1, \dots, n$. In case of multiplying this factor, the results of reconstructing the phase would even look better.

Figure 8.6:

Illustration of adding a global phase to the reconstructed coefficients to fit the original coefficients: The red crosses symbolize the three components of the original wave function coefficient. They are on a fix position. Adding a global phase ϕ_{\min} to the complex reconstructed coefficient via $c_i^{\text{rec}} \cdot e^{i\phi_{\min}}$ corresponds to a rotation of the green circle-like reconstructed wave function coefficient in the complex plain. The phase is selected in a way that the norm of the differences becomes minimal.



Error 2

The physical meaning of the coefficients is given by the probability of presence of the electrons that are spread over the whole coupled nanostructure. The probability of presence is proportional to the square of the absolute value of the coefficients $|c_i^{\text{org}}|^2$ for all quantum dots i . This leads to another way of error calculation:

$$\text{Error2}(c_i^{\text{rec}}, c_i^{\text{org}}) = \sqrt{\sum_{i=1}^n \left| |c_i^{\text{rec}}|^2 - |c_i^{\text{org}}|^2 \right|^2}.$$

The main difference to Eq. (8.6) is that here the phase of the complex coefficients does not contribute any more. Figuratively speaking this means that just the difference between the reconstructed and the origin wave function coefficient is rated for each component and no rotation is executed. Since for this error the global phase plays no role, the optimization process as described in the first error section can be neglected.

This way of error determination does not consider the phase but it has the most physical meaning since the square of the coefficient gives information about the probability of presence.

Tab. 8.2 compares the results of both error calculation ways. For both ways, the relations of the results are almost the same. Since the physical interpretation of the second error is more significant, in the rest of this chapter, especially in Tabs. 8.1, 8.3, 8.4, and 8.5, only Error 2 is considered.

The error value of the reconstructed coefficients for the two-exciton states (see Sec. 8.2.4) are determined in the same way as for the single-excitons and also only the second error is given in Tabs. 8.3, 8.4, and 8.5.

8.2.3 Exciton states

For reconstructing the wave function $c_i^{e_\alpha}$ the signal of the certain state has to be determined. That means, that the signal is around the frequencies $\Omega_1 \approx \Omega_1^\alpha = \omega_{e_\alpha g}$ and $\Omega_2 \approx \Omega_2^\beta = \omega_{f_\beta g}$ where f_β is chosen such that it shows a strong correlation to e_α . Consequently, the denominator of the perfect localized signal of the first pulse (Eq. (8.3)) becomes so small, that the part of e_α and f_β is the dominating part of the sum over e and f , respectively. Thus, the sum over e and f can be eliminated with the approximation that only $e = e_\alpha$ and $f = f_\beta$ contribute to the sum. For this purpose, it is necessary that contributions to other states are well sepa-

rated in the double quantum coherence spectroscopy from this resonance. So the measured signal corresponds with

$$S_{k_{\text{III}}, E_1}^{\text{loc}}(i, e_\alpha, f_\beta, T_3) = \frac{1}{\hbar^3} \sum_{e'} \frac{1}{(\Omega_2^\beta - \xi_{f_\beta g})(\Omega_1^\alpha - \xi_{e_\alpha g})} \cdot \left(\boldsymbol{\mu}_{e' f_\beta} \cdot \mathbf{E}_4^*(\omega_{f_\beta e'}) \boldsymbol{\mu}_{g e'} \cdot \mathbf{E}_3^*(\omega_{e' g}) \boldsymbol{\mu}_{e_\alpha f_\beta}^* \cdot \mathbf{E}_2(\omega_{f_\beta e_\alpha}) c_i^{e_\alpha*} \boldsymbol{\mu}_{g i}^* \cdot \mathbf{E}_{1,i}^{\text{loc}}(\omega_{e_\alpha g}) e^{-i\xi_{f_\beta e'} T_3} \right. \\ \left. - \boldsymbol{\mu}_{g e'} \cdot \mathbf{E}_4^*(\omega_{e' g}) \boldsymbol{\mu}_{e' f_\beta} \cdot \mathbf{E}_3^*(\omega_{f_\beta e'}) \boldsymbol{\mu}_{e_\alpha f_\beta}^* \cdot \mathbf{E}_2(\omega_{f_\beta e_\alpha}) c_i^{e_\alpha*} \boldsymbol{\mu}_{g i}^* \cdot \mathbf{E}_{1,i}^{\text{loc}}(\omega_{e_\alpha g}) e^{-i\xi_{e' g} T_3} \right) \quad (8.7)$$

for a fixed time interval T_3 .

The only part of this signal that depends on the choice of quantum dot i is the factor $c_i^{e_\alpha*} \boldsymbol{\mu}_{g i}^* \cdot \mathbf{E}_{1,i}^{\text{loc}}(\omega_{e_\alpha g})$. Both Liouville diagrams share this part, all other parts do not depend on i . The proportionality can be expressed with a factor A such that

$$c_i^{e_\alpha*} A = S_{E_1}^{\text{loc}}(i, e_\alpha, f_\beta, T_3) / \left(\boldsymbol{\mu}_{g i}^* \cdot \mathbf{E}_{1,i}^{\text{loc}}(\omega_{e_\alpha g}) \right). \quad (8.8)$$

Note that although a Lorentzian broadening in the equations is assumed, this proportionality should not depend on this choice.

While the unknown quantities are on the left hand of Eq. (8.8), all the known parts are on the right hand: $\mathbf{E}_{1,i}^{\text{loc}}(\omega_{e_\alpha g})$ is the field strength of the first pulse for exciting the quantum dot i . The dipole moments are also assumed to be known or are at least identical since they can then be factored out in the normalization step. Eq. (8.8) can be interpreted as an underdetermined system of equations with one equation for each quantum dot i and the $n + 1$ unknowns $c_i^{e_\alpha*}$ for $i = 1, \dots, n$ and A .

The normalization property of wave functions (Eq. (6.24)) provides $\sum_i |c_i^{e_\alpha}|^2 = 1$ and serves as an additional condition for the system of equation, so that the system is no longer underdetermined. Thus, it can be solved and the coefficients $c_i^{e_\alpha}$ can be found. The exciton wave function $|e_\alpha\rangle$ can then be reconstructed via

$$|e_\alpha\rangle = \sum_i c_i^{e_\alpha} |i\rangle$$

for a n -dimensional local basis. All single-exciton states can be reconstructed since e_α represents an arbitrary state.

Demonstration

It will be demonstrated that a reconstruction of wave functions is possible and that information about the quality of reconstruction can be found. As a model, the three coupled quantum dots whose energies are described by the Hamiltonian of Sec. 6.5.5 are used. The localization setup of Sec. 5.5.3 serves as realistic localization model, with an excitation ratio of

$$1 : 0.1205 : 0.0761$$

in frequency domain.

In Tab. 8.1 the absolute value and the phase of all three original single-exciton states e_1 , e_2 , and e_3 , that belong to the chosen Hamiltonian, can be compared with the reconstructed values. In the simplest way to start, values for the frequency Ω_1^α and Ω_2^β very close to the peak of each resonance are chosen. For every single-exciton resonance the coefficients are calculated with a combination of every biexcitonic resonance to find out which combination reaches the best reconstruction. "Best" means minimizing the squared error. The found combina-

8 Localized Spectroscopy

State	Type	Ω_1	Ω_2	$ c_1^e $	$ c_2^e $	$ c_3^e $	$\arg(c_1^e)$	$\arg(c_2^e)$	$\arg(c_3^e)$	Error
e_1	O			0.115	0.104	0.988	0.500	0.500	0.000	
e_1, f_1	R ^a	2.60	3.60	0.154	0.385	0.910	0.287	0.605	0.729	0.20
e_1, f_2	R	2.60	-2.50	0.365	0.445	0.817	0.554	0.562	0.966	0.38
e_1, f_3	R	2.60	0.49	0.221	0.032	0.975	0.471	0.721	0.783	0.05
e_1, f_3	R	3.12	0.49	0.199	0.034	0.979	0.465	0.685	0.707	0.03
e_1, f_3	P ^b	2.60	0.49	0.247	0.077	0.966	0.433	0.281	0.787	0.06
e_1, f_3	P	3.12	0.49	0.205	0.081	0.975	0.414	0.190	0.710	0.04
e_2	O			0.977	0.169	0.131	0.500	0.500	0.500	
e_2, f_1	R	-2.35	3.60	0.895	0.387	0.221	0.554	0.954	0.869	0.20
e_2, f_2	R	-2.35	-2.50	0.913	0.364	0.181	0.781	0.849	0.847	0.16
e_2, f_3	R	-2.35	0.49	0.942	0.204	0.268	0.727	0.714	0.839	0.09
e_2, f_3	R	-3.20	0.49	0.910	0.194	0.366	0.839	0.846	0.919	0.17
e_2, f_3	P	-2.35	0.49	0.969	0.136	0.206	0.725	0.680	0.907	0.03
e_2, f_3	P	-3.20	0.49	0.949	0.110	0.294	0.836	0.820	0.952	0.09
e_3	O			0.180	0.980	0.083	0.000	0.500	0.500	
e_3, f_1	R	0.25	3.60	0.244	0.890	0.386	0.357	0.796	0.893	0.22
e_3, f_2	R	0.25	-2.50	0.509	0.856	0.092	0.582	0.726	0.180	0.32
e_3, f_3	R	0.25	0.49	0.782	0.122	0.611	0.535	0.232	0.965	1.17
e_3, f_1	P	0.25	3.60	0.360	0.858	0.366	0.342	0.792	0.903	0.28

^aReconstructed with realistic localization ratio of (1 : 0.1205 : 0.0761)

^bReconstructed with perfect localization ratio (1:0:0)

Table 8.1:

Comparison of original (O) with reconstructed coefficients (R for realistic, P for perfect localization) for reconstructing single-exciton wave functions: The phase is written in multiples of 2π and the energies are in microelectron volts. The first column shows – additionally to the single-exciton state – the corresponding biexciton state to see immediately at which resonance the signal is measured. The phase of the complex wave function coefficients given here is determined only without a global phase. In the last column the error in relation to the original state is given, calculated as given in Sec. 8.2.2. As an additional information, the values of all worse combination of single-exciton states with biexciton states are shown in gray. Tab. 8.2 shows the combination of the states in order of the error.

tions are listed in Tab. 8.2 in order of recombination quality. The table contains – additionally to the best combinations of exciton and biexciton states – all other combinations, they are shown in gray. All chosen measurement points are also noted in Tab. 8.1.

The results of Tab. 8.2 are reflected in Fig. 8.1a: The resonance that has the least influence of other resonances is at e_2 with f_3 . It is the most separated peak, so just a few factors can distort the reconstruction. The second strongest resonance for e_1 is at f_1 but on the one hand, this resonance is weaker than e_1 with f_3 and on the other hand, there are clearly visible influences from the e_3 with f_1 peak. For the last possible peak at e_1 with f_2 , there is no coupling due to the given Hamiltonians of Sec. 6.5.5. So the elimination of the sum is no acceptable assumption since this resonance does not dominate the other terms of the sum. Doing the assumption anyway, the result is no longer trustworthy. With same arguments, e_2 is linked with f_3 and e_3 with f_1 for reconstruction.

In conclusion, two points have to be considered to find a good evaluation point to measure the spectrum for recombining the wave function coefficients: On the one side, the resonance should have a high oscillator strength to justify eliminating the sum over the exciton states in Eq. (8.7). On the other side one can say, the less neighboring influences interfere, the better the reconstruction.

Pos.	Exc. state	Biexc. state	Error 1	Error 2
1.	e_1	f_3	0.25	0.05
	e_1	f_1	0.47	0.20
	e_1	f_2	0.48	0.38
2.	e_2	f_3	0.19	0.09
	e_2	f_2	0.24	0.16
	e_2	f_1	0.61	0.20
3.	e_3	f_1	0.35	0.22
	e_3	f_2	0.67	0.32
	e_3	f_3	1.23	1.17

Table 8.2:

Comparison of the reconstruction quality of chosen combinations of exciton and biexciton states and comparison of the error calculation values: As an additional information, the values of all worse combination of single-exciton wave functions with two-exciton wave functions are shown in gray. The positions are with respect to error 2 for the realistic localization. Also the two ways of error calculation presented in Sec. 8.2.2 can be compared in this table.

It is possible to improve the reconstructed quantities by moving the measurement points in direction of lower influences of other resonances. Changing Ω_1 for reconstructing e_1 in higher single-exciton energies reduces foreign influences. The quality of reconstruction reaches a maximum choosing $\Omega_1 = 3.12 \mu\text{eV}$ instead of $\Omega_1 = 2.60 \mu\text{eV}$, as shown in Tab. 8.1.

By the same reasoning, reconstructing quality of state e_2 would improve if the measurement point was moved in negative Ω_1 direction. But this is not the case as can be seen also in Tab. 8.1, in the last and third last line of state e_2 . To find an explanation for this, it is necessary to have a more detailed look at the imaginary part of the spectrum (Fig. 8.1b). While the influences of other resonances for higher single-exciton energies have different signs, for lower exciton energies there is just one sign visible. That means that in that special case, although there are more influences on the right hand, the quality of reconstructing decreases for lower energies since the foreign contributions for higher energies interfere destructively. But since the quality of reconstruction is not known by an experimentalist that do not know the origin state and consequently cannot compare the newfound coefficients, however, the point is moved in negative direction. It will show up that the quality of reconstruction then will increase after filtering state e_1 (see Sec. 8.4). Since the third exciton state e_3 is influences from both sides, no new measuring point is chosen.

Although the quality of reconstruction can be improved in Sec. 8.4, up to this point there is an overall good matching for both the amplitude and the relative phase. The coefficients for the reconstructed wave functions are illustrated in Fig. 8.7.

All discussed coefficients thus far are reconstructed with the localization ratio $1 : 0.1205 : 0.0761$. The reconstruction is also executed with a perfect relation of excitations ($1 : 0 : 0$). These recombined states are also listed in Tab. 8.1.

Summary

Input: Dipole moments μ_{gi} for all quantum dots i

Measurement: Full DQCS signal $S(\Omega_1, \Omega_2, T_3)$ to select Ω_1^α and Ω_2^β with a main contribution by a selected single-exciton state, localized DQCS signal $S_{E_1}^{\text{loc}}(i, e_\alpha, f_\beta, T_3)$ for desired single-exciton coefficient $c_i^{e_\alpha}$

Output: Expansion coefficient of the exciton wave function $c_i^{e_\alpha}$ via $c_i^{e_\alpha} = S_{E_1}^{\text{loc}}(i, e_\alpha, f_\beta, T_3) / (\mu_{gi}^* \cdot E_{1,i}^{\text{loc}}(A\omega_{e_\alpha g}))$ where A is found by the normalization of the wave function $|e_\alpha\rangle$

8 Localized Spectroscopy

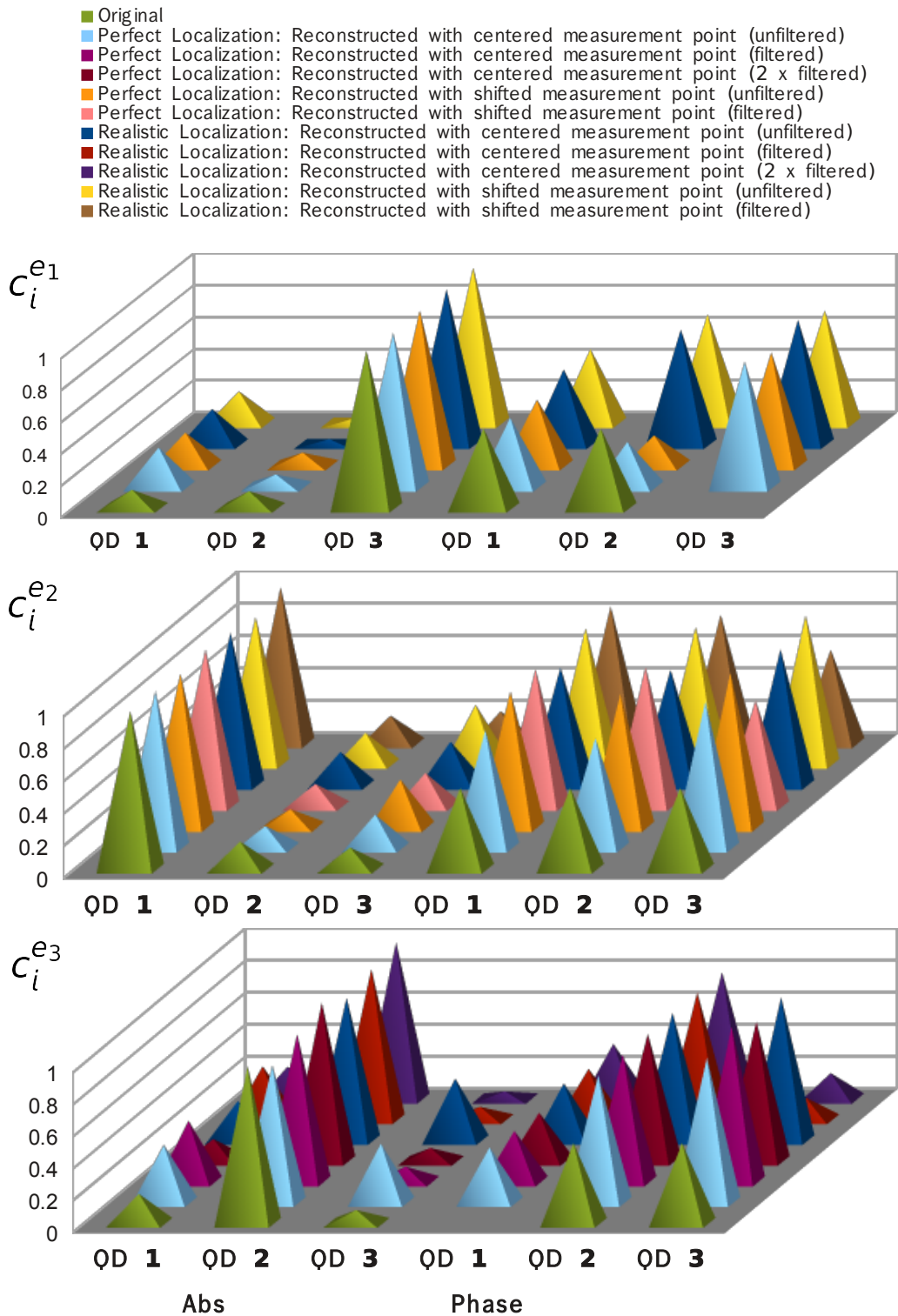


Figure 8.7: Illustration of reconstructed singe-exciton wave function coefficients: The original wave function coefficients are compared with different versions of reconstructing. The measurement points can be found in Tab. 8.1. An overall good agreement is visible.

8.2.4 Biexciton states

Similar to the procedure for excitons, the wave functions can be reconstructed for biexcitons. As a prerequisite, the exciton reconstruction has to be completed and all c_i^e must be known.

Since the Liouville pathway (Fig. 7.10) shows that the second pulse excites the double exciton state, the focus is on signal (8.5). Choosing again e_α as the desired single-exciton state and f_β as the desired double exciton state for reconstructing the wave function coefficients yields analogously to Sec. 8.1.3

$$S_{k_{\text{III}}, E_2}^{\text{loc}}(j, e_\alpha, f_\beta, T_3) = \frac{1}{\hbar^3} \sum_{e'} \sum_{k \neq j} \frac{1}{(\Omega_2^\beta - \xi_{f_\beta g})(\Omega_1^\alpha - \xi_{e_\alpha g})} \cdot \left(\begin{aligned} & \left(\boldsymbol{\mu}_{e' f_\beta} \cdot \mathbf{E}_4^*(\omega_{f_\beta e'}) \quad \boldsymbol{\mu}_{g e'} \cdot \mathbf{E}_3^*(\omega_{e' g}) \quad c_k^{e_\alpha} c_{kj}^{f_\beta^*} \boldsymbol{\mu}_{gj}^* \cdot \mathbf{E}_{2,j}^{\text{loc}}(\omega_{f_\beta e_\alpha}) \quad \boldsymbol{\mu}_{g e_\alpha}^* \cdot \mathbf{E}_1(\omega_{e_\alpha g}) \quad e^{-i\xi_{f_\beta e'} T_3} \right) \\ & - \left(\boldsymbol{\mu}_{g e'} \cdot \mathbf{E}_4^*(\omega_{e' g}) \quad \boldsymbol{\mu}_{e' f_\beta} \cdot \mathbf{E}_3^*(\omega_{f_\beta e'}) \quad c_k^{e_\alpha} c_{kj}^{f_\beta^*} \boldsymbol{\mu}_{gj}^* \cdot \mathbf{E}_{2,j}^{\text{loc}}(\omega_{f_\beta e_\alpha}) \quad \boldsymbol{\mu}_{g e_\alpha}^* \cdot \mathbf{E}_1(\omega_{e_\alpha g}) \quad e^{-i\xi_{e' g} T_3} \right) \end{aligned} \right) \quad (8.9)$$

for a fixed time interval T_3 . The signal is measured again around the frequencies $\Omega_1^\alpha = \omega_{e_\alpha g}$ and $\Omega_2^\beta = \omega_{f_\beta g}$. The corresponding f_β to each single-exciton state is listed in Tab. 8.2. Here, again it is assumed that the part of e_α and f_β dominates the sum over e and f , respectively. The index j of the electric field of pulse 2 disappears in case of a perfect symmetric geometry where the electric field strength does not depend on which quantum dot is excited.

Next, it is still possible to act analogously to Sec. 8.2.3 and introduce again a proportionality factor:

$$\sum_{k \neq j} c_k^{e_\alpha} c_{kj}^{f_\beta^*} B_{e_\alpha}^{f_\beta} = S_{E_2}^{\text{loc}}(j, e_\alpha, f_\beta, T_3) / \left(\boldsymbol{\mu}_{gj}^* \cdot \mathbf{E}_{2,j}^{\text{loc}}(\omega_{e_\alpha g}) \right). \quad (8.10)$$

Here, the factor $B_{e_\alpha}^{f_\beta}$ combines all parts that do not depend on k or j . Both Liouville pathways again share the same distribution. The form of Eq. (8.10) should again not depend on the dephasing model.

Eq.(8.10) represents a system of n equations (n is the number of quantum dots) and is again underdetermined: Although the signal is measured for every quantum dot j and dipole moments and single-exciton wave functions are requested to be known, for n quantum dots there still remain $n^2 - n + 1$ unknowns.

A next logical step for isolating the biexciton wave function $c_{kj}^{f_\beta^*}$ would be bringing the single-exciton wave function $c_k^{e_\alpha}$ to the left hand side of Eq. (8.10). But mind that $B_{e_\alpha}^{f_\beta}$ depends on the single and biexciton states. Thus, it is not possible to apply the orthogonality relation. Dividing by $B_{e_\alpha}^{f_\beta}$ before applying the orthogonality relation is no alternative since these factors are unknown and should consequently not appear on the right hand of the equation.

The solution of this problem is computing the ratio of the factor of two arbitrary exciton states instead of calculating $B_{e_\alpha}^{f_\beta}$ for every e_α .

For this purpose, Eq. (8.10) is multiplied with $c_j^{e_\gamma}$ and the sum over j is taken to obtain

$$\sum_{j, k \neq j} c_k^{e_\alpha} c_j^{e_\gamma} c_{kj}^{f_\beta^*} B_{e_\alpha}^{f_\beta} = \sum_j c_j^{e_\gamma} S_{E_2}^{\text{loc}}(j, e_\alpha, f_\beta, T_3) / \left(\boldsymbol{\mu}_{gj}^* \cdot \mathbf{E}_{2,j}^{\text{loc}}(\omega_{e_\alpha g}) \right).$$

Exchanging e_α and e_γ and the index k with j on the left hand and using that $c_{kj}^{f_\beta^*} = c_{jk}^{f_\beta^*}$ yields

$$\sum_{j, k \neq j} c_j^{e_\gamma} c_k^{e_\alpha} c_{kj}^{f_\beta^*} B_{e_\gamma}^{f_\beta} = \sum_j c_j^{e_\alpha} S_{E_2}^{\text{loc}}(j, e_\gamma, f_\beta, T_3) / \left(\boldsymbol{\mu}_{gj}^* \cdot \mathbf{E}_{2,j}^{\text{loc}}(\omega_{e_\alpha g}) \right),$$

8 Localized Spectroscopy

so that by dividing the two equations the ratio

$$\frac{B_{e_\alpha}^{f_\beta}}{B_{e_\gamma}^{f_\beta}} = \sum_j \frac{c_j^{e_\gamma} S_{E_2}^{\text{loc}}(j, e_\alpha, f_\beta, T_3)}{c_j^{e_\alpha} S_{E_2}^{\text{loc}}(j, e_\gamma, f_\beta, T_3)}$$

is gained. It can be calculated by the measured or derived quantities for each combination of two arbitrary exciton states e_α and e_γ .

As a next step, again another arbitrary exciton state is chosen – e_ζ . Multiplying Eq. (8.10) by $B_{e_\zeta}^{f_\beta}$ and dividing by $B_{e_\gamma}^{f_\beta}$ yields

$$\sum_{k \neq j} c_k^{e_\alpha} c_{kj}^{f_\beta^*} B_{e_\zeta}^{f_\beta} = S_{E_2}^{\text{loc}}(j, e_\alpha, f_\beta, T_3) / \left(\boldsymbol{\mu}_{gj}^* \cdot \mathbf{E}_{2,j}^{\text{loc}}(\omega_{e_\alpha g}) \right) \cdot B_{e_\zeta}^{f_\beta} / B_{e_\alpha}^{f_\zeta}. \quad (8.11)$$

The special about this equation is that the ratio $B_{e_\zeta}^{f_\beta} / B_{e_\gamma}^{f_\zeta}$ is known and consequently the complete right side of Eq.(8.11). The previous calculation of the ratio $B_{e_\zeta}^{f_\beta} / B_{e_\gamma}^{f_\zeta}$ can thus be exploited to obtain that the sum of the left side of Eq. (8.11) does no longer depend on e_α ! Consequently, the goal of isolating the biexciton wave function is getting closer.

It is just necessary to multiply Eq. (8.11) with $c_i^{e_\alpha^*}$, to sum over e_α , and to apply the orthogonality condition (Eq. (6.25)) to obtain

$$c_{ij}^{f_\beta^*} B_{e_\zeta}^{f_\beta} = \sum_{e_\alpha} c_i^{e_\alpha^*} S_{E_2}^{\text{loc}}(j, e_\alpha, f_\beta, T_3) / \left(\boldsymbol{\mu}_{gj}^* \cdot \mathbf{E}_{2,j}^{\text{loc}}(\omega_{e_\alpha g}) \right) \cdot B_{e_\zeta}^{f_\beta} / B_{e_\alpha}^{f_\zeta}.$$

For extracting the coefficients of the biexciton wave function it is possible to use Eq. (6.24) analogously to finding the single-exciton coefficients. With $\sum_{i,j < i} |c_{ij}^{f_\beta}|^2 = 1$ the coefficients $c_{ij}^{f_\beta}$ are obtained. Finally, via

$$|f_\beta\rangle = \sum_{i,j < i} c_{ij}^{f_\beta} |ij\rangle$$

the biexciton wave function of coupled quantum dots can be reconstructed. Since f_β is chosen arbitrarily, every biexciton wave function can be reconstructed.

Demonstration

Here, the example of a three coupled quantum dot system (Hamiltonian showed in Sec. 6.5.5) is continued. Localization is again discussed for the perfect ratio 1 : 0 : 0 and the reached quality in the theoretical way of Ch. 5.

Tab. 8.3 presents the resulting coefficients for reconstructing the biexciton wave functions. Again, absolute value and phases can be compared for the coefficients $c_{ij}^{f_1}$, $c_{ij}^{f_2}$, and $c_{ij}^{f_3}$ for all quantum dot combinations i and j with $i < j$. That means, that in this example for $n = 3$, Eq. (8.10) has $\frac{3^2-3}{2} + 1 = 4$ unknowns: three biexciton wave functions, $c_{12}^{f_\beta^*}$, $c_{13}^{f_\beta^*}$, and $c_{23}^{f_\beta^*}$, and the factor $B_\alpha^{f_\beta}$.

A closer look to Tab. 8.3 shows: Again, original states and reconstructed values agree but not as well as for the exciton state. The reason is that the biexciton wave functions are calculated on basis of the single-exciton wave functions, which are already not exact. The propagation of uncertainty deteriorates the reconstruction in the biexciton case.

State	Type	Ω_1	Ω_2	$ c_{12}^f $	$ c_{13}^f $	$ c_{23}^f $	$\arg(c_{12}^f)$	$\arg(c_{13}^f)$	$\arg(c_{23}^f)$	Error
f_1	O			0.093	0.118	0.989	0.500	0.500	0.000	
	R ^a	centered ^b		0.095	0.409	0.907	0.559	0.691	0.440	0.22
	R	shifted ^c		0.093	0.361	0.928	0.626	0.767	0.512	0.16
	P ^d	centered		0.140	0.377	0.915	0.313	0.709	0.424	0.19
	P	shifted		0.089	0.322	0.939	0.349	0.789	0.503	0.14
f_2	O			0.988	0.113	0.106	0.500	0.500	0.500	
	R	centered		0.726	0.656	0.206	0.635	0.424	0.223	0.61
	R	shifted		0.738	0.647	0.193	0.689	0.484	0.281	0.59
	P	centered		0.778	0.601	0.184	0.705	0.424	0.257	0.51
	P	shifted		0.793	0.586	0.166	0.762	0.508	0.684	0.48
f_3	O			0.124	0.987	0.106	0.000	0.500	0.500	
	R	centered		0.049	0.963	0.264	0.315	0.498	0.276	0.08
	R	shifted		0.041	0.955	0.294	0.719	0.563	0.358	0.10
	P	centered		0.297	0.921	0.253	0.879	0.464	0.270	0.15
	P	shifted		0.273	0.935	0.225	0.981	0.544	0.358	0.12

^aReconstructed with realistic localization ratio of (1 : 0.1205 : 0.0761)

^bThe frequencies for the measurement points for exciton states are all centered at the resonance peak as given in Tab. 8.1.

^cThe frequencies for the measurement points for exciton states are shifted from the center of the resonance as given in Tab. 8.1.

^dReconstructed with perfect localization ratio (1:0:0)

Table 8.3:

Comparison of original (O) with reconstructed coefficients (R for realistic, P for perfect localization) for reconstructing two-exciton wave functions: As for single-exciton states, the phase is written in multiples of 2π and the energies are in microelectron volts. Here, instead of the measurement point frequencies Ω_1 and Ω_2 , it is just given, if the measurement points for calculating the coefficients for the exciton states are centered at or shifted away from the resonance peak for all three coefficients. Otherwise, the frequencies for all three coefficients would have been printed. The values of the centered and the shifted points are the same as in Tab. 8.1. The phase values are reconstructed up to an arbitrary global phase. In the last column the error relative to the original state is given as explained in Sec. 8.2.2.

Summary

Input: Dipole moments μ_{gi} for all quantum dots i and the single-exciton wave function coefficients c_i^e

Measurement: Full DQCS signal $S(\Omega_1, \Omega_2, T_3)$ to find Ω_1^α and Ω_2^β and localized DQCS signal $S_{E_2}^{\text{loc}}(j, e_\alpha, f_\beta, T_3)$ for desired biexciton coefficient $c_{ij}^{f_\beta}$

Output: Expansion coefficient $c_{ij}^{f_\beta}$ of the double-exciton wave function via $c_{ij}^{f_\beta} = \sum_{e_\alpha} c_i^{e_\alpha*} \cdot S_{E_2}^{\text{loc}}(j, e_\alpha, f_\beta, T_3) / (B_{e_\alpha}^{f_\beta} \mu_{gj}^* \cdot E_{2,j}^{\text{loc}}(\omega_{e_\alpha g})) \cdot B_{e_\alpha}^{f_\beta} / B_{e_\alpha}^{f_\gamma}$, with the relation $B_{e_\alpha}^{f_\beta} / B_{e_\alpha}^{f_\gamma} = \sum_j c_j^{e_\gamma} / c_j^{e_\alpha}$. $S_{E_2}^{\text{loc}}(j, e_\alpha, f_\beta, T_3) / S_{E_2}^{\text{loc}}(j, e_\gamma, f_\beta, T_3)$ and $B_{e_\alpha}^{f_\beta}$ is found by the normalization of the biexciton wave function $|f_\beta\rangle$

8.3 Filtering different resonances

In two-dimensional spectra sometimes it is not immediately clear to which exciton state a resonance peak belongs. The spectrum presented in this chapter can serve as an example. The peak at e_3 with f_2 can perhaps be just a side peak of the peak at e_2 with f_2 or a peak by its own that is covered by the resonance with the strong oscillator strength. To find this out, it would be desirable to remove individual contributions for different exciton states.

Protocol

It turns out that it is possible to gain more detailed spectra by removing certain resonances which might occlude important information. For this purpose, Eq. (8.1) is interpreted as sum over individual contributions q_e for different exciton states e :

$$\begin{aligned} S_{k_{\text{III}}}(\Omega_1, \Omega_2, T_3) &= \sum_e \boldsymbol{\mu}_{ge}^* \cdot \mathbf{E}_1(\omega_{eg}) q_e(\Omega_1, \Omega_2, T_3) \\ &\stackrel{(6.27a)}{=} \sum_e \sum_i c_i^{e*} \boldsymbol{\mu}_{gi}^* \cdot \mathbf{E}_1(\omega_{eg}) q_e(\Omega_1, \Omega_2, T_3). \end{aligned} \quad (8.12)$$

For the localized signal (8.3) it is

$$S_{k_{\text{III}}, E_1}^{\text{loc}}(i, \Omega_1, \Omega_2, T_3) = \sum_e c_i^{e*} \boldsymbol{\mu}_{gi}^* \cdot \mathbf{E}_{1,i}^{\text{loc}}(\omega_{eg}) q_e(\Omega_1, \Omega_2, T_3). \quad (8.13)$$

Filtering a contribution of a selected resonance e_α means subtracting the contribution of e_α from the sum over e :

$$\begin{aligned} S_{k_{\text{III}}}^{\text{Filter}}(\Omega_1, \Omega_2, T_3) &= \sum_e \boldsymbol{\mu}_{ge}^* \cdot \mathbf{E}_1(\omega_{eg}) q_e(\Omega_1, \Omega_2, T_3) \\ &\quad - \boldsymbol{\mu}_{ge_\alpha}^* \cdot \mathbf{E}_1(\omega_{e_\alpha g}) q_{e_\alpha}(\Omega_1, \Omega_2, T_3) \\ &\stackrel{(6.27a)}{=} S_{k_{\text{III}}}(\Omega_1, \Omega_2, T_3) - \sum_i c_i^{e_\alpha*} \boldsymbol{\mu}_{gi}^* \cdot \mathbf{E}_1(\omega_{e_\alpha g}) q_{e_\alpha}(\Omega_1, \Omega_2, T_3) \\ &\stackrel{(8.12)}{=} \sum_{e \neq e_\alpha} \sum_i \boldsymbol{\mu}_{ge}^* \cdot \mathbf{E}_1(\omega_{eg}) q_e(\Omega_1, \Omega_2, T_3). \end{aligned} \quad (8.14)$$

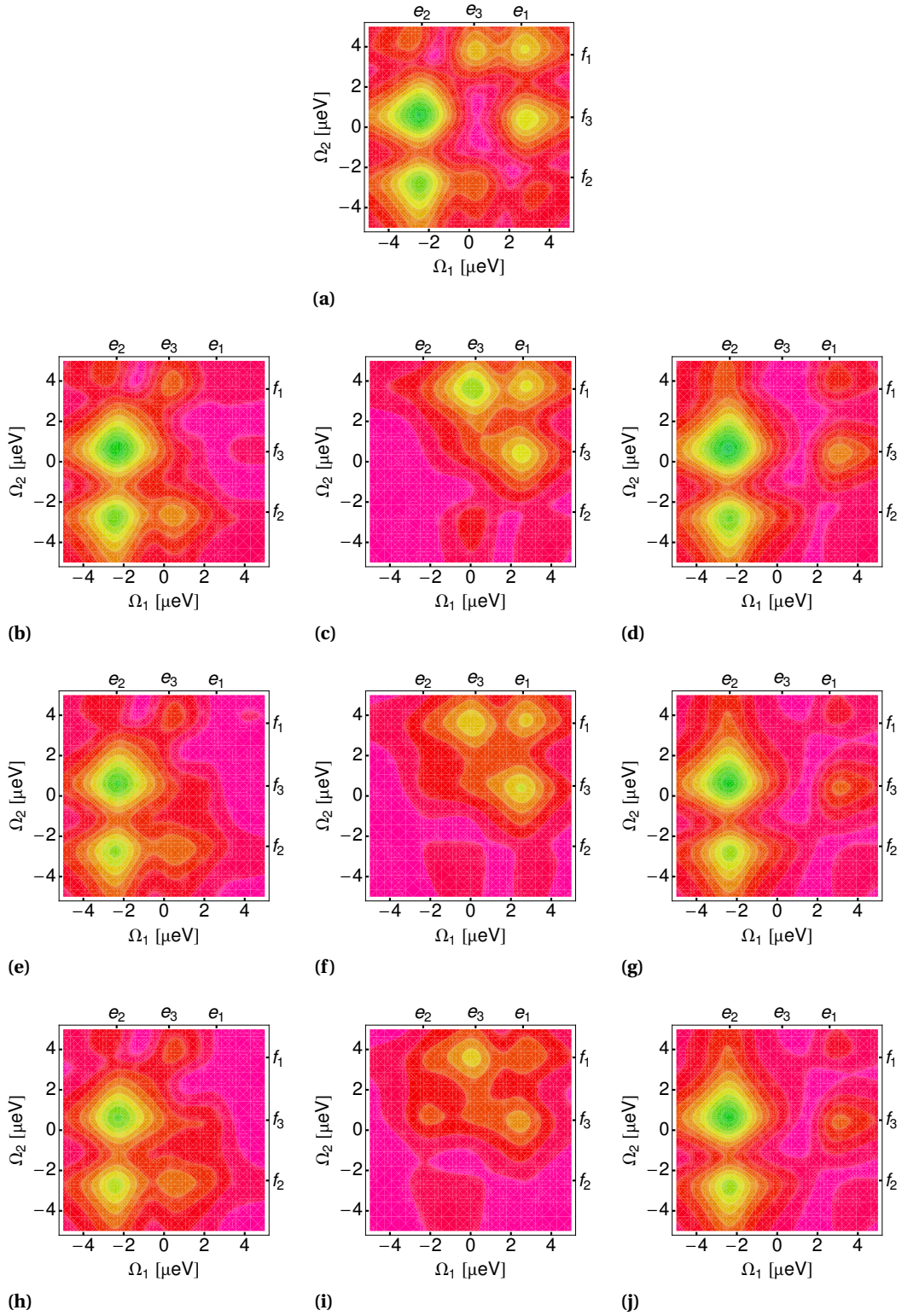
Since the wave function coefficients c_i^e are gained in Sec. 8.2.3 for all i and e , there is only the individual contribution q_{e_α} that has to be derived. It can be found by constructing a scalar product by multiplying Eq. (8.13) with $c_i^{e_\alpha*}$ and summing over i . Again, the orthogonality relation (Eq. (6.25)) is used to obtain only the contributions from the exciton state e_α :

$$q_e(i, \Omega_1, \Omega_2, T_3) = \sum_i c_i^{e_\alpha*} S_{k_{\text{III}}}(i, \Omega_1, \Omega_2, T_3) / \left(\boldsymbol{\mu}_{gi}^* \cdot \mathbf{E}_{1,i}^{\text{loc}}(\omega_{eg}) \right).$$

Finally, the right hand side of Eq. (8.14) serves as filtered spectrum. These contributions can be extracted from the measured data.

Demonstration

In Fig. 8.8b-j the filtered spectrum of the absolute values of the spectrum from Fig. 8.1a is shown. As a reference, Fig 8.1a is plotted again in Fig. 8.8a next to the three filtered spectra for each filtering resonance e_1 , e_2 , and e_3 for a direct comparison. The filtered spectra are presented both, for a perfect localization (Fig 8.8b-d) and for a realistic one in Fig. 8.8e-j. The realistic ones differ additionally in the position of the measuring point.

**Figure 8.8:**

Comparison of filtered spectra: Part (a) shows the absolute values of the original spectrum for the three coupled quantum dot model. Part (b)-(d) presents the filtering method for a perfect localization. While (b) filters the exciton state e_1 , (c) filters state e_2 and (d) filters e_3 . Part (e)-(g) shows same for a realistic localization and in part (h)-(j) the states are removed for the shifted measurement points like discussed in Sec. 8.2.3. All subfigures are plotted in the same range.

All three rows seems very similar at first glance. The first column shows the original spectra without resonances belonging to state e_1 , the center column is almost without peaks for exciton state e_2 and the right column lets the resonances belonging to e_3 vanish. The figures show that the filtering method works quite well.

Similar to Sec. 8.2, the difference between perfect and imperfect localization is not very large. It is although quite visible that the perfect simulation filters the resonances belonging to certain states completely while the second and third row shows larger influences of the other exciton states. In Fig. 8.8f and 8.8i the peak at e_2 with f_2 is much smaller than in Fig. 8.8c. That means that also contributions of e_3 have been removed. Furthermore, not all contributions of e_2 are vanished. In Fig. 8.8i, there is still a clear peak at e_2 with f_3 .

Since the last row shows spectra whose signal is measured at points shifted from the main resonance, the last discussed result shows additionally that for using the filtering method it seems better to use frequencies near the original resonance peak.

Fig. 8.8g does not differ from Fig. 8.8j because shifting the measurement point did not succeed and thus they are calculated with the same signal and consequently the figures are the same.

The peak seen at state e_3 combined with f_3 in all figures on the left, most clearly seen in Fig. 8.8h, shows that the peak at e_3 with f_2 is a peak by its own. That can also be proven by the small resonance at e_3 with f_2 in Figs. 8.8c, f and i. After deducting the contributions of e_2 , still a weak resonance is seen. So that peak is not only a shoulder of the strong resonance at e_2 with f_2 , and the filtering method supplies an answer to the question from the beginning of Sec. 8.3.

8.4 Improvement of reconstructing wave functions with filtering method

The filtering method presented in the previous section can help to improve the quality of the reconstruction: To calculate the expansion coefficients of the wave functions the values of the spectrum near various resonances are used. These values are more accurate the less foreign influences from other resonances come into play. Consequently, it makes sense to subtract states whose coefficients have already been reconstructed.

The results show that filtering can improve the quality of the reconstruction. Tab. 8.4 shows the filtered single and two-exciton states for a perfect localization while Tab. 8.5 gives the results for a realistic localization. Fig. 8.9 visualizes these results for the perfect and realistic localization.

For the exciton state e_3 filtering of two states is possible since the states e_1 and e_2 are now known. The values are not better for every single quantum dot but there is still an overall improvement visible.

Since all exciton states are known, filtering all these states is possible while reconstructing the biexciton states. Again, the filtering technique supplies results of higher quality than without, as can be seen in Tab. 8.3.

8.4 Improvement of reconstructing wave functions with filtering method

State	Type	Ω_1	Ω_2	$ c_1^e $	$ c_2^e $	$ c_3^e $	$\arg(c_1^e)$	$\arg(c_2^e)$	$\arg(c_3^e)$	Error
e_1	O			0.115	0.104	0.988	0.500	0.500	0.000	
e_1, f_3	P	3.12	0.49	0.205	0.081	0.975	0.414	0.190	0.710	0.04
e_2	O			0.977	0.169	0.131	0.500	0.500	0.500	
e_2, f_3	P	-3.20	0.49	0.949	0.110	0.294	0.836	0.820	0.952	0.09
e_2, f_3	F ^a	-3.20	0.49	0.969	0.138	0.205	0.845	0.858	0.650	0.03
e_3	O			0.180	0.980	0.083	0.000	0.500	0.500	
e_3, f_1	P	0.25	3.60	0.360	0.858	0.366	0.342	0.792	0.903	0.28
e_3, f_1	F	0.25	3.60	0.381	0.920	0.093	0.316	0.794	0.968	0.16
e_3, f_1	FF ^b	0.25	3.60	0.138	0.987	0.081	0.302	0.796	0.873	0.02
State	Type	Ω_1	Ω_2	$ c_{12}^f $	$ c_{13}^f $	$ c_{23}^f $	$\arg(c_{12}^f)$	$\arg(c_{13}^f)$	$\arg(c_{23}^f)$	Error
f_1	O			0.093	0.118	0.989	0.500	0.500	0.000	
	P	shifted ^c		0.089	0.332	0.939	0.349	0.789	0.503	0.14
	F ^d	shifted		0.244	0.367	0.898	0.852	0.819	0.525	0.22
f_2	O			0.988	0.113	0.106	0.500	0.500	0.500	
	P	shifted		0.793	0.586	0.166	0.762	0.508	0.684	0.48
	F	shifted		0.845	0.507	0.171	0.628	0.400	0.347	0.36
f_3	O			0.124	0.987	0.106	0.000	0.500	0.500	
	P	shifted		0.273	0.935	0.225	0.981	0.544	0.358	0.12
	F	shifted		0.201	0.946	0.256	0.879	0.580	0.364	0.10

^aReconstructed after filtering state e_1

^bReconstructed after filtering states e_1 and e_2

^cThe frequencies for the measurement points for exciton states are shifted from the center of the resonance as given in Tab. 8.1.

^dReconstruction after filtering all single-exciton states e_1 , e_2 , and e_3

Table 8.4:

Comparison of original (O) and reconstructed coefficients for a perfect localization (P) with coefficients that are calculated after filtering selected states (F for filtering one single-exciton state and FF for filtering two single-excitonic states): The original and reconstructed results are repeated from Tabs. 8.1 and 8.3 for a better comparison. Here, only the results for measurement points shifted from the center of the resonance peak are listed. Still, the phase is written in multiples of 2π (up to an arbitrary global phase), and the energies are in microelectron volts. All columns have the same meaning as in Tabs. 8.1 and 8.3. In Tab. 8.5 the results for a realistic localization are found.

State	Type	Ω_1	Ω_2	$ c_1^e $	$ c_2^e $	$ c_3^e $	$\arg(c_1^e)$	$\arg(c_2^e)$	$\arg(c_3^e)$	Error
e_1	O			0.115	0.104	0.988	0.500	0.500	0.000	
e_1, f_3	R	3.12	0.49	0.199	0.034	0.979	0.465	0.685	0.707	0.03
e_2	O			0.977	0.169	0.131	0.500	0.500	0.500	
e_2, f_3	R	-3.20	0.49	0.910	0.194	0.366	0.839	0.846	0.919	0.17
e_2, f_3	F ^a	-3.20	0.49	0.966	0.169	0.196	0.845	0.795	0.576	0.03
e_3	O			0.180	0.980	0.083	0.000	0.500	0.500	
e_3, f_1	R	0.25	3.60	0.244	0.890	0.386	0.357	0.796	0.893	0.22
e_3, f_1	F	0.25	3.60	0.333	0.940	0.078	0.315	0.792	0.137	0.11
e_3, f_1	FF ^b	0.25	3.60	0.202	0.978	0.047	0.345	0.790	0.161	0.01
State	Type	Ω_1	Ω_2	$ c_{12}^f $	$ c_{13}^f $	$ c_{23}^f $	$\arg(c_{12}^f)$	$\arg(c_{13}^f)$	$\arg(c_{23}^f)$	Error
f_1	O			0.093	0.118	0.989	0.500	0.500	0.000	
	R	shifted ^c		0.093	0.361	0.928	0.627	0.768	0.513	0.16
	F ^d	shifted		0.287	0.360	0.888	0.798	0.789	0.529	0.23
f_2	O			0.988	0.113	0.106	0.500	0.500	0.500	
	R	shifted		0.738	0.647	0.193	0.690	0.485	0.282	0.59
	F	shifted		0.845	0.498	0.194	0.574	0.383	0.362	0.35
f_3	O			0.124	0.987	0.106	0.000	0.500	0.500	
	R	shifted		0.041	0.955	0.295	0.719	0.564	0.358	0.10
	F	shifted		0.210	0.943	0.260	0.766	0.575	0.375	0.11

^aReconstructed after filtering state e_1

^bReconstructed after filtering states e_1 and e_2

^cThe frequencies for the measurement points for exciton states are shifted from the center of the resonance as given in Tab. 8.1.

^dReconstruction after filtering all single-exciton states e_1 , e_2 , and e_3

Table 8.5:

Comparison of original (O) and reconstructed coefficients for a realistic localization (R) with coefficients that are calculated after filtering selected states (F for filtering one single-excitonic state and FF for filtering two single-excitonic states): In comparison to Tab. 8.4, here the results for a realistic localization are found. Again, the original and reconstructed results are repeated from Tabs. 8.1 and 8.3 for a better comparison. Only the results for measurement points shifted from the center of the resonance peak are listed. Still, the phase (that is determined up to an arbitrary global phase) is written in multiples of 2π and the energies are in microelectron volts. All columns have the same meaning as in Tabs. 8.1 and 8.3.

8.4 Improvement of reconstructing wave functions with filtering method

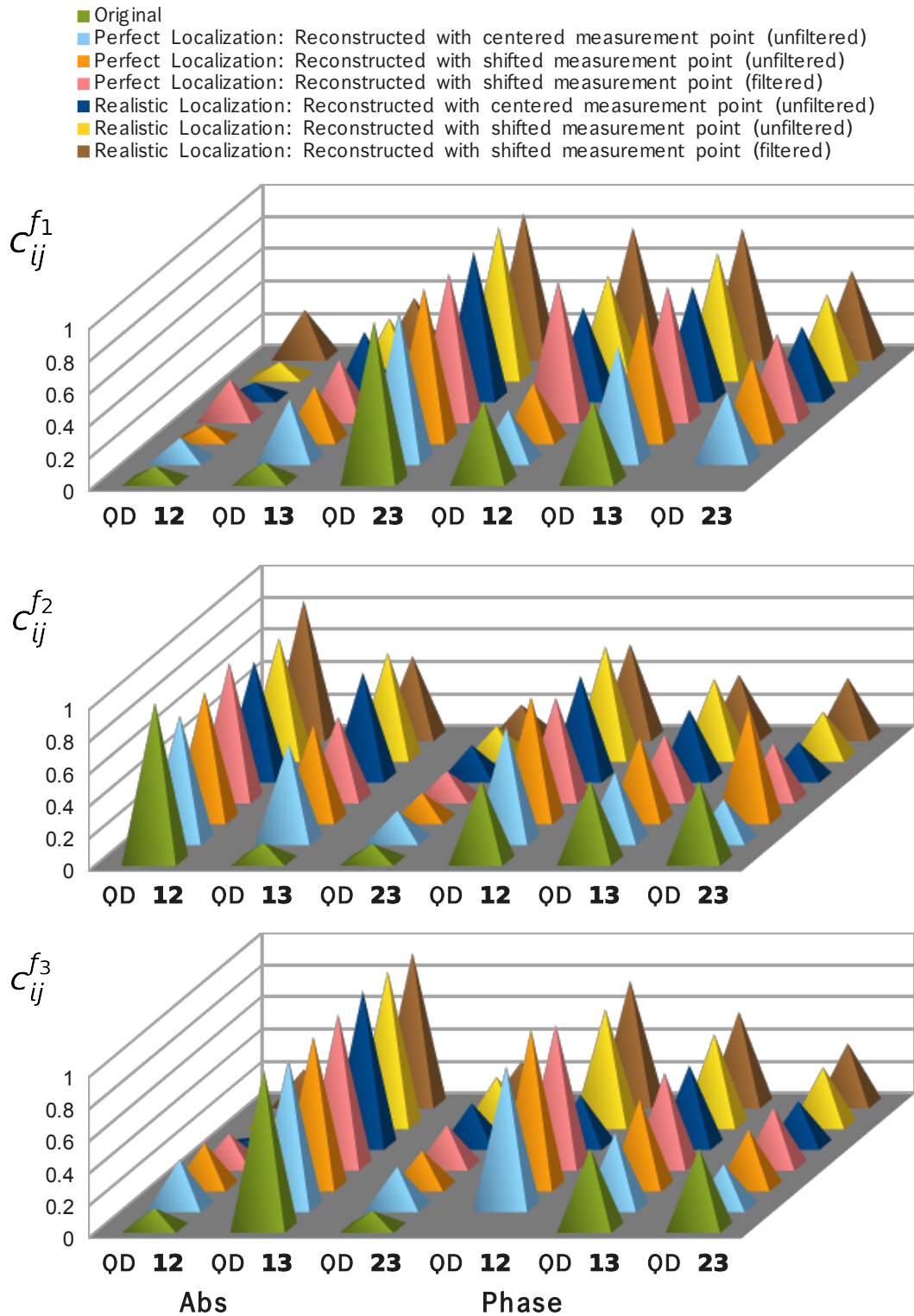


Figure 8.9: Illustration of reconstructed biexciton wave function coefficients: The original wave function coefficients are compared with different versions of reconstructing. The measurement points can also be found in Tab. 8.1.

Part V

Epilogue

9 Conclusion and Outlook

In essence, this thesis is about spatiotemporal control of optical excitations in nanostructures. Foundations and the main results of this topic form part II, the first thematic part of the work. Part III deals with coherent nonlinear spectroscopy methods so that in part IV an application of the localization can be treated.

Part II starts with investigations of many different nanostructures targeted at localization of light. For this purpose, focus lies on the plasmonic properties of metals. A material model is generated based on the introduced theoretical foundations. Band structure calculations are presented and the dipole transition matrix elements and a linear absorption spectrum of light is calculated as first results.

In Ch. 3 the plasmonic effects of nanospheres are investigated. Wavelength dependent enhancements of the electric field near the surface of the sphere are found while the strongest one is always in polarization direction of the incoming light. It has also been shown, that platinum or gold coatings of silver nanospheres can transfer the plasmonic enhancement over long distances. Other metals in vicinity magnify the electric field due to plasmonic interactions.

The examined properties are used in induced surface enhancement technologies like surface enhanced Raman spectroscopy (see Sec. 3.4) or as a main effect that helps controlling light within nanostructures (Ch. 5). All presented structures in that Ch. 5 aim at concentrating light within nanometer length scales and femtosecond time scales. A genetic algorithm is designed, that optimizes the shape of incoming light pulses, to achieve a selected excitation of coupled quantum systems. For this purpose, field distributions for different incoming pulses are calculated by a Maxwell solver based on the finite element method. These distributions are then compared via a cost function.

In the entire work, three coupled self organized GaAs/InAs quantum dots serve as a model to demonstrate the localization of light. It turns out that 120° symmetric structures are particularly suitable for exciting only one arbitrary quantum dot. There exist different waveguide-like geometries or antenna-like geometries that fulfill the requirements of localization. Several different geometries with variable arrangements of the nanostructures are tested but they are not analyzed completely nor even fully understood yet. For example, Tab. 5.1 shows different qualities of optimization for different scales. It is not clear, if the different results are consequences of the randomness of the genetic algorithm or if they are physical effects.

Thus, many more investigations are conceivable. Especially, a future detailed evaluation of the complex electric field in each spatial point in frequency domain may be helpful. This analysis is omitted in this thesis because an already sufficient localization that is necessary for localized spectroscopy is found even without a complete understanding of all physics within the nanostructure.

Most works that try to localize light also use optimization algorithms. The effects of shaped pulses on nanostructures are very complex, so that often physical reasons why a pulse has a certain final form are not fully understood. Some works examine the behavior of light concentration depending on the pulse shape (e.g [MBS⁺11]) – often less by means of physics but more of trial and error. Future investigation may gain new insight.

There also exist many ideas on how the simulation and the genetic algorithm may be improved: for example, chirped pulses could be introduced and more than one population of

9 Conclusion and Outlook

pulses may be calculated parallelly, thus mixing the best children of both populations. It is desirable to find an allocation matrix that maps the electric field components of the incoming pulses to the electric field components of all spatial points of interest within the nanostructure (cf. Sec. 5.2).

Continuing this thesis' research, the achieved localization allows an extension of a multi-dimensional coherent nonlinear spectroscopy method, the double quantum coherence technique. For this purpose, in part III the theoretical foundations of coherent nonlinear spectroscopy methods are given. Combining these techniques with the results of Ch. 5 leads to part IV, which introduces and discusses localized spectroscopy – a method that allows reconstructing delocalized wave functions of coupled quantum dots: A quantum state tomography protocol is given that instructs how complex hybrid wave functions can be disentangled into wave functions of the individual emitters. Detailed information on the couplings of the individual quantum dots is found that is not available in far-field spectroscopy. The localized spectroscopy method can be applied to a broad range of coupled emitters, for example in semiconductor nanostructures, artificial light harvesting, pigments in photosynthesis or composite systems like plasmon lasers.

The coefficients for decomposition the delocalized wave functions in a local basis are found in order to reconstruct these delocalized functions – up to an arbitrary phase. The localization for the first pulse, that is responsible for the ground state to single-exciton transition, leads to the wave function coefficients for single-excitons. An additional localization of the second pulse of double quantum coherence spectroscopy, that excites the single-exciton to the double-exciton state, helps to extract the two-exciton coefficients.

Furthermore it turns out that localized spectroscopy can use as a filtering method to remove unwanted strong resonances of two-dimensional spectra to uncover weak or hidden exciton resonances. This filtering method reduces the influences of neighboring resonances and thus they improve the quality of wave function coefficients reconstruction. Of course, this quality also depends on the quality of light concentration.

This work shows that measuring the signal near a resonance can be improved by moving the measurement point in a direction with lower influences of other resonances. Due to destructive interference this process does not work in every case as is shown by example in Sec. 8.2.3 on page 113: A shifted measuring point worsens the reconstruction quality of exciton state e_2 but after filtering other resonances, the quality improves for e_2 .

Consequently, an idea for further investigation in increasing the quality of reconstruction may be averaging the signal over a number of measurement points. For example, the average of four signal values in each direction of the two-dimensional plot around the resonance peak could improve the reconstruction. Even integrating over a small area around the main peak is conceivable. Additional weighting of the results with a Gaussian centered at the main resonance peak could provide the best results. But generally, the influences of other resonances are not as strong as they seem: A Lorentzian decay is assumed – a Lorentzian shape decreases usually slower than is the case in reality.

As for the area of application of the methods presented in this thesis, they are not limited to the example of coupled self organized GaAs/InAs dots. In principle, they are applicable to any system of dipole coupled two-level system emitters describable by Hamiltonian from Eq. (6.23). Such a system can consist of plasmons in coupled metal nanoparticles, coupled chromospheres, or colloidal quantum dots, as long as a sufficient localization technique exists.

As additional requirement the dipole couplings between the emitters should be greater than the linewidth of the resonances (dephasing time) in order to be able to separate the delocalized states. For achieving a delocalization the detuning of the individual emitter transition

frequency should be smaller than or have the same order of magnitude as the dipole-dipole coupling – but still high enough to separate exciton states. Generalization to emitters with more than two levels is possible although the appearing influences might be difficult.

All features of localized spectroscopy originally found in this thesis are not accessible in standard far-field spectroscopy. The proposed quantum state tomography protocol opens a new path for the detection of many-body interactions on the nanoscale.

A Appendix

A.1 Quantum mechanical approach for equations of motion for the polarization

In Sec. 2.2.2, the equations of motion for the intraband and interband transitions in a metal – described by the dipole density \mathbf{P} – are given. Here, a quantum mechanical approach derives the equation to obtain a well controlled model system.

A.1.1 Intraband transitions

To calculate the equation of motion for the dipole density for intraband transitions in a quantum mechanical approach, a Hamiltonian which describes the free dynamic of an electron in an electric field is used. That means that only the part of the equation that deals with a free electron and the part that deals with the electron-field interaction is of interest:

$$H = \underbrace{\sum_{\mathbf{k}} \epsilon_{\mathbf{k}} a_{\mathbf{k}}^{\dagger} a_{\mathbf{k}}}_{H_0} - i q \underbrace{\sum_{\mathbf{k}} \mathbf{E} \cdot \nabla_{\mathbf{k}} a_{\mathbf{k}}^{\dagger} a_{\mathbf{k}}}_{H_{\text{el-field}}}.$$

The arrow means that nabla only affects the second operator. To obtain the current $\mathbf{j} = \frac{e}{m_{\text{eff}}} \sum_{\mathbf{k}} p \sigma_{\mathbf{k}}$, the equation of motion for the electron occupation $\sigma_{\mathbf{k}} = \langle a_{\mathbf{k}}^{\dagger} a_{\mathbf{k}} \rangle$ are calculated that results in:

$$-i\hbar \left(\frac{\partial}{\partial t} + \frac{q}{\hbar} \mathbf{E} \cdot \nabla_{\mathbf{k}} \right) \sigma_{\mathbf{k}}(t) = 0.$$

To introduce the electron-phonon scattering, the electron occupation is split in a well-known Fermi function and a perturbation term caused by the electric field: $\sigma_{\mathbf{k}} = \sigma_{\mathbf{k}}^0 + \sigma_{\mathbf{k}}^1$. The first part of the equation of motion is the stationary solution and vanishes, to the second part a relaxation rate approximation is applied:

$$\left. \frac{\partial}{\partial t} \sigma_{\mathbf{k}} \right|_{\text{el-ph}} = \left. \frac{\partial}{\partial t} \sigma_{\mathbf{k}}^0 \right|_{\text{el-ph}} + \left. \frac{\partial}{\partial t} \sigma_{\mathbf{k}}^1 \right|_{\text{el-ph}} = 0 - \gamma_{\mathbf{k}} \sigma_{\mathbf{k}}^1.$$

In summary for the electronic transport is obtained:

$$\left(\frac{\partial}{\partial t} + \frac{q}{\hbar} \mathbf{E} \cdot \nabla_{\mathbf{k}} \right) (\sigma_{\mathbf{k}}^0 + \sigma_{\mathbf{k}}^1) = -\gamma_{\mathbf{k}} \sigma_{\mathbf{k}}^1.$$

Reordering and neglect of the part proportional to $E\sigma^1 \sim E^2$ (just linear response) yield:

$$\frac{\partial}{\partial t} \sigma_{\mathbf{k}}^1 = -\frac{e}{\hbar} \mathbf{E} \cdot \nabla_{\mathbf{k}} \sigma_{\mathbf{k}}^1 - \gamma_{\mathbf{k}} \sigma_{\mathbf{k}}^1. \quad (\text{A.1})$$

A Appendix

The current is defined by $\mathbf{j} = \frac{\hbar e}{m_{\text{eff}}} \sum_{\mathbf{k}} \mathbf{k} \sigma_{\mathbf{k}}$. Multiplying equation (A.1) by $\frac{\hbar e}{m_{\text{eff}}} \sum_{\mathbf{k}} \mathbf{k}$ gives

$$\underbrace{\frac{\hbar e}{m_{\text{eff}}} \sum_{\mathbf{k}} \mathbf{k} \frac{\partial}{\partial t} \sigma_{\mathbf{k}}^1}_{\frac{\partial}{\partial t} \mathbf{j}} = - \underbrace{\frac{e}{m_{\text{eff}}} \sum_{\mathbf{k}} \mathbf{k} e \mathbf{E} \cdot \nabla_{\mathbf{k}} \sigma_{\mathbf{k}}^1}_{\frac{e^2}{m_{\text{eff}}} E n} - \underbrace{\gamma_{\text{pl}} \frac{\hbar e}{m_{\text{eff}}} \sum_{\mathbf{k}} \mathbf{k} \sigma_{\mathbf{k}}^1}_{\gamma_{\text{pl}} \mathbf{j}} \quad \text{with } \gamma_{\mathbf{k}} \approx \gamma_{\text{pl}}. \quad (\text{A.2})$$

The ∇ could be evaluated by a partial integration and n is the electron density that results from the sum over the Fermi function.

Eliminating the electron density from equation (2.13) and inserting it into equation (A.2) yield:

$$\frac{\partial}{\partial t} \mathbf{j} = \varepsilon_0 \omega_{\text{pl}}^2 \mathbf{E} - \gamma_{\text{pl}} \mathbf{j}.$$

Using $\frac{\partial}{\partial t} \mathbf{P}_{\text{intra}} = \mathbf{j}$ gives the equation of motion for the polarization (2.16).

A.1.2 Interband transitions

To deduce an equation of motion for the polarization for interband transitions in a quantum mechanical approach, a Hamiltonian is used consisting of the free electron part H_0 and the part H_ω which describes the dipole coupling to a classical electric field in Coulomb gauge. In this simple model the part which represents the Coulomb interaction is neglected. Applying the second quantization for the ground state d and the excited state p yields (see figure 2.2):

$$H^{\text{dp}} = \underbrace{\sum_{\mathbf{k}'} (\epsilon_{\mathbf{k}'}^{\text{p}} a_{\text{p},\mathbf{k}'}^\dagger a_{\text{p},\mathbf{k}'} + \epsilon_{\mathbf{k}'}^{\text{d}} a_{\text{d},\mathbf{k}'}^\dagger a_{\text{d},\mathbf{k}'})}_{H_0^{\text{dp}}} - \underbrace{\sum_{\mathbf{k}''} [d_{\text{dp}} a_{\text{d},\mathbf{k}''}^\dagger a_{\text{p},\mathbf{k}''} + d_{\text{pd}} a_{\text{p},\mathbf{k}''}^\dagger a_{\text{d},\mathbf{k}''}]}_{H_\omega^{\text{dp}}} E(\mathbf{r}, t)$$

where a^\dagger and a are the fermion creation and annihilation operators of the lower d and the upper p state, respectively. The energy of the states is ϵ , d_{dp} is the dipole transition matrix element and \mathbf{E} is the electric field. The sum is taken over the electronic modes.

The macroscopic polarization $\mathbf{P}_{\text{inter}}^{(1)}$ is the sum taken over the microscopic polarizations $\mathbf{p}_{\mathbf{k}'}^{(1)}$ weighted with the corresponding dipole matrix element and divided by the volume V (cf. Eq. (2.21)):

$$\mathbf{P}_{\text{inter}}^{(1)} = \frac{1}{V} \sum_{\mathbf{k}} (\mathbf{p}_{\mathbf{k}}^{(1)} \cdot d_{\text{pd}} + \mathbf{p}_{\mathbf{k}}^{(1)*} \cdot d_{\text{pd}}^*) \quad \text{with } \mathbf{p}_{\mathbf{k}}^{(1)} = \langle a_{\text{d},\mathbf{k}}^\dagger a_{\text{p},\mathbf{k}} \rangle. \quad (\text{A.3})$$

The index '1' denotes the first transition (d-p).

The equation of motion for the microscopic polarization is obtained by Heisenberg's equation of motion:

$$i\hbar \frac{\partial}{\partial t} \mathbf{p}_{\mathbf{k}}^{(1)} = [\mathbf{p}_{\mathbf{k}}^{(1)}, H^{\text{dp}}]_-.$$

A.1 Quantum mechanical approach for equations of motion for the polarization

Therefore two commutators have to be calculated. With

$$\begin{aligned} [\mathbf{p}_k^{(1)}, H_0^{\text{dp}}]_- &= \sum_{k'} (\epsilon_{k'}^{\text{p}} \underbrace{[a_{\text{d},k}^\dagger a_{\text{p},k}, a_{\text{p},k'}^\dagger a_{\text{p},k'}]_-}_{a_{\text{d},k}^\dagger a_{\text{p},k'} \delta_{k',k}} + \epsilon_{k'}^{\text{d}} \underbrace{[a_{\text{d},k}^\dagger a_{\text{p},k}, a_{\text{d},k'}^\dagger a_{\text{d},k'}]_-}_{-a_{\text{d},k'}^\dagger a_{\text{p},k} \delta_{k',k}}) \\ &= (\epsilon_k^{\text{p}} - \epsilon_k^{\text{d}}) \underbrace{a_{\text{d},k}^\dagger a_{\text{p},k}}_{\mathbf{p}_k^{(1)}} \end{aligned}$$

and

$$\begin{aligned} [\mathbf{p}_k^{(1)}, H_\omega^{\text{dp}}]_- &= - \sum_{k''} (d_{\text{dp}} \underbrace{[a_{\text{d},k}^\dagger a_{\text{p},k}, a_{\text{d},k''}^\dagger a_{\text{p},k''}]_-}_0 + d_{\text{pd}} \underbrace{[a_{\text{d},k}^\dagger a_{\text{p},k}, a_{\text{p},k''}^\dagger a_{\text{d},k''}]_-}_{a_{\text{d},k}^\dagger a_{\text{d},k''} \delta_{k'',k} - a_{\text{p},k''}^\dagger a_{\text{p},k} \delta_{k'',k}}) \mathbf{E}(t) \\ &= - d_{\text{pd}} (\underbrace{a_{\text{d},k}^\dagger a_{\text{d},k}}_{n_k^{\text{d}}} - \underbrace{a_{\text{p},k}^\dagger a_{\text{p},k}}_{n_k^{\text{p}}}) \mathbf{E}(t) \end{aligned}$$

result:

$$[\mathbf{p}_k^{(1)}, H^{\text{dp}}]_- = [\mathbf{p}_k^{(1)}, H_0^{\text{dp}}]_- + [\mathbf{p}_k^{(1)}, H_\omega^{\text{dp}}]_- = \underbrace{(\epsilon_k^{\text{p}} - \epsilon_k^{\text{d}})}_{\hbar\omega_1} \mathbf{p}_k^{(1)} - d_{\text{pd}} (n_k^{\text{d}} - n_k^{\text{p}}) \mathbf{E}(t).$$

After repeating all these steps analog for the second transition (p-s instead of d-p), one obtains:

$$[\mathbf{p}_k^{(2)}, H^{\text{ps}}]_- = [\mathbf{p}_k^{(2)}, H_0^{\text{ps}}]_- + [\mathbf{p}_k^{(2)}, H_\omega^{\text{ps}}]_- = \underbrace{(\epsilon_k^{\text{s}} - \epsilon_k^{\text{p}})}_{\hbar\omega_2} \mathbf{p}_k^{(2)} - d_{\text{sp}} (n_k^{\text{p}} - n_k^{\text{s}}) \mathbf{E}(t).$$

The energy difference is given by $\epsilon_k^{\text{p}} - \epsilon_k^{\text{d}} = \hbar\omega_1$ and $\epsilon_k^{\text{s}} - \epsilon_k^{\text{p}} = \hbar\omega_2$. The occupation from the lower bands is obtained from Fermi function calculations and for the upper bands the occupation can be set to zero.

The equation of motion for the microscopic polarizations (see also [CK99, HK04]) reads

$$\begin{aligned} \left[i\hbar \frac{\partial}{\partial t} - (\hbar\omega_1 + i\gamma_1) \right] \mathbf{p}_k^{(1)}(t) &= -(n_k^{\text{d}} - n_k^{\text{p}}) d_{\text{pd}} \mathbf{E}(t) \quad \text{and} \\ \left[i\hbar \frac{\partial}{\partial t} - (\hbar\omega_2 + i\gamma_2) \right] \mathbf{p}_k^{(2)}(t) &= -(n_k^{\text{p}} - n_k^{\text{s}}) d_{\text{sp}} \mathbf{E}(t) \end{aligned} \tag{A.4}$$

where phenomenological damping parameters γ_1 and γ_2 are included, which suit the experiments, to the energy of the band gap. If constant energy gaps $\hbar\omega_1$ and $\hbar\omega_2$ are assumed, equation (A.3) and $N = \frac{1}{V} \sum_k n_k$ can be used to get:

$$\begin{aligned} \left[i\hbar \frac{\partial}{\partial t} - (\hbar\omega_1 + i\gamma_2) \right] \mathbf{P}_{\text{inter}}^{(1)}(t) &= -(N^{\text{d}} - N^{\text{p}}) |d_{\text{pd}}|^2 \mathbf{E}(t) \quad \text{and} \\ \left[i\hbar \frac{\partial}{\partial t} - (\hbar\omega_2 + i\gamma_2) \right] \mathbf{P}_{\text{inter}}^{(2)}(t) &= -(N^{\text{p}} - N^{\text{s}}) |d_{\text{sp}}|^2 \mathbf{E}(t). \end{aligned} \tag{A.5}$$

Comparison with the classical model

This subsection is aimed to write equation (A.5) only with known parameters from section 2.2.3. For this purpose, a transform of equation (A.5) is done to compare it with (A.6), provided by reference [DRK⁺10]:

$$\begin{aligned} \widehat{\chi}(\omega) = & A_1 \epsilon_1 \left(\frac{1}{\hbar\omega_1 - \hbar\omega - i\gamma_1} + \frac{1}{\hbar\omega_1 + \hbar\omega + i\gamma_1} \right) \\ & + A_2 \epsilon_2 \left(\frac{1}{\hbar\omega_2 - \hbar\omega - i\gamma_2} + \frac{1}{\hbar\omega_2 + \hbar\omega + i\gamma_2} \right) \end{aligned} \quad (\text{A.6})$$

where $\epsilon_j = \hbar\omega_j$ for $j = \{1, 2\}$ is used. The factor $e^{i\phi}$ belongs to the more general approach of the dielectric function and can be neglected in two level systems.

The following calculations are only shown for the first transition, the p-s transition works analogously. For the first step an inverse Fourier transform is needed $\widehat{\mathbf{p}}_{\mathbf{k}}^{(1)}(\omega) = \int_{-\infty}^{\infty} \mathbf{p}_{\mathbf{k}}^{(1)}(t) e^{-i\omega t} dt$ to transfer equation (A.4) into the frequency domain (the hat symbolizes the Fourier transform of the function):

$$\int_{-\infty}^{\infty} \left(\underbrace{[i\hbar \frac{\partial}{\partial t} - (\hbar\omega_1 + i\gamma_1)]}_{-\hbar\omega} \mathbf{p}_{\mathbf{k}}^{(1)}(t) \right) e^{-i\omega t} dt = -(n_{\mathbf{k}}^{\text{d}} - n_{\mathbf{k}}^{\text{p}}) d_{\text{pd}} \int_{-\infty}^{\infty} \mathbf{E}(t) e^{-i\omega t} dt.$$

The replacement of the time derivation follows from $\int_{-\infty}^{\infty} f'(t) e^{-i\omega t} dt = i\omega \widehat{f}(\omega)$. This equation can be shown by partial integration. The microscopic polarization in frequency domain reads:

$$\widehat{\mathbf{p}}_{\mathbf{k}}^{(1)}(\omega) = \frac{-(n_{\mathbf{k}}^{\text{d}} - n_{\mathbf{k}}^{\text{p}}) d_{\text{pd}} \widehat{\mathbf{E}}(\omega)}{-\hbar\omega - \hbar\omega_1 - i\gamma_1}. \quad (\text{A.7})$$

To find the conjugated microscopic polarization, equation (A.4) is conjugated and transformed again with $\widehat{\mathbf{p}}_{\mathbf{k}}^{(1)*}(\omega) = \int_{-\infty}^{\infty} \mathbf{p}_{\mathbf{k}}^{(1)*}(t) e^{-i\omega t} dt$:

$$\left[\underbrace{-i\hbar \frac{\partial}{\partial t}}_{\hbar\omega} - (\hbar\omega_1 - i\gamma_1) \right] \underbrace{\int_{-\infty}^{\infty} \mathbf{p}_{\mathbf{k}}^{(1)*}(t) e^{-i\omega t} dt}_{\widehat{\mathbf{p}}_{\mathbf{k}}^{(1)*}(\omega)} = -(n_{\mathbf{k}}^{\text{d}} - n_{\mathbf{k}}^{\text{p}}) d_{\text{pd}}^* \underbrace{\int_{-\infty}^{\infty} \overbrace{\mathbf{E}^*(t)}^{\mathbf{E}(t) \in \mathbb{R}} e^{-i\omega t} dt}_{\widehat{\mathbf{E}}(\omega)}.$$

That yields:

$$\widehat{\mathbf{p}}_{\mathbf{k}}^{(1)*} = \frac{-(n_{\mathbf{k}}^{\text{d}} - n_{\mathbf{k}}^{\text{p}}) d_{\text{pd}}^* \widehat{\mathbf{E}}(\omega)}{\hbar\omega - \hbar\omega_1 + i\gamma_1}. \quad (\text{A.8})$$

Now equation (A.7) and (A.8) is inserted into the macroscopic polarization

$$\widehat{\mathbf{P}}(\omega) = \frac{1}{V} \sum_{\mathbf{k}} \left[\widehat{\mathbf{p}}_{\mathbf{k}}^{(1)}(\omega) d_{\text{dp}} + \widehat{\mathbf{p}}_{\mathbf{k}}^{(1)*}(\omega) d_{\text{dp}}^* + \widehat{\mathbf{p}}_{\mathbf{k}}^{(2)}(\omega) d_{\text{ps}} + \widehat{\mathbf{p}}_{\mathbf{k}}^{(2)*}(\omega) d_{\text{ps}}^* \right].$$

If a constant energy gap $\hbar\omega_1$ and $\hbar\omega_2$ is assumed, with $N = \frac{1}{V} \sum_{\mathbf{k}} n_{\mathbf{k}}$ can be found:

$$\begin{aligned} \widehat{\mathbf{P}}(\omega) = & -(N^{\text{d}} - N^{\text{p}}) |d_{\text{pd}}|^2 \widehat{\mathbf{E}}(\omega) \left(\frac{1}{-\hbar\omega - \hbar\omega_1 - i\gamma_1} + \frac{1}{\hbar\omega - \hbar\omega_1 + i\gamma_1} \right) \\ & - (N^{\text{p}} - N^{\text{s}}) |d_{\text{sp}}|^2 \widehat{\mathbf{E}}(\omega) \left(\frac{1}{-\hbar\omega - \hbar\omega_2 - i\gamma_2} + \frac{1}{\hbar\omega - \hbar\omega_2 + i\gamma_2} \right). \end{aligned} \quad (\text{A.9})$$

A.1 Quantum mechanical approach for equations of motion for the polarization

Because of the identity

$$\begin{aligned}\widehat{\mathbf{D}}(\mathbf{r}, \omega) &= \varepsilon_0 \widehat{\mathbf{E}}(\mathbf{r}, \omega) + \widehat{\mathbf{P}}_{\text{intra}}(\mathbf{r}, \omega) = \varepsilon_0 \widehat{\mathbf{E}}(\mathbf{r}, \omega) + \varepsilon_0 \widehat{\chi}(\mathbf{r}, \omega) \widehat{\mathbf{E}}(\mathbf{r}, \omega) \\ &= \varepsilon_0 (1 + \widehat{\chi}(\mathbf{r}, \omega)) \widehat{\mathbf{E}}(\mathbf{r}, \omega) = \varepsilon_0 \widehat{\varepsilon}(\mathbf{r}, \omega) \widehat{\mathbf{E}}(\mathbf{r}, \omega)\end{aligned}$$

with $\widehat{\varepsilon}(\mathbf{r}, \omega)$ as Fourier transform of $\varepsilon(\mathbf{r}, t)$ in the Drude model, equation (A.9) has to be divided by $\widehat{\mathbf{E}}(\omega)$ and ε_0 to obtain the susceptibility:

$$\begin{aligned}\widehat{\chi}(\omega) &= \frac{1}{\varepsilon_0} (N^{\text{d}} - N^{\text{p}}) |d_{\text{pd}}|^2 \left(\frac{1}{\hbar\omega_1 - \hbar\omega - i\gamma_1} + \frac{1}{\hbar\omega_1 + \hbar\omega + i\gamma_1} \right) \\ &\quad + \frac{1}{\varepsilon_0} (N^{\text{p}} - N^{\text{s}}) |d_{\text{sp}}|^2 \left(\frac{1}{\hbar\omega_2 - \hbar\omega - i\gamma_2} + \frac{1}{\hbar\omega_2 + \hbar\omega + i\gamma_2} \right).\end{aligned}\tag{A.10}$$

Now, this equation can be compared with equation (A.6) of the interband transition part of the dielectric function and the relations between the parameters provide

$$A_1 \varepsilon_1 = \frac{1}{\varepsilon_0} (N^{\text{d}} - N^{\text{p}}) |d_{\text{pd}}|^2 \quad \text{and} \quad A_2 \varepsilon_2 = \frac{1}{\varepsilon_0} (N^{\text{p}} - N^{\text{s}}) |d_{\text{sp}}|^2$$

that yields to the equation of motion of the polarization with the known parameters (2.17).

A.2 Atomic wave functions

In this section the hydrogen wave functions and the atomic orbitals are given explicitly as needed in Sec. 2.3.2.

A.2.1 Hydrogenic wave functions

In general, the hydrogen wave function can be split in the hydrogen radial part R and in spherical harmonics Y :

$$\Psi_{nlm} = R_{nl}(r) Y_{lm}(\theta, \phi).$$

The explicit form of the hydrogen wave functions of the outer orbitals are (according to [Dem05] and [Bei02]):

$$\begin{aligned} \Psi_{5,0,0}(x, y, z, Z_{\text{eff}}) &= \frac{1}{46875 a_0^4 \sqrt{5\pi}} e^{-\frac{\sqrt{x^2+y^2+z^2} Z_{\text{eff}}}{5a_0}} \sqrt{\frac{Z_{\text{eff}}^3}{a_0^3}} \\ &\times (9375 a_0^4 - 7500 a_0^3 \sqrt{x^2 + y^2 + z^2} Z_{\text{eff}} + 1500 a_0^2 \sqrt{x^2 + y^2 + z^2}^2 Z_{\text{eff}}^2 \\ &- 100 a_0 \sqrt{x^2 + y^2 + z^2}^3 Z_{\text{eff}}^3 + 2 \sqrt{x^2 + y^2 + z^2}^4 Z_{\text{eff}}^4) \end{aligned}$$

$$\begin{aligned} \Psi_{4,1,0}(x, y, z, Z_{\text{eff}}) &= \frac{1}{512 a_0^3 \sqrt{5\pi}} e^{-\frac{\sqrt{x^2+y^2+z^2} Z_{\text{eff}}}{4a_0}} z Z_{\text{eff}} \sqrt{\frac{Z_{\text{eff}}^3}{a_0^3}} \\ &\times (80 a_0^2 - 20 a_0 \sqrt{x^2 + y^2 + z^2} Z_{\text{eff}} + \sqrt{x^2 + y^2 + z^2}^2 Z_{\text{eff}}^2) \end{aligned}$$

$$\begin{aligned} \Psi_{4,1,\pm 1}(x, y, z, Z_{\text{eff}}) &= \mp \frac{1}{512 a_0^3 \sqrt{10\pi}} e^{-\frac{\sqrt{x^2+y^2+z^2} Z_{\text{eff}}}{4a_0} \pm i \arctan(x,y)} \sqrt{x^2 + y^2} Z_{\text{eff}} \sqrt{\frac{Z_{\text{eff}}^3}{a_0^3}} \\ &\times (80 a_0^2 - 20 a_0 \sqrt{x^2 + y^2 + z^2} Z_{\text{eff}} + \sqrt{x^2 + y^2 + z^2}^2 Z_{\text{eff}}^2) \end{aligned}$$

$$\begin{aligned} \Psi_{4,2,0}(x, y, z, Z_{\text{eff}}) &= \frac{1}{1536 a_0^2 \sqrt{\pi}} e^{-\frac{\sqrt{x^2+y^2+z^2} Z_{\text{eff}}}{4a_0}} \left(-1 + \frac{3z^2}{\sqrt{x^2 + y^2 + z^2}^2}\right) (\sqrt{x^2 + y^2 + z^2})^2 Z_{\text{eff}} \sqrt{\frac{Z_{\text{eff}}^3}{a_0^3}} \\ &\times \left(6 - \frac{\sqrt{x^2 + y^2 + z^2} Z_{\text{eff}}}{2 a_0}\right) \end{aligned}$$

$$\begin{aligned} \Psi_{4,2,\pm 1}(x, y, z, Z_{\text{eff}}) &= \mp \frac{1}{256 a_0^2 \sqrt{6\pi}} e^{-\frac{\sqrt{x^2+y^2+z^2} Z_{\text{eff}}}{4a_0} \pm i \arctan(x,y)} z \sqrt{x^2 + y^2} Z_{\text{eff}} \sqrt{\frac{Z_{\text{eff}}^3}{a_0^3}} \\ &\times \left(6 - \frac{\sqrt{x^2 + y^2 + z^2} Z_{\text{eff}}}{2 a_0}\right) \end{aligned}$$

$$\begin{aligned} \Psi_{4,2,\pm 2}(x, y, z, Z_{\text{eff}}) &= \frac{1}{512 a_0^2 \sqrt{6\pi}} e^{-\frac{\sqrt{x^2+y^2+z^2} Z_{\text{eff}}}{4a_0} \pm 2i \arctan(x,y)} \sqrt{x^2 + y^2}^2 Z_{\text{eff}} \sqrt{\frac{Z_{\text{eff}}^3}{a_0^3}} \\ &\times \left(6 - \frac{\sqrt{x^2 + y^2 + z^2} Z_{\text{eff}}}{2 a_0}\right) \end{aligned}$$

The wave functions are transferred into Cartesian coordinates for an easier calculation of the overlap with other orbitals with known lattice positions in Cartesian coordinates. Here, a_0 is the Bohr radius and Z_{eff} the effective atomic number. Mind the case differentiation between positive and negative values of the arccosine function [BSMM00].

A.2.2 Atomic orbitals

The orbitals φ_m corresponds to the hydrogen wave functions as shown here [AF96, Dem05]:

$$\begin{aligned} \varphi_1(x, y, z) = s = \Psi_{5,0,0} &= \frac{1}{46875 a_0^4 \sqrt{5\pi}} e^{-\frac{\sqrt{x^2+y^2+z^2} Z_{\text{eff}}}{5a_0}} \sqrt{\frac{Z_{\text{eff}}^3}{a_0^3}} \\ &\times (9375 a_0^4 - 7500 a_0^3 \sqrt{x^2 + y^2 + z^2} Z_{\text{eff}} + 1500 a_0^2 \sqrt{x^2 + y^2 + z^2}^2 Z_{\text{eff}}^2 \\ &- 100 a_0 \sqrt{x^2 + y^2 + z^2}^3 Z_{\text{eff}}^3 + 2 \sqrt{x^2 + y^2 + z^2}^4 Z_{\text{eff}}^4) \end{aligned}$$

$$\begin{aligned} \varphi_2(x, y, z) = p_z = \Psi_{4,1,0} &= \frac{1}{512 a_0^3 \sqrt{5\pi}} e^{-\frac{\sqrt{x^2+y^2+z^2} Z_{\text{eff}}}{4a_0}} z Z_{\text{eff}} \sqrt{\frac{Z_{\text{eff}}^3}{a_0^3}} \\ &\times (80 a_0^2 - 20 a_0 \sqrt{x^2 + y^2 + z^2} Z_{\text{eff}} + \sqrt{x^2 + y^2 + z^2}^2 Z_{\text{eff}}^2) \end{aligned}$$

$$\begin{aligned} \varphi_3(x, y, z) = p_x &= \frac{1}{\sqrt{2}}(p_- - p_+) = \frac{1}{\sqrt{2}}(\Psi_{4,1,-1} - \Psi_{4,1,1}) \\ &= \frac{1}{512 a_0^3 \sqrt{5\pi}} e^{-\frac{\sqrt{x^2+y^2+z^2} Z_{\text{eff}}}{4a_0}} x Z_{\text{eff}} \sqrt{\frac{Z_{\text{eff}}^3}{a_0^3}} \\ &\times (80 a_0^2 - 20 a_0 \sqrt{x^2 + y^2 + z^2} Z_{\text{eff}} + \sqrt{x^2 + y^2 + z^2}^2 Z_{\text{eff}}^2) \end{aligned}$$

$$\begin{aligned} \varphi_4(x, y, z) = p_y &= \frac{i}{\sqrt{2}}(p_- + p_+) = \frac{i}{\sqrt{2}}(\Psi_{4,1,-1} + \Psi_{4,1,1}) \\ &= \frac{1}{512 a_0^3 \sqrt{5\pi}} e^{-\frac{\sqrt{x^2+y^2+z^2} Z_{\text{eff}}}{4a_0}} y Z_{\text{eff}} \sqrt{\frac{Z_{\text{eff}}^3}{a_0^3}} \\ &\times (80 a_0^2 - 20 a_0 \sqrt{x^2 + y^2 + z^2} Z_{\text{eff}} + \sqrt{x^2 + y^2 + z^2}^2 Z_{\text{eff}}^2). \end{aligned}$$

Mind, that the orbitals p_x and p_y cannot be related directly to the hydrogen wave functions. The real p_x and p_y orbitals are replaced by a linear combination of the imaginary p_+ and p_- orbitals, with $p_{\pm} = \Psi_{4,1,\pm 1}$.

Analogous for $d_{\pm 1}$ and $d_{\pm 2}$ one obtains:

$$\begin{aligned} \varphi_5(x, y, z) = d_{3z^2-r^2} = d_{z^2} = \Psi_{4,2,0} &= \left(\frac{5}{16\sqrt{\pi}}\right)^{\frac{1}{2}} R_{42}(r) (3z^2 - r^2) r^{-2} \\ &= \left(\frac{1}{4\sqrt{\pi}}\right)^{\frac{1}{2}} \left(\frac{Z_{\text{eff}}}{4a_0}\right)^3 e^{-\frac{Z_{\text{eff}}\sqrt{x^2+y^2+z^2}}{4a_0}} \left(1 - \frac{Z_{\text{eff}}\sqrt{x^2+y^2+z^2}}{12a_0}\right) (2z^2 - x^2 - y^2) \end{aligned}$$

$$\varphi_6(x, y, z) = d_{x^2-y^2} = \frac{1}{\sqrt{2}}(d_{+2} + d_{-2}) = \frac{1}{\sqrt{2}}(\Psi_{4,2,2} + \Psi_{4,2,-2}) = \left(\frac{15}{16\sqrt{\pi}}\right)^{\frac{1}{2}} R_{42}(r) (x^2 - y^2) r^{-2}$$

A Appendix

$$\begin{aligned}
&= \left(\frac{3}{4\sqrt{\pi}} \right)^{\frac{1}{2}} \left(\frac{Z_{\text{eff}}}{4a_0} \right)^3 e^{-\frac{Z_{\text{eff}}\sqrt{x^2+y^2+z^2}}{4a_0}} \left(1 - \frac{Z_{\text{eff}}\sqrt{x^2+y^2+z^2}}{12a_0} \right) (x^2 - y^2) \\
\varphi_7(x, y, z) = d_{xy} &= \frac{1}{i\sqrt{2}} (d_{+2} - d_{-2}) = \frac{1}{i\sqrt{2}} (\Psi_{4,2,2} - \Psi_{4,2,-2}) = \left(\frac{15}{4\sqrt{\pi}} \right)^{\frac{1}{2}} R_{42}(r) xy r^{-2} \\
&= \left(\frac{3}{\sqrt{\pi}} \right)^{\frac{1}{2}} \left(\frac{Z_{\text{eff}}}{4a_0} \right)^3 e^{-\frac{Z_{\text{eff}}\sqrt{x^2+y^2+z^2}}{4a_0}} \left(1 - \frac{Z_{\text{eff}}\sqrt{x^2+y^2+z^2}}{12a_0} \right) xy \\
\varphi_8(x, y, z) = d_{yz} &= \frac{1}{i\sqrt{2}} (d_{+1} + d_{-1}) = \frac{1}{i\sqrt{2}} (\Psi_{4,2,1} + \Psi_{4,2,-1}) = \left(\frac{15}{4\sqrt{\pi}} \right)^{\frac{1}{2}} R_{42}(r) yz r^{-2} \\
&= \left(\frac{3}{\sqrt{\pi}} \right)^{\frac{1}{2}} \left(\frac{Z_{\text{eff}}}{4a_0} \right)^3 e^{-\frac{Z_{\text{eff}}\sqrt{x^2+y^2+z^2}}{4a_0}} \left(1 - \frac{Z_{\text{eff}}\sqrt{x^2+y^2+z^2}}{12a_0} \right) yz \\
\varphi_9(x, y, z) = d_{zx} &= \frac{1}{\sqrt{2}} (d_{+1} - d_{-1}) = \frac{1}{\sqrt{2}} (\Psi_{4,2,1} - \Psi_{4,2,-1}) = \left(\frac{15}{4\sqrt{\pi}} \right)^{\frac{1}{2}} R_{42}(r) zx r^{-2} \\
&= \left(\frac{3}{\sqrt{\pi}} \right)^{\frac{1}{2}} \left(\frac{Z_{\text{eff}}}{4a_0} \right)^3 e^{-\frac{Z_{\text{eff}}\sqrt{x^2+y^2+z^2}}{4a_0}} \left(1 - \frac{Z_{\text{eff}}\sqrt{x^2+y^2+z^2}}{12a_0} \right) zx.
\end{aligned}$$

For the radial part $R_{42} = 2\sqrt{\frac{1}{5}} \left(\frac{Z_{\text{eff}}}{4a_0} \right)^{\frac{3}{2}} e^{-\frac{Z_{\text{eff}}r}{4a_0}} \left(\frac{Z_{\text{eff}}r}{4a_0} \right)^2 \left(1 - \frac{Z_{\text{eff}}r}{12a_0} \right)$ is used [Dem05]. The nomenclature of the indices shows the dependence of the non-radial part of the orbital function [AF96].

A.3 Fitting the effective atomic number with overlap calculations

Eq. (2.19b) gives the overlap matrix elements S for two orbitals φ_n and φ_m :

$$S_{nm} = \sum_{\mathbf{R}_j} e^{i\mathbf{k}\cdot(\mathbf{R}_j - \mathbf{R}_i)} \int \varphi_n^*(\mathbf{r} - \mathbf{R}_i) \varphi_m(\mathbf{r} - \mathbf{R}_j) dV. \quad (\text{A.11})$$

The results of these overlap elements S are given in [Pap86] by the Slater-Koster parameters. This enables a reconstruction of the effective atomic number because the orbitals φ depends on Z_{eff} .

The overlap is calculated between the same orbitals at a fixed wave vector $\mathbf{k} = 0$. The sum of Eq. (A.11) is taken only over the twelve nearest neighbors. Their contribution is too small. Instead, the overlap of the atom with itself contributes. Its value is 1 and so the main contribution of the sum. Together, the 13 integrals read

$$\begin{aligned} S_m = & \int \varphi_m^*(x, y, z, Z_{\text{eff}}) \varphi_m(x, y, z, Z_{\text{eff}}) dV \\ & + \int \varphi_m^*(x, y, z, Z_{\text{eff}}) \varphi_m(x - g, y - g, z, Z_{\text{eff}}) dV + \int \varphi_m^*(x, y, z, Z_{\text{eff}}) \varphi_m(x - g, y + g, z, Z_{\text{eff}}) dV \\ & + \int \varphi_m^*(x, y, z, Z_{\text{eff}}) \varphi_m(x + g, y - g, z, Z_{\text{eff}}) dV + \int \varphi_m^*(x, y, z, Z_{\text{eff}}) \varphi_m(x + g, y + g, z, Z_{\text{eff}}) dV \\ & + \int \varphi_m^*(x, y, z, Z_{\text{eff}}) \varphi_m(x - g, y, z - g, Z_{\text{eff}}) dV + \int \varphi_m^*(x, y, z, Z_{\text{eff}}) \varphi_m(x + g, y, z - g, Z_{\text{eff}}) dV \\ & + \int \varphi_m^*(x, y, z, Z_{\text{eff}}) \varphi_m(x, y - g, z - g, Z_{\text{eff}}) dV + \int \varphi_m^*(x, y, z, Z_{\text{eff}}) \varphi_m(x, y + g, z - g, Z_{\text{eff}}) dV \\ & + \int \varphi_m^*(x, y, z, Z_{\text{eff}}) \varphi_m(x - g, y, z + g, Z_{\text{eff}}) dV + \int \varphi_m^*(x, y, z, Z_{\text{eff}}) \varphi_m(x + g, y, z + g, Z_{\text{eff}}) dV \\ & + \int \varphi_m^*(x, y, z, Z_{\text{eff}}) \varphi_m(x, y - g, z + g, Z_{\text{eff}}) dV + \int \varphi_m^*(x, y, z, Z_{\text{eff}}) \varphi_m(x, y + g, z + g, Z_{\text{eff}}) dV. \end{aligned}$$

The twelve nearest neighbors are located from the central atom at position $\mathbf{R}_i = 0$ in two of the three Cartesian directions with a distance of the lattice constant g (see Fig. 2.9). The functions φ_m describe the nine different orbital basis function from Sec. A.2.2.

The atomic number Z_{eff} is optimized for supplying values for S_m that give a good agreement with the Slater-Koster parameters of [Pap86]. The results of these calculations are given in Tab. 2.2.

A.4 Céa's lemma

Céa's lemma says that it exists a constant C independent of V_h with

$$\|u - u_h\| \leq C \inf_{v_h \in V_h} \|u - v_h\|.$$

The next lines outline the proof of this lemma, using the Galerkin orthogonality condition and the Lax-Milgram theorem.

Since $v_h \in V_h \subset V$, the variational equation (4.1) supplies $a(u, v_h) = b(v_h)$ for all $v_h \in V$. Subtracting the discrete problem (4.4) from this equation provides the *Galerkin orthogonality condition* [BWS10]:

$$a(u - u_h, v_h) = 0 \quad \forall v_h \in V_h,$$

that can be used to get the equality

$$a(u - u_h, u - u_h) = a(u - u_h, u - v_h) \tag{A.12}$$

since $v_h - u_h \in V_h$.

For the following three conditions are assumed: for the bilinear form a and the linear form f exists constants $\alpha > 0, \beta, \gamma$ with

- (1) $a(v, v) \geq \alpha \|v\|^2 \quad \forall v \in V$ (“ a is positive”),
- (2) $|a(u, v)| \leq \beta \|u\| \|v\| \quad \forall u, v \in V$ (“ a is continuous”),
- (3) $|f(v)| \leq \gamma \|v\| \quad \forall v \in V$ (“ f is continuous”).

According to the *Lax-Milgram theorem*, with these conditions there is an unique solution $u \in V$ with $a(u, v) = b(v)$ for all $v \in V$. So

$$\alpha \|u - u_h\|^2 \stackrel{(1)}{\leq} a(u - u_h, u - u_h) \stackrel{(A.12)}{=} a(u - u_h, u - v_h) \stackrel{(2)}{\leq} \beta \|u - u_h\| \|u - v_h\|$$

and consequently $\|u - u_h\| \leq \frac{\beta}{\alpha} \|u - v_h\|$ can be concluded. Since that inequality is valid for all $v_h \in V_h$, Céa's lemma (4.8) is satisfied. Poisson's equation satisfies the conditions (1-3).

Bibliography

- [ABB⁺07] AESCHLIMANN, M.; BAUER, M.; BAYER, D.; BRIXNER, T.; DE ABAJO, F. J. G.; PFEIFFER, W.; ROHMER, M.; SPINDLER, C.; and STEEB, F. *Adaptive subwavelength control of nano-optical fields*. *Nature*, 446:301–304 (2007)
- [ABB⁺10] AESCHLIMANN, M.; BAUER, M.; BAYER, D.; BRIXNER, T.; CUNOVIC, S.; DIMLER, F.; FISCHER, A.; PFEIFFER, W.; ROHMER, M.; SCHNEIDER, C.; STEEB, F.; STRÜBER, C.; and VORONINE, D. *Spatiotemporal control of nanooptical excitations*. *Proc. Natl. Acad. Sci. USA*, 107(12):5329–5333 (2010)
- [ABF⁺11] AESCHLIMANN, M.; BRIXNER, T.; FISCHER, A.; KRAMER, C.; MELCHIOR, P.; PFEIFFER, W.; SCHNEIDER, C.; STRÜBER, C.; TUCHSCHERER, P.; and VORONINE, D. V. *Coherent Two-Dimensional Nanoscopy*. *Science*, 333(6050):1723–1726 (2011)
- [ABP07] DE ABAJO, F. J. G.; BRIXNER, T.; and PFEIFFER, W. *Nanoscale force manipulation in the vicinity of a metal nanostructure*. *Journal of Physics B: Atomic, Molecular and Optical Physics*, 40(11):S249 (2007)
- [ACRS74] ANTONANGELI, F.; COLAVITA, E.; ROSEI, R.; and SALUSTI, S. *Optical gaps and interband matrix elements of silver as a function of temperature*. *Il Nuovo Cimento B* (1971-1996), 24:121–129 (1974)
- [AF96] ATKINS, P. W. and FRIEDMAN, R. S. *Molecular Quantum Mechanics*. Oxford University Press, USA, 3rd edn. (1996)
- [AK04] AXT, V. M. and KUHN, T. *Femtosecond spectroscopy in semiconductors: a key to coherences, correlations and quantum kinetics*. *Rep. Prog. Phys.*, 67:433 (2004)
- [Ali96] ALIVISATOS, A. P. *Semiconductor Clusters, Nanocrystals, and Quantum Dots*. *Science*, 271(5251):933–937 (1996)
- [AM07] ASHCROFT, N. and MERMIN, D. *Festkörperphysik*. Oldenbourg Wissenschaftsverlag, 3rd edn. (2007)
- [AP10] ATWATER HARRY A. and POLMAN ALBERT. *Plasmonics for improved photovoltaic devices*. *Nat Mater*, 9(3):205–213 (2010)
- [APV⁺09] ABRAMAVICIUS, D.; PALMIERI, B.; VORONINE, D. V.; SANDA, F.; and MUKAMEL, S. *Coherent Multidimensional Optical Spectroscopy of Excitons in Molecular Aggregates; Quasiparticle vs. Supermolecule Perspectives*. *Chem. Rev.*, 109:2350–2408 (2009)
- [AVM08] ABRAMAVICIUS, D.; VORONINE, D. V.; and MUKAMEL, S. *Double-quantum resonances and exciton-scattering in coherent 2D spectroscopy of photosynthetic complexes*. *PNAS*, 105(25):8525–8530 (2008)
- [BAS⁺06] BRIXNER, T.; DE ABAJO, F. J. G.; SCHNEIDER, J.; SPINDLER, C.; and PEIFFER, W. *Ultrafast adaptive optical near-field control*. *Phys. Rev. B*, 73:125437 (2006)

Bibliography

- [BASP05] BRIXNER, T.; GARCÍA DE ABAJO, F. J.; SCHNEIDER, J.; and PFEIFFER, W. *Nanoscopic Ultrafast Space-Time-Resolved Spectroscopy*. Phys. Rev. Lett., 95(9):093901 (2005)
- [BASP06] BRIXNER, T.; GARCÍA DE ABAJO, F.; SPINDLER, C.; and PFEIFFER, W. *Adaptive ultrafast nano-optics in a tight focus*. Applied Physics B: Lasers and Optics, 84:89–95 (2006)
- [BDE03] BARNES, W.; DEREUX, A.; and EBBESEN, T. *Surface plasmon subwavelength optics*. Nature, 424(6950):824–830– (2003)
- [Bei02] BEISER. *Concepts of Modern Physics*. Mcgraw Hill Higher Education, 6th edn. (2002)
- [Ber94] BERENGER, J.-P. *A Perfectly Matched Layer for the Absorption of Electromagnetic Waves*. Journal of Computational Physics, 114:185–200 (1994)
- [BG01] BRIXNER, T. and GERBER, G. *Femtosecond polarization pulse shaping*. Opt. Lett., 26(8):557–559 (2001)
- [BHLK88] BANYAI, L.; HU, Y. Z.; LINDBERG, M.; and KOCH, S. W. *Third-order optical nonlinearities in semiconductor microstructures*. Phys. Rev. B, 38:8142–8153 (1988)
- [BL07] BORRI, P. and LANGBEIN, W. *Four-wave mixing dynamics of excitons in InGaAs self-assembled quantum dots*. J. Phys.: Condens. Matter, 19(29):295201 (2007)
- [BLMH99] BORRI, P.; LANGBEIN, W.; MØRK, J.; and HVAM, J. *Heterodyne pump-probe and four-wave mixing in semiconductor optical amplifiers using balanced lock-in detection*. Opt. Commun., 169(1-6):317 – 324 (1999)
- [BLMZ06] BORRI, P.; LANGBEIN, W.; MULJAROV, E. A.; and ZIMMERMANN, R. *Dephasing of excited-state excitons in InGaAs quantum dots*. Phys. Status Solidi B, 243(15):3890–3894 (2006)
- [BLS⁺01] BORRI, P.; LANGBEIN, W.; SCHNEIDER, S.; WOGGON, U.; SELLIN, R. L.; OUYANG, D.; and BIMBERG, D. *Ultralong Dephasing Time in InGaAs Quantum Dots*. Phys. Rev. Lett., 87(15):157401 (2001)
- [BLS⁺02] BORRI, P.; LANGBEIN, W.; SCHNEIDER, S.; WOGGON, U.; SELLIN, R. L.; OUYANG, D.; and BIMBERG, D. *Relaxation and Dephasing of Multiexcitons in Semiconductor Quantum Dots*. Phys. Rev. Lett., 89(18):187401 (2002)
- [BLW⁺05] BORRI, P.; LANGBEIN, W.; WOGGON, U.; STAVARACHE, V.; REUTER, D.; and WIECK, A. D. *Exciton dephasing via phonon interactions in InAs quantum dots: Dependence on quantum confinement*. Phys. Rev. B, 71:115328 (2005)
- [Bor02] BORRI, P. *Ultrafast Optical Properties of Quantum Dot Amplifiers*. In M. Grundmann (Ed.), *Nano-Optoelectronics*, NanoScience and Technology, pp. 411–430. Springer Berlin Heidelberg (2002)
- [Bra07] BRAESS, D. *Finite Elements: Theory, Fast Solvers, and Applications in Solid Mechanics*. Cambridge University Press, 3rd edn. (2007)
- [BS64] BERGLUND, C. N. and SPICER, W. E. *Photoemission Studies of Copper and Silver: Experiment*. Phys. Rev., 136:A1044–A1064 (1964)

- [BS03] BERGMAN, D. J. and STOCKMAN, M. I. *Surface Plasmon Amplification by Stimulated Emission of Radiation: Quantum Generation of Coherent Surface Plasmons in Nanosystems*. Phys. Rev. Lett., 90:027402 (2003)
- [BSK⁺10] BRINKS, D.; STEFANI, F. D.; KULZER, F.; HILDNER, R.; TAMINIAU, T. H.; AVLASEVICH, Y.; MULLEN, K.; and VAN HULST, N. F. *Visualizing and controlling vibrational wave packets of single molecules*. Nature, 465(7300):905–908 (2010)
- [BSMM00] BRONSTEIN, I. N.; SEMENDJAJEW, K. A.; MUSIOL, G.; and MÜHLIG, H. *Taschenbuch der Mathematik*. Deutsch (Harri) (2000)
- [BSV⁺05] BRIKNER TOBIAS; STENGER JENS; VASWANI HARSHA M.; CHO MINHAENG; BLANKENSHIP ROBERT E.; and FLEMING GRAHAM R. *Two-dimensional spectroscopy of electronic couplings in photosynthesis*. Nature, 434(7033):625–628 (2005)
- [BWS10] BABUSKA, I.; WHITEMAN, J.; and STROUBOULIS, T. *Finite Elements: An Introduction to the Method and Error Estimation*. Oxford University Press, USA (2010)
- [BZ83] BLÜMICH, B. and ZIESSOW, D. *Multidimensional spectroscopy*. Molecular Physics, 48(5):955–968 (1983)
- [BZPS08] BURGER, S.; ZSCHIEDRICH, L.; POMPLUN, J.; and SCHMIDT, F. *JCMSuite: An Adaptive FEM Solver for Precise Simulations in Nano-Optics*. In *Integrated Photonics and Nanophotonics Research and Applications* (2008)
- [Bän91] BÄNSCH, E. *Local mesh refinement in 2 and 3 dimensions*. IMPACT of Computing in Science and Engineering, 3(3):181 – 191 (1991)
- [Cho08] CHO, M. *Coherent Two-Dimensional Optical Spectroscopy*. Chemical Reviews, 108(4):1331–1418 (2008)
- [Cho09] CHO, M. *Two-Dimensional Optical Spectroscopy*. CRC Press, 1st edn. (2009)
- [Chr72] CHRISTENSEN, N. E. *The Band Structure of Silver and Optical Interband Transitions*. physica status solidi (b), 54(2):551–563 (1972)
- [Chr76] CHRISTENSEN, N. E. *High-energy band structure of gold*. Physical Review B, 13:2698–2701 (1976)
- [CK99] CHOW, W. W. and KOCH, S. W. *Semiconductor-Laser Fundamentals: Physics of the Gain Materials*. Springer, 1st edn. (1999)
- [CK07] CORKUM, P. B. and KRAUSZ, F. *Attosecond science*. Nat Phys, 3(6):381–387 (2007)
- [CKR09] CARMELE, A.; KNORR, A.; and RICHTER, M. *Photon statistics as a probe for exciton correlations in coupled nanostructures*. Phys. Rev. B, 79:035316 (2009)
- [CMN⁺10] CHRISTENSSON, N.; MILOTA, F.; NEMETH, A.; PUGLIESI, I.; RIEDLE, E.; SPERLING, J.; PULLERITS, T.; KAUFFMANN, H. F.; and HAUER, J. *Electronic Double-Quantum Coherences and Their Impact on Ultrafast Spectroscopy: The Example of \dot{I}^2 -Carotene*. The Journal of Physical Chemistry Letters, 1(23):3366–3370 (2010)
- [CRR67] CLEMENTI, E.; RAIMONDI, D. L.; and REINHARDT, W. P. *Atomic Screening Constants from SCF Functions. II. Atoms with 37 to 86 Electrons*. The Journal of Chemical Physics, 47(4):1300–1307 (1967)

Bibliography

- [CS71] CHRISTENSEN, N. E. and SERAPHIN, B. O. *Relativistic Band Calculation and the Optical Properties of Gold*. Phys. Rev. B, Vol. 4:3321–3344 (1971) http://prb.aps.org/abstract/PRB/v4/i10/p3321_1
- [CS80] CHARI, M. V. K. and SILVESTER, P. P. *Finite Elements in Electrical and Magnetic Field Problems (Wiley Series in Numerical Methods in Engineering)*. John Wiley & Sons Inc, first edition edn. (1980)
- [CSB⁺02] CHEN, G.; STIEVATER, T. H.; BATTEH, E. T.; LI, X.; STEEL, D. G.; GAMMON, D.; KATZER, D. S.; PARK, D.; and SHAM, L. J. *Biexciton Quantum Coherence in a Single Quantum Dot*. Phys. Rev. Lett., 88:117901 (2002)
- [CSFM92] CHO, M.; SCHERER, N. F.; FLEMING, G. R.; and MUKAMEL, S. *Photon echoes and four-wave-mixing spectroscopies*. J. Chem. Phys., 96(8):5618–5629 (1992)
- [CTDL07] COHEN-TANNOUDJI, C.; DIU, B.; and LALOË, F. *Quantenmechanik*. No. Bd. 1 in *Quantenmechanik*. De Gruyter (2007)
- [DAFK06] DANCKWERTS, J.; AHN, K. J.; FÖRSTNER, J.; and KNORR, A. *Theory of ultrafast nonlinear optics of Coulomb-coupled semiconductor quantum dots: Rabi oscillations and pump-probe spectra*. Phys. Rev. B, 73(16):165318 (2006)
- [Dav09] DAVID, C. *Theory of Plasmonic Optical Enhancement in Hybrid Metal-Molecule Structures*. Technische Universität Berlin, Institut für Theoretische Physik, Diploma Thesis (2009)
- [Dem05] DEMTRÖDER, W. *Experimentalphysik 3: Atome, Moleküle und Festkörper (Springer-Lehrbuch) (German Edition)*. Springer, 3rd edn. (2005)
- [DMR⁺10] DACHNER, M.-R.; MALIC, E.; RICHTER, M.; CARMELE, A.; KABUSS, J.; WILMS, A.; KIM, J.-E.; HARTMANN, G.; WOLTERS, J.; BANDELOW, U.; and KNORR, A. *Theory of carrier and photon dynamics in quantum dot light emitters*. physica status solidi (b), 247(4):809–828 (2010)
- [DRK⁺10] DAVID, C.; RICHTER, M.; KNORR, A.; WEIDINGER, I. M.; and HILDEBRANDT, P. *Image dipoles approach to the local field enhancement in nanostructured Ag–Au hybrid devices*. The Journal of Chemical Physics, 132(2):024712 (2010)
- [EBW87] ERNST, R. R.; BODENHAUSEN, G.; and WOKAUN, A. *Principles of nuclear magnetic resonance in one and two dimensions* (1987)
- [ECR⁺07] ENGEL, G. S.; CALHOUN, T. R.; READ, E. L.; AHN, T.-K.; MANCAL, T.; CHENG, Y.-C.; BLANKENSHIP, R. E.; and FLEMING, G. R. *Evidence for wavelike energy transfer through quantum coherence in photosynthetic systems*. Nature, 446:782–786 (2007)
- [Eic86] EICHLER, H. J. *Laser-Induced Dynamic Gratings (Springer Series in Optical Sciences)*. Springer-Verlag (1986)
- [ELG09] EL, R.; LEE, H.; and GR, F. *Photon echo studies of photosynthetic light harvesting*. Photosynth. Res., 101(2-3):233–43 (2009)
- [Ems89] EMSLEY, J. *The Elements*. Oxford University Press, USA (1989)

- [EP62] EHRENREICH, H. and PHILIPP, H. R. *Optical Properties of Ag and Cu*. Phys. Rev., 128:1622–1629 (1962)
- [ERM06] ETCHEGOIN, P. G.; RU, E. C. L.; and MEYER, M. *An analytic model for the optical properties of gold*. J. Chem. Phys., 125:164705 (2006)
- [ERM07] ETCHEGOIN, P. G.; RU, E. C. L.; and MEYER, M. *Erratum: "An analytic model for the optical properties of gold"*. J. Chem. Phys., 127:189901 (2007)
- [Fan57] FANO, U. *Description of States in Quantum Mechanics by Density Matrix and Operator Techniques*. Rev. Mod. Phys., 29(1):74–93 (1957)
- [FG00] FREY, P. and GEORGE, P. *Mesh generation: application to finite elements*. Hermès Science (2000)
- [FGHW10] FENG, J.-J.; GERNERT, U.; HILDEBRANDT, P.; and WEIDINGER, I. M. *Induced SER-Activity in Nanostructured Ag-Silica-Au Supports via Long-Range Plasmon Coupling*. Advanced Functional Materials, 20(12):1954–1961 (2010)
- [FGS⁺09] FENG, J.-J.; GERNERT, U.; SEZER, M.; KUHLMANN, U.; MURGIDA, D. H.; DAVID, C.; RICHTER, M.; KNORR, A.; HILDEBRANDT, P.; and WEIDINGER, I. M. *Novel Au-Ag Hybrid Device for Electrochemical SE(R)R Spectroscopy in a Wide Potential and Spectral Range*. Nano Letters, 9(1):298–303 (2009)
- [För65] FÖRSTER, T. *Delocalized Excitation and Excitation Transfer*. In O. Sinanoglu (Ed.), *Modern Quantum Chemistry*, pp. 93–137. Academic Press, New York (1965)
- [FS75] FLATEN, C. J. and STERN, E. A. *Optical constants of some silver alloys*. Phys. Rev. B, 11:638–650 (1975)
- [FSW⁺98] VON FREYMAN, G.; SCHIMMEL, T.; WEGENER, M.; HANEWINKEL, B.; KNORR, A.; and KOCH, S. W. *Computer simulations on near-field scanning optical microscopy: Can subwavelength resolution be obtained using uncoated optical fiber probes?* Appl. Phys. Lett., 73(9):1170–1172 (1998)
- [FTB⁺90] FUSTER, G.; TYLER, J. M.; BRENER, N. E.; CALLAWAY, J.; and BAGAYOKO, D. *Electronic structure and related properties of silver*. Physical Review B, 42:7322–7329 (1990)
- [GCF09] GINSBERG, N. S.; CHENG, Y.-C.; and FLEMING, G. R. *Two-Dimensional Electronic Spectroscopy of Molecular Aggregates*. Accounts Chem. Res., 42(9):1352–1363 (2009)
- [GEI⁺99] GUENTHER, T.; EMILIANI, V.; INTONTI, E.; LIENAU, C.; ELSAESSER, T.; NOTZEL, R.; and PLOOG, K. H. *Femtosecond near-field spectroscopy of a single GaAs quantum wire*. Appl. Phys. Lett., 75(22):3500–3502 (1999)
- [GKW⁺10] GEORG, S.; KABUSS, J.; WEIDINGER, I. M.; MURGIDA, D. H.; HILDEBRANDT, P.; KNORR, A.; and RICHTER, M. *Distance-dependent electron transfer rate of immobilized redox proteins: A statistical physics approach*. Phys. Rev. E, 81:046101 (2010)
- [GLE⁺02] GUENTHER, T.; LIENAU, C.; ELSAESSER, T.; GLANEMANN, M.; AXT, V. M.; KUHN, T.; ESHLAGHI, S.; and WIECK, A. D. *Coherent Nonlinear Optical Response of Single Quantum Dots Studied by Ultrafast Near-Field Spectroscopy*. Phys. Rev. Lett., 89:057401 (2002)

Bibliography

- [GMK75] GENZEL, L.; MARTIN, T. P.; and KREIBIG, U. *Dielectric function and plasma resonances of small metal particles*. Zeitschrift für Physik B Condensed Matter, 21:339–346 (1975)
- [GRT93] GOERING, H.; ROOS, H.; and TOBISKA, L. *Finite-Element-Methode*. Akad.-Verl. (1993)
- [GWH⁺10] GERHARDT, I.; WRIGGE, G.; HWANG, J.; ZUMOFEN, G.; and SANDOGHDAR, V. *Coherent nonlinear single-molecule microscopy*. Phys. Rev. A, 82(6):063823 (2010)
- [HAFJ98] HYBL, J. D.; ALBRECHT, A. W.; FAEDER, S. M. G.; and JONAS, D. M. *Two-dimensional electronic spectroscopy*. Chemical Physics Letters, 297(3-4):307 – 313 (1998)
- [Ham05] HAMM, P. *Principles of Nonlinear Optical Spectroscopy: A Practical Approach* (2005)
- [HFH⁺93] HÖVEL, H.; FRITZ, S.; HILGER, A.; KREIBIG, U.; and VOLLMER, M. *Width of cluster plasmon resonances: Bulk dielectric functions and chemical interface damping*. Phys. Rev. B, 48:18178–18188 (1993)
- [HK04] HAUG, H. and KOCH, S. W. *Quantum Theory of the Optical and Electronic Properties of Semiconductors, Fourth Edition*. World Scientific Publishing Company, 4th edn. (2004)
- [HLK90] HU, Y. Z.; LINDBERG, M.; and KOCH, S. W. *Theory of optically excited intrinsic semiconductor quantum dots*. Phys. Rev. B, 42:1713–1723 (1990)
- [HM08] HARBOLA, U. and MUKAMEL, S. *Superoperator nonequilibrium Green's function theory of many-body systems; applications to charge transfer and transport in open junctions*. Phys.Rep., 465(5):191 – 222 (2008)
- [HNES09] HUANG, X.; NERETINA, S.; and EL-SAYED, M. A. *Gold Nanorods: From Synthesis and Properties to Biological and Biomedical Applications*. Advanced Materials, 21(48):4880–4910 (2009)
- [HVT⁺09] HUANG, J. S.; VORONINE, D. V.; TUCHSCHERER, P.; BRIXNER, T.; and HECHT, B. *Deterministic spatiotemporal control of optical fields in nanoantennas and plasmonic circuits*. Phys. Rev. B, 79:195441 (2009)
- [HZ11] HAMM, P. and ZANNI, M. *Concepts and Methods of 2d Infrared Spectroscopy*. Cambridge University Press (2011)
- [IF10] ISHIZAKI, A. and FLEMING, G. R. *Quantum superpositions in photosynthetic light harvesting: delocalization and entanglement*. N. J. Phys., 12(5):055004 (2010)
- [IF12] ISHIZAKI, A. and FLEMING, G. R. *Quantum Coherence in Photosynthetic Light Harvesting*. Annu. Rev. of Condens. Matter Physics, 3(1):333–361 (2012)
- [Jac98] JACKSON, J. D. *Classical Electrodynamics Third Edition*. Wiley, 3rd edn. (1998)
- [JC72] JOHNSON, P. B. and CHRISTY, R. W. *Optical Constants of noble metals*. Phys. Rev. B, Vol. 6:4370–4379 (1972) http://prb.aps.org/abstract/PRB/v6/i12/p4370_1

- [Jen06] JENSEN, F. *Introduction to Computational Chemistry*. Wiley, 2nd edn. (2006)
- [JHW98] JACAK, L.; HAWRYLAK, P.; and WÓJS, A. *Quantum Dots*. Springer, New-York (1998)
- [Jin02] JIN, J. *The Finite Element Method in Electromagnetics*. A Wiley-Interscience publication. Wiley (2002)
- [Jon03a] JONAS, D. M. *Optical Analogs of 2D NMR*. *Science*, 300(5625):1515–1517 (2003)
- [Jon03b] JONAS DM. *Two-dimensional femtosecond spectroscopy*. *Annual review of physical chemistry*, 54:425–63 (2003)
- [JS83] JOHNSTON, N. A. and SHOLL, C. A. *Charge densities in FCC transition metals*. *Journal of Physics F: Metal Physics*, 13(5):945 (1983)
- [KAK02] KRUMMHEUER, B.; AXT, V. M.; and KUHN, T. *Theory of pure dephasing and the resulting absorption line shape in semiconductor quantum dots*. *Phys. Rev. B*, 65(19):195313 (2002)
- [Kaw01] KAWATA, S. (Ed.). *Near-Field Optics and Surface Plasmon Polaritons*. Springer-Verlag (2001)
- [KCCM07] KAPTEYN, H.; COHEN, O.; CHRISTOV, I.; and MURNANE, M. *Harnessing Attosecond Science in the Quest for Coherent X-rays*. *Science*, 317(5839):775–778 (2007)
- [KCZS03] KELLY, K. L.; CORONADO, E.; ZHAO, L. L.; and SCHATZ, G. C. *The Optical Properties of Metal Nanoparticles: The Influence of Size, Shape, and Dielectric Environment*. *The Journal of Physical Chemistry B*, 107(3):668–677 (2003)
- [KFR90] KÄMMEL, G.; FRANECK, H.; and RECKE, H. *Einführung in die Methode der finiten Elemente*. Hanser (1990)
- [KMS09] KIM, J.; MUKAMEL, S.; and SCHOLE, G. D. *Two-Dimensional Electronic Double-Quantum Coherence Spectroscopy*. *Acc. Chem. Res.*, 42(9):1375–1384 (2009)
- [KT01] KATO, T. and TANIMURA, Y. *Multi-dimensional vibrational spectroscopy measured from different phase-matching conditions*. *Chemical Physics Letters*, 341:329 – 337 (2001)
- [KTW99] KEUSTERS, D.; TAN, H.-S.; and WARREN. *Role of Pulse Phase and Direction in Two-Dimensional Optical Spectroscopy*. *J. Phys. Chem. A*, 103(49):10369–10380 (1999)
- [KYF⁺09] KINKHABWALA, A.; YU, Z.; FAN, S.; AVLASEVICH, Y.; MULLEN, K.; and MOERNER, W. E. *Large single-molecule fluorescence enhancements produced by a bowtie nanoantenna*. *Nat Photon*, 3(11):654–657 (2009)
- [LCF07] LEE, H.; CHENG, Y.-C.; and FLEMING, G. R. *Coherence Dynamics in Photosynthesis: Protein Protection of Excitonic Coherence*. *Science*, 316(5830):1462–1465 (2007)
- [LCH08] LAL, S.; CLARE, S. E.; and HALAS, N. J. *Nanoshell-Enabled Photothermal Cancer Therapy: Impending Clinical Impact*. *Accounts of Chemical Research*, 41(12):1842–1851 (2008)

Bibliography

- [Lee85] LEE, D.; ALBRECHT, A. C. *Advances in Infrared and Raman Spectroscopy*. Wiley-Heyden: Chichester, 1st edn. (1985)
- [Lia70] LIANG, W. Y. *Excitons*. *Physics Education*, 5(4):226 (1970)
- [LKF⁺12] LY, H. K.; KÖHLER, C.; FISCHER, A.; KABUSS, J.; SCHLOSSER, F.; SCHOTH, M.; KNORR, A.; and WEIDINGER, I. M. *Induced Surface Enhancement in Coral Pt Island Films Attached to Nanostructured Ag Electrodes*. *Langmuir*, 28(13):5819–5825 (2012)
- [LKK⁺08] LOBINO, M.; KORYSTOV, D.; KUPCHAK, C.; FIGUEROA, E.; SANDERS, B. C.; and LVOVSKY, A. I. *Complete Characterization of Quantum-Optical Processes*. *Science*, 322(5901):563–566 (2008)
- [LKR⁺93] LEONARD, D.; KRISHNAMURTHY, M.; REAVES, C. M.; DENBAARS, S. P.; and PETROFF, P. M. *Direct formation of quantum-sized dots from uniform coherent islands of InGaAs on GaAs surfaces*. *Applied Physics Letters*, 63(23):3203–3205 (1993)
- [LRNB03] LOVETT, B. W.; REINA, J. H.; NAZIR, A.; and BRIGGS, G. A. D. *Optical schemes for quantum computation in quantum dot molecules*. *Phys. Rev. B*, 68:205319 (2003)
- [LW08] LACKNER, M. and WINTER, F. (Eds.). *Lasers in Chemistry*. Wiley-VCH, 1st edn. (2008)
- [LWS⁺03] LI, X.; WU, Y.; STEEL, D.; GAMMON, D.; STIEVATER, T. H.; KATZER, D. S.; PARK, D.; PIERMAROCCHI, C.; and SHAM, L. J. *An All-Optical Quantum Gate in a Semiconductor Quantum Dot*. *Science*, 301(5634):809–811 (2003)
- [LZBC06] LI, X.; ZHANG, T.; BORCA, C. N.; and CUNDIFF, S. T. *Many-Body Interactions in Semiconductors Probed by Optical Two-Dimensional Fourier Transform Spectroscopy*. *Phys. Rev. Lett.*, 96:057406 (2006)
- [Mai07] MAIER, S. A. *Plasmonics: Fundamentals and Applications*. Springer, 1st edn. (2007)
- [Max65] MAXWELL, J. C. *A Dynamical Theory of the Electromagnetic Field*. *Philosophical Transactions of the Royal Society of London*, 155:459–512 (1865)
- [MBS⁺11] MELCHIOR, P.; BAYER, D.; SCHNEIDER, C.; FISCHER, A.; ROHMER, M.; PFEIFFER, W.; and AESCHLIMANN, M. *Optical near-field interference in the excitation of a bowtie nanoantenna*. *Phys. Rev. B*, 83:235407 (2011)
- [MCM97] MEIER, T.; CHERNYAK, V.; and MUKAMEL, S. *Femtosecond photon echoes in molecular aggregates*. *J. Chem. Phys.*, 107(21):8759–8780 (1997)
- [ME00] MEYER, S. and ENGEL, V. *Non-perturbative wave-packet calculations of time-resolved four-wave-mixing signals*. *Applied Physics B: Lasers and Optics*, 71:293–297 (2000)
- [MHM⁺06] MALIC, E.; HIRTSCHULZ, M.; MILDE, F.; KNORR, A.; and REICH, S. *Analytical approach to optical absorption in carbon nanotubes*. *Phys. Rev. B*, 74(19):195431 (2006)

- [MHM08] MARX, C. A.; HARBOLA, U.; and MUKAMEL, S. *Nonlinear optical spectroscopy of single, few, and many molecules: Nonequilibrium Green's function QED approach*. Phys. Rev. A, 77(2):022110 (2008)
- [MJ77] MARTON, J. P. and JORDAN, B. D. *Optical properties of aggregated metal systems: Interband transitions*. Phys. Rev. B, 15 No. 4:1719–1727 (1977)
- [MKZ⁺08] MERLEIN, J.; KAHL, M.; ZUSCHLAG, A.; SELL, A.; HALM, A.; BONEBERG, J.; LEIDERER, P.; LEITENSTORFER, A.; and BRATSCHEITSCHE, R. *Nanomechanical control of an optical antenna*. Nat. Photonics, 2(4):230–233 (2008)
- [ML86] MUKAMEL, S. and LORING, R. F. *Nonlinear response function for time-domain and frequency-domain four-wave mixing*. J. Opt. Soc. Am. B, 3(4):595–606 (1986)
- [MM96] MECOZZI, A. and MØRK, J. *Theory of heterodyne pump-probe experiments with femtosecond pulses*. J. Opt. Soc. Am. B, 13(11):2437–2452 (1996)
- [MOY07] MUKAMEL, S.; OSZWALDOWSKI, R.; and YANG, L. *A coherent nonlinear optical signal induced by electron correlations*. J. Chem. Phys., 127(22):221105 (2007)
- [MP96] MEHL, M. J. and PAPACONSTANTOPOULOS, D. A. *Applications of a tight-binding total-energy method for transition and noble metals: Elastic constants, vacancies, and surfaces of monatomic metals*. Phys. Rev. B, 54:4519–4530 (1996)
- [MPF06] MANCAL, T.; PISLIAKOV, A. V.; and FLEMING, G. R. *Two-dimensional optical three-pulse photon echo spectroscopy. I. Nonperturbative approach to the calculation of spectra*. J. Chem. Phys, 124(23):234504 (2006)
- [MTH09] MUKAMEL, S.; TANIMURA, Y.; and HAMM, P. *Coherent Multidimensional Optical Spectroscopy*. Acc. Chem. Res., 42(9):1207–1209 (2009)
- [Muk95] MUKAMEL, S. *Principles of nonlinear optical spectroscopy*. Oxford University Press, New York (1995)
- [Muk00] MUKAMEL, S. *Multidimensional femtosecond correlation spectroscopies of electronic and vibrational excitations*. Annu. Rev. Phys. Chem., 51(1):691–729 (2000)
- [Muk03] MUKAMEL, S. *Superoperator representation of nonlinear response: Unifying quantum field and mode coupling theories*. Phys. Rev. E, 68(2):021111 (2003)
- [NH11] NOVOTNY, L. and VAN HULST, N. *Antennas for light*. Nat Photon, 5(2):83–90 (2011)
- [NLB⁺05] NAZIR, A.; LOVETT, B. W.; BARRETT, S. D.; REINA, J. H.; and BRIGGS, G. A. D. *Anticrossings in Förster coupled quantum dots*. Phys. Rev. B, 71:045334 (2005)
- [NV73] NORRIE, D. H. and DE VRIES, G. *Finite Element Method: Fundamentals and Applications*. Academic Press Inc, first edition edn. (1973)
- [Pal85] PALIK, E. D. *Handbook of Optical Constants of Solids, Five-Volume Set: Handbook of Optical Constants of Solids: Volume 1 (Academic Press Handbook)*. Academic Press (1985)
- [Pap86] PAPACONSTANTOPOULOS, D. A. *Handbook of the Band Structure of Elemental Solids*. Springer, 1st edn. (1986)

Bibliography

- [PBZS07] POMPLUN, J.; BURGER, S.; ZSCHIEDRICH, L.; and SCHMIDT, F. *Adaptive finite element method for simulation of optical nano structures*. Phys. Status Solidi B, 244:3419 – 3434 (2007)
- [PM03] PAPACONSTANTOPOULOS, D. A. and MEHL, M. J. *The Slater-Koster tight-binding method: a computationally efficient and accurate approach*. Journal of Physics: Condensed Matter, 15(10):R413 (2003)
- [Pom09] POMPLUN, J. *Reduced basis method for electromagnetic scattering problems*. Ph.D. thesis (2009)
- [PRP⁺04] PETTINGER, B.; REN, B.; PICARDI, G.; SCHUSTER, R.; and ERTL, G. *Nanoscale Probing of Adsorbed Species by Tip-Enhanced Raman Spectroscopy*. Phys. Rev. Lett., 92(9):096101 (2004)
- [PS69] PELLIS, G. P. and SHIGA, M. *The optical properties of copper and gold as a function of temperature*. Journal of Physics C: Solid State Physics, 2(10):1835 (1969)
- [PS85] PREPARATA, F. and SHAMOS, M. *Computational Geometry: An Introduction*. Texts and Monographs in Computer Science. Springer-Verlag (1985)
- [Que92] QUE, W. *Excitons in quantum dots with parabolic confinement*. Phys. Rev. B, 45:11036–11041 (1992)
- [RAK⁺06] RICHTER, M.; AHN, K. J.; KNORR, A.; SCHLIWA, A.; BIMBERG, D.; MADJET, M. E.-A.; and RENGER, T. *Theory of excitation transfer in coupled nanostructures - from quantum dots to light harvesting complexes*. Phys. Status Solidi B, 243(10):2302–2310 (2006)
- [Ram70] RAMCHANDANI, M. G. *Energy band structure of gold*. Journal of Physics C: Solid State Physics, 3(1S):S1 (1970)
- [Rec73] RECHENBERG, I. *Evolutionsstrategie: Optimierung technischer Systeme nach Prinzipien der biologischen Evolution (Problemata, 15) (German Edition)*. Frommann-Holzboog (1973)
- [RM09] REICHELT, M. and MEIER, T. *Shaping the spatiotemporal dynamics of the electron density in a hybrid metal-semiconductor nanostructure*. Opt. Lett., 34(19):2900–2902 (2009)
- [RM10a] RAHAV, S. and MUKAMEL, S. *Multidimensional attosecond photoelectron spectroscopy with shaped pulses and quantum optical fields*. Phys. Rev. A, 81(6):063810 (2010)
- [RM10b] RICHTER, M. and MUKAMEL, S. *Ultrafast double-quantum-coherence spectroscopy of excitons with entangled photons*. Phys. Rev. A, 82:013820 (2010)
- [RSS⁺12] RICHTER, M.; SCHLOSSER, F.; SCHOTH, M.; BURGER, S.; SCHMIDT, F.; KNORR, A.; and MUKAMEL, S. *Reconstruction of the wave functions of coupled nanoscopic emitters using a coherent optical technique*. Phys. Rev. B, 86:085308 (2012)
- [SBC⁺10] SCHULLER, J. A.; BARNARD, E. S.; CAI, W.; JUN, Y. C.; WHITE, J. S.; and BRONGERSMA, M. L. *Plasmonics for extreme light concentration and manipulation*. Nat. Mat., 9(3):193–204 (2010)

- [SCCG⁺09] SCHLAU-COHEN, G. S.; CALHOUN, T. R.; GINSBERG, N. S.; READ, E. L.; BALLOTTARI, M.; BASSI, R.; VAN GRONDELLE, R.; and FLEMING, G. R. *Pathways of Energy Flow in LHCII from Two-Dimensional Electronic Spectroscopy*. J. Phys. Chem. B, 113(46):15352–15363 (2009)
- [SCDF12] SCHLAU-COHEN, G.; DAWLATY, J.; and FLEMING, G. *Ultrafast Multidimensional Spectroscopy: Principles and Applications to Photosynthetic Systems*. IEEE J. Sel. Top. Quant., 18(1):283–295 (2012)
- [Sch91] SCHWARZ, H. R. *Methode der finiten Elemente*. Teubner B.G. GmbH (1991)
- [SCIF11] SCHLAU-COHEN, G. S.; ISHIZAKI, A.; and FLEMING, G. R. *Two-dimensional electronic spectroscopy and photosynthesis: Fundamentals and applications to photosynthetic light-harvesting*. Chem. Phys., 386:1–22 (2011)
- [SDW⁺11] STOCK, E.; DACHNER, M.-R.; WARMING, T.; SCHLIWA, A.; LOCHMANN, A.; HOFFMANN, A.; TOROPOV, A. I.; BAKAROV, A. K.; DEREBEZOV, I. A.; RICHTER, M.; HAISLER, V. A.; KNORR, A.; and BIMBERG, D. *Acoustic and optical phonon scattering in a single In(Ga)As quantum dot*. Phys. Rev. B, 83:041304 (2011)
- [SFB02] STOCKMAN, M. I.; FALEEV, S. V.; and BERGMAN, D. J. *Coherent Control of Femtosecond Energy Localization in Nanosystems*. Phys. Rev. Lett., 88(6):067402 (2002)
- [SHW⁺01] STAHPREBERG, K.; HERRMANN, T.; WILMERS, K.; ESSER, N.; RICHTER, W.; and LEE, M. J. G. *Optical properties of copper and silver in the energy range 2.5–9.0 eV*. Phys. Rev. B, 64:115111 (2001)
- [SK54] SLATER, J. C. and KOSTER, G. F. *Simplified LCAO Method for the Periodic Potential Problem*. Phys. Rev., 94:1498–1524 (1954)
- [SKMR12] SCHLOSSER, F.; KNORR, A.; MUKAMEL, S.; and RICHTER, M. *Using localized double quantum coherence spectroscopy for retrieving the biexciton wave function (unpublished, submitted to N. J. Phys.)* (2012)
- [Sla30] SLATER, J. C. *Atomic Shielding Constants*. Phys. Rev., 36:57–64 (1930)
- [SM01] SCHEURER, C. and MUKAMEL, S. *Design strategies for pulse sequences in multidimensional optical spectroscopies*. J. Chem. Phys., 115(11):4989–5004 (2001)
- [SM02] SCHEURER, C. and MUKAMEL, S. *Magnetic Resonance Analogies in Multidimensional Vibrational Spectroscopy*. Bulletin of the Chemical Society of Japan, 75(5):989–999 (2002)
- [SM08] SCHWEIGERT, I. V. and MUKAMEL, S. *Simulating multidimensional optical wave-mixing signals with finite-pulse envelopes*. Phys. Rev. A, 77:033802 (2008)
- [SNB03] SOSA, I. O.; NOGUEZ, C.; and BARRERA, R. G. *Optical Properties of Metal Nanoparticles with Arbitrary Shapes*. The Journal of Physical Chemistry B, 107(26):6269–6275 (2003)
- [SRKR12] SCHOTH, M.; RICHTER, M.; KNORR, A.; and RENGER, T. *Line Narrowing of Excited-State Transitions in Nonlinear Polarization Spectroscopy: Application to Water-Soluble Chlorophyll-Binding Protein*. Phys. Rev. Lett., 108:178104 (2012)

Bibliography

- [SS05] SCHMIDT, A. and SIEBERT, K. *Design of Adaptive Finite Element Software: The Finite Element Toolbox Alberta*. Lecture Notes in Computational Science and Engineering. Springer (2005)
- [SSB⁺11] SCHLOSSER, F.; SCHOTH, M.; BURGER, S.; SCHMIDT, F.; KNORR, A.; MUKAMEL, S.; and RICHTER, M. *Ultrafast nonlinear spectroscopy with spatially confined fields*. AIP Conference Proceedings, 1398(1):94–96 (2011)
- [SSB⁺12] SCHLOSSER, F.; SCHOTH, M.; BURGER, S.; SCHMIDT, F.; KNORR, A.; MUKAMEL, S.; and RICHTER, M. *Coherent Nonlinear Spectroscopy with Spatiotemporally Controlled Fields*. In *CLEO: QELS-Fundamental Science*, p. QF3D.6. Optical Society of America (2012)
- [SSH⁺12] SCHLOSSER, F.; SCHOTH, M.; HIREMATH, K.; BURGER, S.; SCHMIDT, F.; KNORR, A.; MUKAMEL, S.; and RICHTER, M. *Combining nanooptical fields and coherent spectroscopy on systems with delocalized excitons*. Ultrafast Phenomena and Nanophotonics XVI, 8260(1):82601V (2012)
- [Sto11a] STOCKMAN, M. I. *Nanoplasmonics: past, present, and glimpse into future*. Opt. Express, 19(22):22029–22106 (2011)
- [Sto11b] STOCKMAN, M. I. *Nanoplasmonics: The physics behind the applications*. Physics Today, 64(2):39–44 (2011)
- [TKSW03] TIAN, P.; KEUSTERS, D.; SUZAKI, Y.; and WARREN, W. S. *Femtosecond Phase-Coherent Two-Dimensional Spectroscopy*. Science, 300(5625):1553–1555 (2003)
- [UML⁺05] UNOLD, T.; MUELLER, K.; LIENAU, C.; ELSAESSER, T.; and WIECK, A. D. *Optical Control of Excitons in a Pair of Quantum Dots Coupled by the Dipole-Dipole Interaction*. Phys. Rev. Lett., 94:137404 (2005)
- [Vek94] VEKTRAI, G. *A new approach to the molecular biexciton theory*. J. Chem. Phys., 101(4):3031 (1994)
- [VVKH12] VAN VLACK, C.; KRISTENSEN, P. T.; and HUGHES, S. *Spontaneous emission spectra and quantum light-matter interactions from a strongly coupled quantum dot metal-nanoparticle system*. Phys. Rev. B, 85:075303 (2012)
- [Wat81] WATSON, D. F. *Computing the n-dimensional Delaunay tessellation with application to Voronoi polytopes*. The Computer Journal, 24(2):167–172 (1981)
- [WBSC⁺11] WEBER-BARGIONI, A.; SCHWARTZBERG, A.; CORNAGLIA, M.; ISMACH, A.; URBAN, J. J.; PANG, Y.; GORDON, R.; BOKOR, J.; SALMERON, M. B.; OGLETREE, D. F.; ASHBY, P.; and CABRINI, S. A. *Hyperspectral Nanoscale Imaging on Dielectric Substrates with Coaxial Optical Antenna Scan Probes*. Nano Lett., 11(3):1201–1207 (2011)
- [Wit11] WIT, A. D. (Ed.). *Solvay*, vol. 3 of *Procedia Chemistry* (2011)
- [Wri11] WRIGHT, J. C. *Multiresonant Coherent Multidimensional Spectroscopy*. Annual Review of Physical Chemistry, 62(1):209–230 (2011)
- [YF99a] YANG, M. and FLEMING, G. R. *Third-order nonlinear optical response of energy transfer systems*. J. Chem. Phys., 111(1):27–39 (1999)

- [YF99b] YANG, M. and FLEMING, G. R. *Two-color three-pulse photon echoes as a probe of electronic coupling in molecular complexes*. J. Chem. Phys., 110(6):2983–2990 (1999)
- [YM08a] YANG, L. and MUKAMEL, S. *Dissecting quantum pathways in two-dimensional correlation spectroscopy of semiconductors*. Journal of Physics: Condensed Matter, 20(39):395202 (2008)
- [YM08b] YANG, L. and MUKAMEL, S. *Revealing exciton-exciton couplings in semiconductors using multidimensional four-wave mixing signals*. Phys. Rev. B, 77(7):075335 (2008)
- [YM08c] YANG, L. and MUKAMEL, S. *Two-Dimensional Correlation Spectroscopy of Two-Exciton Resonances in Semiconductor Quantum Wells*. Phys. Rev. Lett., 100(5):057402 (2008)
- [YZAG11] YUEN-ZHOU, J. and ASPURU-GUZI, A. *Quantum process tomography of excitonic dimers from two-dimensional electronic spectroscopy. I. General theory and application to homodimers*. J. Chem. Phys., 134(13):134505 (2011)
- [ZBK⁺05] ZSCHIEDRICH, L.; BURGER, S.; KLOSE, R.; SCHÄDLE, A.; and SCHMIDT, F. *JCM-mode: an adaptive finite element solver for the computation of leaky modes*. In Y. Sidorin and C. A. Wächter (Eds.), *Integrated Optics: Devices, Materials, and Technologies IX*, vol. 5728, pp. 192 – 202 (2005)
- [ZBPS07] ZSCHIEDRICH, L.; BURGER, S.; POMPLUN, J.; and SCHMIDT, F. *Goal oriented adaptive finite element method for precise simulation of optical components*. In Y. Sidorin and C. A. Waechter (Eds.), *Proc. SPIE, Integrated Optics: Devices, Materials, and Technologies XI*, vol. 6475 (2007)
- [ZC09] ZHUKOV, V. P. and CHULKOV, E. V. *The femtosecond dynamics of electrons in metals*. Physics-Uspokhi, 52(2):105 (2009)
- [ZCM99] ZHANG, W. M.; CHERNYAK, V.; and MUKAMEL, S. *Multidimensional femtosecond correlation spectroscopies of electronic and vibrational excitons*. J. Chem. Phys., 110:5011–5028 (1999)
- [ZKSS06] ZSCHIEDRICH, L.; KLOSE, R.; SCHÄDLE, A.; and SCHMIDT, F. *A new finite element realization of the Perfectly Matched Layer Method for Helmholtz scattering problems on polygonal domains in 2D*. J. Comput. Appl. Math., 188:12 – 32 (2006)
- [ZMCM97] ZHANG, W. M.; MEIER, T.; CHERNYAK, V.; and MUKAMEL, S. *Exciton-migration and three-pulse femtosecond optical spectroscopies of photosynthetic antenna complexes*. J. Chem. Phys., 108(18):7763 (1997)
- [Zsc09] ZSCHIEDRICH, L. *Transparent boundary conditions for Maxwell's equations: Numerical concepts beyond the PML method*. Ph.D. thesis (2009)
- [ZWBW⁺09] ZHANG, Z.; WEBER-BARGIONI, A.; WU, S. W.; DHUEY, S.; CABRINI, S.; and SCHUCK, P. J. *Manipulating Nanoscale Light Fields with the Asymmetric Bowtie Nano-Colorsorter*. Nano Lett., 9(12):4505–4509 (2009)

Index

- absorption, 24
- absorption coefficient, 13
- adaptive mesh refinement, 44
- ansatz function, 40
- antenna-like geometries, 57
- approximate solution, 39
- atomic number, effective, 22

- band structure, 19
- basis
 - biexciton, 72
 - delocalized, 74
 - exciton, 72
 - local, 73
- Beer-Lambert law, 13
- biexciton basis, 72
- Bravais lattice, 19

- Céa's lemma, 42
- coherent spectroscopy, 77
- continuity equation, 10
- control mechanisms, 49
- convergence, 42
- cost function, 53
- coupled nanospheres, 30
- coupled quantum systems, 71
- current density, 9

- Delaunay triangulation, 44
- density operator, 65
- dielectric displacement, 9
- dielectric function, 12
- dipole plasmon resonance, 28
- dipole transition matrix element, 24
- Dirac picture, 69
- Dirichlet boundary condition, 38
- Dirichlet-to-Neumann operator, 46, 47
- discrete problem, 39
- displacement, dielectric, 9
- double quantum coherence spectroscopy,
94
- double-exciton basis, 72
- doubled-sided Feynman diagram, 81
- Drude conductivity, 14
- Drude model, 13
- Dyson series, 68

- effective atomic number, 22
- electric field, 9
- Electromagnetism, 9
- electron configuration, 19, 21
- evaluation, 53
- excited state absorption, 91
- excited-state stimulated emission, 91
- exciton basis, 72
- excitons, 71
- extinction coefficient, 13

- Förster coupling, 72
- face-centered cubic, 19
- Fermi level, 20
- Feynman diagram, doubled-sided, 81
- filtering different resonances, 117
- finite element method, 37
- fitness function, 53
- flip algorithm, 44
- four-wave mixing, 85
- frequency, angular, 11

- Galerkin orthogonality condition, 140
- genetic algorithm, 52
- ground state bleaching, 91

- Hamiltonian, system, 73
- Heisenberg picture, 68
- Helmholtz equation, 11
- heterodyne detection, 88
- Hilbert space, 66
- homodyne detection, 88
- hybrid nanospheres, 29
- hydrogen wave functions, 21

- interaction picture, 69

Index

- inverse photon echo spectroscopy, 90
- Lax-Milgram theorem, 140
- LCAO, 19
- linear combination of atomic orbitals, 19
- linear optical response, 78
- linear polarization, 78
- Liouville pathways, 82
- Liouville representation, 67
- Liouville-Von Neumann equation, 67
- local oscillator, 88
- localized spectroscopy, 99
- long range plasmon excitation, 30

- magnetic field, 9
- magnetic flux density, 9
- mass matrix, 41
- material equations, 10
- material model, 13
- Maxwell solver, 37
- Maxwell's equations, 9
- mesh, adaptive refinement, 44
- metal nanospheres, 27
- metals, 9
- multidimensional spectroscopy, 77
- multiwave mixing, 85
- mutation, 52
- mutation step size, 54

- nanoplasmonics, 27
- nanospheres
 - coupled, 30
 - hybrid, 29
 - metal, 27
- Nitsche's trick, 43
- nonlinear response function, 79, 80
- nonlinear spectroscopy, 77
- nonlinearity, 78
- nuclear magnetic resonance, 77

- optical linear response, 78

- perfectly matched layers (PML), 47
- perturbation expansion, 69
- phase cycling, 87
- phase matching, 86
- photon echo spectroscopy, 90
- plane waves, 11
- plasma frequency, 14
- Poisson's equation, 42
- polarization, linear, 78

- problem classes, 44
- pump-probe spectroscopy, 77

- quantum dots, 71
- quasistatic approximation, 27

- random geometries, 56
- refractive index, 12
- response function, nonlinear, 79, 80
- response, linear optical, 78
- rotating wave approximation, 83
- rotating wave approximation (RWA), 84

- scattering problem, 45
- Schrödinger equation, 66
- Schrödinger picture, 68
- selection, 53
- spatiotemporal control, 49
- spectra, two-dimensional, 90
- spectroscopy
 - double quantum coherence, 94
 - inverse photon echo, 90
 - localized, 99
 - multidimensional coherent nonlinear, 77
 - photon echo, 90
 - pump-probe, 77
- statistical average, 66
- stiffness matrix, 41
- susceptibility, dielectric, 10
- system Hamiltonian, 73

- third-order techniques, 88
- time evolution operator, 67
- transition matrix element, 24
- transparent boundary conditions, 46
- triangulation, 44
- two-dimensional spectra, 90
- two-exciton basis, 72

- variational equation, 38

- wave equations, 11
- wave, plane, 11
- waveguide-like geometries, 58
- wavenumber, angular, 11

Danksagung

Bedanken möchte ich mich bei all jenen, die mir das Entstehen dieser Arbeit überhaupt ermöglicht und erleichtert haben. Dazu gehört – allen voran – mein Doktorvater Professor Andreas Knorr, der mich herzlich in seine Arbeitsgruppe aufgenommen hat und mich jederzeit hervorragend unterstützte und ermutigte. In diesem Sinne gilt ebenfalls mein besonderer Dank Marten Richter, der selbst in 10000 Kilometern Entfernung um eine intensive Betreuung bemüht war. Sein Wissen und seine Ideen wirken unbegrenzt. Nicht von Ungefähr kommt der Spruch: „Marten hat immer recht“.

Professorin Ulrike Woggon danke ich dafür, dass sie den Prüfungsvorsitz übernommen hat, und Professor Frank Schmidt für das Erstellen des Zweitgutachtens.

Weiteren Dank spreche ich Professor Shaul Mukamel für die Zusammenarbeit auf dem Gebiet der Spektroskopiemethoden aus. Innerhalb meines Schwerpunktprojekts möchte ich Frank Schmidt, Sven Burger, Jan Pomplun und Kiran Hiremath vom Zuse-Institut Berlin danken, unter anderem für die gute Betreuung hinsichtlich „JCMSuite“. Außerdem gilt mein Dank Jens Förstner, Matthias Reichelt und Professor Torsten Meier aus Paderborn für die wertvollen Diskussionen über die Anwendbarkeit von genetischen Algorithmen, Professor Rudolf Bratschitsch für die nützlichen Gespräche über Nanoantennen und Professor Martin Aeschlimann für die Anregungen über verschiedene Geometrien für Nanostrukturen. Für die Zusammenarbeit im Nanoplasmonikprojekt danke ich Julia Kabuß und Christopher Köhler sowie Inez Weidinger und ihrer Arbeitsgruppe. Julia Kabuß danke ich auch für die Anmerkungen zu einem Teil der Arbeit. Professor Stephan Koch und seiner Arbeitsgruppe aus Marburg danke ich für die gute Zusammenarbeit.

Ich habe mich in der Arbeitsgruppe von Andreas Knorr immer sehr wohl gefühlt, was an jedem einzelnen Mitglied lag. Dafür möchte ich mich hiermit bei allen Arbeitskollegen bedanken. Ein riesiges Dankeschön hat Mario Schoth verdient! Er lieferte mir nicht nur für einen Großteil dieser Arbeit Anmerkungen, sondern unterstützte mich auch in besonderem Maße während der ganzen Zeit durch seine unermüdliche Hilfsbereitschaft und Kenntnisse sowohl thematisch als auch bei Computerproblemen aller Art. Zudem sei ihm für seinen Einsatz im Ultrafast-Nanooptics-Schwerpunktprojekt gedankt. Ein Dankeschön an meine Bürokollegen (besonders dafür, dass sie mein ständiges Naschen ertragen haben) und an alle Mensabegleiter. Insbesondere danke ich Uyen Dang für ihre beruhigenden Worte und Hilfen in allen Lebenslagen und für ihre Anmerkungen zur Arbeit, Evgeny Bobkin und Torben Winzer für ihren Humor (Torben und Mario auch für den schönen Amerikaaufenthalt), Sandra Kuhn für ihr offenes Ohr bei Problemen aller Art und Frank Milde für seine vielfältigen Unterstützung und dafür, dass ich mich seinetwegen beim Essen nie hetzen musste. Auch Franz Schulze, Sverre Theuerholz und Pierce Munnelly sei für ihre Anmerkungen zur Arbeit gedankt.

Herzlichen Dank möchte ich allen meinen Freunden aussprechen. Sie haben nicht nur mein Leben neben der Arbeit bereichert, sondern motivierten mich auch immer wieder. In besonderem Maße danke ich Florian für seine vielfache, oft kurzfristige Unterstützung während der gesamten Zeit, obwohl er bis heute noch nicht an die Abgabe der Arbeit glaubt.

Abschließend danke ich natürlich meinen Eltern und meiner Omi, ohne deren großzügige Unterstützung alles nicht möglich gewesen wäre.